GROWTH AND CHARACTERISATION OF COPPER INDIUM SELENIDE FILMS

by

SYDNEY NIGRIN, B.Sc.

A thesis submitted in partial fulfilment of
the requirements for the degree of
Doctor of Philosophy of the University
of London and for the Diploma of Imperial College

Department of Electrical Engineering
Imperial College of Science and Technology
London, SW7 2BT

June 1983

ABSTRACT

Thin films of Copper Indium Selenide ($CuInSe_2$) have been prepared by evaporating powders of the compound synthesised by the fusion of a stoichiometric mixture of the elements.

The structure and chemical composition of the bulk material were investigated by X-ray diffraction and Electron Probe Microanalysis (EPMA), to act as a basis for comparison with thin film properties. Bragg reflections extra to those tabulated for $CuInSe_2$ have been detected and some of these have been attributed to unreported weak chalcopyrite reflections. The rest of the spurious diffraction lines were confirmed by EPMA to be due to a second phase in the ingot. Evidence for a wide existence region for the $CuInSe_2$ phase was also obtained from the composition analysis.

In order to establish reproducible deposition conditions, the rate of evaporation of the powders has been monitored. This revealed the occurrence of three distinct evaporation regimes in which the composition of the vapour changed from Se to In-Se and finally to a Se-Cu mixture.

The adopted evaporation technique yielded thin films with good structural and compositional reproducibility despite the inhomogeneous nature of the starting powder.

The films, which were deposited mainly onto cold glass substrates, consisted initially of a stratified structure. Single-phased p- and n-type $CuInSe_2$ films were obtained by a post deposition anneal at 350°C. Transmission electron micrographs indicated that the films were polycrystalline, having an average crystallite size approximately equal to the film thickness.

The refractive index and absorption coefficients of the homogeneous $CuInSe_2$ films below and above the band edge have been obtained by optical

transmission and reflection measurements. The comparison with single crystal data, confirmed the quality of the films.

D.C electrical resistivity, Hall effect and thermoelectric power measurements indicated that the films were highly conductive. Prolonged annealing up to 35 hours at 350°C resulted an increase in the carrier concentration of the p-type films and a decrease in the carrier density of the n-type films. This was attributed to the net creation of indium vacancies.

A change of majority carrier type from p- to n-type was observed after an anneal at 450°C. It was proposed that the formation of a highly conducting surface oxide layer could account for such a conversion.

The temperature dependence of mobility of the films was also studied and it was concluded that the mobility limiting mechanism was scattering due to ionised impurities.

ACKNOWLEDGEMENTS

I am deeply grateful to Dr. M.J. Lee for his continuing keen interest, guidance and constructive criticisms during the course of this work. I would also like to express my gratitude to Professor J.C. Anderson for providing me with the opportunity to undertake this project.

My thanks are also due to all my colleagues in the Materials Section for many stimulating discussions and assistance and I especially thank Mr. C.P. Judge for his advice and help during the Transmission Electron Microscopy studies. I am also grateful to Mr. K.G. White for his technical assistance at various stages of this work.

I wish to thank Miss C.D.M. Collins for undertaking the arduous task of typing the text and to Mr. R. Puddy for preparing some of the drawings and photographs.

I also acknowledge with gratitude the financial support of the Science Research Council, which has made it possible for me to undertake this research.

Finally, I am indebted to my mother and my brother for their continual encouragement and patience throughout the duration of this study.

CONTENTS

Page

CHAPTER 1

INTRODUCTION

1.1 THE THIN FILM TRANSISTOR

The thin film transistor (TFT) is the thin film equivalent of the Silicon MOS-FET and was introduced by Weimer[1] as an active device to be incorporated with thin film passive components on insulator substrates by relatively low cost processes. While TFT circuits may not compete with the highly advanced Silicon technology in which a high density of devices are packed over a small area, they are suitable in applications where relatively large areas must be covered by a large number of active devices. In this respect the TFT offers an attractive solution to the problem of addressing large area liquid crystal matrix displays, where each picture point requires a switching element.

While both p- and n-type channel TFT's have been produced over the years, using various materials, a complementary TFT has not been prepared. The characteristic of this device is that it integrates both p-channel and n-channel FET's on the same substrate with the potential of obtaining switching devices with very low power consumption.

Various approaches may be taken to prepare the semiconductor channels in a complementary TFT. One way would be the deposition of two different materials having n- and p-type conductivities respectively. Alternatively, one could deposit a single semiconductor film and attempt to dope it by extrinsic impurities. Another possibility would be the use of a semiconductor which can be made in n- and p-type film form by changing its stoichiometry, in other words doping it intrinsically to prepare the respective channels of the TFT's.

From the point of view of fabrication processes, compatibility and complexity, the last approach is the more promising method. Hence

semiconductor materials that exist in both n- and p-type form by virtue of slight compositional variations, and having properties suitable for TFT applications, will have to be found and assessed.

In the TFT, the main requirement is that the source-drain channel current can be modulated over many orders of magnitude by inducing carriers through the application of a gate voltage. For useful transistor behaviour this effectively means that the carrier concentration of the semiconductor film be less than about 10^{17} cm^3 for practically controllable film thicknesses of about 1000 Å.

It is also preferable that the carriers in the semiconductor film have high mobilities as this results in improved switching speeds. While well known high mobility materials like InSb[3], InAs[4], PbS[5], PbTe[6] and Te[7] have been tried for TFT applications, these compounds were found to be susceptible to carrier inversion at sufficiently high operating voltages[6] due to their low band gap. It now appears that a high mobility and low carrier concentration semiconductor film is not a sufficient prerequisite and that the material suitable for TFT's must also have a band gap somewhat larger than about 1 eV. This is evidenced by the success of the larger band gap compounds CdS[8] and CdSe[2].

With the above-mentioned material requirements in mind, a survey of the band gap, electrical properties and stoichiometry of a range of semiconductor materials was made. For a short list the reader may refer to Pamplin et al [9]. From such a survey Copper Indium Selenide ($CuInSe_2$) was chosen for further study as its band gap of about 1 eV, its high carrier mobilities and the fact that it exists in n- and p-type form makes it a potentially good candidate for TFT applications.

This ternary compound had recently attracted considerable interest as the photovoltaically active semiconductor in thin film solar cells, because of its band gap. In photovoltaic cell applications the other main requirement for the absorber film is a low resistivity, in the range

10^{-2} - 1 Ω.cm[10], and a n-CdS/p-$CuInSe_2$ thin film solar cell was first reported by Kazmerski et al[11] in 1977.

Since the demonstration of a feasible thin film photovoltaic device, employing this ternary compound, work has gone into the preparation of $CuInSe_2$ films by various methods for use in low cost cells. However, a survey of the literature (see Section 3.1), indicated that considerable difficulties existed in producing good quality films.

Thus the aim of the work reported in this thesis is to attempt to grow by a reproducible and low cost method, Copper Indium Selenide films which are single phased and stoichiometric for TFT and solar cell applications.

1.2 ORGANISATION OF THESIS

As background information for the interpretation of the experimental data, the rest of this introductory chapter deals with the physical and chemical properties of bulk $CuInSe_2$.

In the preparation of compound films, it is essential that these have the correct ratio of the constituent elements so that the control of stoichiometry of the films will be of utmost importance. This is difficult for binary compounds[12] and will be expected to be even more complex for ternary compounds in which the volatility of each constituent is different. In this work a procedure based on the thermal evaporation of bulk $CuInSe_2$ was adopted to prepare films with reproducible properties and it is, therefore, necessary to correlate the properties of the starting material and the films.

The chemical composition and homogeneity of the bulk ingot was determined using X-ray diffraction and Electron Microprobe Analysis and these are described in Chapter 2. This chapter also presents the compositional changes occurring during the free evaporation of $CuInSe_2$ as monitored by the change in frequency shift rate of an oscillating quartz

crystal. These experiments were performed to obtain the practical evaporation conditions from which stoichiometric thin films could be prepared.

In Chapter 3, the preparation method of $CuInSe_2$ thin films is described and their structure, as examined by X-ray diffraction and Transmission Electron Microscopy, is subsequently presented as a function of heat treatment procedures. The chemical composition of the films, as determined by Electron Probe Microanalysis, is used to indicate that single phased $CuInSe_2$ films are obtainable reproducibly with the growth method adopted. This chapter also looks briefly at the effects of oxygen on the structural and compositional properties of $CuInSe_2$ films.

In Chapter 4, the optical properties of the films are given to confirm their good quality. The D.C. resistivity, Hall effect and thermoelectric power measurements of the films are also presented in this chapter and discussed in the light of structural changes occurring after anneals. Conclusions about the electrical transport processes are also drawn from the study of the electrical properties as a function of temperature.

Finally, Chapter 5 gives a summary and concluding remarks on the work presented in this thesis.

1.3 PROPERTIES OF $CuInSe_2$

In this section some properties of bulk $CuInSe_2$ relevant in this study are presented.

1.3.1 Crystal Structure

Copper Indium Selenide belongs to the chalcopyrite family of semiconductors with the general formula I-III-VI_2. These materials are the ternary analogs of the binary compound of the II-VI family.

Their crystallographic structure is derived from the sphalerite (Zincblende) structure shown in Figure 1.1(a). In Zincblende (ZnS), the Zn atoms are regularly placed on a face centred cubic lattice and the S atoms are placed on a similar lattice, translated with respect to the first by a quarter of the length of the cube body diagonal. ZnS is tetrahedrally coordinated and each Zn atom is bonded to four nearest S atoms, while each S atom is bonded to four nearest Zn atoms.

The chalcopyrite structure may be derived if the Zn atoms are replaced by two metals, one of lower valence, Cu for instance, and one of higher valence, In for instance. As the average number of valence electrons is not changed in this substitution, it is possible for the new structure, the chalcopyrite, to retain the tetrahedral arrangement of the original sphalerite. However the ordered replacement results in the cubic Bravais lattice being doubled and, by definition, this takes place along the z-direction, resulting in a tetragonal superstructure of Zincblende. This is shown in Figure 1.1(b) for $CuInSe_2$ where each Cu and each In atom is tetrahedrally coordinated to four Se atoms, while each Se atom is tetrahedrally coordinated to two Cu and two In atoms. This implies that the bonding is primarily covalent with Sp^3 hybrid bonds prevailing, although some degree of ionicity is also present due to the electro-negativity differences of the atoms.

The chalcopyrites belong to the tetragonal space group $I\bar{4}2d$, with four formula units per cell and the atomic distribution for $CuInSe_2$ is as follows[13]:

4 Cu atoms in positions $\quad 000;\ 0\ \frac{1}{2}\ \frac{1}{4};\ \frac{1}{2}\ \frac{1}{2}\ \frac{1}{2};\ \frac{1}{2}\ 0\ \frac{3}{4}$

4 In atoms in positions $\quad 00\frac{1}{2};\ 0\ \frac{1}{2}\ \frac{3}{4};\ \frac{1}{2}\ \frac{1}{2}\ 0;\ \frac{1}{2}\ 0\ \frac{1}{4}$

8 Se atoms in positions $\quad x\ \frac{1}{4}\ \frac{1}{8};\ \bar{x}\ \frac{3}{4}\ \frac{1}{8};\ \frac{3}{4}\ x\ \frac{7}{8};\ \frac{1}{4}\ \bar{x}\ \frac{7}{8};$

$$x + \frac{1}{2}\ \frac{3}{4}\ \frac{1}{2};\ \frac{1}{2} - x\ \frac{1}{4}\ \frac{5}{8};\ \frac{1}{4}\ x + \frac{1}{2}\ \frac{3}{8};\ \frac{3}{4}\ \frac{1}{2} - x\ \frac{3}{8}$$

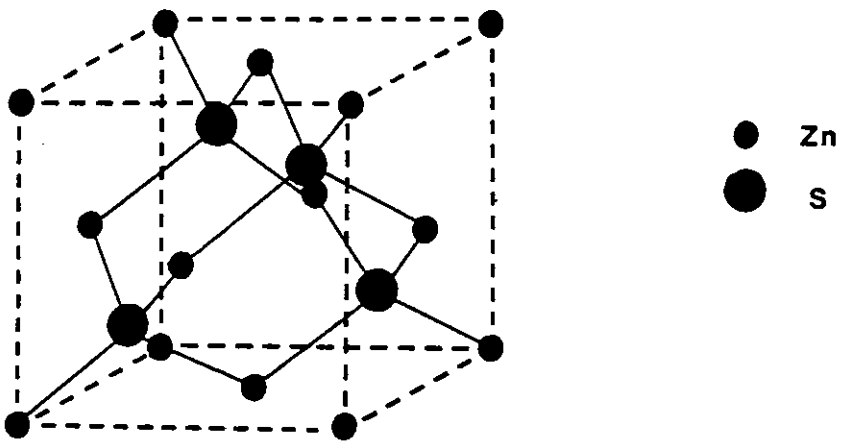

Fig. 1.1(a): Sphalerite Structure of ZnS

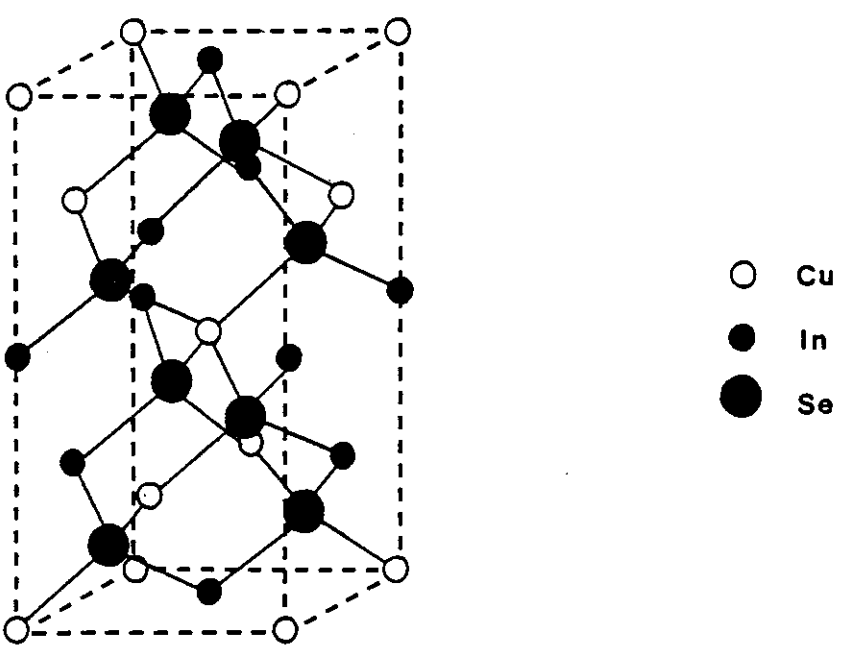

Fig. 1.1(b): Chalcopyrite Structure of $CuInSe_2$

The positions of the Copper and Indium atoms are sphalerite-like and the selenium positions would also correspond to the sphalerite structure if $x = \frac{1}{4}$. The value of x, known as the free parameter, locates the position of Se atoms and has been determined as $x = 0.224$[14] and $x = 0.235$[15] for $CuInSe_2$.

The accepted lattice parameters for $CuInSe_2$ are $a = 5.782$ Å and $c = 11.620$ Å[15] and the X-ray powder lines are tabulated in the Joint Committee on Powder Diffraction Standards (JCPDS) file No. 23-209.

1.3.2 Phase Diagram

Unlike their binary counterpart II-VI compounds, the chalcopyrites show stoichiometry variations of several percent. The existence region of the chalcopyrite at room temperature must strictly speaking be represented in an isothermal section of the ternary phase diagram. Such diagrams are scarce in the literature, however, and only a few have been determined. An example of such a ternary phase relations around $CuGaSe_2$[16] is reproduced in Fig. 1.2. This compound also belongs to the I-III-VI_2 chalcopyrite family and its existence region is shown in the middle of the diagram. It is evdident that the chalcopyrite phase exists in a wide composition region with excess solubility for Se, Ga-Se and Cu-Ga. The shaded areas in the phase diagram distinguish two phase regions from three phase regions. These indicate that unless the chemical composition is well controlled, the ternary compound will contain many unwanted secondary phase precipitates.

As far as other chalcopyrites are concerned, only the I_2VI-III_2VI_3 pseudobinary joins of the ternary phase diagram have been so far determined. These diagrams are like conventional binary phase diagrams and represent a vertical cross section of the composition-temperature relationship of the ternary diagram. Such a phase plot for $CuInSe_2$ was first presented by Palatnik et al[17] and later confirmed by Parkes et al[24].

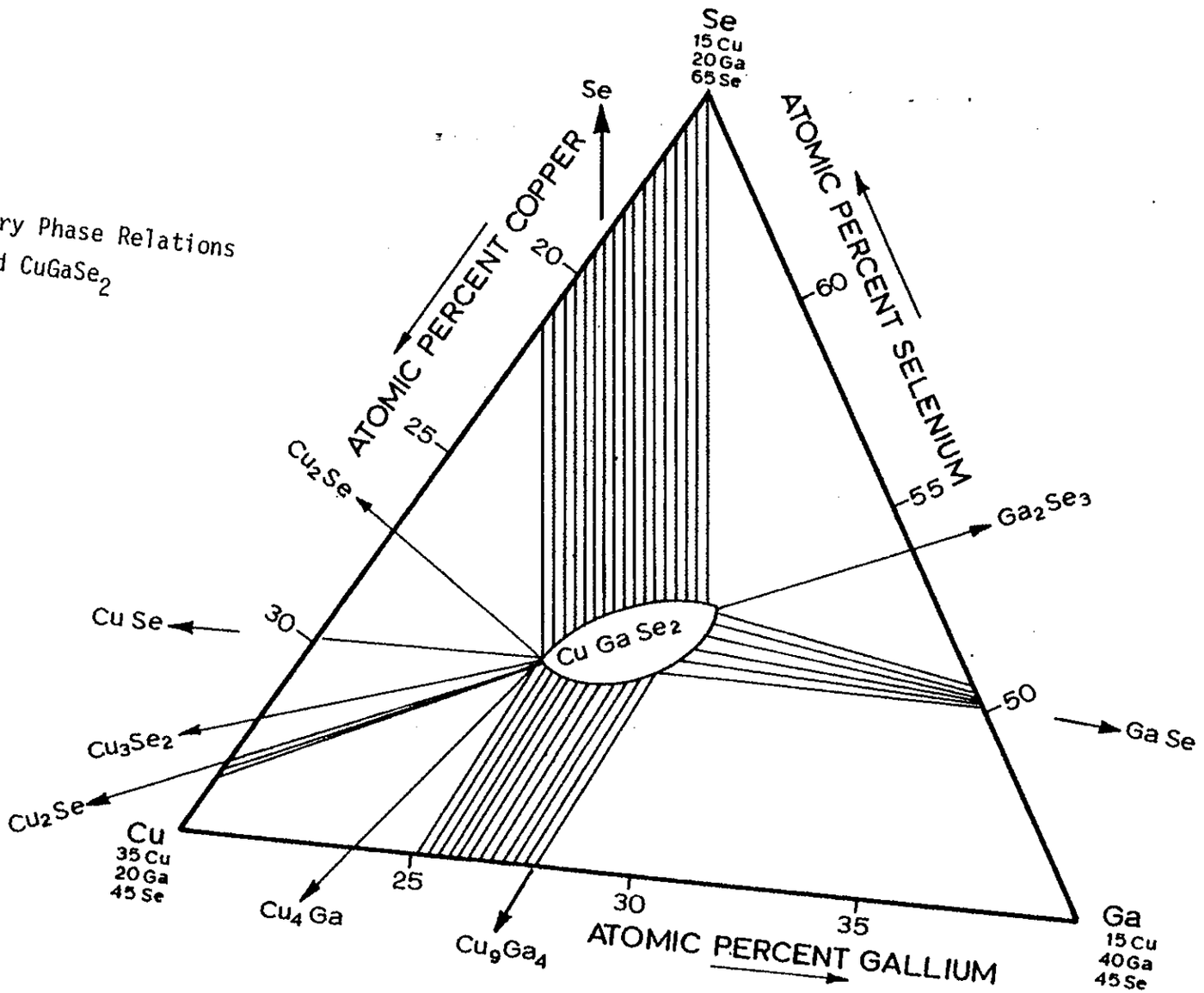

Fig. 1.2: Ternary Phase Relations around $CuGaSe_2$

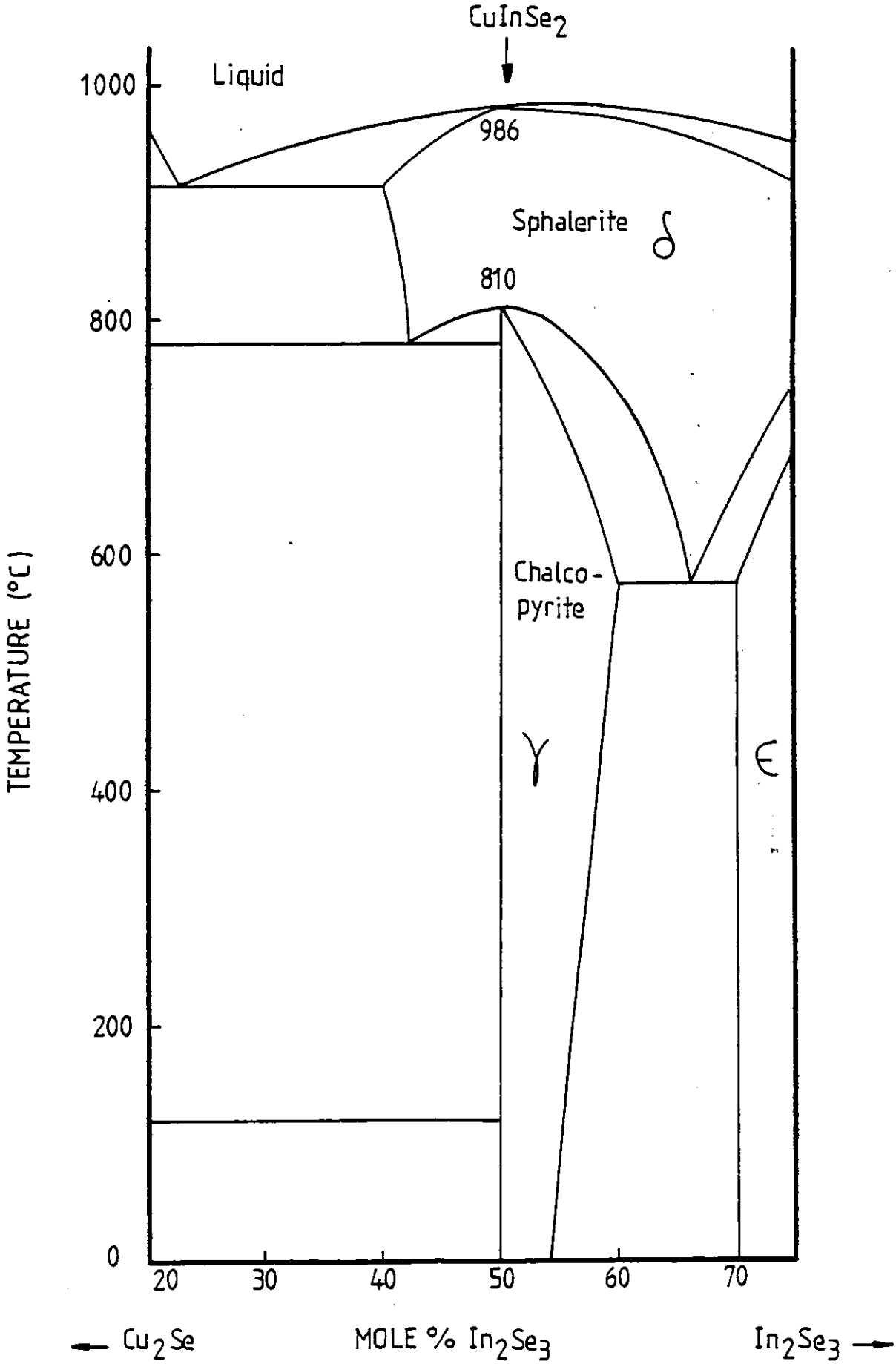

Fig. 1.3: Pseudo-binary Phase Diagram of the Cu_2Se-In_2Se_3 System

As shown in Figure 1.3, two solid phases γ and ε exist at room temperature with the stoichiometric formulae of $CuInSe_2$ and $Cu_2In_4Se_7$ respectively[18]. The chalcopyrite $CuInSe_2$ has some solubility for excess In_2Se_3 but a complete absence of homogeneity for Cu_2Se and this seems to be a general feature for all other I-III-VI_2 chalcopyrite compounds[17].

$CuInSe_2$ undergoes a solid state transition at 810°C with a disorder occurring in the Cu-In cation sublattice. At these high temperatures, the tetragonal $CuInSe_2$ transforms into a disordered sphalerite structure with lattice parameter a = 5.78 Å[18]. This Zincblende modification of $CuInSe_2$ melts approximately at 986°C and may be retained at room temperature by quenching of the melt. The Bragg angles of the diffraction lines and their intensities of this modification are virtually identical with the strong reflections of the chalcopyrite structure and the presence of the latter may only be confirmed by the weaker superlattice reflections. The sphalerite modification of $CuInSe_2$ has been observed in thin film form in the absence of the chalcopyrite $CuInSe_2$[19,20].

1.3.3 Electrical Properties of Bulk $CuInSe_2$

The variation in stoichiometry of the chalcopyrite compounds results in a spread of electrical conductivity from highly conducting to semi-insulating values and for $CuInSe_2$ this leads in addition to a majority carrier conversion[21]. Crystals of $CuInSe_2$ prepared from nominally stoichiometric melts plus excess Selenium are p-type, whereas those prepared with excess Indium are n-type[22]. Crystals with excess Copper have not been reported because of the lack of homogeneity of $CuInSe_2$ in the Cu rich side of the phase diagram.

Doping studies of bulk crystals were first reported by Tell et al[21] and Migliorato et al[22] who determined that anneals in an evacuated ampoule in the presence of $CuInSe_2$ and Se powders (maximum Se

pressure) resulted in p-type crystals. Anneals in the presence of $CuInSe_2$ and In powders (minimum Se pressure) produced always n-type crystals. The room temperature carrier concentrations and mobilities were independent of temperature of anneal and of the original conductivity type of the crystals, for temperatures between 400-700°C. Similar findings were reported by Neumann et al[23] who annealed n-type crystals under maximum Selenium pressure over the same temperature range. No clear correlation between anneal temperatures and hole concentrations was found and these authors concluded that the heat treatment resulted in the simultaneous change in the concentration of acceptors and donors in the crystals.

Doping of $CuInSe_2$ with Indium was reported by Parkes et al[24] who annealed various crystals having an Indium layer evaporated onto their surface, at 200°C for 30 minutes. They determined that this treatment produced n^+ regions on n-type crystals and n-type regions on p-type crystals. The influence of in-diffusion of Indium on p-$CuInSe_2$ crystals was subsequently reported by Neumann et al[23] who confirmed that their crystals were converted to n-type.

Diffusion of Copper into p-type crystals from evaporated Cu layers at 200°C has also been reported[25]. This resulted in n-type regions on p-type bulk, but complete conversion of the crystals to n-type was not mentioned.

In all the above doping investigations the electrical measurements were not supplemented by chemical composition analysis, so it is not known in which region of the phase diagram the p- and n-type crystals of various authors lay. Nevertheless, the changes in conductivity type are considered to arise from changes in the intrinsic defect chemistry of the chalcopyrite. In this respect a vacancy in the cation sublattice, that is a Cu or In vacancy, will act as an acceptor, whereas a vacancy in

anion sublattice, that is a Se vacancy, will be a donor. In a similar fashion Cu or In interstitials will act as donors whereas Se interstitials will behave like acceptors.

It is not clear whether the introduction of excess Indium produces In interstitials or Se vacancies and similarly whether excess Copper leads to Cu interstitials or Se vacancies, which all act as donors. Also growth of crystals under excess Selenium or anneal of crystals in Se vapour, may form acceptors in the form of Se interstitials or vacancies in the cation sublattice.

The intrinsic impurity states in $CuInSe_2$ have been studied by alectrical transport and optical measurements. Donor levels at 6-12 meV[23,24,26] and at 180-250 meV[19,26] have been determined, while acceptor levels at 12-40 meV[22,26,27], 85-95 meV[19,28] and 380-420 meV[19,28] have also been reported.

The various preparation conditions and anneals leads to a wide range of carrier concentration and mobilities in $CuInSe_2$. The electron concentrations reported so far[21-23,26,28] vary between 10^{15}-10^{17} cm^{-3}, with Hall mobilities in the range 50-900 $cm^2\ V^{-1}\ s^{-1}$. As for p-type crystals, hole densities in the range 10^{14}-10^{18} cm^{-3} with mobilities of 5-485 $cm^{-2}\ V^{-1}\ s^{-1}$ have been reported[21-24,26-28].

1.3.4 Optical Properties

The band gap of $CuInSe_2$ single crystals as determined by absorption and reflectance measurements is 1.02 eV[29]. This value was later confirmed by Hörig et al[31] and Sun et al[30] from transmission measurements of thin polycrystalline films of $CuInSe_2$.

The optical transitions have been determined to be direct with the minimum in the conduction band and maximum in the valence band occurring at k = 0. The valence band consists of a heavy hole band and a light hole band which are degenerate at k = 0[32]. The conduction band and the valence bands are characterised by a spherical constant energy surface in k-space

corresponding to a parabolic energy dispersion with scalar effective masses, with values of $m_c = 0.09\ m_o$, $m_{hh} = 0.71\ m_o$ and $m_{\ell h} = 0.092\ m_o$ for the conduction, heavy hole and light hole bands respectively.

The refractive index of single crystals at photon energies below the fundamental edge have been determined by transmission and reflection measurements to be about 2.8[33].

REFERENCES - CHAPTER 1

(1) P.K. WEIMER, "The TFT - A New Thin-film Transistor", Proc. IRE 50 1462 (1962)

(2) M.J. LEE, S.W. WRIGHT and C.P. JUDGE, "Electrical Structural Properties of Cadmium Selenide Thin Film Transistors" Solid St.Electron. 23 671 (1980)

(3) V.L. FRANTZ, "Indium Antimonide Thin Film Transistor", Proc. IEEE 53 760 (1965)

(4) T.P. BRODY and H.E. KUNIG, "A High Gain InAs Thin Film Transistor", Appl. Phys. Lett. 9 259 (1966)

(5) W.B. PENNEBAKER, "PbS Thin Film Transistors", Solid-St. Electron. 8 509 (1965)

(6) D. LILE and J.C. ANDERSON, "The Application of Polycrystalline Layers of InSb and PbTe to a Field Effect Transistor", Solid St. Electron. 12 735 (1969)

(7) P.K. WEIMER, "A p-type Tellurium Thin Film Transistor", Proc. IEEE 52 608 (1964)

(8) P.K. WEIMER, "The Insulated-gate Thin-film Transistor", Physics of Thin Films 2 147 (1964) Eds. R. Thun and G. Haas, Academic Press

(9) B.R. PAMPLIN, "Tables of Properties of Semiconductors" in CRC Handbook of Chemistry and Physics E-101 (1980), Ed. R.C. Weast, CRC Press Inc.

(10) N. ROMEO, "Solar Cells Made by Chalcopyrite Materials", Japan J. J. Appl. Phys. 19 (Suppl. 19-3) 5 (1980)

(11) L.L. KAZMERSKI, "The Utilisation of I-III-VI_2 Ternary Compound Semiconductor in Thin Film Heterojunction and Homojunction Photovoltaic Devices", Third Intern. Conf. on Ternary Compounds, Edinburgh (April 1977) p.217 (Inst. of Phys. Conf. Series No.35)

(12) R. GLANG, "Vacuum Evaporation" in Handbook of Thin Film Technology, Eds. L.I. Maissel and R. Glang, McGraw-Hill (1970)

(13) J.L. SHAY and J.H. WERNICK, "Ternary Chalcopyrite Semiconductors: Growth, Electronic Properties and Applications", Pergamon Press (1975)

(14) H.W. SPIESS, V.HAEBERLEN, G.B. RANDT, A. RAUBER and J. SCHNEIDER, "Nuclear Magnetic Resonance in I_B-III-VI_2 Semiconductors", Phys. Stat. Sol.(b) 62 183 (1974)

(15) J. PARKES, R.D. TOMLINSON and M.J. HAMPSHIRE, "Crystal Data for $CuInSe_2$", J. Appl. Cryst. 6 414 (1973)

(16) J.C. MIKKELSEN, Jr., "Ternary Phase Relations of the Chalcopyrite Compound $CuGaSe_2$", J. Electron. Mater. 10 541 (1981)

(17) L.S. PALATNIK and E.I. ROGACHEVA, "Phase Diagrams and Structure of Some Semiconductor $A_2^I C^{VI}$ - $B_2^{III} C^{VI}$ Alloys", Soviet Phys. - Doklady 12 503 (1967)

(18) R. LESUEUR, C. DJEGA-MARIADASSON, P. CHARPIN and J.H. ALBANY, "Evidence for a New Cubic Ordered Phase in the Cu-in-Se System", Third Intern. Conf. on Ternary Compounds, Edinburgh (April 1977) p.15,(Institute of Physics Conf. Series No. 35)

(19) H. NEUMANN, G. KÜHN and B. SCHUMANN, "Adamantine Ternary Epitaxial Layers", Prog. Crystal. Growth Charact. 3 157 (1981)

(20) J. PIEKOSZEWSKI, J.J. LOFERSKI, R. BEAULIEU, J. BEALL, B. ROESSLER AND J. SHEWCHUN, "RF Sputtered $CuInSe_2$Thin Films", Solar Energy Mater. 2, 363 (1980)

(21) B. TELL and J.L. SHAY, "Room Temperature Electrical Properties of Ten I-III-VI_2 Semiconductor", J. Appl. Phys. 43 2469 (1972)

(22) P. MIGLIOARATO, J.L. SHAY, H.M. KASPER and S. WAGNER, "Analysis of the Electrical and Luminescent Properties of $CuInSe_2$", J. Appl. Phys.46 1777 (1975)

(23) H. NEUMANN, E. NOWAK and G. KÜHN, "Impurity States in $CuInSe_2$", Cryst. Res. Technol. 16 1369 (1981)

(24) J. PARKES, R.D. TOMLINSON and M.J. HAMPSHIRE, "The Fabrication of p- and n-type Single Crystals of $CuInSe_2$", J. Cryst. Growth 20 315 (1973)

(25) R.D. TOMLINSON, E. ELLIOTT, J. PARKES and M.J. HAMPSHIRE, "Homojunction Fabrication in $CuInSe_2$ by Copper Diffusion", Appl. Phys.Lett. 26 383 (1975)

(26) T. IRIE, S. ENDO and S. KIMURA, "Electrical Properties of p- and n-type $CuInSe_2$ Single Crystals", Japan J. Appl. Phys. 18 1303 (1979)

(27) H. NEUMANN, R.D. TOMLINSON, E. NOWAK and N. AUGERINOS, "Electrical Properties of p-type $CuInSe_2$ Single Crystals", Phys. Stat. Sol. (a) 56 K137 (1979)

(28) B. SCHUMANN, C. GEORGI, A. TEMPEL, G. KÜHN, N. VANNAM, H. NEUMANN, and W. HÖRIG, "Epitaxial Layers of $CuInSe_2$ on GaAs", Thin Solid Films 52 45 (1978)

(29) J.N. GAN, J. TAUC, V.G. LAMBRECHT, Jr. and M. ROBBINS, "Optical Properties of the $(CuInSe_2)_{1-x}$-$(2ZnSe)_x$ System", Phys. Rev. B12 5797 (1975)

(30) L.Y. SUN, L.L. KAZMERSKI, A.H. CLARK, P.J. IRELAND and D.W. MORTON, "Absorption Coefficient Measurements for Vacuum-deposited Cu-ternary Thin Films", J. Vac. Sci. Technol. 15 265 (1978)

(31) W. HÖRIG, H. NEUMANN, H. SOBOTA, B. SCHUMANN and G. KÜHN, "The Optical Properties of $CuInSe_2$ Thin Films", Thin Solid Films 48 67 (1978)

(32) H. NEUMANN, H. SOBOTA, W. KISSINGER, V. RIEDE and G. KÜHN, "Hole Effective Masses in $CuInSe_2$", Phys. Stat. Sol. (b) 108 483 (1981)

(33) H. SOBOTA, H. NEUMANN, V. RIEDE, G. KÜHN, J. SELTMANN and D. OPPERMANN, "Influence of Impurities and Free Carriers on the Optical Properties of $CuInSe_2$, Phys. Stat. Sol. (a) 60 531 (1980)

CHAPTER 2

THE STRUCTURE AND COMPOSITION OF BULK $CuInSe_2$ AND ITS EVAPORATION CHARACTERISTICS

2.1 INTRODUCTION

In this chapter the characterisation of bulk $CuInSe_2$ is described.

Since the aim in this work was to prepare thin films of $CuInSe_2$, using the bulk compound as the starting material, it is very important that the chemical composition and overall homogeneity of the ingot be established. This would then form a basis for comparison with the structural and compositional properties of Copper Indium Selenide films. For this purpose the bulk $CuInSe_2$ was examined by X-ray powder diffraction techniques and Electron Probe Microanalysis (EPMA) and the first part of this chapter is devoted to these analyses.

The rest of this chapter is allocated to the investigation of compositional changes occurring during the thermal evaporation of $CuInSe_2$ powders so as to establish the conditions for depositing stoichiometric films reproducibly.

The bulk Copper Indium Selenide, used in this study, was synthesised by BDH Chemicals Ltd., from the melts of the constituent elements. Very high purity Copper, Selenium and Indium powders, in the stoichiometric weight composition of $Cu_{18.9\%}$ $In_{34.1\%}$ and $Se_{47\%}$, were placed into a quartz ampoule. This was evacuated to a pressure less than 10^{-5} torr and was subsequently sealed. The capsule was then transferred to a horizontal furnace and heated very slowly to 1100°C, above the melting point of $CuInSe_2$, and soaked at this temperature for a few hours. After this period, the furnace was switched off and the ampoule left to cool slowly to room temperature. The resulting metallic grey ingot was

subsequently broken into lumps and stored in a glass bottle.

Four large lumps were chosen from the broken ingot and were analysed to check the homogeneity of the ingot. These big lumps were labelled as batches A, B, C and D and their powders were later used to deposit thin $CuInSe_2$ films.

2.2 X-RAY DIFFRACTION ANALYSIS OF $CuInSe_2$

2.2.1 Experimental Procedure

A Debye-Scherrer camera and a Guinier-de Wolff camera were used to study the powder diffraction lines of $CuInSe_2$.

In the Debye-Scherrer method, a 114.6 mm diameter camera with an asymmetric Straumani film mounting was employed. This allowed hkℓ reflections with Bragg angles θ = 0 - 90° to be recorded with 1 mm on the film corresponding to θ = 0.5°.

The Guinier-de Wolff camera had a diameter of 114.6 mm and was of the quadruple type. It permitted the recording of the front reflection region θ = 0-45° of four powder samples simultaneously. The advantage of this camera is that 1 mm on the film corresponds to θ = 0.25° so that its ability to resolve diffraction lines from planes of almost the same d-spacing is twice that of Debye-Scherrer camera. Furthermore because this camera employs an almost pure monochromatic X-ray radiation, the elimination of white radiation results in photographs having always a very low background darkening, thus permitting the detection and precise measurement of very low intensity diffraction lines.

The radiation employed in this study was Copper Kα which was Nickel filtered in the Debye-Scherrer method. The X-ray beam was provided by a Phillips generator operating typically at 30 kV accelerating voltage with beam currents of 20 mA.

The specimens for examination were prepared by crushing pieces from the ingot to a size small enough to pass through a 325-mesh screen

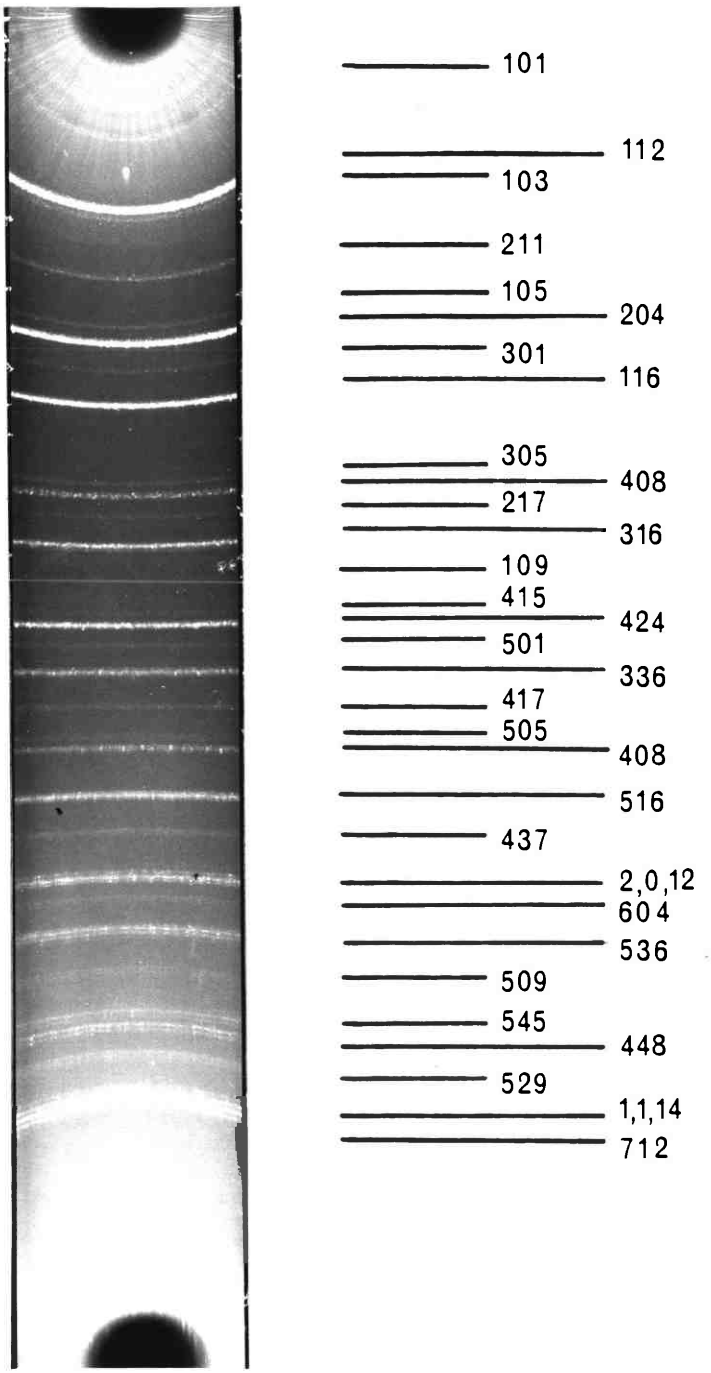

Fig. 2.1: Debye-Scherrer Powder Photograph of $CuInSe_2$

(average grain size of 45 μm). The powders were then mixed with Canada Balsam, which acted as an amorphous binder and the pastes were then coated onto the specimen holders.

2.2.2 Results

A typical Debye-Scherrer pattern for $CuInSe_2$ powders is shown in Figure 2.1 where each diffraction line has been indexed according to the chalcopyrite structure of $CuInSe_2$. Table 2.1 gives a full list of the observed reflections and compares the experimental d-spacings with those tabulated in the powder file[1,2]. The agreement between the measurements and the file listing is excellent but the powder photographs contain faint lines which are not listed under $CuInSe_2$. As all these extra lines occurred at low Bragg angles, the front reflection region was investigated in the Guinier-de Wolff camera. The patterns obtained in this camera also contained the same spurious lines.

The origin of these extra lines was immediately suspected to be due to foreign material other than $CuInSe_2$. In order to identify this alien substance a search through the JCPD powder file was made. The elements Cu, In and Se and their oxides, as well as all the possible compounds in the systems Cu-In, Cu-Se, In-Se and any other oxides associated with these, were considered. In cases where the powder file did not contain information on a particular compound of interest, d-spacings were obtained from the literature. Also, whenever possible, the powder data from more than one author were compared and taken into consideration.

On this basis some of the observed extra diffraction lines were associated with one of the compounds in the Cu-Se, namely Cu_3Se_2. In Table 2.2, a comparison between the experimental values of d-spacings with those of Cu_3Se_2[3] is made.

d(observed) Å	d(powder file) Å	hkℓ	d(observed) Å	d(powder file) Å	hkℓ
5.1930	5.20	101	1.3115	-	-
3.5651	-	-	1.2547	1.256	109,307
3.3531	3.34	112	1.1990	1.200	415
3.2019	3.20	103	1.1807	1.181	228,424
3.1322	-	-	1.1522	1.151	431,501
2.8851	-	-	1.1134	1.114	336,512
2.5110	2.52	211	1.070	1.070	417,521
2.2580	-	-	1.0386	1.035	435,505
2.1443	2.15	105,213	1.0224	1.025	408,440
2.0442	2.04	204,220	0.9772	0.9777	516,532
1.8982	1.900	301	0.9483	0.9482	437,507
1.8203	-	-	0.9167	0.9180	2,0,12
1.7789	-	-	0.9134	0.9140	604,620
1.7413	1.743	116,312	0.8823	0.8821	536;3,2,11
1.7274	-	-	0.8608	0.8609	439,509
1.6625	-	-	0.8413	0.8415	545,633
1.5901	-	-	0.8358	0.8357	448
1.4785	1.480	305,323	0.8349	0.8255	529
1.4471	1.446	008,400	0.8132	0.8134	1,1,14
1.3950	1.393	217,411	0.8296	0.8097	552,712
1.3275	1.327	316,332			

Table 2.1: List of all the diffraction lines observed in $CuInSe_2$ Powders

d(extra) Å	d(Cu_3Se_2) Å	(Intensity)
3.565	3.55 ;	(100%)
3.133	3.11 ;	(60%)
2.895	-	
2.262	2.264 ;	(45%)
1.820	1.831 ;	(80%)
1.779	1.780 ;	(60%)
1.727	-	
1.662	-	
1.590	-	
1.311	-	

Table 2.2: Comparison of the d-spacings of Cu_3Se_2 diffraction lines with the observed extra powder lines

It is evident that the agreement is very good and all the strongest Cu_3Se_2 reflections match some of the spurious lines very well, indicating that some Cu_3Se_2 must exist as a second phase material in the bulk $CuInSe_2$ powders.

The rest of the extra powder lines could not be identified with other compounds involving any combination of Copper, Selenium, Indium and Oxygen. A further search in the powder file for any other material could not produce a match with the experimental data either.

The possibility of some of these unaccounted lines originating from specimen holders was dismissed on the grounds that both the Debye and the Guinier cameras, having different substrate materials, had recorded these extra lines.

The possibility of contamination from the X-ray source itself was also taken into consideration. For example, in an X-ray tube, the Tungsten from the filament emitting the electrons would start to deposit on the surface of the Copper target after long use. While the normal accelerating voltage used to excite the Cu-Kα radiation is not sufficient to excite the W-Kα, it can nevertheless excite the very strong w-Lα_1 line at $\lambda_{W\text{-}L\alpha_1} = 1.47635$ Å[4]. This radiation would not be attenuated by the Nickel filter and would act as a secondary source of X-ray radiation. This would manifest itself, in a pattern taken with Cu radiation, by the formation of spurious lines with d-spacings d_s such that:

$$d_s = d_{hk\ell}\frac{(\lambda_{Cu\text{-}K\alpha})}{\lambda_{W\text{-}L\alpha_1}}$$

where Cu-Kα is the Cu-Kα radiation at 1.54178 Å and $d_{hk\ell}$ is the d-spacing of the strongest powder lines of the sample under study.

In the Guinier-de Wolff camera, which employs a monochromator, the above type of contamination would be eliminated because the crystal monochromator is set to diffract only the strong Cu-Kα component of the general radiation from the X-ray tube. However the crystal monochromator does introduce spurious radiation at $\lambda/2$ and $\lambda/3$ of the main wavelength λ of the radiation employed, with the $\lambda/2$ component being strongest[5]. The effect of this would be to effectively introduce extra diffraction lines at:

$$d_s = 2\, d_{hk\ell}$$

Since the d-spacings of the spurious lines would be different in both type of cameras should contamination from the X-ray source be present, it must be concluded that the origin of the observed extra powder lines could not be attributed to the above effect.

The other alternative in explaining the origin of the unaccounted diffraction lines, must remain with $CuInSe_2$. In order to ascribe them to the ternary compound however, they must satisfy the selection rules of the space group, $I\bar{4}2d$, to which the chalcopyrites belong. Furthermore, their intensity must be calculated to verify that they are theoretically observable in the powder patterns.

2.2.2.1 Allowed $CuInSe_2$ hkℓ Reflections

The limiting conditions for allowed Bragg reflections for the space group $I\bar{4}2d$ are given in the X-ray crystallography tables[6]. For $CuInSe_2$ these are:

Reflection type	Limiting Condition
hkℓ	$h + k + \ell = 2n$
hkℓ	$2k + \ell = 2n + 1$ or $4n$
0Kℓ	$k + \ell = 2n$
hhℓ	$\ell = 2n$; $2h + \ell = 4n$
h00	$h = 2n$
hh0	$h = 2n$

where n is an integer 1,2,3 .... and hkℓ are the Miller indices for the reflections.

A list of all the reflections for $CuInSe_2$ can be written down by taking various permutations of hkℓ. By applying the above limiting conditions and by noting that a hkℓ reflection is equivalent to a khℓ reflection in the tetragonal system, a table of allowed reflections for $CuInSe_2$ can then be obtained. For each allowed hkℓ reflection, the interplanar d-spacing may subsequently be calculated frmom the formula[5]:

$$d_{hk\ell} = \left[\frac{1}{a^2}\left(h^2 + k^2 + \frac{\ell^2}{(c/a)^2}\right)\right]^{-\frac{1}{2}}$$

where a and c are the lattice parameters of the unit cell of $CuInSe_2$, taken as 5.782 Å and 11.620 Å respectively.

Such a calculation was carried out for $d_{hk\ell}$ values down to 1.00 Å, covering the low Bragg angle region in which the spurious lines were observed. When all the reflections already tabulated in the Powder File[2] for $CuInSe_2$ were allowed for, the above exercise yielded quite a few hkℓ reflections not reported previously. These are shown in Table 2.3 where they are compared with the unaccounted lines of Table 2.2.

While the calculated reflections do not match with the extra lines previously associated with Cu_3Se_2, they tie in quite well with the remaining spurious lines. Thus it appears that these lines can be indexed under the chalcopyrite structure of $CuInSe_2$. It must be noticed that Table 2.3 also contains the calculated 433,503 and 1,0,11; 523 reflections which are also allowed. However these will not be observed in the diffraction patterns because their d-spacings are too near the strong 336,512 and 435,505 reflections of $CuInSe_2$.

2.2.2.2 Calculated Intensity of $CuInSe_2$ Reflections

In order to confirm conclusively that the additional lines belong to $CuInSe_2$, their intensity was calculated. For this purpose the structure factor F(hkℓ), which expresses the combined scattering in a particular direction of all the atoms in the unit cell, was first evaluated.

In general for a unit cell comprising of N atoms of the same kind, the structure factor is a complex number given by[5]

$$F(hk\ell) = f\left[\sum_{1}^{N} \text{Cos } 2\pi\,(hx_n + ky_n + \ell_{zn}) + j \sum_{1}^{N} \text{Sin } 2\pi\,(hx_n + ky_n + \ell z_n)\right]$$

hkℓ	$d_{hk\ell}$ calculated (Å)	$d_{hk\ell}$ unaccounted lines (Å)
(004)	(2.9050)	2.8934
(200)	(2.8910)	
(215)	(1.7285)	1.7287
(303)	(1.7255)	
224	1.6718	1.6705
(107)	(1.5955)	1.5910
(321)	(1.5886)	
(325)	(1.3199)	1.3173
(413)	(1.3186)	
(433)	1.1081	-
(503)		
(1011)	1.0392	-
(523)	1.0347	

Table 2.3: d-spacings of theoretically allowed hkℓ $CuInSe_2$ reflections compared with d-spacing of unaccounted lines

where x_n, y_n, z_n are the fractional coordinates of the atoms in the unit cell, and f is the atomic scattering factor, which is the ratio of the amplitude scattered in a particular direction, by one atom, to the amplitude scattered in the same direction by one electron. Its value increases with the atomic number of the atom and these are tabulated for every element in the international tables for X-ray Crystallography[7] as a function of Sin θ/λ. Here θ is the Bragg angle of the particular hkℓ reflection and λ is the wavelength of X-ray employed.

The structure factor for $CuInSe_2$ may be written as

$$F(hk\ell) = (a_{Cu} + a_{In} + a_{Se}) + j\,(b_{Cu} + b_{In} + b_{Se})$$

where

$$a_{Cu} = f_{Cu}\left[1 + \cos\pi\left(h + \frac{\ell}{2}\right) + \cos\pi(h+k+\ell) + \cos\pi\left(k + \frac{3\ell}{2}\right)\right]$$

$$b_{Cu} = f_{Cu}\left[\sin\pi\left(h + \frac{\ell}{2}\right) + \sin\pi(h+k+\ell) + \sin\pi\left(k + \frac{3\ell}{2}\right)\right]$$

$$a_{In} = f_{In}\left[\cos\pi\ell + \cos\pi\left(h + \frac{3\ell}{2}\right) + \cos\pi(h+k) + \cos\pi\left(k + \frac{\ell}{2}\right)\right]$$

$$b_{In} = f_{In}\left[\sin\pi\ell + \sin\pi\left(h + \frac{3\ell}{2}\right) + \sin\pi(h+k) + \sin\pi\left(k + \frac{\ell}{2}\right)\right]$$

$$a_{Se} = f_{Se}\left[\begin{array}{l} \cos\pi\left(2hx + \frac{k}{2} + \frac{\ell}{4}\right) + \cos\pi\left(-2hx + \frac{3k}{2} + \frac{\ell}{4}\right) + \cos\pi\left(\frac{3h}{2} + 2kx + \frac{7\ell}{4}\right) \\ + \cos\pi\left(\frac{h}{2} - 2hx + \frac{7\ell}{4}\right) + \cos\pi\left(2hx + h + \frac{3h}{2} + \frac{5\ell}{4}\right) + \cos\pi\left(h - 2hx + \frac{k}{2} + \frac{5\ell}{4}\right) \\ + \cos\pi\left(\frac{h}{2} + k + 2hx + \frac{3\ell}{4}\right) + \cos\pi\left(\frac{3h}{2} + k - 2kx + \frac{3\ell}{4}\right) \end{array}\right]$$

$$b_{Se} = f_{Se}\left[\begin{array}{l} \sin\pi\left(2hx + \frac{k}{2} + \frac{\ell}{4}\right) + \sin\pi\left(-2hx + \frac{3k}{2} + \frac{\ell}{4}\right) + \sin\pi\left(\frac{3h}{2} + 2kx + \frac{7\ell}{4}\right) \\ + \sin\pi\left(\frac{h}{2} - 2hx + \frac{7\ell}{4}\right) + \sin\pi\left(2hx + h + \frac{3k}{2} + \frac{5\ell}{4}\right) + \sin\pi\left(h - 2hx + \frac{k}{2} + \frac{5\ell}{4}\right) \\ + \sin\pi\left(\frac{h}{2} + k + 2kx + \frac{3\ell}{4}\right) + \sin\pi\left(\frac{3h}{2} + k - 2kx + \frac{3\ell}{4}\right) \end{array}\right]$$

where f_{Cu}, f_{In} and f_{Se} are the X-ray scattering factors of Copper, Indium and Selenium respectively and x is the free parameter taken in turn as x = 0.224 and x = 0.235.

Having calculated the structure factor for each allowed $CuInSe_2$ hkℓ reflection, these were then used to calculate the relative integrated intensity of the powder lines, I, from the formula[5]

$$I(hk\ell) = |F(hk\ell)|^2 \, mLP$$

where the square of the modulus of the structure factor is now considered and m is the multiplicity factor, which takes into account the different planes contributing to the intensity of the same diffraction line. Its value depends on the crystal structure and type of reflections. For the tetragonal structure of $CuInSe_2$ its values are

Type of Reflection	hkℓ	hhℓ	h0ℓ	hk0	hh0	h00	00ℓ
Multiplication Factor m	16	8	8	8	4	4	2

In the intensity formula, L is the Lorentz factor which takes into account that crystal planes oriented at an angle slightly away from the exact Bragg angle, θ, still contribute to the intensity at the angle θ. Its value is given by:

$$L = \frac{1}{\sin^2 \theta \cos \theta}$$

Finally, in the integrated intensity, P, is the polarisation factor, which arises because the unpolarised radiation from the X-ray tube becomes polarised after being diffracted. The amount of polarisation depends upon the angle of diffraction through:

$$P = 1 + \cos^2 2\theta$$

The results of the intensity calculations for the extra lines are given in Table 2.4, where the intensities are relative to the 112 reflections which were determined to be the 100% intensity line.

hkℓ	d_{exp} (Å)	I_{calc}(%)
004,200	2.8934	0.7
215,303	1.7287	1
224	1.6705	0.4
107,321	1.5910	2
325,413	1.3200	2

Table 2.4: Calculated intensity of unreported $CuInSe_2$ hkℓ reflections

As expected the calculated relative intensities are quite low but by no means impossible to detect, since the theoretical intensities of other previously reported $CuInSe_2$ reflections lay also in the 1-2% region. This point is made clear in Table 2.5 where the calculated intensities of all allowed reflections in the low Bragg angle region are tabulated with the previously unreported reflections being marked with an asterisk. This table also contains the relative intensities estimated visually from the powder patterns, and shows that theory and calculations agree very well for both values of the free parameter $x = 0.224$ and $x = 0.235$.

The indexing and intensity calculations have thus shown the weak powder lines observed at d = 2.89 Å, 1.73 Å, 1.67 Å, 1.59 Å and 1.32 Å are due to chalcopyrite $CuInSe_2$ reflections not reported in the powder file. The other extra lines at d = 3.56 Å, 3.13 Å, 2.62 Å, 1.83 Å and 1.78 Å have been determined to be due to second phase Cu_3Se_2.

hkℓ	Experimental Intensity	Calculated Intensity	
		I_{calc} for x = 0.224 (%)	I_{calc} for x = 0.235 (%)
101	m^+	7	6
112	VVS	100	100
103	m^+	2	2
*004,220	W	0.7	0.6
211	m^+	6	4
105,213	m^+	1	1
204,220	VVS	71	72
301	m	1	0.6
116,312	VS	42	43
*215,303	m	1	0.7
*224	VW	0.2	0.3
*107,321	VW	2	1
305,323	m	1	0.6
208,400	S	11	11
217,411	m	1	0.7
316,332	S	16	17
*325,413	m	2	1
109,307	W	0.4	0.3
415	W	1	1
228,424	S^+	21	23

Table 2.5: List of calculated intensity of all allowed low angle $CuInSe_2$ reflections

VVS = Very very strong; VS = Very strong; S^+ = Quite strong;

S = Strong; m^+ = Less strong; m = Medium; W = Weak; VW = Very weak

* = Previously not reported reflections

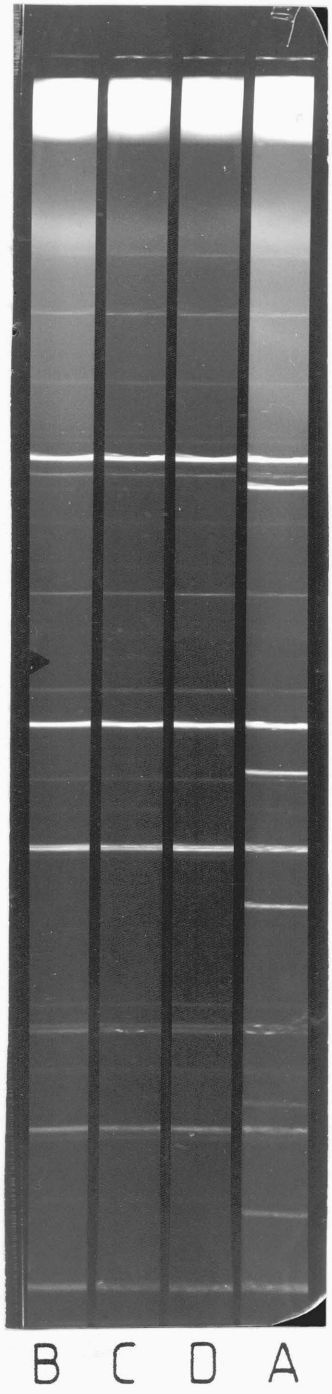

Fig. 2.2: Guinier-de Wolff Diffraction Patterns of $CuInSe_2$ Powders A, B, C and D

In order to check the homogeneity of the bulk material, four big lumps A,B,C and D had been chosen and their powder patterns were compared in the Guinier-de Wolff camera. This is shown in Figure 2.2 where each strip on the photograph represents a sample. The patterns are characterised by the three strong reflections 112; 204,220 and 116,312 of $CuInSe_2$. In addition powder A which was mixed with Silicon as an internal standard, has the 111, 220, 311, 400 and 331 reflections of Si superimposed.

A close examination of each pattern revealed that powders A, B and C had all the extra lines due to Cu_3Se_2 and $CuInSe_2$ as tabulated in Table 2.2, whilst the powder D did not have the extra lines due to Cu_3Se_2 but only the extra lines associated with the weak unreported chalcopyrite reflections as tabulated in Table 2.3. These observations indicated that Cu_3Se_2 precipiates were not uniformly distributed throughout the bulk ingot and that certain regions contained less or even no secondary phase.

2.2.3 Conclusions

In conclusion, the X-ray diffraction investigations of bulk $CuInSe_2$ has shown that the starting material was not homogeneous and contained Cu_3Se_2 precipitates. The X-ray analysis has also given evidence of the presence of previously unreported weak chalcopyrite $CuInSe_2$ reflections.

2.3 ELECTRON PROBE MICROANALYSIS OF $CuInSe_2$

2.3.1 Introduction

Electron Probe Microanalysis is an essentially non-destructive analytical technique which is used to determine the chemical composition of specimens having a volume as small as a few cubic micrometers.

During the analysis, the selected area of the sample is bombarded with a beam of electrons accelerated to energies in therange 10 to 30 keV. The electron beam which is focussed to typically 0.1-1 μm diameter size, causes the emission of an X-ray spectrum that consists of characteristic X-ray lines of all the elements present in the bombarded volume.

The composition analysis is accomplished by identifying the wavelength of the characteristic X-ray lines and by measuring their intensities. The wavelength in the emission spectrum establishes the definite presence of a particular element and the line intensities are related to the weight fractions of the corresponding elements.

For a quantitative analysis, the X-ray count rates in the specimen are compared with the count rates from a standard containing the element in question. As a first approximation, the relative count rates of specimen to standard gives the weight concentration of the particular element in the sample. However, because the intensity of the characteristic X-ray line emitted by an element in the sample depends to a great extent on the presence of other elements in it, the measured intensities must be corrected. The correction takes into account the difference in the Atomic Number, Absorption Coefficient and Fluorescence effects between the sample and the standard. These correction factors, which themselves depend on the weight concentration of each element present in the specimen, are calculated by an iterative technique using a computer.

In general, the accuracy of the Electron Probe Microanalysis will depend on the concentration of the elements present in the specimen, the type of theoretical model and computer program used in the iteration and, of course, on the instrumental and experimental errors. In order to investigate the accuracy of the Probe Microanalysis, Beeman et al[8] have collated the EPMA composition results of different laboratories, on carefully prepared and well characterised specimens. They concluded that the overall accuracy of the composition analysis is likely to be around ±3% of the concentration, provided that the amount of constituent elements in the sample exceeds ~20 wt%. Such an accuracy should also be valid for $CuInSe_2$ because the weight fractions of the constituents are ~18.9 wt%,Cu 47 wt% Se and 34.1 wt% In.

The Electron Probe Microanalysis, of all samples investigated in this study, was performed at the Imperial College Analytical Services Laboratory. An accelerating voltage of 25 kV at a beam current of 5×10^{-8} A was employed and was found not to cause beam damage. The analysis was performed on the intensities of the characteristic X-ray lines CuKα, SeKα and InLα. The X-ray counts of each of these lines were measured over a period of 60 seconds and this was repeated for five randomly chosen areas on each specimen. The average count rates were subsequently used in the quantitative analysis and the standards used were pure Copper, pure Indium and well characterised Cadmium Selenide.

The spatial homogeneity of the sample compositions were checked by a qualitative analysis in which the X-ray count rates of each element were monitored while the sample was swept under the stationary electron beam in a line scan.

2.3.2 Composition and Homogeneity of $CuInSe_2$

From the previously chosen four large lumps, A,B,C and D of the ingot, smaller specimens were cut off and analysed on two different occasions. A loose grain E picked out randomly from the rest of the ingot was also examined. Table 2.6 gives the results of the analysis and also tabulates the mean composition of each of the batches A,B,C,D and E, in atomic percentages. It can be seen that the variation of composition within each large lump is not great and is less than 2% of the mean composition in each case. This implies that the composition of $CuInSe_2$ within each batch is quite homogeneous and also that the reproduciblity of the microanalysis technique used is quite good. If the average compositions of the various lumps are compared with one another, it will be apparent that there is a slight variation in composition. It should also be noticed that in all cases the composition of $CuInSe_2$ deviates away from the theoretical composition of 25 at % Cu, 25 at % In and 50 at % Se.

Batch identification	Results of EPMA at%Cu	at%Se	at%In	Mean Composition at%Cu	at%Se	at%In
A	23.8	50.5	25.7	23.6	50.6	25.8
	23.3	50.8	25.9			
B	22.6	51.5	25.9	22.3	51.2	26.5
	22.1	50.9	27.1			
C	23.3	51.4	25.3	23.2	51	25.8
	23.1	50.6	26.3			
D	22.9	54.9	22.2	22.8	54.7	22.5
	22.6	54.5	22.9			
E	21	51.3	27.7	21	51.4	27.6
	21	51.5	27.5			

Table 2.6: EPMA composition of bulk $CuInSe_2$

The line scans across the samples showed that the composition was not spatially homogeneous and that second phase regions existed. A typical scan is shown in Figure 2.3 where the X-ray count rates of Cu, In and Se are plotted as a function of distance along a random direction in the specimen. The start of the scan is shown to occur in the region containing Copper Indium Selenide where the spatial variations of the count rates are well below about ±3%, confirming the homogeneity of $CuInSe_2$ in these matrix regions. The line scan is then characterised by regions in which the Copper count increases drastically while the Indium count drops to very low levels. The Selenium count rates also decrease in these regions but by a much smaller factor than the Indium count rates. These are indications of the presence of second phase regions which contain mainly Copper and Selenium. The fact that some Indium counts are still being measured in some of these second phase regions, is due to the variation of the position of the Cu-Se precipitates from the surface of the specimen. In some regions therefore the counts measured will be the combined effect of the matrix and precipitates.

The line scans indicated that the size of the second phase regions was in the 10-40 μm region and that their amount varied from batch to batch. In this respect lump A contained a higher density of these precipitates whereas the amounts in batches B and C were much lower whilst lump D and grain E were not found to contain any significant number of second phase regions.

By measuring the count rates in the larger second phase regions, an estimate of their composition could be made. Two separate measurements gave 59.6 at % Cu, 40.4 at % Se and 56.8 at % Cu, 43.2 at % Se, which correspond to more or less the composition of Cu_3Se_2, the phase which was identified as secondary material in the X-ray diffraction analysis.

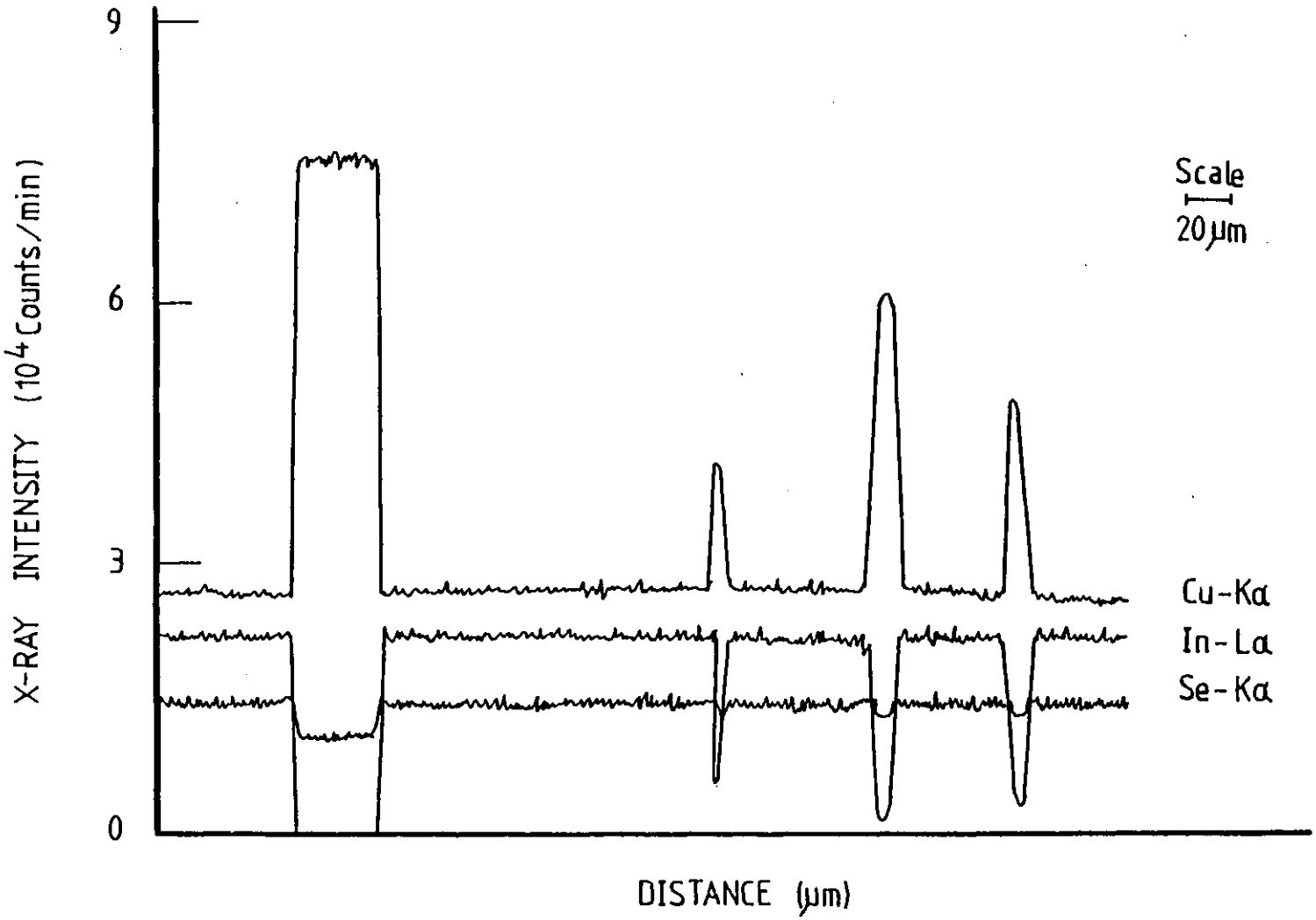

Fig. 2.3: Electron Probe Line Scan of Bulk $CuInSe_2$

2.3.3 Existence Region of $CuInSe_2$

At present the homogeneity region of $CuInSe_2$ is not known and thus there is a need for investigating the nature and chemical composition of phases at room temperature around the nominal composition of 25at% Cu 25 at% In 50 at% Se. While this may prove to be a tedious and complex task, an approximate existence region for single phase $CuInSe_2$ could be determined, if the chemical composition of crystals prepared by various laboratories were available and compiled. Unfortunately in the literature, the characterisation of bulk $CuInSe_2$ consists usually only of X-ray diffraction analysis and to date only Möller et al[9] have published compositional data on $CuInSe_2$. In an attempt to construct an approximate single phase region for $CuInSe_2$ the mean compositional data of lumps A to E of our bulk ingot were plotted on an enlarged portion of the ternary phase diagram in the vicinity of the theoretical atomic composition of $CuInSe_2$. The composition diagram shown in Figure 2.4 also includes data from a single crystal $CuInSe_2$, labelled as, S, and the published data of Möller et al[9] denoted as 1,2 and 3.

Sample S was a single crystal of Copper Indium Selenide grown by R.D. Tomlinson[18] at Salford University which was compositionally analysed however at the Imperial College Laboratories, using the same procedure for samples A-E. The Salford sample was determined to be homogeneous and did not contain any precipitates. The compositional data of Möller et al[9] had also been obtained by Electron Probe Micro-analysis and these authors had reported the presence of $Cu_{2-x}Se$ precipitates at different parts of their sample.

In Figure 2.4, the average composition of each sample is plotted and the error bars reflect the spread of composition when more than one measurement is made on a particular sample. Looking at the composition of our samples, it is apparent the $CuInSe_2$ composition of lumps A,B,C and E lies along the pseudo-binary Cu_2Se-In_2Se_3 join of the phase diagram.

Fig. 2.4: Ternary Phase Relations around $CuInSe_2$

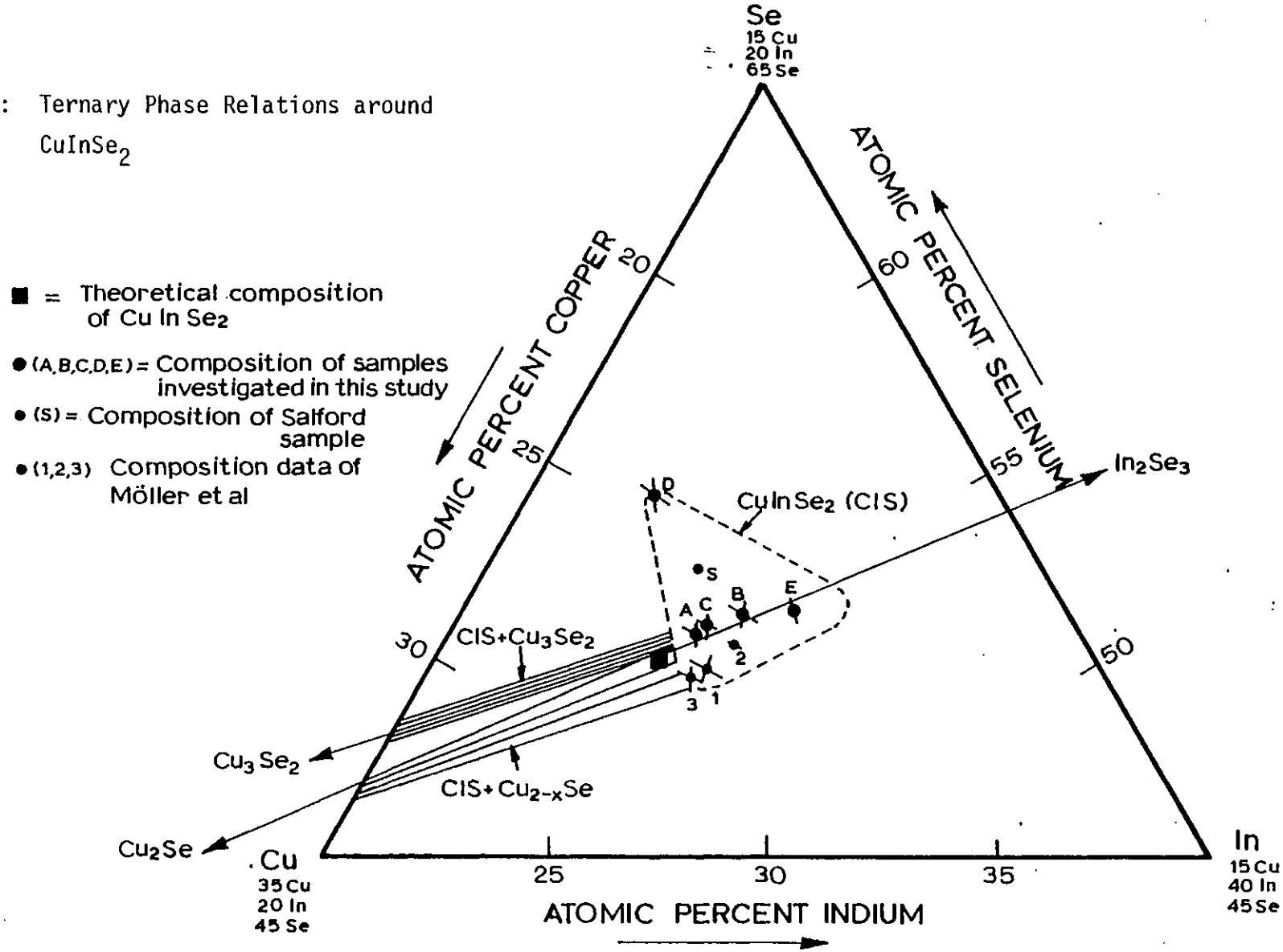

In each case, the composition is towards the In_2Se_3 rich side and the excess mole fraction of In_2Se_3 is calculated to be 2%, 2.5%, 4.2% and 6.5% for samples A,C,B and E respectively. Sample D on the other hand has Indium to Copper atomic ratio of nearly unity and consequently lies along the CuIn-Se join of the phase diagram. It is characterised by an excess solubility for Selenium which was calcualted to be around 2.5 mole %.

The single crystal from Salford also had excess Selenium but this was somewhat less than our sample D.

The EPMA data of Möller et al[9] lay in the region along the Cu_2Se-In_2Se_3, but as opposed to our samples A,C,B and E, their composition values are below the pseudo-binary join. They also report excess solubility for In_2Se_3 and their composition labelled as 2 in the ternary plot of Figure 2.4 indicates approximately 3.5 at% excess In_2Se_3.

The EPMA of bulk $CuInSe_2$ as obtained in this work and by Möller et al[9], indicates that Copper Indium Selenide is always Copper deficient. This is in good agreement with the findings of Palatnik et al[10], that there is an absence of a homogeneity region on the Copper rich side of the phase diagram of $CuInSe_2$.

The existence region of $CuInSe_2$ on a ternary diagram has not yet been determined but by comparing the experimental data of Figure 2.4 with the homogeneity regions of other similar compounds in the I-III-VI_2 family, an approximate single phase region boundary may be defined.

In determining the phase regions near the chalcopyrite $CuGaS_2$, Kokta et al[11] have shown that this compound could dissolve up to 6% excess Ga_2S_3. The sample E composition in this study is very similar to this and may thus be taken to represent the single phase boundary on the Cu_2Se-In_2Se_3 join. $CuGaS_2$ was found also to have extensive solubility for Selenium and this was a maximum at a composition with Ga/Cu ratio of

nearly unity. Though Kokta et al[11] do not state the exact amount of excess Se that is soluble, this can be estimated to be around 3-4% from their phase diagram. This is again very similar to the composition of our sample D which may therefore be taken to give the maximum Se solubility in $CuInSe_2$. $CuGaS_2$ is also characterised by an absence of homogeneity in the Copper rich side of the phase plot and its homogeneity region extends towards Cu-Ga phases, i.e. well below the Cu_2S-Ga_2S_3 join.

By taking the above features of $CuGaS_2$ into account, a rough single phase boundary for $CuInSe_2$ has been obtained and this is shown by the dashed lines in Figure 2.4. This indicates that $CuInSe_2$ (CIS) has an extensive homogeneity region and if a sample has a composition which falls outside this region, then it will be expected to contain other secondary phases in addition to $CuInSe_2$.

Since the samples analysed in this work had Cu_3Se_2 as secondary phase, then this is indicative of the existence of a two-phase region between $CuInSe_2$ and Cu_3Se_2. In the ternary phase diagram of Figure 2.4, this two-phase region is shown by the shaded region labelled as CIS + Cu_3Se_2.

Similarly since the samples of Möller et al[9] contained $Cu_{2-x}Se$ precipitates, a two-phase region involving $CuInSe_2$ and $Cu_{2-x}Se$ must exist and this is shown by the dashed region labelled as CIS + $Cu_{2-x}Se$ in Figure 2.4.

2.3.4 Conclusions

In conclusion, the Electron Probe Microanalysis of bulk $CuInSe_2$ samples showed that different parts of the ingot had different compositions and that $CuInSe_2$ exists in a wide single phase region of the ternary phase diagram around the theoretical composition of 25at% Cu, 25at% In, 50at% Se.

The Electron Probe line scans confirmed the findings of the X-ray analysis in that Cu_3Se_2 precipitates with dimensions of a few tens of microns exist together with $CuInSe_2$ in some parts of the bulk ingot.

The above results indicated that the properties of films prepared from powders, obtained from different parts of the bulk ingot, must be carefully compared and correlated with the starting powder batch.

2.4 COMPOSITIONAL VARIATION DURING EVAPORATION OF $CuInSe_2$

2.4.1 Introduction

The vacuum evaporation technique is the most widely used method of preparing thin films of materials. It relies on heating the substance under vacuum to high enough temperatures so as to initiate a high vapour pressure and hence to provide the transfer of material from the bulk onto a substrate.

In order to use this method successfully a knowledge of the evaporation characteristics of the material in question is necessary. The properties of importance are the type of evaporating species and their partial pressure as a function of temperature. These can be converted easily to specific evaporation rates which are of more interest in practice. If the material to be evaporated is a compound then the precise knowledge of the evaporation characteristic is very crucial for controlling the composition of the layers being deposited.

The only study of the evaporation of $CuInSe_2$ reported so far has been that of Strelchenko et al[13] who used a mass spectrometer equipped with a Knudsen cell. Their investigation showed that over the temperature region 900-1160K, the chalcopyrite is characterised by incongruent evaporation. The evaporating species in the vapour were identified as In_2Se and Se_2 and their partial pressure over $CuInSe_2$ were:

$$\log_{10} P_{In_2Se} = 6.503 - 9758/T$$

$$\log_{10} P_{Se_2} = 10.732 - 16097/T$$

where the partial pressures are given in torr when the temperature T is in Kelvin. These partial pressures have been plotted in Figure 2.5 and indicate

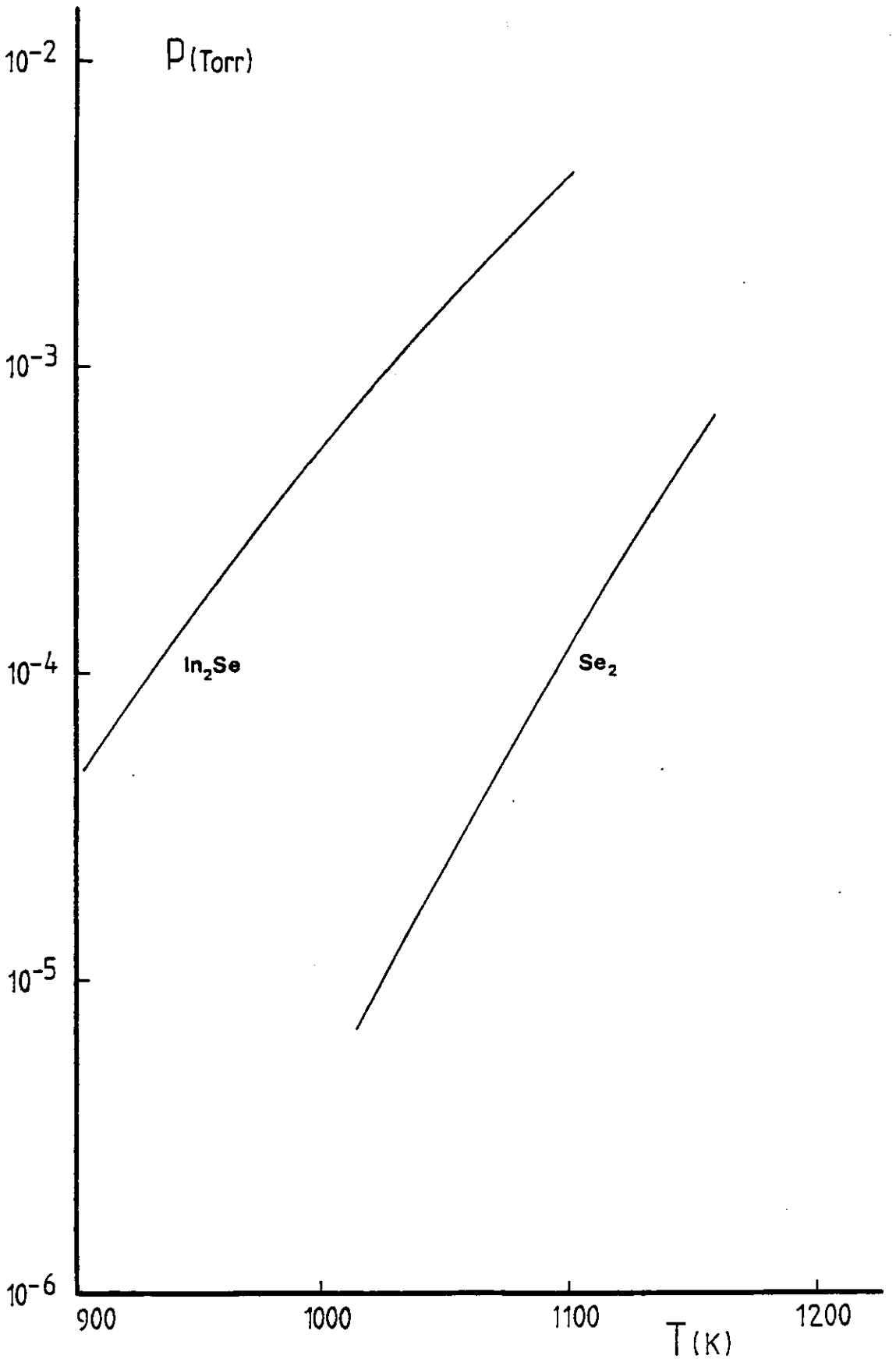

Fig. 2.5: Partial Pressure of Vapours above $CuInSe_2$

that in the temperature range investigated In_2Se has a higher pressure than Se_2. Since no elemental Copper or Copper containing molecules were detected in this temperature region then it is obvious that, if free evaporation is allowed, the composition of $CuInSe_2$ will move more and more towards the Cu-rich region of the phase diagram. Eventually it would be expected that, after prolonged evaporation at high temperatures, Copper Indium Selenide will have decomposed into Copper, the less volatile phase of the constituent elements. It is clear, therefore, that sufficiently high temperatures (estimated to be greater than 1600K from the vapour pressure of Copper[14]) will be required to evaporate the remaining Copper, if the correct composition in the deposited layers is to be attained.

It is thus important to establish the exact conditions under which Copper Indium Selenide can be evaporated to give films with the required stoichiometry. Also, since the vapour pressure data of Strelchenko et al is given only up to 1200K, a knowledge of the evaporation characteristics above the temperature will shed light into the dissociation processes of $CuInSe_2$. With these objectives in mind, the free evaporation behaviour of $CuInSe_2$ was investigated by monitoring its evaporation rate in vacuum, as a function of time and temperature.

2.4.2 Experimental Procedure

The evaporation rates were recorded by detecting the change in the oscillating frequency of a thin quartz crystal onto which the evaporant condensed.

The instantaneous frequency shift rate of the crystal, $\frac{d\Delta f}{dt}$, gives a direct measure of the mass evaporation rate of a substance through the relationship[15]

$$\frac{d\Delta f}{dt} = C_f \, G \, A_e R_e$$

where C_f is the mass determination sensitivity of the crystal in Hz gm^{-1} cm^2, G is a geometrical factor which takes into account the emission characteristics of the source having area A_e, and R_e is the mass evaporation rate in gm s^{-1} cm^{-2}.

The factor C_fG will be fixed for a given crystal type and monitor to source geometry used. It was determined to be ~1.7 x 10^5 Hz gm^{-1}, by evaporating a known weight of material to completion and noting the total frequency change Δf that has thereby occurred.

For the evaporation area A_e of the source used, the experimental frequency shift rates can be converted to mass evaporation rate through:

$$R_e = 4.5 \times 10^5 \frac{d\Delta f}{dt}$$

where R_e is in gm s^{-1} cm^{-2} when $\frac{d\Delta f}{dt}$ is in units of Hz s^{-1}.

The quartz crystals used were obtained from Marconi Communications Ltd. and operated at a frequency of 6 MHz. They were AT cut and so had a high mass sensitivity and a very low temperature coefficient of frequency. The crystals were provided with heat shielding to minimise drifts due to rise in temperature.

An Edwards Film Thickness Monitor Speedivac 1 was used to detect the frequency shift during the evaporation. The instantaneous frequency shift rates were obtained from the Rate Controller output terminal which delivered a 0-5V signal.

This signal and the temperature of the source as measured by a thermocouple welded at the bottom of the evaporating cell, were simultaneously plotted on a J.J. Instruments Ltd. chart recorder, as a function of time. The minimum measurable frequency shift rate corresponded to 0.1 Hz s^{-1} on the most sensitive scale of the ratemeter. Temperatures as translated from the charts were to the nearest 4°K.

The sensitivity of the oscillating frequency on temperature was assessed by heating the empty evaporation boat slowly so as to simulate a normal experiment. The direct radiant heat from the source caused a change but the rate was less than about ~0.5 Hz s^{-1} after continuous slow heating. Since this was well below the usual rates of 10-100 Hz s^{-1}, no corrections to the measured evaporation rates were made.

Because the evaporation material was in the form of loosely packed fine powder grains with sizes in the range 150-250 μm, poor thermal contact between the grains and hence a temperature difference between the boat temperature and the actual powder temperature may be expected. This aspect was investigated in an experiment by monitoring simultaneously the boat thermocouple and a similar thermocouple embedded into the powder. As the boat was warmed up slowly it was observed that the powder temperature lagged behind the cell temperature. The powder was about 20°K lower at 350K, 80K lower at 500K and 150K lower at 900K. This temperature difference gradually diminished with further heating of the cell and was about 120K at a boat temperature of 1100K. The temperature difference was less than 60K after a boat temperature of 1250K and above. The results of this exercise indicated that while there was a lag, the boat temperature was a fair representation of the actual powder temperature and so no corrections to the temperatures measured during the evaporating experiments were therefore deemed necessary.

2.4.3 Results

The evaporation experiments indicated there were distinct temperature regions over which evaporation occurred. In the temperature interval room temperature to 700K, very small evaporation rates were recorded. In the high temperature region extending from about 1000K to 1800K, very much higher evaporation rates were observed.

In Figure 2.6(a) a typical plot of temperature versus time is shown and Figure 2.6(b) gives the evaporation rate as evaporation proceeds.

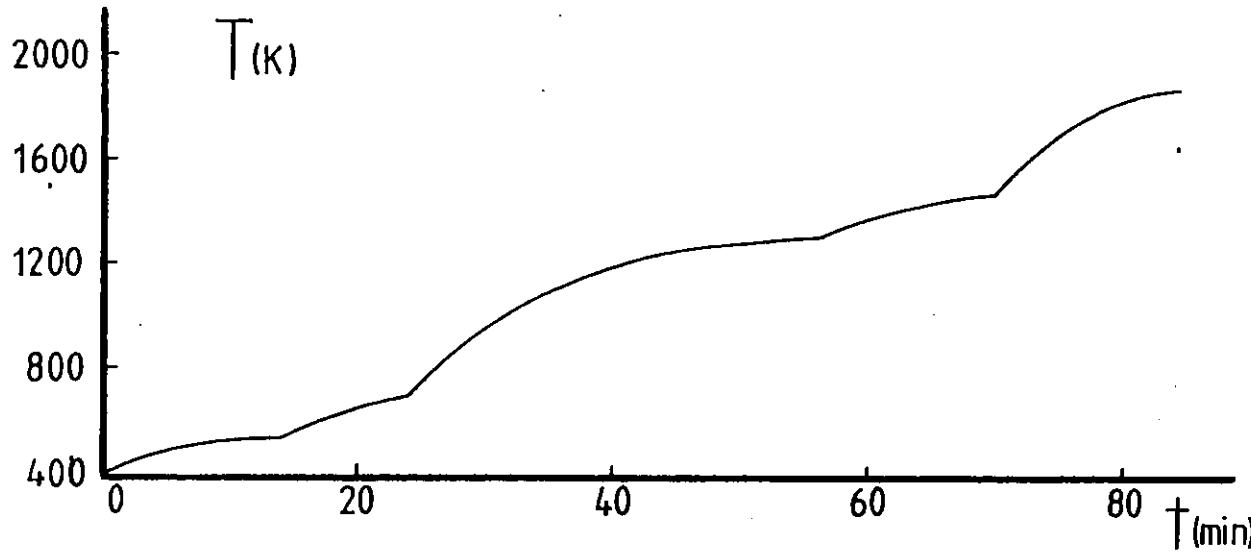

Fig. 2.6(a): Crucible Temperature as a Function of Time

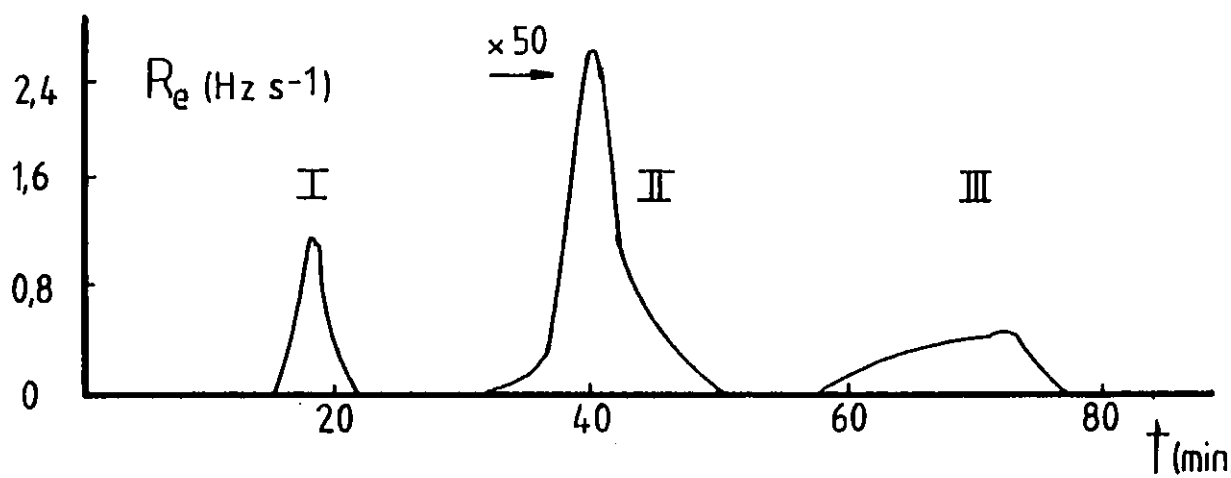

Fig. 2.6(b): Evaporation Rate as a Function of Time

Up to a temperature of ~580K no evaporation is detected. As the cell warms past this temperature, a small evaporation rate is recorded. This reaches a maximum around 630K and then decays to zero as the boat is continually heated up further. No more evaporation is observed until higher temperatures are reached and this small evaporation region is labelled as regime I.

At around 1000K the evaporation increases again, reaches a peak rate at around 1200K and then starts to decrease even though the source temperature is still rising. Eventually the evaporation becomes very low and this region is labelled as regime II.

As the temperature is increased further from ~1300K, the evaporation rate rises once again reaching a smaller maximum before falling away at temperatures of ~1800K. No more evaporation is detectable above this temperature, implying that the charge of $CuInSe_2$ has been evaporated to completion. This third evaporation region is labelled as regime III.

Each of the evaporation regimes observed is obviously associated with the decomposition of $CuInSe_2$ and in order to establish the chemical compositions of the evaporating molecules within each regime, their total evaporants were condensed onto cold glass substrates. As the amount of material evaporated under regime I was very small, condensates were obtained by placing the glass slides about 1 cm directly above the boat opening. The variation of the composition of the evaporating species during the individual evaporation regimes were also investigated. Fractions of evaporants, within each regime, were collected by placing the substrates in the vapour stream, at different stages of evaporation. The composition of each type of condensate was then determined by Electron Probe Micro-analysis.

Table 2.7 gives the composition analysis results and indicates that the composition of the vapour in each evaporation regime is very different.

Evaporation Regime	Percentage by weight of evaporant collected	Composition At%Cu	At%Se	At%In
I	100%	-	100	-
II	First 75%	0.5	38.90	60.6
	100%	0.6	49.1	50.3
	100%	0.4	56.6	43.3
III	First 60%	34.7	65.3	0
	Last 40%	74.6	25.4	0
	100%	52.6	47.1	0.3
	100%	55.4	44.4	0.2

Table 2.7: EPMA composition of vapour at different stages of evaporation of $CuInSe_2$ powders.

In regime I, the vapour consisted exclusively of Selenium whereas in regime II, the vapour contained Indium and Selenium only, with the small traces of Copper determined being most probably due to statistical counting errors in the Electron Probe Microanalysis. Regime III, on the other hand, is characterised by a vapour which does not contain any significant Indium but which consists solely of Copper and Selenium.

As far as the variation of the composition of the vapour phase during evaporation is concerned, it is clear that in the initial stages of regime II, $CuInSe_2$ loses more Indium than Selenium. However at the later stages more Selenium evaporates and the composition of total material evaporated corresponds to approximately 53at% In 47at% Se. In regime III the vapour is initially Selenium rich with appreciable amounts of Copper also evaporating. Gradually at the later stages the Selenium gets depleted and the vapour becomes more Copper rich and the total amount of material evaporated in this last regime corresponds to roughly 54at% Cu and 46at%Se.

So far no mention was made on the effect of the various powder batches on the evaporation characteristics. In the evaporation studies only powder batches A,B and D, which had the extreme compositions of $CuInSe_2$, were compared. While powders A and B had Cu_3Se_2 as secondary phase and powder D had excess Selenium, the evaporation behaviour of all the three batches was determined to be essentially similar, with all three evaporation regimes being observed.

2.4.4 Discussion of Results

Each of the evaporation regimes I, II and III of $CuInSe_2$ powders will now be looked at in more detail and compared with theoretical evaporation rates wherever possible.

2.4.4.1 Evaporation Regime I

The small amount of Selenium evaporated in regime I is highly likely to arise from excess Cu_3Se_2 and Se from the powders, because such an evaporation had not been detected by the mass spectrometric studies of vapour pressure of $CuInSe_2$[13]. This can be verified by comparing the experimental evaporation rates with calculated values.

For powders A and B, the Selenium in regime I is expected to arise from the Cu_3Se_2 phase dispersed in the starting charge. According to the phase diagram of the Cu-Se system[16], the compound Cu_3Se_2 dissociates at 386K into the solid phases $Cu_{2-x}Se$ and CuSe. The vapour pressure of Cu_3Se_2 at temperatures in the vicinity of 600K, where regime I is observed, will be thus expected to be due to the two-phase $Cu_{2-x}Se$ + CuSe region. A mass spectrometric investigation of the vapour above this two-phase region determined that[17], in the temperature range 530-645K, the vapour consisted of Selenium only. The mass evaporation rates calculated from the vapour pressure data of Mills[17] can be compared with experimentally observed evaporation rates in regime I. This is shown in Figure 2.7 where curve (a) is the theoretical Se_2 mass evaporation from Cu_3Se_2 and the dots are

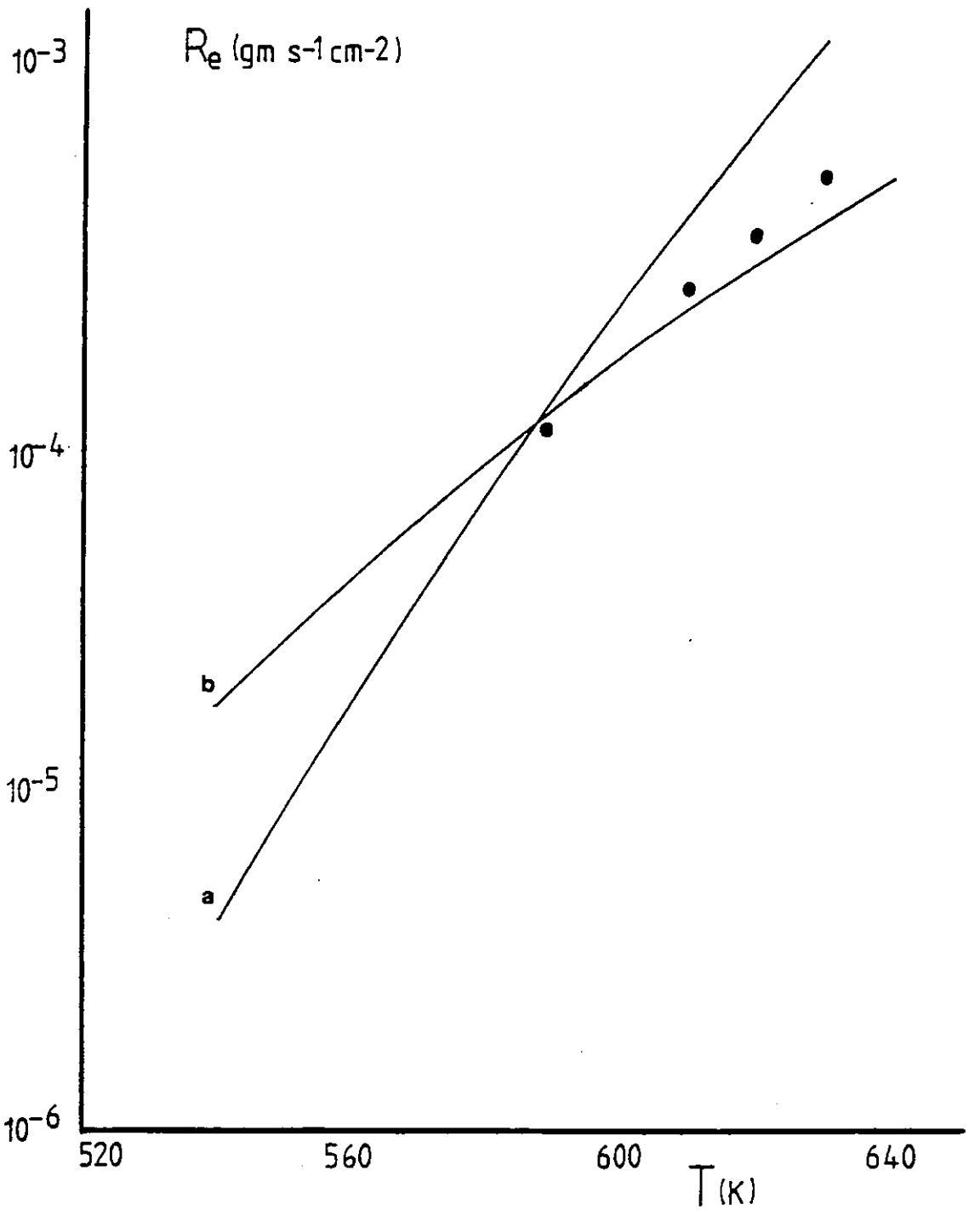

Fig. 2.7: Experimental Mass Evaporation Rate in Regime I (dots) Compared with Calculated Evaporation Rate of Selenium from:

(a) Cu_3Se_2

(b) Alloy with 2.5 at % Se

typical evaporation rates converted from the measured Hz s^{-1} units into gm s^{-1} cm^{-2} units using the expression:

$$R_e = 4.5 \times 10^{-5} \frac{d\Delta f}{dt}$$

It is apparent that the agreement between the experimental and calculated evaporation is quite good.

For the case of Powders D, which did not contain Cu_3Se_2 second phase material, the Selenium observed in evaporation regime I must be due to the excess Selenium dissolved (up to 2.5at%). In alloys, the vapour pressure of the alloy component may be estimated by modifying the vapour pressure of the pure element by its mole fraction so that

$$R_e^{alloy} = R_e^{element} x_b$$

where R_e^{alloy} is the evaporation of alloy component, $R_e^{element}$ is the evaporation of the component in pure element state and x_b is the mole fraction. Thus for direct comparison of experimental regime I evaporation rates from powders D with theory, the mass evaporation rates of Selenium forming an alloy with $x_b = 0.025$ was calculated. This is shown in Figure 2.7 as the curve labelled (b). This curve can be compared with typical experimental points (dots) and can be seen to be in very good agreement as well.

In conclusion, the evaporation of Selenium in regime I at low temperatures, is confirmed to be due to Cu_3Se_2 precipitates dispersed in powders A and B and due to dissolved excess Se in powders D.

2.4.4.2 Evaporation Regime II

The evaporation processes in regime II must be associated with the decomposition of $CuInSe_2$ into In-Se and so this region may be compared with the mass spectrometric investigation of Strelchenko et al[13]. The mass evaporation rates calculated from their vapour pressure relationships

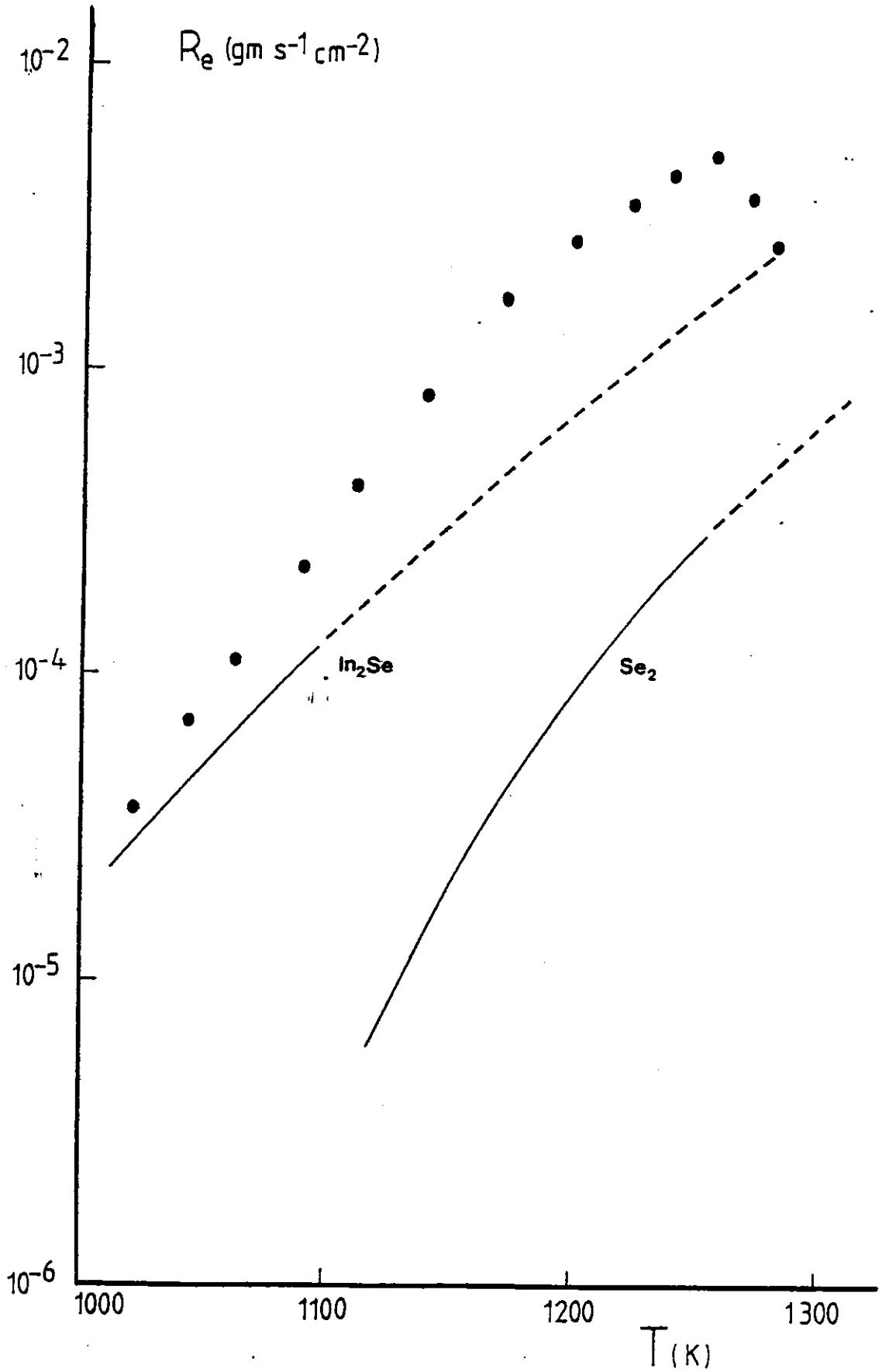

Fig. 2.8: Experimental Mass Evaporation Rate in Regime II (dots) Compared with Evaporation Rates of In_2Se and Se_2 Calculated from their Vapour Pressure

have been plotted in Figure 2.8 for the principal dissociation products, namely In_2Se and Se_2. The region of these curves, shown by dashed lines, corresponds to the extrapolation of their data to higher temperatures. Typical experimental evaporation rates are shown by dots and it is apparent that up to temperatures of 1250K there is good agreement with calculated data. It should be noticed that the data of Strelchenko predicts that the vapour over $CuInSe_2$ is dominated by In_2Se molecules at the lower temperatures. This is in good agreement with our chemical composition analysis of the initial stages in evaporation regime II. As given in Table 2.7 the vapour was determined to be predominantly Indium rich. The decrease of experimental evaporation rates after about 1250K is an indication that In_2Se molecules are no longer dominating the evaporation and that the Indium in the finite $CuInSe_2$ charge is becoming depleted. This would be in conformity with our chemical composition analysis that the vapour in the latter stages of regime II had relatively more Selenium.

2.4.4.3 Evaporation Regime III

It would appear from composition analysis that, after all the Indium has evaporated from the source, the remaining phase in the boat has a composition of about 53% Cu and 47% Se. The fact that the evaporation rate at the end of regime II drops to very low levels must be indicative that this phase has very low vapour pressure at temperatures of ~1300K. Vapour pressure data for the Cu-Se system at these high temperatures are not available and so a direct comparison of our experimental data with other published values cannot be made. Nevertheless, the composition analysis indicates that in this regime III, initially the vapour is dominated by Selenium. Gradually the vapour becomes Copper rich and at temperatures greater than 1800K, all the remaining Cu-Se phase evaporates to completion.

2.5 SUMMARY

The X-ray diffraction analysis of $CuInSe_2$ powders have indicated the presence of extraneous diffraction lines, not reported in the JCPD file for $CuInSe_2$. The lines with d-spacing values 2.89Å, 1.73Å, 1.67Å, 1.59Å and 1.32Å have been indexed in terms of previously unreported chalcopyrite reflections 004,200; 215,303; 224; 107,321 and 325,413 respectively. A theoretical intensity calculation confirmed that these spurious lines are part of the Copper Indium Selenide powder pattern. The fact that these reflections had not been observed by Parkes et al[1,2], may be due to their use of an X-ray diffractometer. As the intensities of the extra reflections are quite weak it is quite conceivable that they were not distinguishable from the background noise levels.

The powder patterns of $CuInSe_2$ powders also contained additional diffraction lines of d-spacings of 3.56Å, 3.13Å, 2.26Å, 1.83Å and 1.78Å. These matched the strongest powder lines of Cu_3Se_2 indicating that this compound was present as secondary phase material. Electron Probe line scans confirmed the nature of these precipiates and indicated that they were distributed non-uniformly throughout the ingot.

The chemical composition of $CuInSe_2$ from various lumps from the bulk, indicated considerable variation. Single phased $CuInSe_2$ had excess solubility for Se and In_2Se_3. Such solubilities appear to be a common feature among the I-III-VI_2 chalcopyrite compounds which are also characterised by an absence of homogeneity for the Copper rich side of the stoichiometric composition. The composition data of the samples used in this work and that of Möller et al were combined to define an approximate single phase existence region for $CuInSe_2$.

To determine conditions that would yield thin films with the correct chemical composition the compositional variation during evaporation of $CuInSe_2$ has been investigated by monitoring the evaporation rate and by

composition analysis of condensates obtained at different stages during evaporation.

Three distinct evaporation regimes were detected. In regime I, which occurred around 600K, Selenium was found to evaporate originating from excess Cu_3Se_2 or Se in the powders. In regime II occurring at 1000 to 1300K, the vapour consisted of Indium and Selenium only. This regime was associated with the complete depletion of all the Indium in the starting evaporating charge. Regime III occurred from 1300 to 1800K and was due to the evaporation of Cu-Se phase remaining behind in the evaporating charge.

The thermal evaporation experiments indicated that at all temperatures the composition of the vapour above $CuInSe_2$ is not stoichiometric. This necessitates special deposition techniques if films with the correct composition are to be prepared. As the bulk ingot was determined to be inhomogeneous, the identity of the actual lumps used as the evaporating powder must be taken into consideration in the discussion of the thin film properties.

REFERENCES - CHAPTER 2

(1) J. PARKES, R.D. TOMLINSON and M.J. HAMPSHIRE, "Crystal data for $CuInSe_2$". J. Appl. Cryst. 6 414 (1973)

(2) Joint Committee on Powder Diffraction Standards No. 23-209 (1973)

(3) Joint Committee on Powder Diffraction STandards No. 19-402 (1969)

(4) H.P. KLUG and L.E. ALEXANDER, "X-ray diffraction procedures for polycrystalline and amorphous materials". John Wiley and Sons (1974)

(5) B.D. CULLITY, "Elements of X-ray diffraction". 2nd edition, Addison-Wesley Publishing Co. (1978)

(6) International Tables for X-ray Crystallography, vol. I. The International Union of Crystallography (1952)

(7) International Tables for X-ray Crystallography, vol. III. The International Union of Crystallography (1962)

(8) D.R. BEEMAN and J.A. ISASI, "Electron beam microanalysis". ASTM STP 506 (1972). American Society for Testing and Materials

(9) W. MÖLLER, G. KÜHN and W. BEIER, "Electron probe microanalysis of $CuInSe_2$ and $CuGaSe_2$ crystals". Krista und Tech. 13 1439 (1978)

(10) L.S. PALATNIK and E.I. ROGACHEVA, "Phase diagrams and structure of some semiconductor $A_2^{I}C^{VI}$ - B_2C^{VI} alloys". Soviet. Phys-Doklady 12 503 (1967)

(11) M. KOKTA, J.R. CARRUTHERS, M. GRASSO, H.M. KASPER and B. TELL, "Ternary phase relations in the vicinity of chalcopyrite Copper Gallium Sulphide". J. Electron. Mater. 5 69 (1976)

(12) J.C. MIKKELSEN, Jr., "Ternary phase relations of the chalcopyrite compound $CuGaSe_2$". J. Electron Mater. 4 541 (1981)

(13) S.S. STRELCHENKO, S.A. BONDAR, A.D. MOLODYK, L.I. BERGER and A.E. BALANEVSKAYA, "Mass-spectrometrometric investigation of the sublimation of certain ternary semiconductors of the $A^{I}B^{III}C^{VI}_2$ type". Inorg. Matls 5 502 (1969)

(14) R.E. HONIG and D.A. KRAMER, "Vapour pressure data for the solid and liquid elements". RCA Review 30 285 (1969)

(15) R. GLANG, "Vacuum evaporation" in Handbook of Thin Film Technology, Eds. L.I. Maissel and R. Glang, McGraw-Hill (1970)

(16) R.M. MURRAY and R.D. HEYDING, "The Copper-Selenium system at Temperatures to 850K and pressures to 50 kbar". Can. J. Chem. 53 878 (1975)

(17) K.C. MILLS, "Thermodynamic data for inorganic sulphides, selenides and tellurides", p.252, Butterworths (1974)

(18) R.D. TOMLINSON, private communication. Elec. Eng. Dept., Salford University.

CHAPTER 3

THE DEPOSITION OF $CuInSe_2$ FILMS AND THEIR STRUCTURAL AND COMPOSITIONAL PROPERTIES

3.1 INTRODUCTION

In this chapter a simple deposition technique for obtaining stoichiometric $CuInSe_2$ thin films is described, and the experimental conditions for preparing homogeneous single phased chalcopyrite $CuInSe_2$ films are established through X-ray diffraction, Tranmission Electron Microscopy and Electron Probe Microanalysis techniques. The chapter also includes some observations of the effect of oxygen on the surface properties of $CuInSe_2$.

In the previous chapter it was concluded that due to thermal dissociation of $CuInSe_2$, special deposition techniques must be used to prepare films with correct composition and structure. To date most thin film preparations of $CuInSe_2$ have been made using the bulk as the starting powder and the following methods have been used:

1. Flash Evaporation: In this technique the starting material is in the form of finely ground powder and is continuously dispensed onto a refractory metal source held at temperatures high enough to evaporate the less volatile constituent of the compound. As each powder grain hits the hot source it vaporises instantaneously, with some fractionation occurring. This leads to stratification of the order of a few monolayers, in the films, which can be made homogeneous by keeping the substrates hot.

The flash evaporation method suffers from considerable loss of material in the form of falling grains which 'spit' from the hot source and in the form of falling grains being lifted away before reaching the source by the current of rising vapours at the source. Unless special precautions

are taken these grains may be splattered onto the substrates causing inhomogeneities and pinholes. Another problem with this method of evaporation is that, despite extensive heat shielding, the temperature in the evaporating system rises during the deposition. This may have two consequences: firstly the substrate temperature can rise uncontrollably to high values so that some unwanted re-evaporation of the volatile component of the compound may occur. Secondly, outgassing from the surfaces surrounding the source may cause a poor vacuum and might result in the increased interaction of oxygen and water vapour in the chamber with the deposits.

Preparation of $CuInSe_2$ films by flash evaporation has been reported by Elliott et al[1]. Their films were not of good quality however and had a powdery appearance apparently containing undissociated particles of $CuInSe_2$. No composition data is reported but the chalcopyrite structure of the films was confirmed with an X-ray powder diffractometer. There were significant variations in the electrical properties, with p- and n-type films resulting at substrate temperatures > 400°C. Schumann et al[2] also used flash evaporation to deposit epitaxial layers of $CuInSe_2$ on GaAs and films deposited on substrates below 450°C were n-type and those above were p-type. Recently Tomlinson et al[3] determined that unless source temperatures greater than 1250°C are used, flash evaporated $CuInSe_2$ have compositions which are grossly non-stoichiometric.

2. Fast Evaporation: In this modified form of flash evaporation a fixed amount of bulk powder is placed in a cold source. The charge is then evaporated to completion at very high deposition rates, by heating the source to very high temperatures almost instantaneously.

The stratification of the films is more severe in this method and large compositional gradients may be expected in the resulting films, unless hot substrates are employed. Some spitting may also be expected, but

heating problems commonly encountered in flash evaporation will not be present.

Fray et al[4] used this technique to deposit films onto substrates held between 150-350°C. They added extra Selenium to the starting charge to obtain p-type films. However, the chemical composition and X-ray diffraction analyses indicated that the layers had a lot of compositional scatter and contained CuSe or $Cu_{2-x}Se$ as secondary phases, presumably due to excess Selenium in the source and some re-evaporation of In_2Se from the hot substrate.

3. Direct Evaporation: In this method of preparation, a large quantity of the bulk compound is heated to sufficiently high temperatures that the constituent elements appear together in the vapour phase. In order to deposit films with the correct composition the method requires precise shutter opening times at some prescribed temperature. This is likely to result in non-reproducibility of the composition between runs and probably is one of the least controllable methods of evaporation of an incongruently evaporating compound.

Such a single source evaporation technique has been employed by Kazmerski et al[5] who adjusted the final stoichiometry of the films by choosing appropriate substrate temperatures. While no details of the composition of their layers are given, they reported that n-type films can be obtained only at a substrate temperature T_s of $200 < T_s < 325$°C. P-type films were prepared by a two-source method in which Selenium was evaporated simultaneously with $CuInSe_2$[6]. Kokubun et al[7] who also used a two-source technique demonstrated that p-type films were obtained when the Selenium source temperature was in the range 180-250°C, but large scatter in the electrical properties occurred.

4. Multiple Source Evaporation: This consists of evaporating the constituent elements of the compound from separate cells and having the

vapours interact on the heated substrate.

The method requires strict control of the four deposition parameters and difficulties with reproducibility of individual flux rates have been reported by Grindle et al[8] who used a Molecular Beam Epitaxy method to grow $CuInSe_2$ films. These authors found that p-type $CuInSe_2$ films were Copper rich and may contain some spurious binary compounds.

5. Sputtering: In this method cold pressed targets of powdered $CuInSe_2$ are bombarded with positive ions from a gaseous plasma, resulting in the ejection of surface atoms which consequently deposit on the substrates. However, because different elements in a compound have different sputtering yields and sticking coefficients the problem of fractionation will be encountered and, to obtain single phased films with correct stoichiometry, various deposition parameters will have to be adjusted.

An evaluation of the properties of $CuInSe_2$ films prepared by RF sputtering have been done by Samaan et al[9] who reported that considerable variations in composition and structure occurred due to various combinations of RF power, (DC bias) voltage, and substrate temperature. In general, low resistivity p-type films were produced at substrate temperatures of less than 250°C. A similar investigation by Piekoszewski et al[10] revealed that the properties of the films were additionally influenced by the particle size of the powder from which the target was prepared. These authors reported that although their films were stoichiometric to within ±5%, they contained weak traces of unidentified second phase material.

The above survey of deposition techniques indicates that considerable difficulties exist in preparing stoichiometric single phased $CuInSe_2$ thin films. This is not too surprising in view of the many experimental parameters that have to be adjusted and controlled in a particular method chosen. It is, therefore, desirable to minimise these variables in order to prepare good quality films in a relatively simple

and economical manner.

Proposed Technique in this Work

In this project an evaluation of the properties of $CuInSe_2$ films obtained by evaporating a fixed amount of bulk $CuInSe_2$ onto mainly cold substrates was made.

The substrates were kept at room temperature so as to minimise the possibility of any re-evaporation of the condensing vapours and hence to keep the composition of the films as close to that of the source. The powders were evaporated by the fast heating technique because this led to high supersaturations at the substrate so that re-evaporation would again be less likely. Furthermore, using high deposition rates would also decrease the influence of any residual gas molecules impinging on the films during deposition. A rapid heating technique as opposed to flash evaporation was chosen to avoid any excessive heating in the system and to allow the outgassing of the powders. The latter is important because if the bulk contains second phase precipitates, which was certainly the case here, then their incorporation in the films will not be desirable.

With this technique it was anticipated that the films may be stratified and contain compositional gradients. However, provided the stoichiometry of the starting source is also preserved in the thin films, it was thought that fractionation might not be a serious problem and that the films could be made homogeneous by solid state interdiffusion and reaction processes during a suitable anneal. For this purpose the films were heat treated at various temperatures and their stoichiometry and structure were monitored.

In order to see the effect of substrate temperature on the composition and structure of the films, a few films were also deposited onto hot substrates.

3.2 THE PREPARATION OF FILMS

3.2.1 The Vacuum System and the Thin Film Deposition Assembly

The thin film samples were all prepared in a vacuum system which consisted of a 40 cm diameter vacuum chamber evacuated by an Edwards diffusion pump using Silicone 705 oil. A liquid nitrogen cold trap, situated between the chamber and the diffusion pump, prevented the back-streaming of oil vapour and reduced the partial pressure of the gases present. The system was capable of a pressure of ~4 x 10^{-6} torr as measured by an ionisation gauge.

The vacuum chamber was partitioned into three sections which meant that it was possible to carry out up to three different depositions in the same pump-down. The three sources were for the evaporation of the semiconductor and for laying down different metal contacts. A schematic diagram of a deposition section is shown in Figure 3.1. The substrate-mask assembly was placed about 15 cm away from the evaporation source and was shielded by a shutter which was rotated away to permit film deposition. A quartz crystal for monitoring the evaporation rate was placed below the shutter but near the substrate. A pyrex evaporation shield was placed around the evaporation source to minimise the spread of evaporant and hence contamination inside the chamber walls. This shield was etched clean prior to any evaporation.

For the evaporation cell material, molybdenum was considered to be suitable because it is stable at high temperatures, conducts heat well and can be machined rather easily. More importantly, its interaction with the constituents of Copper Indium Selenide is expected to be minimal[11]. According to Elliott[12], the solubility of Indium in molybdenum is vanishingly small and less than 2% Copper has been determined to be soluble in molybdenum. However molybdenum does react with Selenium to form M_oSe_2 at very high temperatures. In order to verify the extent of reaction of the molybdenum cell with the above elements, powders of $CuInSe_2$

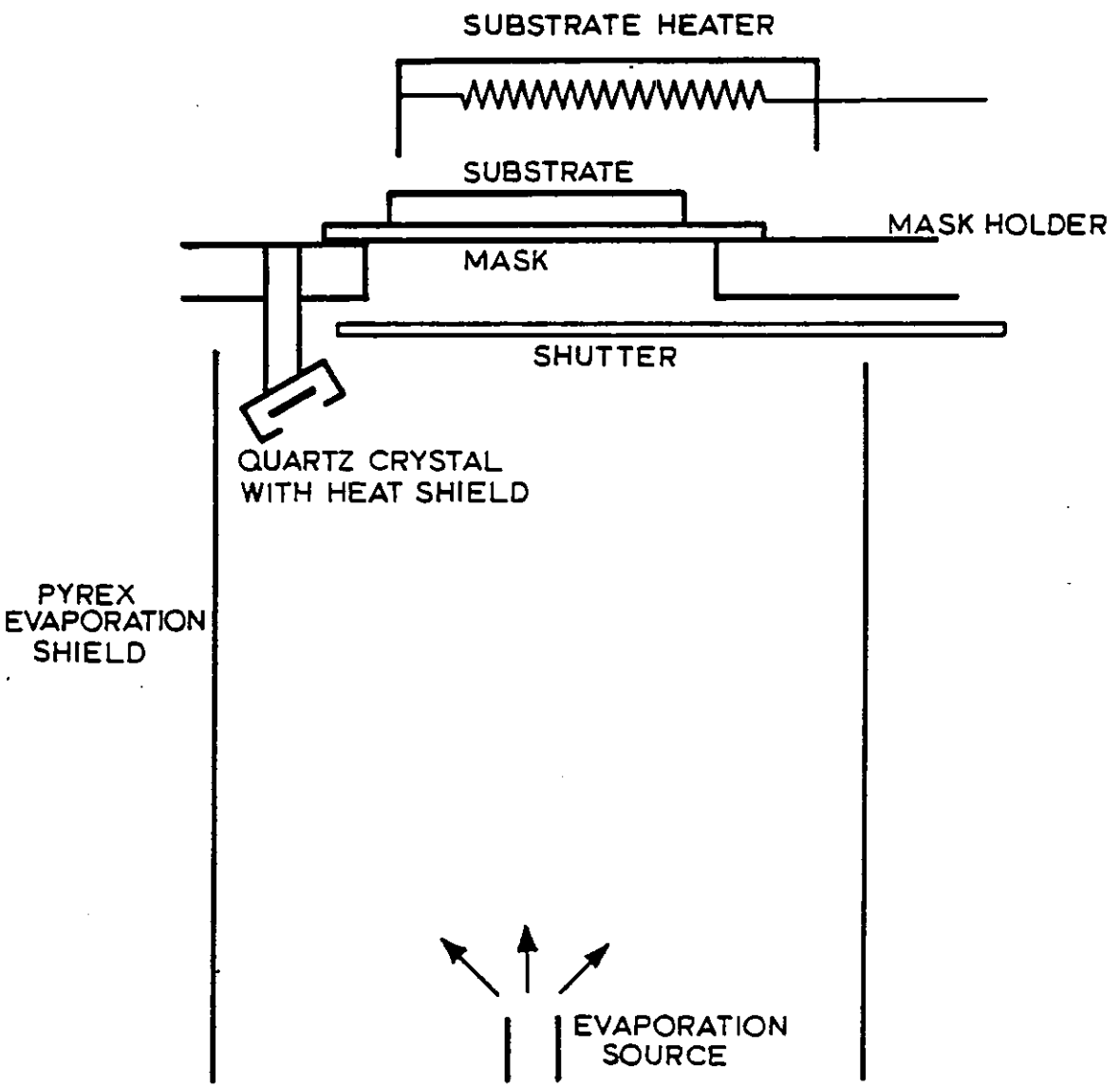

Fig. 3.1: Schematic Drawing of Thin Film Deposition Section

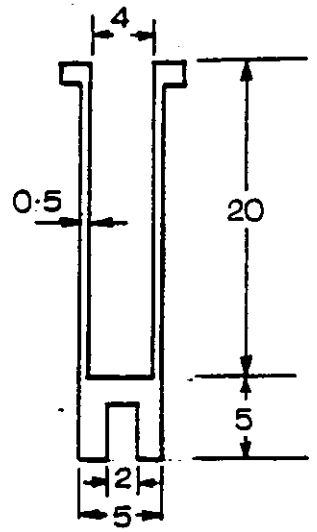

All dimensions in mm

Fig. 3.2(a): Evaporation Crucible

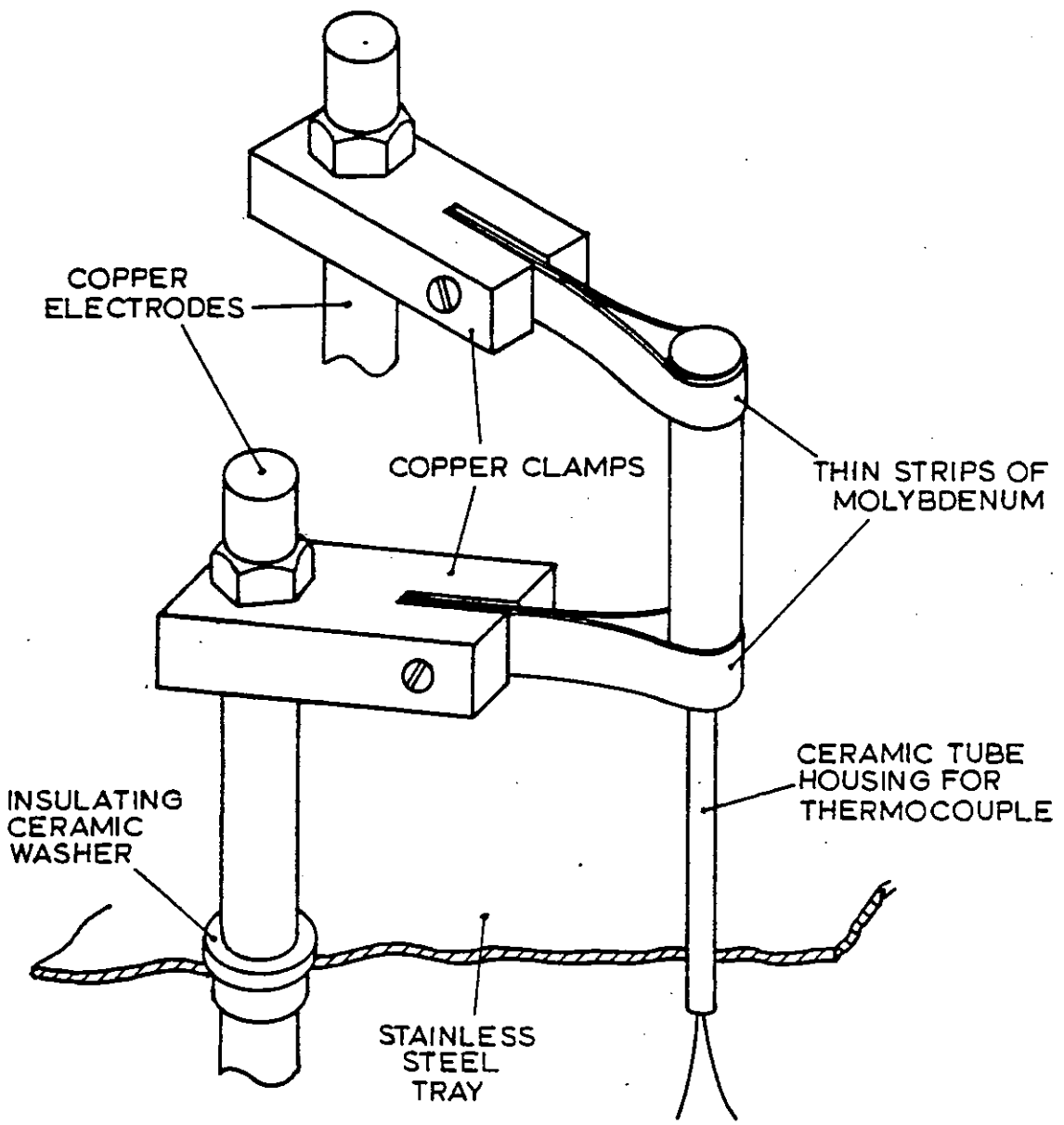

Fig. 3.2(b): Evaporation Source Assembly

were evaporated from hot strips of molybdenum and the inner surface composition of the boat after evaporation was examined by Electron Probe Microanalysis. From spectral scans across the boat for each element, Cu, In and Se, it was concluded that their presence was extremely dubious, probably well below ~0.1%.

The evaporation crucible used in this study had the shape shown in Figure 3.2(a). This boat enabled large quantities of material to be evaporated at high evaporation rates. The cell was prepared by carefully drilling out a 6 mm diameter molybdenum rod. A small recess at the bottom enabled the insertion of a thin thermocouple. This was of Pt-Pt 13% Rh type and allowed the recording of temperature up to ~1800°C.

The heating of the molybdenum crucible was achieved by passing large currents ~300 Amperes along its length. As shown in Figure 3.2(b), thin molybdenum strips were wound around the neck and bottom of the boat and were welded to the main body by repeated heating of the empty cell to very high temperatures. The molybdenum strips were clamped at the other end by thick copper clamps connected to copper electrodes. These provided a very low electrical resistance and allowed the conduction of heat quickly once the cell was heated and then cooled down.

3.2.2 Evaporation Procedure

All the thin film structures were deposited through stainless steel masks onto glass substrates. The latter were thoroughly washed in liquid detergent and then rinsed in distilled water. They were subsequently degreased in an iso-propyl alcohol reflux condenser and placed immediately into the vacuum system.

As soon as the required vacuum pressure (~10^{-6} torr) was reached, the starting charge of ~250 mg $CuInSe_2$ powder was gently warmed towards 750°K over a period of approximately 30 minutes. The shutter was closed during this outgassing period and any excess Selenium from evaporation regime I

(see section 2.4) was not allowed to reach the substrates.

The molybdenum boat was then heated rapidly from ~750°K towards ~2000°K by turning up the variac instantaneously to a previously predetermined value and allowing currents of ~300 Amperes to pass through. It must be recalled that the free evaporation experiments had established that a boat temperature greater than 1750°K was needed to evaporate $CuInSe_2$ to completion. A final boat temperature of 2000°K was aimed at to make sure that the starting charge evaporated completely and in as small a period of time as possible. Higher boat temperatures were not used because of the limitations imposed by the melting of the platinum element of the thermocouple, which occurs at ~2043°K.

The boat temperature and instantaneous deposition rate of $CuInSe_2$ during a typical fast evaporation experiment are shown in Figure 3.3(a) and 3.3(b) respectively, where they are plotted against time of evaporation. It should be noticed that the whole evaporation lasts typically ~30 seconds or so and during the first 20 seconds after the variac was turned up, the boat temperature increased typically at a rate of ~50 °K s^{-1}. The heating rate then drops and eventually the boat reaches a steady state temperature ~2000°K.

During this period, the evaporation rate goes through the evaporation regimes II and III, determined previously in section 2.4, but now there is some overlap occurring and these are shown by the dashed lines. It should be noticed that the evaporation rates are very high and reach a maximum of ~4000 Hz s^{-1}, which corresponds to approximately 180 mg s^{-1} cm^{-2}.

The substrate temperature which was monitored during the evaporation did not increase by more than about 10° due to radiant heating and so the substrates can be considered to be essentially at a constant temperature.

Complete evaporation of 250 mg of powdered $CuInSe_2$ resulted in film thickness in the region of ~6700 Å as measured by a Talysurf stylus instrument. Thinner films for transmission microscopy studies could be

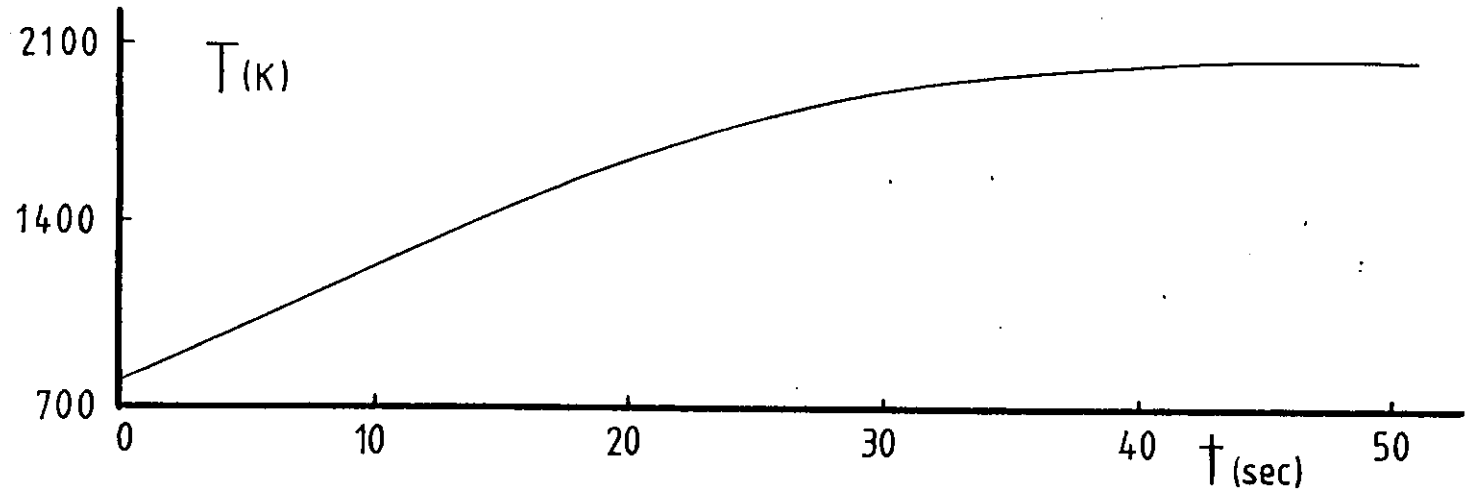

Fig. 3.3(a): Crucible Temperature as a Function of Time During Film Preparation Run

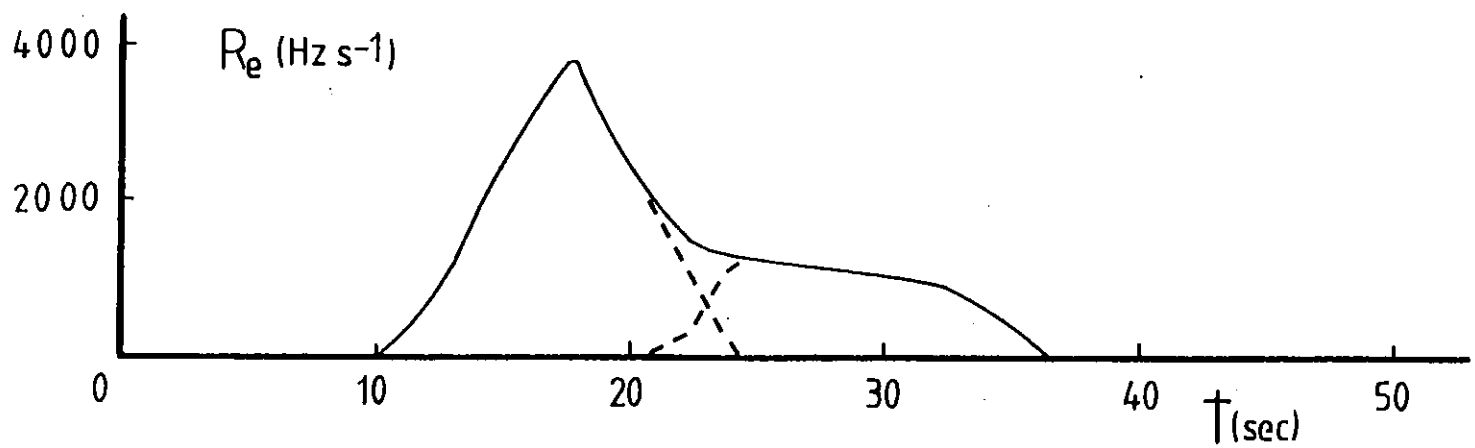

Fig. 3.3(b): Evaporation Rate as a Function of Time During Film Preparation Run

obtained by evaporating half the amount of the starting powder.

The film thicknesses had a variation of ~800Å in between runs and this was due to some spitting of grains during the rapid heating up. This was observed clearly after the completion of evaporation, by the presence of unmolten powder dispersed on the bottom tray of the source assembly. However, in all cases there was no evidence of splattering of material against the substrate and the films were pinhole free, indicating that the height attained by any grain during spitting was less than the source to substrate distance.

All the films were subsequently heat treated in a flowing nitrogen environment at temperatures of 150°C, 350°C and 450°C for various times. Limited numbers of anneals were performed also in forming gas (10% N_2, 90% H_2) and oxygen ambients as well.

3.3 X-RAY DIFFRACTION ANALYSIS OF FILMS

3.3.1 Experimental Procedure

The thin films of $CuInSe_2$ were examined in a GEC X-ray Texture Camera which was very recently designed for the study of thin films on substrates[13].

In this camera, whose schematic diagram is given in Figure 3.4, the powder diffraction patterns of the film and its substrate are recorded on a cylindrical film whose axis coincides with the incident beam. To limit the penetration of the X-ray beam and thus to enhance the diffraction pattern of the film with respect to the substrate, a glancing angle geometry is used and the flat specimen is inclined at angle, i, to the incident beam. The specimen is continously rotated in its own plane so that the irradiated area describes an annulus on the surface.

The resulting diffraction patterns consist of straight lines and their d-spacings are determined by measuring the position of the lines, y, along the camera axis. This is shown in Figure 3.5(a) where the incident and diffracted beams, for a (hkℓ) plane at a Bragg angle θ are considered.

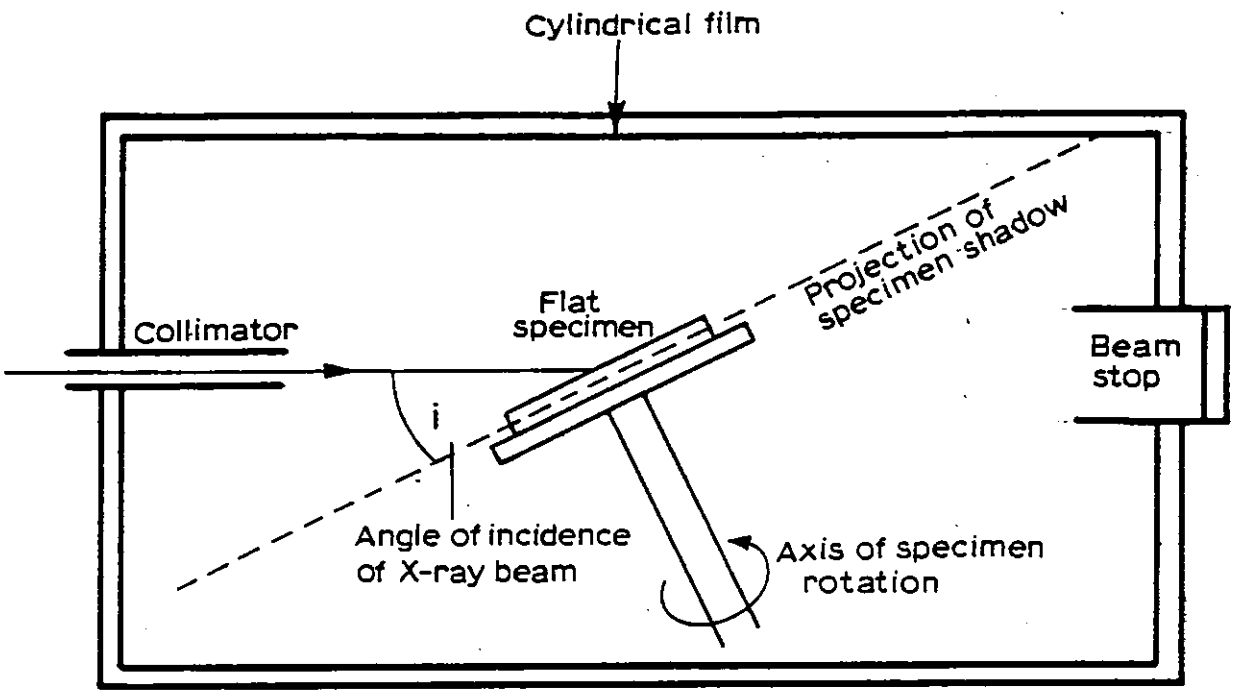

Fig. 3.4: Schematic View of the X-ray Cylindrical Texture Camera

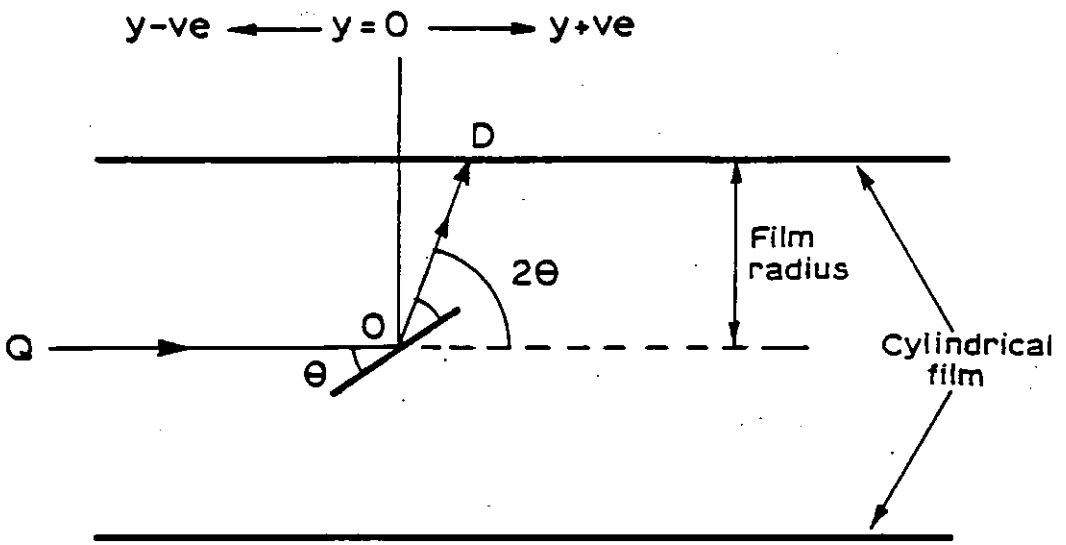

Fig. 3.5(a): Diagram Showing the Relationship Between Measured y-values and Bragg Angles θ

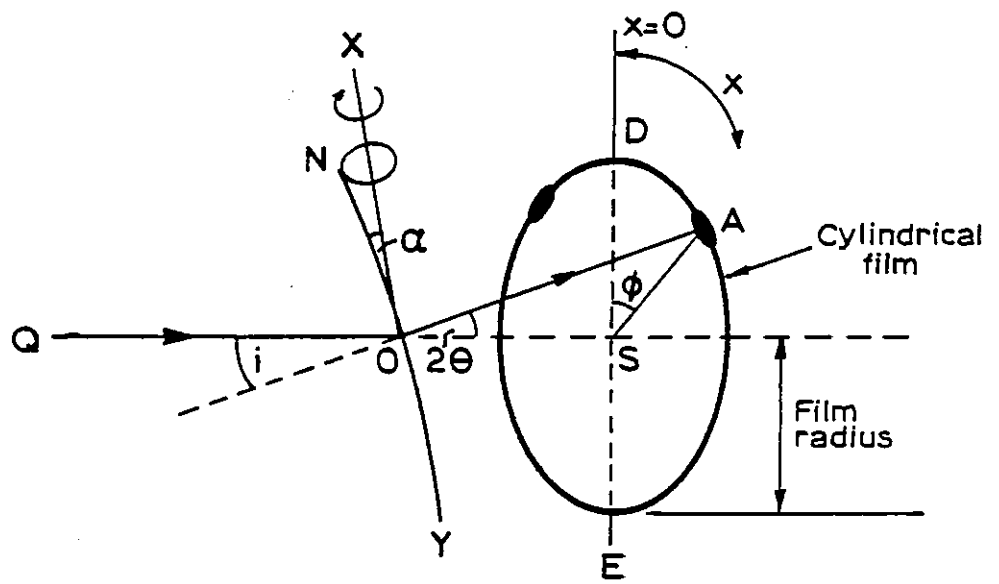

Fig. 3.5(b): Diagram Showing the Relationship Between the x-coordinate and Preferred Orientation

The camera also records any preferred orientation effects in the films as revealed by intensity modulations of the diffraction lines along the x-axis. This is shown, in Figure 3.5(b), for a crystallographic plane (hkℓ) whose normal ON makes an angle, α, with the normal to the specimen surface XY. As the specimen is rotated about the XY axis, the (hkℓ) plane will move into a position which satisfies the Bragg condition and a reflection will flash out to give an intense spot A on the appropriate diffraction line for the plane. The positions of spot A, along the x-axis of the film, will be a function of the Bragg angle θ, the orientation angle, α, and the X-ray incident beam angle, i[13]. Thus, by measuring the position of intensity maxima along the diffraction lines the plane (or planes) which is preferentially aligned parallel to the surface of the substrate may be deduced.

The angle of incidence, i, of the X-ray beam with respect to the substrate sets the range of Bragg angles that may be recorded so that reflections with $2\theta < i$ will not be observed. Wallace et al[13] recommend the use of i = 30° but with CuKα radiation, this setting would result in the cutting off of the low angle $CuInSe_2$ reflections of 101 at 2θ = 17.05°; 112 at 2θ = 26.69°; and 103 at 2θ = 27.88°. Among these the 112 reflection is the very intense line which characterises $CuInSe_2$ and this means that $i < 27°$ must be employed. The possibility of second phases existing in the films must not be ruled out, however, and a review of the intense lines in the system Cu-In-Se-O revealed that most of the intense lines of these materials occurred at $2\theta \leq 25°$. Therefore an incidence angle of i = 22° was used throughout this study and this allowed any reflection with d-spacing up to 4Å to be recorded in the photographs, with Copper radiation.

For the interpretation of any preferred orientations in the films a chart, which gives lines of constant orientation angle, α, versus Bragg angles, 2θ, has been constructed for an incidence angle i = 22°. The chart,

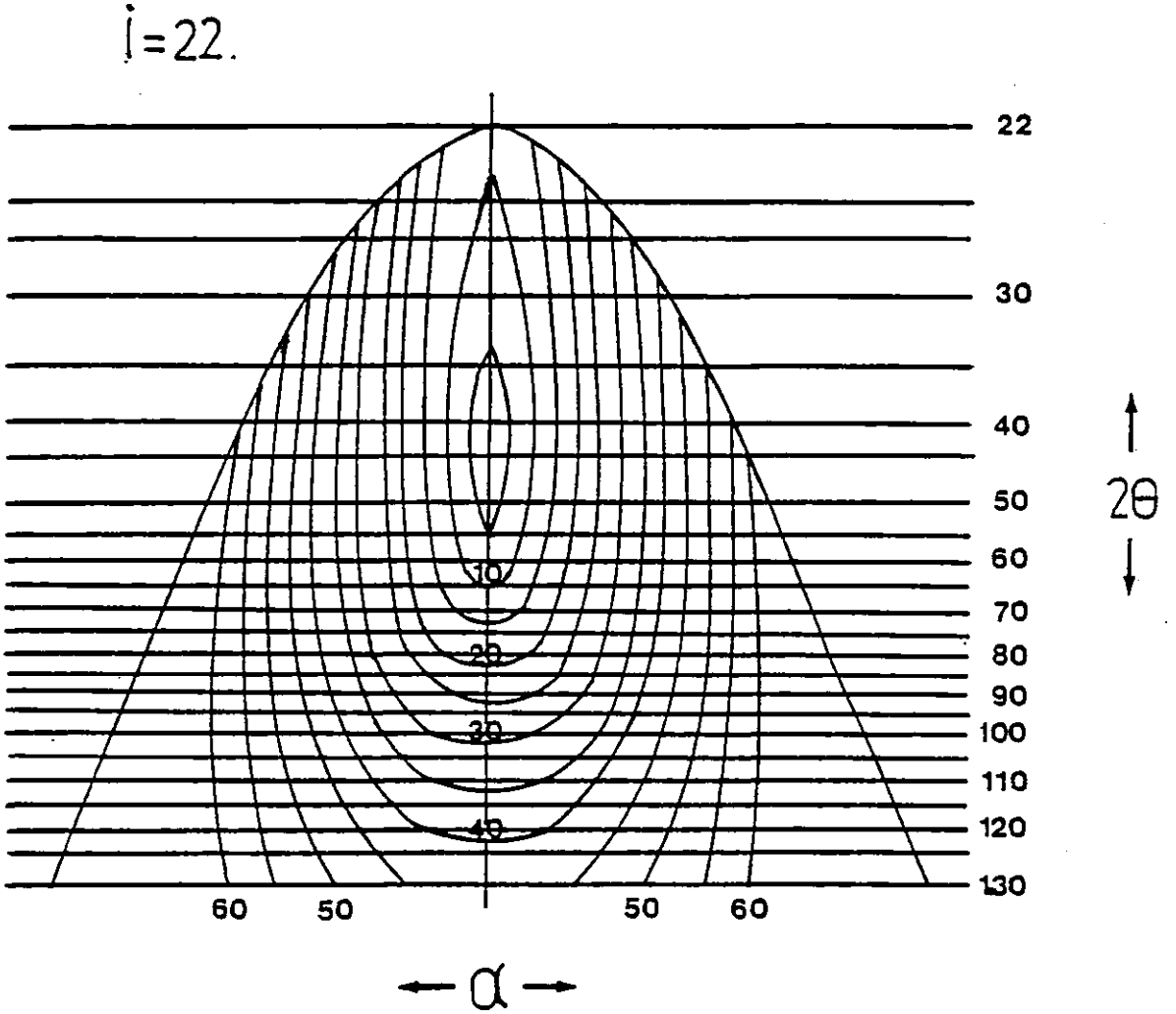

Fig. 3.6: Chart Giving α and 2θ Values for the Determination of Film Orientation in the Texture Camera

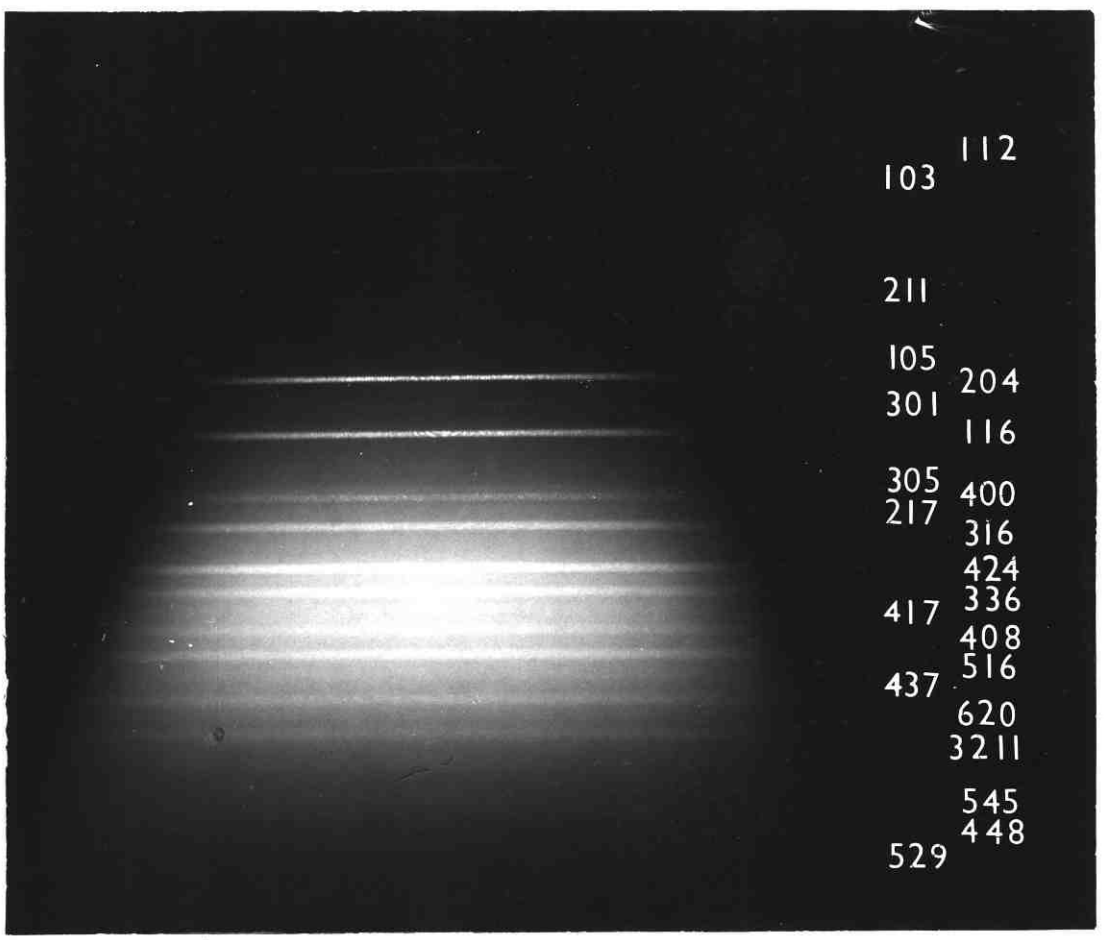

Fig. 3.7: X-ray Diffraction Photograph of $CuInSe_2$ Powder using the Texture Camera

which has been reproduced in Figure 3.6, allowed the simple determination of the orientation angle α at an intensity maxima occurring for any Bragg reflection.

In order to obtain, precisely, the position of the diffraction lines of Copper Indium Selenide and determine a scale of their intensity in the texture camera, bulk $CuInSe_2$ powders were photographed. The powders, with an average grain size of < 45 µm, were mixed thoroughly with Canada Balsam and coated on a thin microscope slide. Before the thick paste had dried, some more powder was sprinkled and the specimen was made as flat as possible. A cylindrical texture pattern from these $CuInSe_2$ powders is shown in Figure 3.7. The diffraction lines have been indexed and were used as a basis for comparison with the X-ray patterns of $CuInSe_2$ films, taken with the same camera settings.

3.3.2 Structure of Films Deposited on Cold Substrates

The variation of the structure of the deposited films before and after annealing was investigated by examining their X-ray diffraction patterns. Typical photographs for a film in the as-deposited state, after a heat treatment at 150° for 3 hrs and after a heat treatment at 350°C for 3 hrs, are shown in Figures 3.8, 3.9 and 3.10 respectively and these indicate that the films are polycrystalline.

3.3.2.1 Unannealed Films

At first glance, it is evident that the X-ray pattern of the films prior to heat treatment does not resemble that of bulk $CuInSe_2$ powder shown in Figure 3.7. The measurements of the d-spacings of these lines indicated that only some were due to $CuInSe_2$ reflections. A comparison of the intensity and $d_{hk\ell}$ values of the experimental reflections with the d-spacings and intensities of the various compounds in the systems Cu-Se, In-Se, Cu-In and their oxides, concluded that the rest of the reflection in the photograph were due to Cu_3Se_2. These experimental data and the assigned

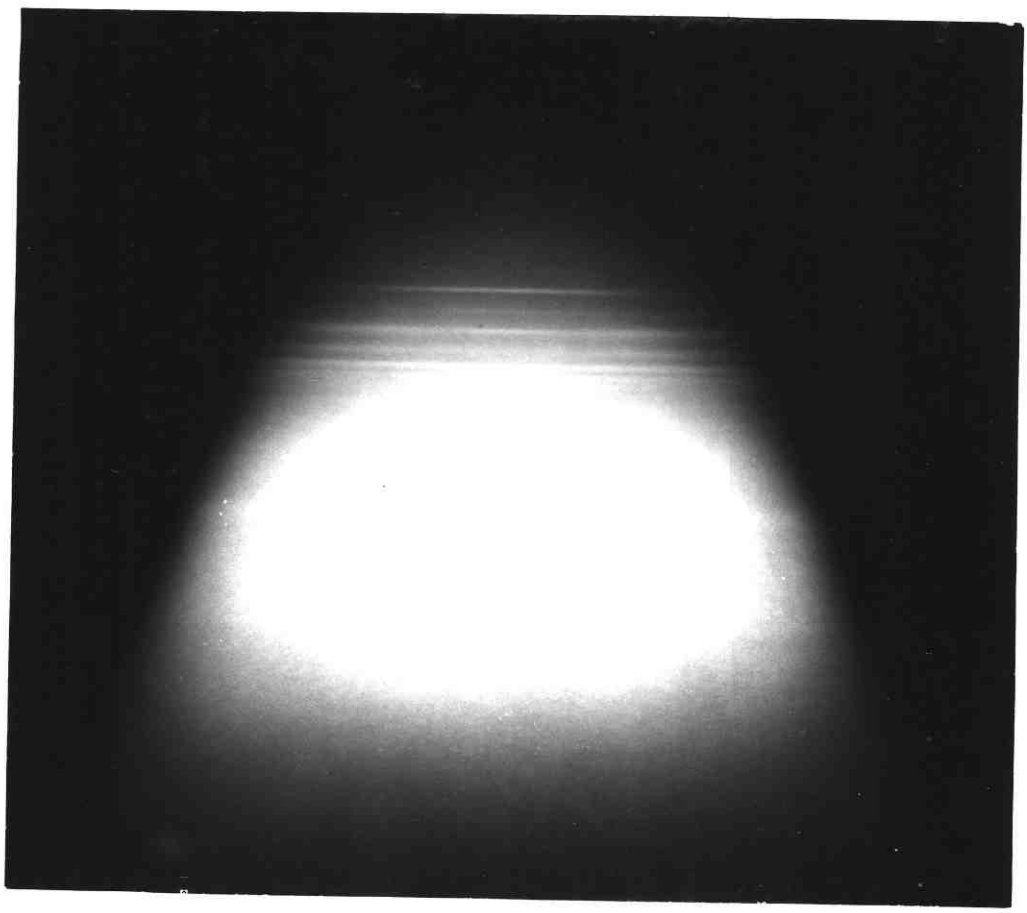

Fig. 3.8: Texture Camera X-ray Diffraction Pattern of a $CuInSe_2$ Film before Anneal

As-deposited Films

Line identification	d_{exp} Å	Assigned hkℓ index
a	3.56	Cu_3Se_2 (101)
b	3.34	$CuInSe_2$ (112)
c	3.21	Cu_3Se_2 (200)
d	3.10	Cu_3Se_2 (111)
e	2.87	Cu_3Se_2 (210)
f	2.57	Cu_3Se_2 (201)
g	2.39	Cu_3Se_2 (211)
h	2.27	Cu_3Se_2 (220)
i	2.15	Cu_3Se_2 (002)
j	2.04	Cu_3Se_2 (310) + $CuInSe_2$ (204,220)
k	1.92	Cu_3Se_2 (301)
l	1.84	Cu_3Se_2 (311)
m	1.77	Cu_3Se_2 (202)
n	1.74	$CuInSe_2$ (116,312)
o	1.65	Cu_3Se_2 (321)
p	1.44	$CuInSe_2$ (008,400)
q	1.19	$CuInSe_2$ (228,424)

Table 3.1: X-ray diffraction lines of as-deposited films

indices from the observed reflections are given in Table 3.1. These results indicate that in the as-deposited state, the films are not homogeneous and are multiphased.

3.3.2.2 Films Annealed at 150°C

The effect of a low temperature anneal at 150°C was to strengthen the intensity of the $CuInSe_2$ reflections present in the as-deposited films. This is evident in Figure 3.9 where, in addition, new X-ray diffraction lines were also observable. The measurement of the d-spacings of these reflections confirmed that they belonged to $CuInSe_2$. A comparison of the pattern of as-deposited and annealed films also revealed that the intensity of all Cu_3Se_2 reflections had decreased. As a consequence, some low intensity Cu_3Se_2 reflections which were detectable in the as-deposited films, had disappeared after the heat treatment. These observations indicated that a solid state reaction towards forming the compound $CuInSe_2$ occurred in the film and that this reaction was speeded up with an increase in temperature.

3.3.2.3 Films Annealed at 350°C

When the films were annealed at 350°C for 3 hours, the X-ray examination revealed that all the Cu_3Se_2 reflections had disappeared and that the X-ray patterns contained the $CuInSe_2$ reflections only (see Figure 3.10). The intensities of all the lines were high enough that the X-ray photographs had recorded even the weaker intensity chalcopyrite reflections at the low Bragg angles. These reflections 103; 211; 105; 213 and 301 were clearly discernible and a comparison of the pattern of the films annealed at 350° with that of bulk $CuInSe_2$ of Figure 3.7 revealed that all the $CuInSe_2$ reflections present in the bulk powder were also present in the thin films.

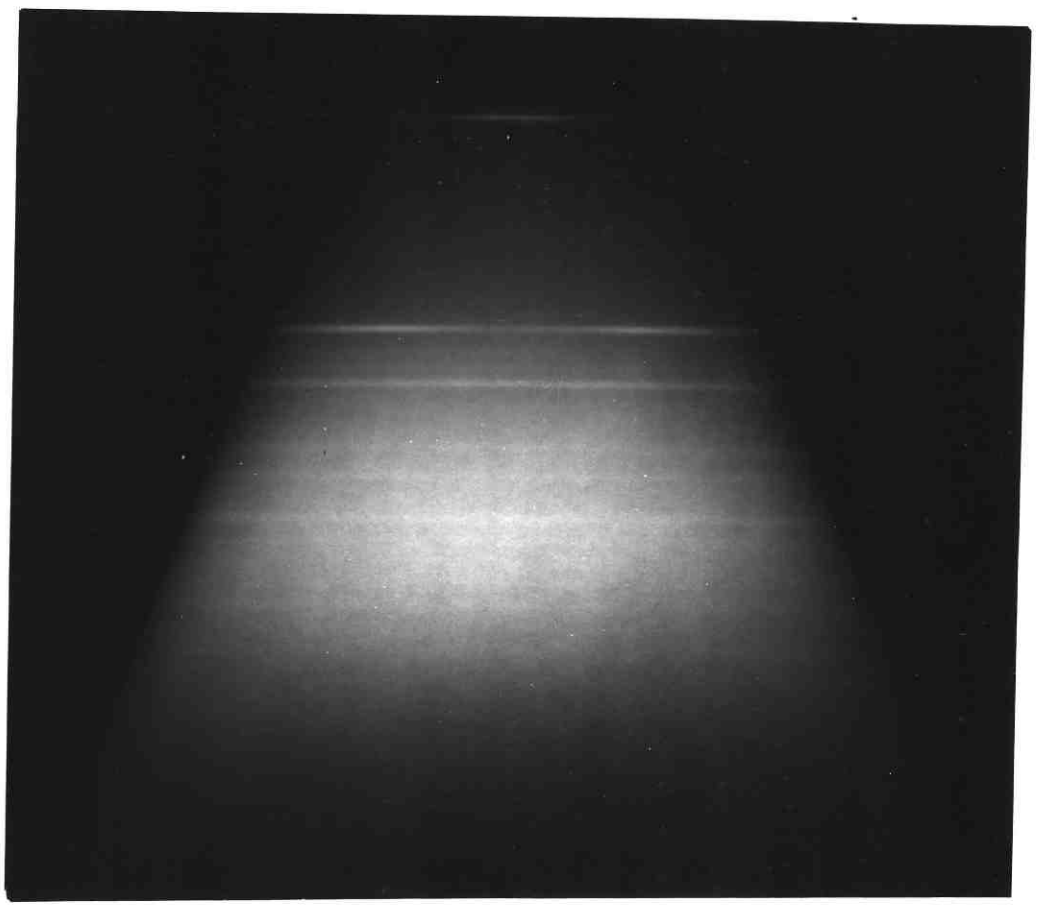

Fig. 3.9: Texture Camera X-ray Diffraction Pattern of a $CuInSe_2$ Film after Anneal at 150°C

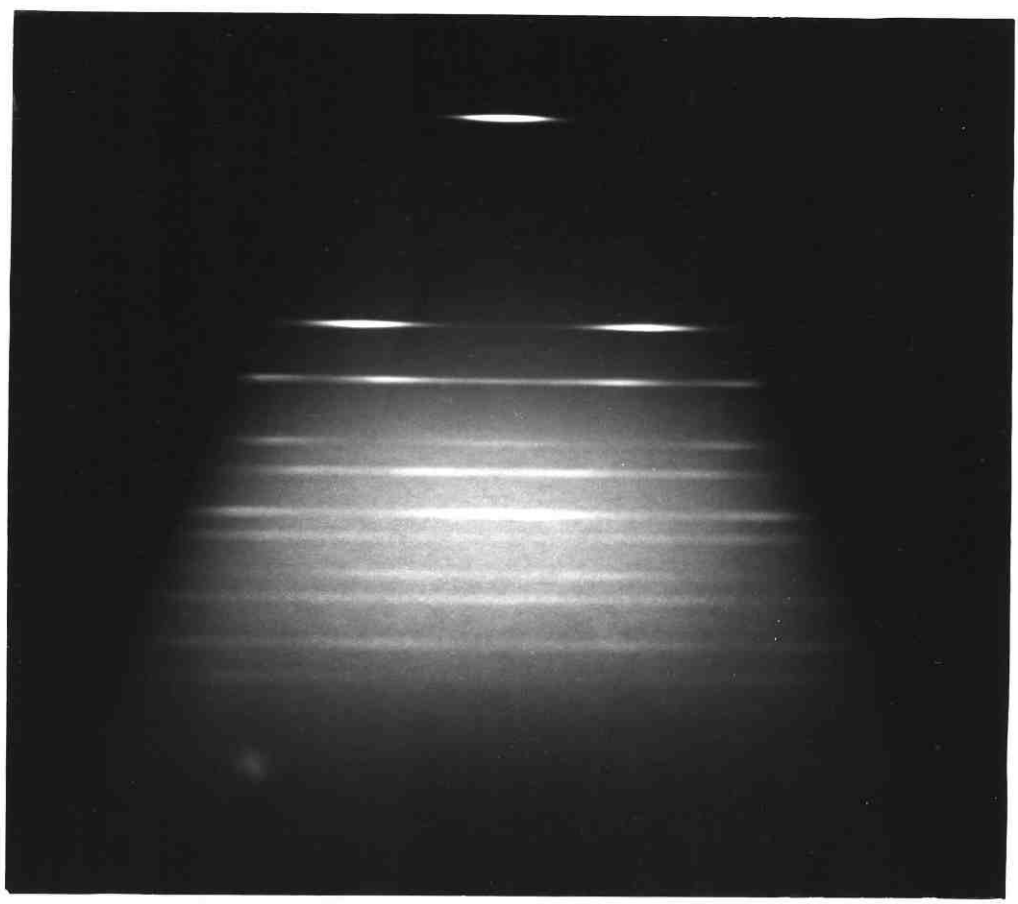

Fig. 3.10: Texture Camera X-ray Diffraction Pattern of a $CuInSe_2$ Film after Anneal at 350°C

The X-ray diffraction of the films has thus shown that although films deposited onto cold substrates are multi-phased, they could be made homogeneous and converted into chalcopyrite $CuInSe_2$ by a heat treatment at 350°C for 3 hours. This is a very important result because it established the experimental conditions required for preparing single phased $CuInSe_2$ thin films, starting from the evaporation of the powder of the compound.

At this stage it should be mentioned that the X-ray investigations were repeated for layers prepared from the different starting batches A, B and D, as these had been found to have various compositions and varying amounts of second phase material. In all cases, the results were identical so that the type and actual composition of the starting powder did not affect the structural properties of the films.

The structural stability of the $CuInSe_2$ films with respect to prolonged anneal at 350°C and also with respect to higher temperature anneals were also investigated. No difference in the X-ray patterns of films annealed at 350°C for 3 hours and 30 hours was noticed. There were no extra lines present and the intensity of all the reflections were, as far as the naked eye could distinguish, very similar. This indicated that the films were structurally stable after long heat treatments in inert gas atmosphere at 350°C.

3.3.2.4 Films Annealed at 450°C

To investigate the effect of a high temperature anneal, some samples already annealed at 350°C were further annealed at 450°C. The X-ray pattern after such an anneal indicated that in addition to the chalcopyrite reflections, new diffraction lines were present. The d-spacings of these lines were measured to be 2.93Å, 1.79Å and 1.53Å respectively. These were identified as the strong 222, 440 and 622 reflections of In_2O_3[14]. Another strong reflection 400, coincided with

the 211 reflection of $CuInSe_2$ so that the intensity of this weak chalcopyrite line appeared somewhat stronger. This result was somewhat unexpected in view of the fact that the anneals were performed in flowing nitrogen.

The detection limit of diffraction lines using the glancing angle reflection X-ray technique is not known precisely but it has been reported that very faint but interpretable lines may be recorded from films as thin as 200Å[16]. The fact that the reflections of the Indium Oxide were quite intense implied that this was present in appreciable amounts perhaps in the region of 1000Å or so. Such an oxide thickness is the result of thermal oxidation and since oxygen was not admitted on purpose into the furnace, it is thought that the oxidation reaction occurred with water vapour desorbing from the walls of the anneal tube, during the 450°C heat treatment. Since In_2O_3 reflections were not observed in the X-ray patterns of films annealed at 350°C, it would seem that oxygen is not present in appreciable quantities in the anneal tube at this lower temperature so that any oxide layer that may have formed is below the limit of detection by X-rays.

3.3.3 Structure of Films Deposited on Hot Substrates

The effect of substrate temperature on the phase structure of $CuInSe_2$ films was investigated by depositing films at temperatures in the range 150°-300°C.

The structure of the films evaporated onto 150°C substrates, consisted of $CuInSe_2$ and Cu_3Se_2. This was the same as in the film deposited on cold substrates and subsequently heat treated at 150°C. This indicated that at this substrate temperature the solid state reaction to form $CuInSe_2$ was not complete.

On the other hand, at higher substrate temperatures of 250°C, the X-ray diffraction pattern consisted of the powder lines of $CuInSe_2$ only. This showed that the condensing molecules had reacted to completion to

form the ternary compound.

When a slightly higher substrate temperature of 300°C was employed, the X-ray analysis indicated that there was, in addition to $CuInSe_2$, another phase. This was identified by many of its high intensity reflections, as Cu_7In_4[15], one of intermetallic phases in the Cu-In system.

From the above results it is apparent that, with the fast evaporation technique, single phased $CuInSe_2$ can also be deposited at substrate temperatures around 250°C.

3.3.4 Preferred Orientation of Films

The X-ray diffraction photographs of $CuInSe_2$ layers displayed intensity modulations which were quite pronounced at the 112; 204, 220; 116; 312; 008,400; 316,332 and 228,424 reflections of the chalcopyrite. This was a manifestation of some sort of texture in the films and in order to determine the preferred orientation of the crystallites, the orientation angle, α, at the intensity maxima of each of the above $hk\ell$ reflections was determined with the aid of the chart in Figure 3.6.

It must be recalled that the measured angle, α, is the preferred angle between the normal to the family of planes $\{hk\ell\}$ and the normal to the substrate surface. If, however, as in uniaxial or fibre textures, a particular set of planes $\{HKL\}$ is parallel to the substrate plane, then the experimentally determined α becomes effectively the angle between the planes $\{hk\ell\}$ and $\{HKL\}$. Therefore the planes $\{HKL\}$ which are preferentially aligned with surface may be determined by comparing the measured angles, α, with the calculated interplanar angles ϕ.

For the tetragonal system, the angles ϕ between the $\{HKL\}$ and $\{hk\ell\}$ are given by[17]:

$$\phi = \cos^{-1}\left(\frac{hH + kK + \frac{\ell L}{(c/a)^2}}{[(h^2 + k^2 + \frac{\ell^2}{(c/a)^2})(H^2 + K^2 + \frac{L^2}{(c/a)^2})]^{\frac{1}{2}}}\right)$$

hkℓ reflection	Measured angle (α)	Calculated angle (φ) between planes	HKL and hkℓ
112	<8°	0; 70.66	112 112
211	30°	28.08; 50.78; 67.82	211
(204)	35°	35.33; 90	204
(220)		35.13; 90	220
(116)	30; 57.5	29.52; 58.66	116
(312)		29.48; 58.45	312
(008)	55°	54.87	008
(400)		54.67	400
(316)	22.5; 47.5	22.04; 48.62; 82.36	316
(332)		21.93 82.45	332
(228)	20; 62.5	19.47; 62.02	228
(424)		19.46; 61.80; 90	424

Table 3.2: Comparison of measured orientation angles and theoretical interplanar angles, indicating the (112) preferred orientation of annealed $CuInSe_2$ films.

and for $CuInSe_2$: $c = 11.862\text{Å}$

and $a = 5.782\text{Å}$

were used in the computation.

From the examination of the cylindrical texture camera photographs, Figure 3.10, the preferred orientation may be guessed at first glance as the plane (hkℓ) at which $\alpha = 0$. In other words, the reflection hkℓ in which a maximum intensity occurs, at the centre of the diffraction line at $x = 0$ with very small values of α, gives the index of the plane preferentially aligned parallel to the substrate[13].

In the $CuInSe_2$ films, the 112 reflection had an intensity maximum at the centre of the diffraction line with $\alpha \to 0$, and could thus be assigned tentatively as the plane (HKL) being preferentially oriented. In order to confirm this the experimental angles, α, shown in Table 3.2 were compared with the interplanar angles, ϕ, between (hkℓ) and (HKL) ≡ 112.

It is evident that the calculations match the experimental observations very well for all the Bragg reflections, confirming that the $CuInSe_2$ films have a uniaxial structure with the (112) planes growing parallel to the substrate plane. The fact that some calculated values of ϕ are not observed in the texture photographs is because the cylindrical camera does not register reflections from all possible values of orientation angle, [13].

3.3.5 Conclusions

In conclusion, the X-ray diffraction investigations of the films have shown that thin films deposited onto substrates held at temperatures lower than 150°C and higher than 300°C were multiphased. Single phased chalcopyrite $CuInSe_2$ films could be obtained by depositing onto substrates at 250°C or by depositing onto cold substrates followed by an anneal at 350°C. These homogeneous films had a (112) type preferred orientation.

3.4 TRANSMISSION ELECTRON MICROSCOPY OF FILMS

3.4.1 Experimental Procedure

The microstructure of the $CuInSe_2$ films was examined using an A.E.I. EM7 Transmission Electron Microscope (TEM). The samples for film structure study were taken from the same substrates where all the other characterisation of the films had been done.

The microscopy specimens were removed from the glass substrates by, first,dipping the slides in a 50:50 (vol %) hydrofluoric acid - distilled water solution - and then floating off the films in a dish containing distilled water. The small pieces of stripped films were subsequently caught on to 3 mm diameter microscope copper grids which had been previously etched in a 10 vol % hydrochloric acid-distilled water solution.

An accelerating voltage of 1000 kV resulted in the transmission of the electron beam through samples around 3000Å thick with sufficient image contrast in bright field viewing. The samples yielded good quality electron diffraction patterns and there was no evidence of beam damage arising from heating effects due to high operating voltages and the use of relatively thick samples.

A series of electron micrographs and selected area diffraction photographs were obtained for films in the as-deposited states and after the heat treatments. The crystallite size distributions in these samples were determined by a method of linear analysis[18,19] and for this purpose bright field micrographs at M = x 6300 magnification were taken so as to include as many grains as possible in the field of view. These micrographs were then photographically enlarged by a further four times and projected on A4 size plain paper having a series of straight parallel lines drawn across it. The mean size of each grain intersected by the lines was subsequently measured and to obtain a statistically representative size distribution more than 200 grains were counted. The size of the

crystallites was taken as the mean value of the maximum and minimum dimensions of each grain intercepted by the lines and the accuracy of these measurements was to within ±80Å.

In order to index the electron diffraction patterns, the electron microscope camera constant K, must first be determined. This constant relates the radius, R, of a diffraction spot or ring as measured from the central spot, through the formula:

$$K = d_{hk\ell} R$$

where $d_{hk\ell}$ is the d-spacing of the plane giving rise to diffraction. In principle the camera constant, K, can be determined from

$$K = L\lambda$$

where L is the camera length setting and λ is the wavelength of electrons at a particular accelerating voltage. The above parameters are only known very approximately for given operating conditions and strictly, K, should be determined by measurement of the diffraction pattern of a substance whose d-spacing values are well known. In this study, a specimen established as consisting of $CuInSe_2$ by X-ray diffraction analysis, was used as an internal standard to calculate the value of K.

3.4.2 Results

3.4.2.1 Unnannealed Films

A typical bright field micrograph of a Copper Indium Selenide film of ~3000Å thickness, in the as-deposited state, is shown in Fig. 3.11(a). The main feature here is the long dark lines which are bend contours occurring due to local buckling of the specimen and these indicate regions which are strongly diffracting. The fact that some of these contours spread over a considerable length implies the presence of large crystalline regions and a long grain boundary, can be seen (shown with an arrow) in the centre of the micrograph.

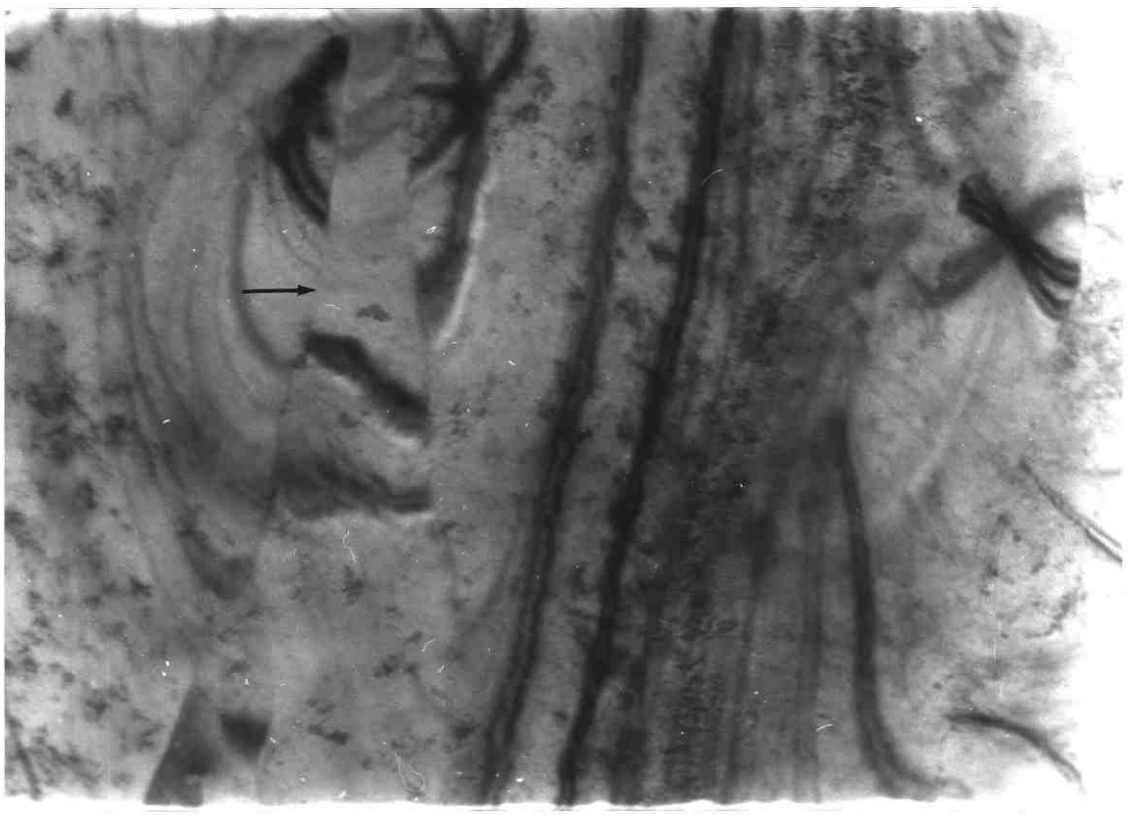

Fig. 3.11(a): Transmission Electron Micrograph of a $CuInSe_2$ Film before Anneal (Mag. = x 75,000)

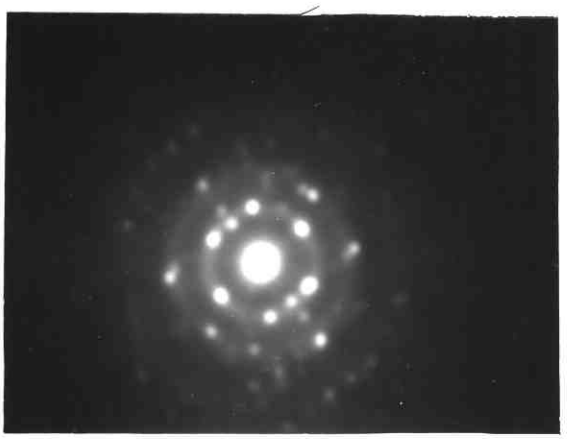

Fig. 3.11(b): Electron Diffraction Pattern of a $CuInSe_2$ Film before Anneal

A selected area electron diffraction pattern for the as-deposited film taken with a selector aperture of 35 μm which corresponds to a circular area of 1 μm diameter on the specimen surface is shown in Fig. 3.11(b). This consists of strong diffraction spots and broad rings. The spots are indicative of relatively large crystalline regions, confirming the bright field micrograph observations. The d-spacings of these spots were determined to be due to the Cu_3Se_2 in the mixed phase as-deposited films. The diffraction rings were too diffuse to make an accurate measurement but the presence of In_2Se[22] could not be ruled out. This compound was not detected by the X-ray diffraction investigations; this and the fact that the electron diffraction rings are diffuse imply that it must be in the amorphous state in the unannealed films.

Overall, the electron microscopy studies of the unannealed films confirmed that these consist of a multilayered structure with amorphous In_2Se and large crystalline Cu_3Se_2 phases being the major constituents.

3.4.2.2 Films Annealed at 150°C

A micrograph of the same $CuInSe_2$ sample after heat treatment at 150°C for 3 hours is shown in Fig. 3.12(a). It is evident that annealing has resulted in films which are highly polycrystalline and consist of fine grains dispersed among larger ones. The grain boundaries are not well defined in these films but it is estimated that the mean size is around ~500Å for a 3000Å thick film.

The electron diffraction pattern shown in Fig. 3.12(b) was taken wth a 100 μm aperture and corresponds to a circular area of ~3.5 μm diameter on the specimen. The pattern consists of a ring structure which is typical of polycrystalline samples and the fact that the diffraction rings contain intense spots superimposed on them, is due to existence of larger grains within the observed area. The measurement of the d-spacings confirmed

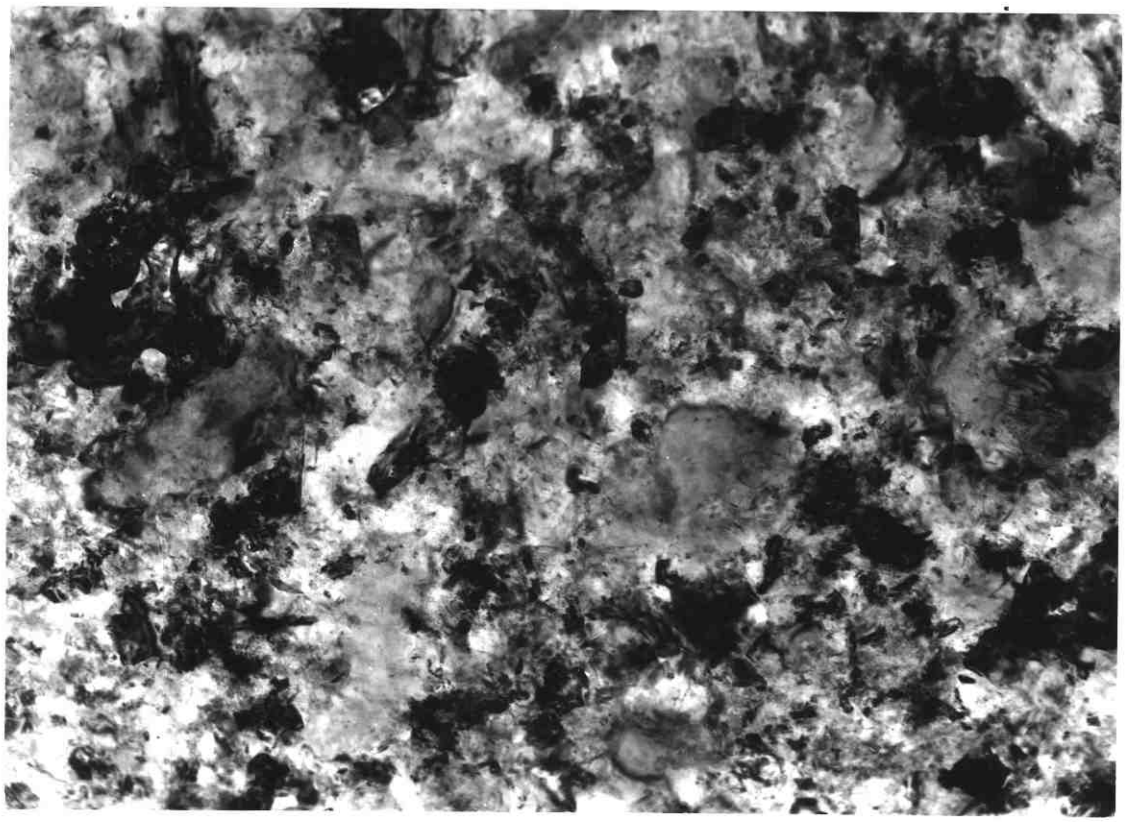

Fig. 3.12(a): Transmission Electron Micrograph of a $CuInSe_2$ Film after Anneal at 150°C (Mag = x 30,000)

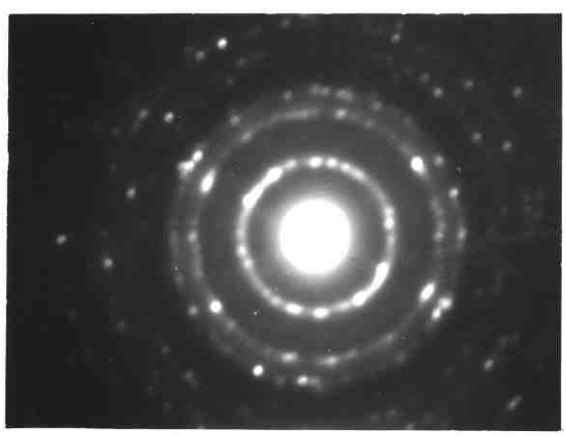

Fig. 3.12(b): Electron Diffraction Pattern of a $CuInSe_2$ Film after Anneal at 150°C

the presence of $CuInSe_2$ and the index of hkℓ reflections, in order of increasing distance from the central spot, are 112; 204; 220; 116,312; 332,316 and 424,228 reflections of the chalcopyrite.

The electron microscopy measurements confirmed the X-ray findings that inhomogeneous as-deposited layers are converted into homogeneous $CuInSe_2$ phase.

3.4.2.3 Films Annealed at 350°C

In Fig. 3.12(a) is shown the microstructure of the samples after heat treatment at 350°C for 3 hours. The comparison with Fig. 3.9(a) indicates that the anneal has resulted in the considerable growth of grains. This is also reflected in the electron diffraction pattern of Fig. 3.13(b) where now the diffraction rings have broken up into spots. It must be stressed that the selector aperture in these patterns was also 100 μm and so the 'spotty' pattern is indeed due to larger grains contributing to diffraction.

The size distribution of the grains has been determined and the result is shown as a histogram in Fig. 3.14. The mean grain sizes vary from 500 to 5000Å and the mean crystallite size, as obtained from the arithmetic mean of the distribution, was about 2500Å for a ~3000Å thick film.

The transmission electron micrograph and the corresponding electron diffraction pattern after a total of 30 hours at 350°C is shown in Fig. 3.15(a) and Fig. 3.15(b) respectively from which it is evident that the microstructure of the $CuInSe_2$ films has not changed drastically from the 3 hour anneal. The selected area diffraction pattern, taken with a 100 μm selector aperture, had somewhat fewer spots and indicated a very slight increase in grain size to have occurred. This was confirmed by the measurement of the grain sizes, which had a distribution very similar to that of Fig. 3.14 but with a slightly high arithmetic mean of ~2600Å.

Fig. 3.13(a): Transmission Electron Micrograph of a $CuInSe_2$ Film after Anneal at 350°C for 3 hours (Mag = x 30,000)

Fig. 3.13(b): Electron Diffraction Pattern of a $CuInSe_2$ Film after Anneal at 350°C for 3 hours

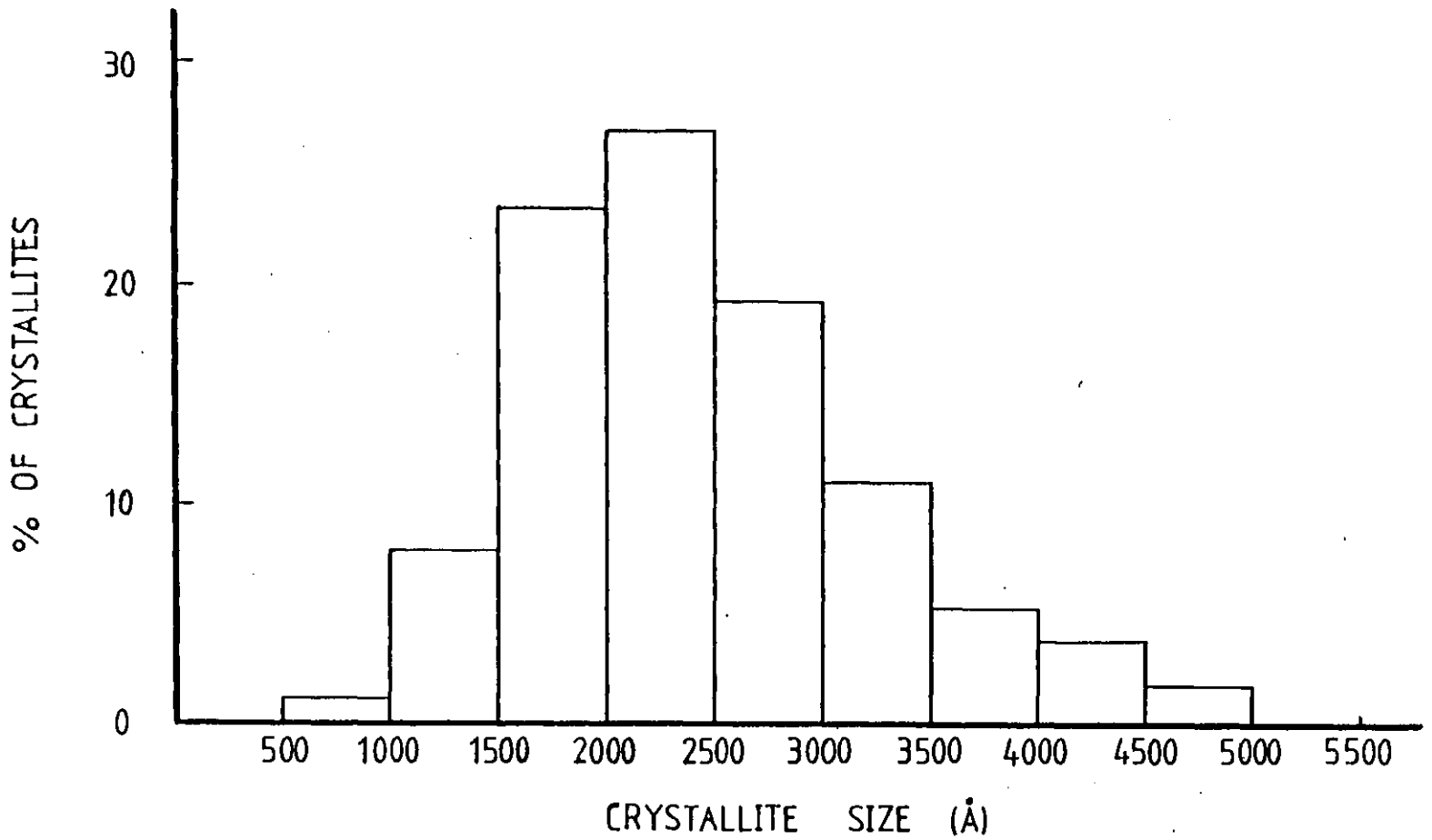

Fig. 3.14: Histogram showing the Crystallite Size Distribution of a 3000 Å Thick $CuInSe_2$ Film after Anneal at 350°C for 3 hours

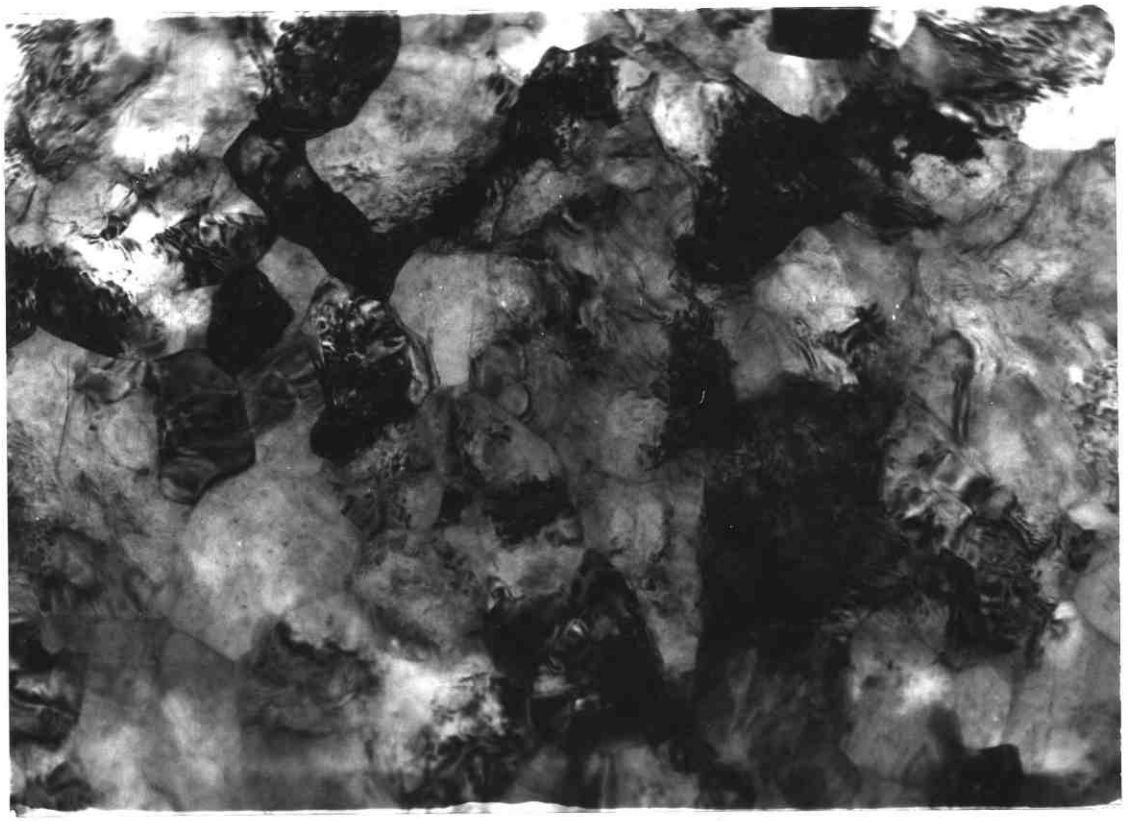

Fig. 3.15(a): Transmission Electron Micrograph of a $CuInSe_2$ Film after Anneal at 350°C for 30 hours (Mag = x 30,000)

Fig. 3.15(b): Electron Diffraction Pattern of a $CuInSe_2$ Film after Anneal at 350°C for 30 hours

3.4.3 Conclusions

The TEM investigations have confirmed the X-ray analysis results that films deposited onto cold substrates are multiphased and that conversion to $CuInSe_2$ occurs at anneal temperatures of 150°C. Considerable grain growth of crystallites occurred after an anneal at 350°C for 3 hours. The mean crystallite size was determined to be approximately equal to the film thickness with no significant grain size increases ocurring after prolonged anneals.

3.5 ELECTRON PROBE MICROANALYSIS OF FILMS

The chemical composition of the films was determined by Electron Probe Microanalysis using the same procedure described in Section 2.3. The analysis was performed on films deposited onto substrates held at various temperatures and after anneals. The effect of the nature and composition of the starting powder on the stoichiometry of the films was also considered.

3.5.1 Composition of Films Deposited on Cold Substrates

3.5.1.1 As-deposited Films

The compositions of some unannealed films are given in Table 3.3 where they have been grouped according to the powder batch from which they were deposited.

Powder Batch	Sample	EPMA Composition		
		At%Cu	At%Se	At%In
A	MC56	21.9	4 9	29.1
	MC47	22.1	50.6	27.3
B	MC54	22.4	49.4	28.2
	MC53	21.0	50.6	28.4
D	MC59	21.4	50.7	27.9
	MC50	21.6	51.3	27.1

Table 3.3: Composition of as-deposited $CuInSe_2$ films

It is evident that all the films are compositionally very similar and are all characterised by a slight deficiency in copper a feature which was also observed for the bulk $CuInSe_2$ samples.

The fact that films evaporated from any particular powder type have essentially similar compositions is indicative of the good reproducibility of the deposition technique between preparation runs.

3.5.1.2 Annealed Films

The effect of the heat treatments on the composition of the films is shown in Table 3.4 for a typical sample. The table includes composition results of specimens taken from different parts of the same thin film sample. This was done to check the compositional uniformity of the films and it was determined that over the substrate area the composition did not deviate more than ±3% of the mean value. Such good reproducibility was also observed in bulk $CuInSe_2$ specimens.

Comparing the mean composition of the as-deposited films with that after an anneal at 150°C, it is apparent that a definite compositional change has occurred. Upon anneal at this low temperature the results indicated that there was an apparent decrease in copper concentration. This effect was observed in all the samples investigated and implied that as-deposited films subjected to heat treatment lost copper.

This is somewhat difficult to accept because copper is the least volatile component in the films. If loss of elements should occur during the anneal it would be more likely to be in the form of Se_2 or In_2Se molecules, as these are the major evaporating species in the Cu-In-Se, Cu-Se and In-Se systems at low temperatures[20,21].

The explanation for the observed apparent anomaly lies in the fact that the unannealed films were determined by X-ray and TEM analyses to be multiphased. Also the thermal evaporation had indicated that the films were deposited as layers of In-Se mixture followed by a Se-Cu

State of film	EPMA Composition			Mean Composition		
	At%Cu	At%Se	At%In	At%Cu	At%Se	At%In
As-deposited	22.2	48.4	29.4	21.9	49	29.1
	21.5	49.6	28.9			
After anneal at 150°C for 3 hours	20.9	49.5	29.6	20.8	49.5	29.7
	20.7	49.5	29.8			
After anneal at 350°C for 3 hours	20.5	49.5	30.0	20.7	49.4	29.9
	21.4	5.0	28.6			
	20.1	49.3	30.6			
	20.9	48.6	30.5			

Table 3.4: Composition of a $CuInSe_2$ film after various heat treatments

mixture. These observations mean that before an anneal there will be concentration gradients of elements through the thickness of the layers. A relatively high copper concentration will be distributed near the film-air interface whilst a high concentration of indium will be expected to be near the film-substrate interface.

In EPMA the X-ray photons generated at any particular depth within the specimen will be absorbed by overlying layers before reaching the detector. In the as-deposited films since Cu is distributed near the surface the characteristic Cu X-rays will be absorbed relatively less than if the copper was distributed uniformly throughout the thickness. Similarly the degree of absorption of the characteristic In X-ray line will be relatively greater in the unannealed films. The net effect as far as EPMA composition of the as-deposited layers is concerned would thus be an artificial enhancement of the copper concentration and an artificial decrease of the indium concentration.

The fact that after annealing at 150°C the Cu concentration in the films decreased while that of In increased indicates that any concentration gradients in the films have been removed. This means that the distribution of the elements, after the anneal, becomes spatially homogeneous and this is in good conformity with the structural analysis of the films which demonstrated that $CuInSe_2$ became the major phase.

The effect of heat treatment at 350°C for 3 hours is also shown in Table 3.4. The comparison of the composition of these films with that after the anneal at 150°C will reveal that no compositional changes hve occurred. This indicated that the $CuInSe_2$ films were stable after the heat treatment at 350°C and confirmed the structural observations that the films were homogeneous.

3.5.1.3 Films prepared from different starting powders

The mean composition of films after 150°C and 350°C thermal treatments may be correlated with the composition of the starting powders from which they were prepared. In Figs. 3.16, 3.17 and 3.18 are shown the composition plots of films evaporated from lumps A, B and D respectively chosen from the bulk ingot. In each of these diagrams the composition of the bulk powder is also plotted and the dashed boundary identifies the single phase $CuInSe_2$ region as defined approximately from the bulk composition results of Section 2.3.

Examination of each of the above ternary composition diagrams will reveal that the film compositions always lie away from their powder composition. Furthermore, for any particular starting powder the composition of films are very similar, indicating good reproducibility of the composition between runs. The other striking feature of these ternary plots is that the composition of bulk $CuInSe_2$ is not related to the composition of the films and that all the film compositions lie more or less in the same region of the phase diagram, irrespective of the starting powder used.

Table 3.5 gives a list of compositions of various samples of $CuInSe_2$ films and these have all been plotted on the same ternary diagram shown in Fig. 3.19. It is apparent that all film compositions lie along the $CuInSe_2$-InSe join of the phase plot. It was calculated that the film compositions correspond to $CuInSe_2$ having approximately 8.5 mole% excess InSe. In terms of a mixture, this is equivalent to about 73 mole% $CuInSe_2$ with 27 mole% InSe. If, as mentioned previously, 200Å is taken as the minimum thickness of a film detectable by glancing angle X-ray technique, it may be estimated that for a film ~7500Å thick the detection limit of a phase in a mixture of phases will be 3-6% by the X-ray technique. Since the chemical composition indicates that InSe is present in much greater quantities than this, it would have been

Fig. 3.16: EPMA Composition of $CuInSe_2$ Films Deposited from Powder A

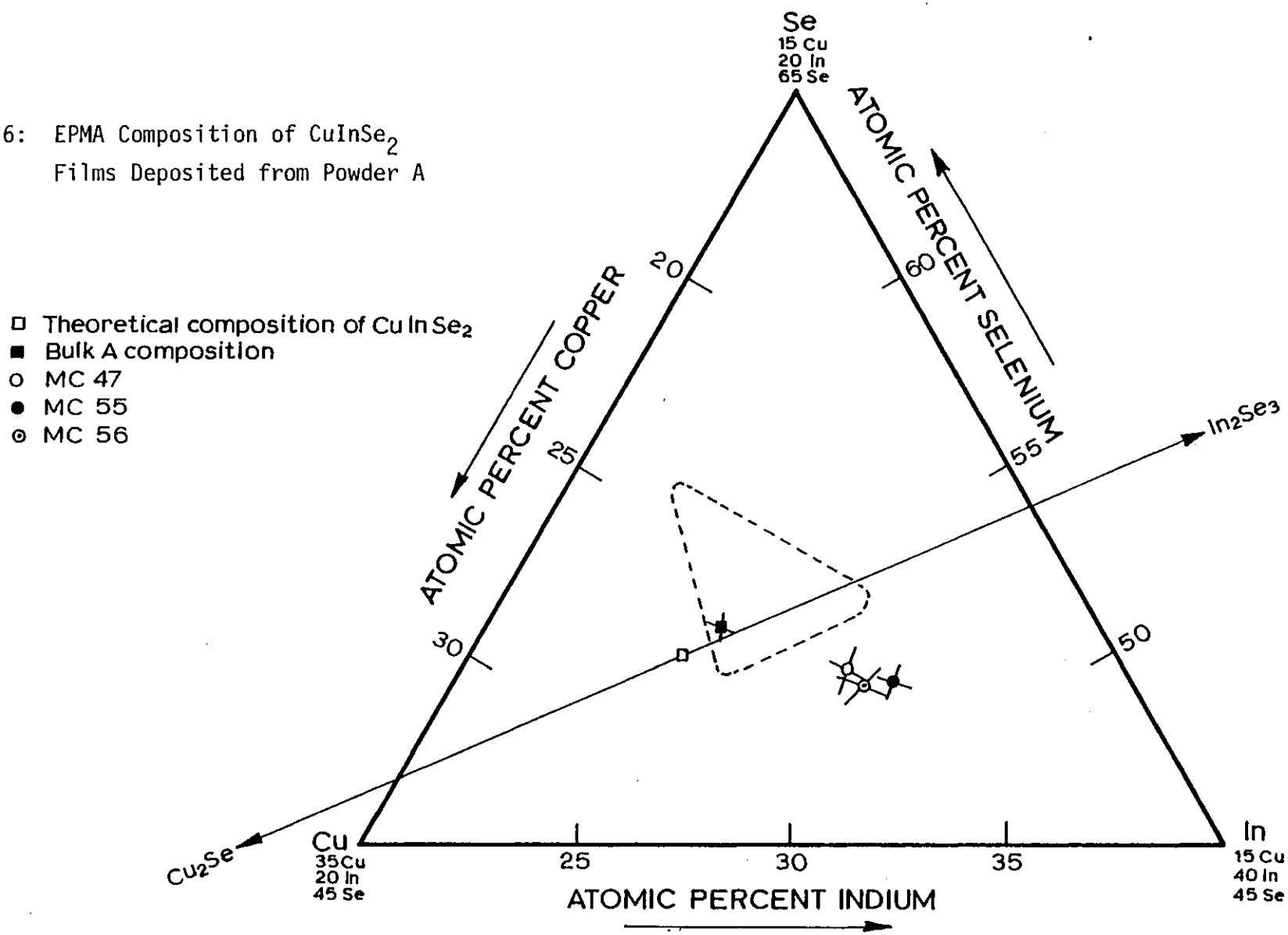

Fig. 3.17: EPMA Composition of $CuInSe_2$ Films Deposited from Powder B

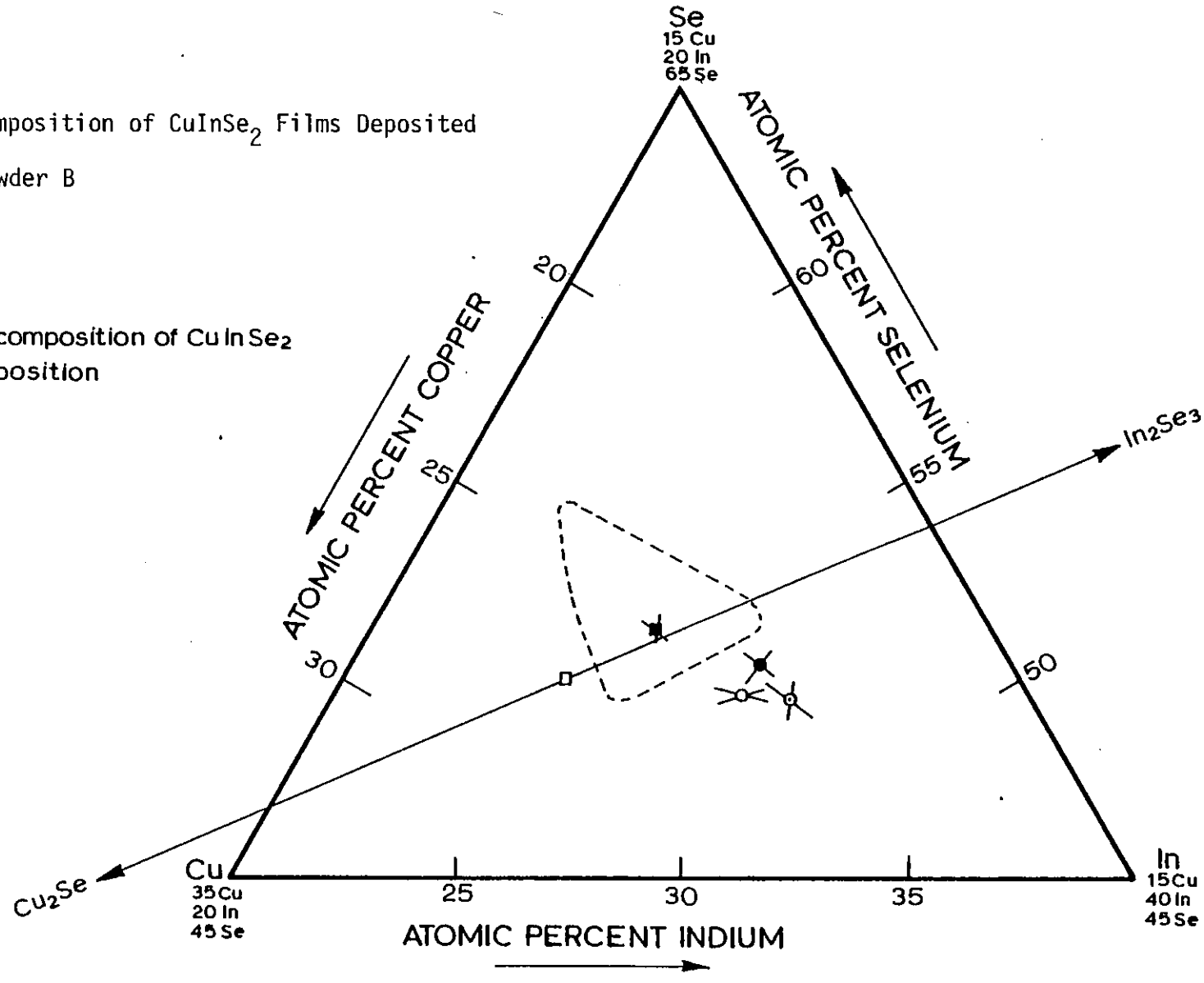

Fig. 3.18: EPMA Composition of $CuInSe_2$ Films Deposited from Powder D

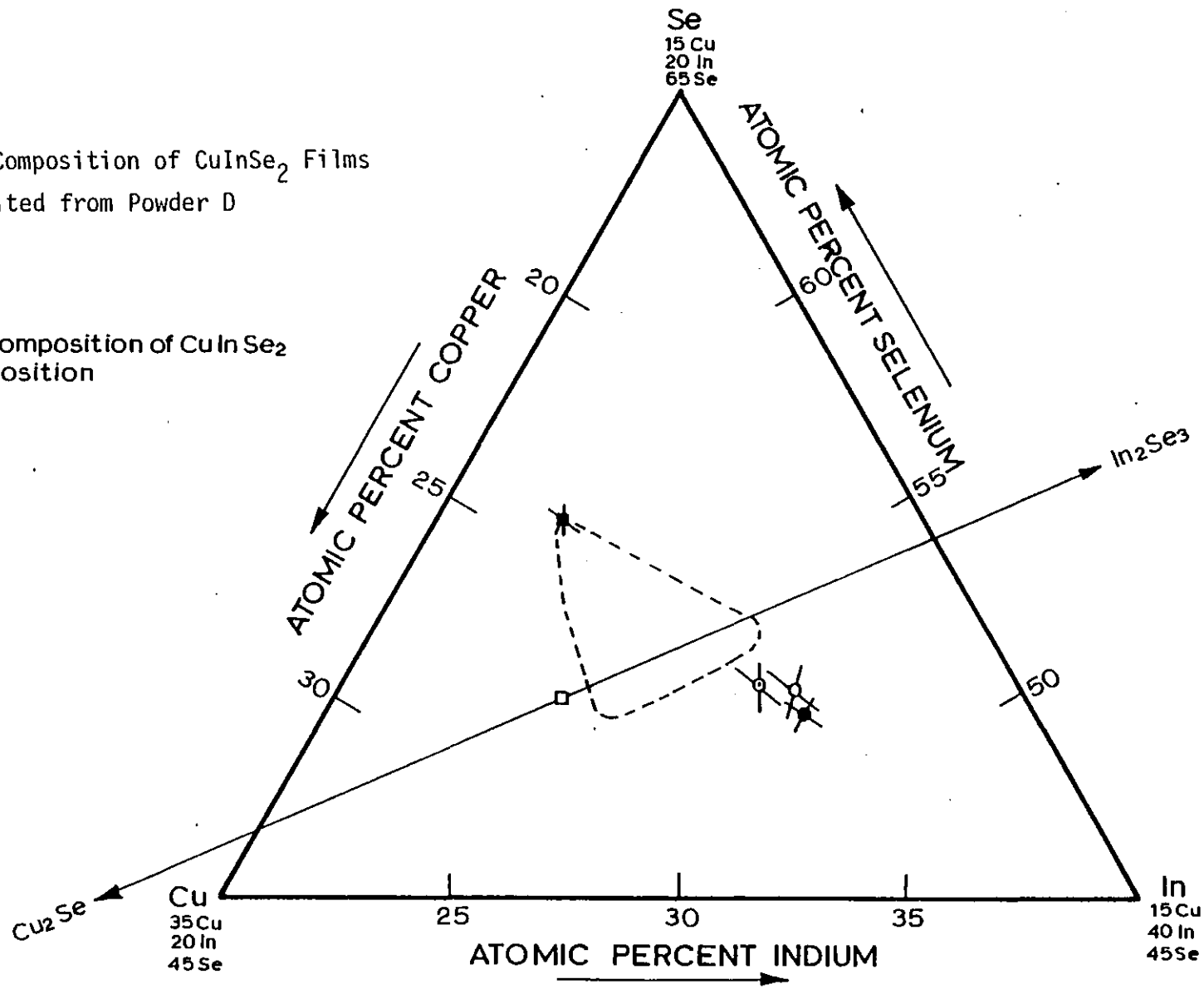

Powder Batch	Sample	EPMA Composition		
		At%Cu	At%Se	At%In
D	MC46	20	49.7	30.3
A	MC47	21.4	49.4	29.2
D	MC50	20.5	50.3	29.2
B	MC53	20.3	49.5	30.2
B	MC54	21	49.6	29.4
A	MC55	20.4	49.4	30.2
A	MC56	20.8	49.3	29.9
D	MC59	20.2	50.5	29.3
B	MC62	20.7	50.3	29.0
B	MC63	20.9	49.4	29.8
B	MC65	20.6	50.6	28.8
B	MC67	20.8	49.6	29.6

Table 3.5: EPMA composition of $CuInSe_2$ thin films after heat treatment at 350°C

Fig. 3.19: EPMA Composition of Thin Films and Bulk $CuInSe_2$

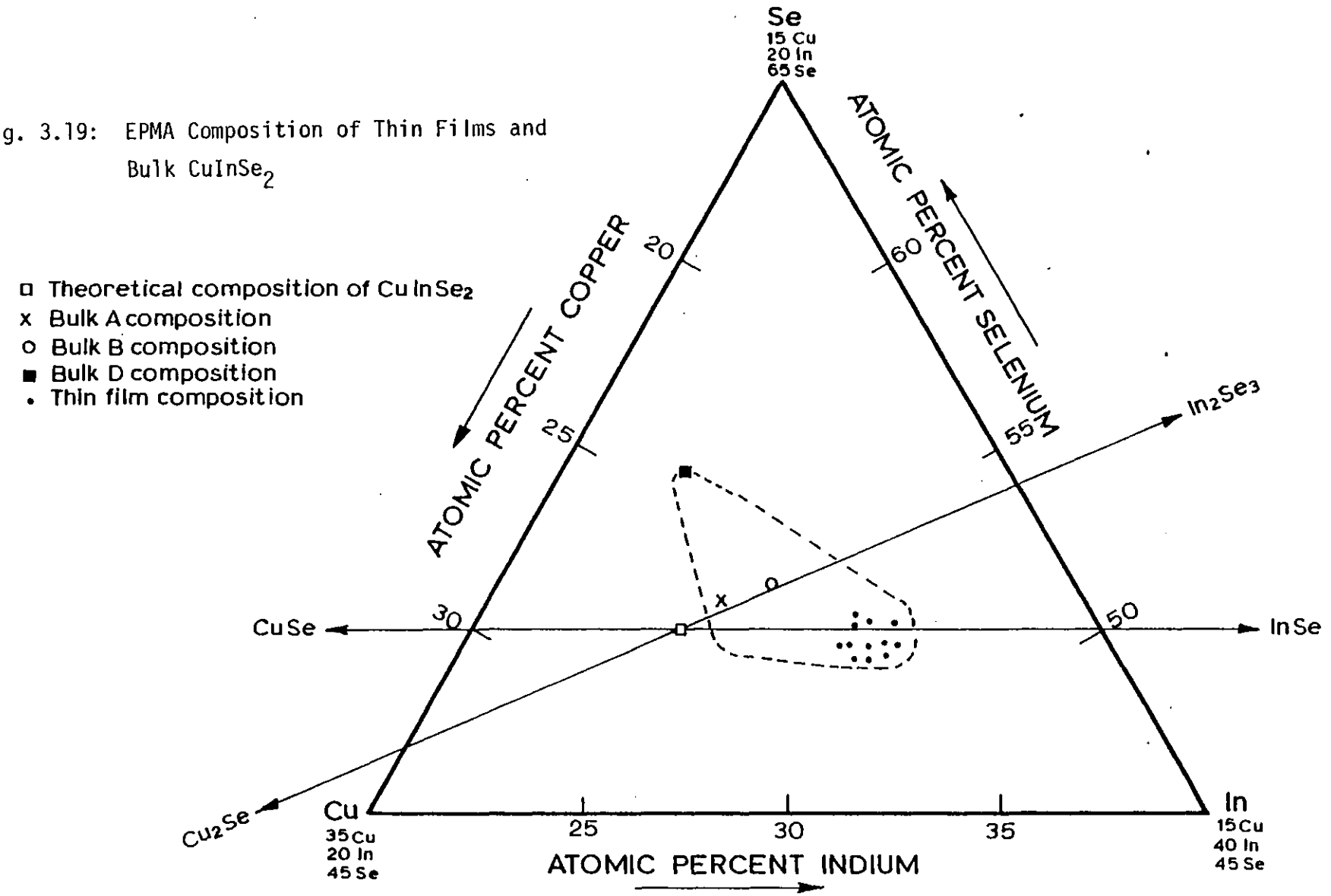

detected if it was in the form of a second phase material. It must be recalled that the structural examination had not revealed the presence of any foreign material other than $CuInSe_2$ in films annealed at 350°C. It must thus be concluded that the excess InSe detected by EPMA is dissolved in $CuInSe_2$.

Extensive solubility of GaSe in $CuGaSe_2$ and GaS in $CuGaS_2$ had been reported[23,24] and this in conjunction with our results on $CuInSe_2$ films, would indicate that excess homogeneity for A_IB_{VI} compounds is a general feature of I-III-VI_2 chalcopyrite semiconductors. The thin film composition data can thus be combined with the bulk composition data of Section 2.3 to define the single phase boundary at the InSe rich side of the phase diagram. This is shown by the dashed lines in Fig. 3.19 where for completeness the bulk composition data have also been reproduced.

3.5.1.4 Composition of Films Annealed at 450°C

The compositional stability of $CuInSe_2$ layers after a prolonged anneal at 350°C and after a higher temperature anneal at 450°C is shown in Table 3.6 and Table 3.7 respectively.

Sample	Composition after 350°C for 3 hours			Composition after 350°C for 30 hours		
	At%Cu	At%Se	At%In	At%Cu	At%Se	At%In
MC54	21	49.6	29.4	20.8	49.5	29.7
MC56	20.8	49.3	29.9	21.1	49.3	29.6

Table 3.6: Composition of $CuInSe_2$ films after prolonged anneal at 350°C

The EPMA indicated that the stoichiometry of the films did not change for anneal periods of up to 30 hours at 350°C, confirming the X-ray and electron microscopy investigations that films are stable.

Sample	Composition after 350°C for 3 hours			Composition after 450°C for 3 hours		
	At%Cu	At%Se	At%In	At%Cu	At%Se	At%In
MC53	20.3	49.5	30.2	22.6	45.6	31.8
MC56	20.8	49.3	29.9	23.2	44.4	32.4

Table 3.7: Composition of $CuInSe_2$ films after anneal at 450°C

As can be seen in Table 3.7, a definite change in composition occurred after annealing at 450°C. The relative selenium concentration decreased while both the copper and indium mole fractions increased. This meant that a net loss of selenium had occurred after the anneal at 450°C.

Since the films before the 450°C heat treatment had excess InSe dissolved, it is tempting to ascribe the loss of Se to the evaporation of InSe. A mass spectrometric investigation of the vapour in equilibrium with this compound had revealed that InSe evaporates congruently in the form of In_2Se and Se_2 molecules[21]. Therefore, should dissociation of InSe be the reason for the loss of Se from the films, then loss of an equal amount of indium from the layers should have occurred in the process. However this was certainly not the case and rules out the above possibility.

As the X-ray analysis had established that In_2O_3 had formed in the films after the anneal at 450°C it is thought that the loss of selenium from the films during the anneals is connected with the oxidation process. In order to confirm this point some $CuInSe_2$ samples were subjected to an anneal in oxygen gas at the lower temperature of 350°C. The reasoning behind this was that, since films annealed at 350°C in inert gas environment have a constant composition and are single phased, then any change at the same temperature of anneal but in an oxidising atmosphere would clearly establish the influence of oxygen on the film properties. Indeed, after O_2 anneals at 350°C In_2O_3 was detected and a definite loss of selenium had also occurred. This confirmed that the observations after anneal at 450°C were due to the reaction of oxygen with $CuInSe_2$ leading to a loss of selenium and the formation of In_2O_3.

3.5.2 Composition of Films Deposited on Hot Substrates

The compositions of some films deposited directly onto hot substrates were determined in order to check whether any re-evaporation occurred and whether stoichiometric thin films of $CuInSe_2$ can be prepared on hot substrates. The results for three substrate temperatures of 150°C, 250°C and 300°C are given in Table 3.8.

Sample	Substrate Temperature	EPMA Composition At%Cu	At%Se	At%In
MC73	150°C	20.6	50.1	29.3
MC74	250°C	20.1	49.7	30.2
MC75	300°C	24.3	44.7	31.0

Table 3.8: Composition of $CuInSe_2$ films deposited onto hot substrates

It is apparent that, for substrate temperatures up to about 250°C, the chemical compositions are very similar to films deposited onto cold substrates and subsequently annealed. On the other hand the composition of films deposited at 300°C shows that there is an excess of copper and indium due to some re-evaporation of selenium. These films are grossly non-stoichiometric, which is in good conformity with the X-ray analysis which detected the presence of Cu_7In_4 as a second phase in addition to $CuInSe_2$.

3.5.3 Conclusions

In conclusion, the Electron Probe Microanalysis of the films has shown that films deposited up to substrate temperatures of 250°C and films annealed at 350°C for up to 30 hours had essentially similar and reproducible compositions.

Films annealed at 450°C incurred a loss of selenium due to thermal oxidation of $CuInSe_2$ whilst deposition at substrate temperatures greater than 300°C resulted in the re-evaporation of Se leading to excess Cu_7In_4 precipitating as a second phase.

3.6 THERMAL OXIDATION OF $CuInSe_2$ FILMS

The results of X-ray and Electron Probe Microanalyses of $CuInSe_2$ films heat treated in an oxidising environment can be combined to give a scheme of thermal oxidation of copper indium selenide.

Oxygen, either in elemental gas form or in water molecules, reacts with $CuInSe_2$ and leads to the formation of In_2O_3 at the surface. This is the preferred oxide, presumably because of its higher heat of formation[21,25] of -221 kcal/mole as compared with -53.8 kcal/mole for SeO_2, -44.1 kcal/mole for SeO_3, -40.7 kcal/mole for Cu_2O and -35.62 kcal/mole for CuO. Following the formation of In_2O_3, the remaining selenium and copper atoms at the surface are left to rearrange themselves.

As the $CuInSe_2$ layers are already copper deficient, it is likely that these copper atoms will diffuse to fill some of the Cu vacancies. This would be in accord with the fact that no copper oxide was detected in the layers. These events would then result in some selenium to remain free at the surface region.

It would seem that there are three options open for these selenium atoms. Firstly, they may diffuse into the bulk and remain as excess selenium; secondly, they may evaporate off the film and join the gas phase and, thirdly, they may react with oxygen to form SeO_2 or SeO_3. However at temperatures greater than about 300°C, these selenium oxides are volatile and will exist in gaseous state[21,26].

The observed loss of selenium from the films after the anneals in an oxygen environment, supports the latter two processes in which selenium either in pure elemental form or in oxide molecular form is transported away in the gas phase.

In conclusion the thermal oxid ation of $CuInSe_2$, at temperatures greater than 350°C, results in the formation of In_2O_3 while at the same time causing the evaporation of some selenium.

Our observations can be directly compared with the only study of oxidation of $CuInSe_2$ that has appeared in the literature towards the end of this project. Kazmerski et al[26] have estimated that over the temperature range 150-300°C, the composition of a thermally grown oxide on single crystal $CuInSe_2$ was approximately 90%In_2O_3 and 10%SeO_2. No elemental Cu or copper oxide were determined at the oxide crystal interface, within the detection limit of Auger Electron Spectroscopy, but the presence of a thin Cu_xSe was reported.

The results of Kazmerski et al are in very good agreement with our results in that In_2O_3 is the primary oxide of $CuInSe_2$ and that no Cu_2O or CuO was detected. However the above authors do not report a change in composition due to loss of selenium and imply that after the

formation of In_2O_3, the surface Se atoms are present in the form of SeO_2 and Cu_xSe. This is not at variance with the results reported in this thesis because Kazmerski et al studied the oxidation mechanism only up to 300°C. Below this temperature the selenium oxide is still relatively stable and exists as a solid phase so that loss of selenium due to evaporation of SeO_2 will not occur.

3.7 SUMMARY

Films of $CuInSe_2$ have been deposited by a fast evaporation technique in which 250 mg of bulk powders were evaporated to completion. The evaporation method was not expensive to set up and was simple in the sense that the adjustable experimental variables were kept to a minimum. This resulted in the deposition of uniform films of ~7000Å thickness quite reproducible between runs.

A glancing angle X-ray camera and 1 MeV Transmission Electron Microscope were used to examine the structure of the films. These revealed that the as-deposited films were stratified containing In_2Se, Cu_3Se_2 and $CuInSe_2$. Single phase $CuInSe_2$ films were obtained by annealing at 350°C for 3 hours and by depositing onto substrates held at 250°C. A grain size distribution indicated that the mean crystallite size was approximately equal to the film thickness and that any increase with further annealing was not significant.

The Electron Probe Microanalysis composition of the films indicated that up to substrate temperatures of 250°C and for anneal temperature of 350°C the films were indium and selenium rich and reproducible between preparation runs. The composition of films obtained from various starting powders were also found to be essentially the same.

The film compositions and the bulk compositions of Chapter 2 were combined to define an approximate single phase region for $CuInSe_2$. This was characterised by extensive solubilities for Se, In_2Se_3 and InSe

but lack of solubility in the Cu-Se rich side of the phase plot.

Investigations revealed that any oxidising environment during the anneal must be strictly avoided. The presence of oxygen at temperatures above 350°C resulted in the formation of a layer of In_2O_3 and a simultaneous loss of selenium from $CuInSe_2$.

REFERENCES - CHAPTER 3

(1) E. ELLIOTT, R.D. TOMLINSON, J. PARKES and M.J. HAMPSHIRE, "Some properties of flash evaporated $CuInSe_2$ thin films". Thin Solid Films 20 525 (1974)

(2) B. SCHUMANN, C. GEORGE, A. TEMPEL, G. KÜHN, N. VANNAM, N. NEUMANN and W. HÖRIG, "Epitaxial layers of $CuInSe_2$ on GaAs". Thin Solid Films 52 45 (1978)

(3) R.D. TOMLINSON, D. OMEZI, J. PARKES and M.J. HAMPSHIRE, "Some observations on the effect of evaporation source temperature on the composition of $CuInSe_2$ thin films". Thin Solid Films 65 L3 (1980)

(4) A.F. FRAY and P. LLOYD, "Electrical and optical properties of thin p-type films prepared by vacuum evaporation from the chalcopyrite $CuInSe_2$". Thin Solid Films 58 29 (1979)

(5) L.L. KAZMERSKI, M.S. AYYAGARI, F.R. WHITE and G.A. SANBORN, "Growth and properties of vacuum deposited $CuInSe_2$ thin films". J. Vac. Sci. Technol. 13 139 (1976)

(6) L.Y. SUN, L.L. KAZMERSKI, A.H. CLARK, P.J. IRELAND and D.W. MORTON, "Absorption coefficient measurements for vacuum deposited Cu ternary thin films". J. Vac. Sci. Technol. 15 265 (1978)

(7) Y. KOKUBUN and M. WADA, "Photovoltaic effect in $CuInSe_2$/CdS Heterojunctions". Japan J. Appl. Phys. 16 879 (1977)

(8) S.P. GRINDLE, A.H. CLARK, S. REZAIE-SEREJ, E. FALCONER, J. McNEILY and L.L. KAZMERSKI, "Growth of $CuInSe_2$ by molecular beam epitaxy". J. Appl. Phys. 51 5464 (1980)

(9) A.N.Y. SAMAAN, N. ABDUL-KARIM ABDUL-HUSSEIN, R.D. TOMLINSON, A.E. HILL and D.G. ARMOUR, "An evaluation of some physical characteristics of $CuInSe_2$ thin films produced by RF sputtering". Japan J. Appl. Phys. 19 (Supplement 19-3) 15 (1980)

(10) J. PIEKOSZEWSKI, J.J. LOFERSKI, R. BEAULIEU, J. BEALL, B. ROESSLER and J. SHEWCHUN, "RF sputtered $CuInSe_2$ thin films". Solar Energy Mater. 2 363 (1980)

(11) R. GLANG, "Vacuum Evaporation" in Handbook of Thin Film Technology, Eds. L.I. MAISSEL and R. GLANG, McGraw-Hill (1970)

(12) R.P. ELLIOTT, "Constitution of Binary Alloys, First Supplement". McGraw-Hill (1965)

(13) C.A. WALLACE and R.C.C. WARD, "An X-ray cylindrical texture camera for the examination of thin films". J. Appl. Cryst. 8 255 (1975)

(14) Joint Committee on Powder Diffraction Standards No. (06-0416) (1956)

(15) Joint Committee on Powder Diffraction Standards No. (26-523) (1976)

(16) B. BORIE, "A diffraction measurement of the structure of Cu_2O films grown on copper". Acta. Cryst. 13 542 (1960)

(17) H.P. KLUG and L.E. ALEXANDER, "X-ray diffraction procedures for polycrystalline and amorphous materials". John-Wiley and Sons (1974)

(18) W. ROSTOKER and J.R. DVORAK, "Interpretation of metallographic structures". 2nd edition, Academic Press (1977)

(19) H. MODIN and S. MODIN, "Metallurgical Microscopy". Butterworths (1973)

(20) S.S. STRELCHENKO, S.A. BONDAR, A.D. MOLODYK, L.I. BERGER and A.E. BALANEVSKAYA, "Mass spectrometric investigation of the sublimation of certain ternary semiconductors of the $A^{I}B^{III}C_2^{VI}$ type"

(21) K.C. MILLS, "Thermodynamic data for inorganic sulphides selenides and tellurides". Butterworths (1973)

(22) G.K. SLANOVA and A.A. ELISSEV, "X-ray investigation of indium-selenium alloys". Rus. J. Inorg. Chem. 8, 861 (1963)

(23) J.C. MIKKELSEN, Jr., "Ternary phase relations of the chalcopyrite compound $CuGaSe_2$". J. Electron. Mater. 10 541 (1981)

(24) M. KOKTA, J.R. CARRUTHERS, M. GRASSO, H.M. KASPER and B. TELL, "Ternary phase relations in the vicinity of chalcopyrite copper gallium sulphide". J. Electron. Mater. 5 69 (1976)

(25) I. BARIN, O. KNACKE and O. KUBASCHEWSKI, "Thermochemical properties of inorganic substances". Vol. I (1973) and Vol. II (1977), Springer-Verlag

(26) L.L. KAZMERSKI, P.J. IRELAND, O. JAMJOUM and A.H. CLARK, "Microanalysis of oxide/$CuInSe_2$ interfaces". Scan. Electron. microscopy 1 285 (1981)

CHAPTER 4

OPTICAL AND ELECTRICAL PROPERTIES OF $CuInSe_2$ FILMS

4.1 INTRODUCTION

The first part of this chapter is devoted to the characterisation of the $CuInSe_2$ films by optical transmission and reflection measurements in the visible to infra red region of the spectrum.

In the second part of the chapter, the electrical transport parameters and the D.C. conduction models relevant in this study are introduced.

Room temperature resistivity, theremopower and Hall effect measurements are described and the results are related to structural and stoichiometric changes occurring in the films after the heat treatments.

The temperature dependence of the electrical properties is also presented and discussed in the light of carrier scattering pertinent to thin polycrystalline semiconductor films.

4.2 OPTICAL PROPERTIES OF FILMS

4.2.1 Theory of Optical Transmission and Reflection

For a slab with plane parallel faces illuminated by monochromatic light wavelength, λ, the measured transmittance, T, and reflectance, R, under normal incidence are defined by:

$$T = \frac{I_T}{I_0} \quad , \quad R = \frac{I_R}{I_0} \tag{4.1}$$

where

I_0 is the intensity of the incident beam

I_T is the intensity of the transmitted beam

I_R is the intensity of the reflected beam

The forms of T and R at normal incidence are given by[1-3]:

$$T = \frac{[(1-r^2) + 4\sin^2\psi]\exp(-\alpha d)}{[1-r^2\exp(-\alpha d)]^2 + 4r^2\exp(-\alpha d)\sin^2(\phi+\psi)} \tag{4.2}$$

$$R = \frac{r[1-\exp(-\alpha d))^2 + 4\exp(-\alpha d)\sin^2\phi]}{[1-r^2\exp(-\alpha d)]^2 + 4r^2\exp(-\alpha d)\sin^2(\phi+\psi)} \tag{4.3}$$

where d is the thickness of the slab and r is the reflection coefficient at the air-slab interface and is given by:

$$r = \frac{(n-1)^2 + k^2}{(n+1)^2 + k^2} \tag{4.4}$$

in which n is the refractive index and k is the extinction coefficient, both of which are related to the complex refractive index $\bar{n}$ by:

$$\bar{n} = n - jk \tag{4.5}$$

in equations (4.2) and (4.3) α is the absorption coefficient defined as:

$$\alpha = \frac{4\pi k}{\lambda} \tag{4.6}$$

Also ϕ is the phase change of the incident wave upon one complete transversal of the thickness such that

$$\phi = \frac{2\pi nd}{\lambda} \tag{4.7}$$

ψ is the phase angle occurring at the interface and is given by:

$$\psi = \tan^{-1}\left(\frac{2k}{n^2+k^2+1}\right) \tag{4.8}$$

The term $\sin^2(\phi+\psi)$ describes the periodic variation of the reflectance and transmittance with wavelength due to constructive and destructive interference of waves reflected from the front and rear surfaces of the slab.

The interference fringe term can be averaged to yield the mean transmittance and reflectance[2,3]:

$$T = \frac{(1-r)^2 \exp(-\alpha d)}{1-r^2 \exp(-2\alpha d)} \tag{4.9}$$

$$R = r\left[\frac{1 + (1-2r)\exp(-2\alpha d)}{1 - r^2 \exp(-2\alpha d)}\right] \tag{4.10}$$

and

$$R = r[1 + T \exp(-\alpha d)] \tag{4.11}$$

If the reflection coefficient, r, is known by an independent measurement, then the absorption coefficient can be obtained from the transmittance alone:

$$\alpha = \frac{1}{d} \ln \left[\frac{(1-r)^2}{2T} + \left(r^2 + \left[\frac{(1-r)^2}{2T}\right]^2\right)^{\frac{1}{2}}\right] \tag{4.12}$$

If r is not known a priori, then equations (4.9) to (4.11) must be used together and the absorption coefficient of the slab can be determined by solving the third degree equation for $\exp(-\alpha d)$[3]:

$$[\exp(-\alpha d)]^3 + \left[\left(\frac{1-R}{T}\right)^2 - 1 + \frac{1}{T}\right][\exp(-\alpha d)]^2 + \left[\left(\frac{1-R}{T}\right)^2 - 2\right](\exp(-\alpha d)] - \frac{1}{T} = 0 \tag{4.13}$$

If the value of $\exp(-\alpha d)$ from the solution of equation (4.13) is now substituted into equation (4.11) the reflection coefficient, r, may also be determined. This value of r can be subsequently used to calculate the

refractive index, n, from equation (4.4) which can be rewritten as

$$n = \frac{1 + r + [4r - (1-r^2)k^2]^{\frac{1}{2}}}{1-r} \tag{4.14}$$

Thus n and α as a function of wavelength can, in principle, be determined from the experimental measurement of transmittance and reflectance.

If the interference fringes are resolved in the weak absorbing slabs, then these fringes can be used advantageously to determine the refractive index as well. From equation (4.7), transmission maxima and a corresponding reflection minima will occur when

$$2\phi = m\pi = \frac{4\pi nd}{\lambda}$$

where m is an even integer. Also transmission minima and simultaneous reflection maxima will occur when $2\phi = m\pi$, where m is now an odd integer. These relationships will enable the determination of the refractive index at wavelengths corresponding to the interference extrema.

When the transmittance and reflectance of a thin film deposited on a substrate are to be interpreted, the formulae relating the optical constants of the film and substrate become more complex[4]. The special case of a thin film on a relatively thick glass substrate has been treated by Harris et al[5]. The authors assumed that over the entire range of measurements the glass was transparent, i.e. its extinction coefficient is zero. Furthermore, the substrate is assumed to have non-uniform thickness so that any interference effects within the substrate may be neglected. The internal reflections in such a system will then be as shown in Fig. (4.1),for light incident on the film side.

The total transmittance and reflectance will then be given by:

$$T = T_1 + T_2 + T_3 + \ldots = \frac{Taf(1-Rga)}{1-Rga\ Rgf} \tag{4.15}$$

$$R = R_1 + R_2 + R_3 + \ldots = Raf + \frac{Taf^2 Rga}{1-Rga\ Rgf} \tag{4.16}$$

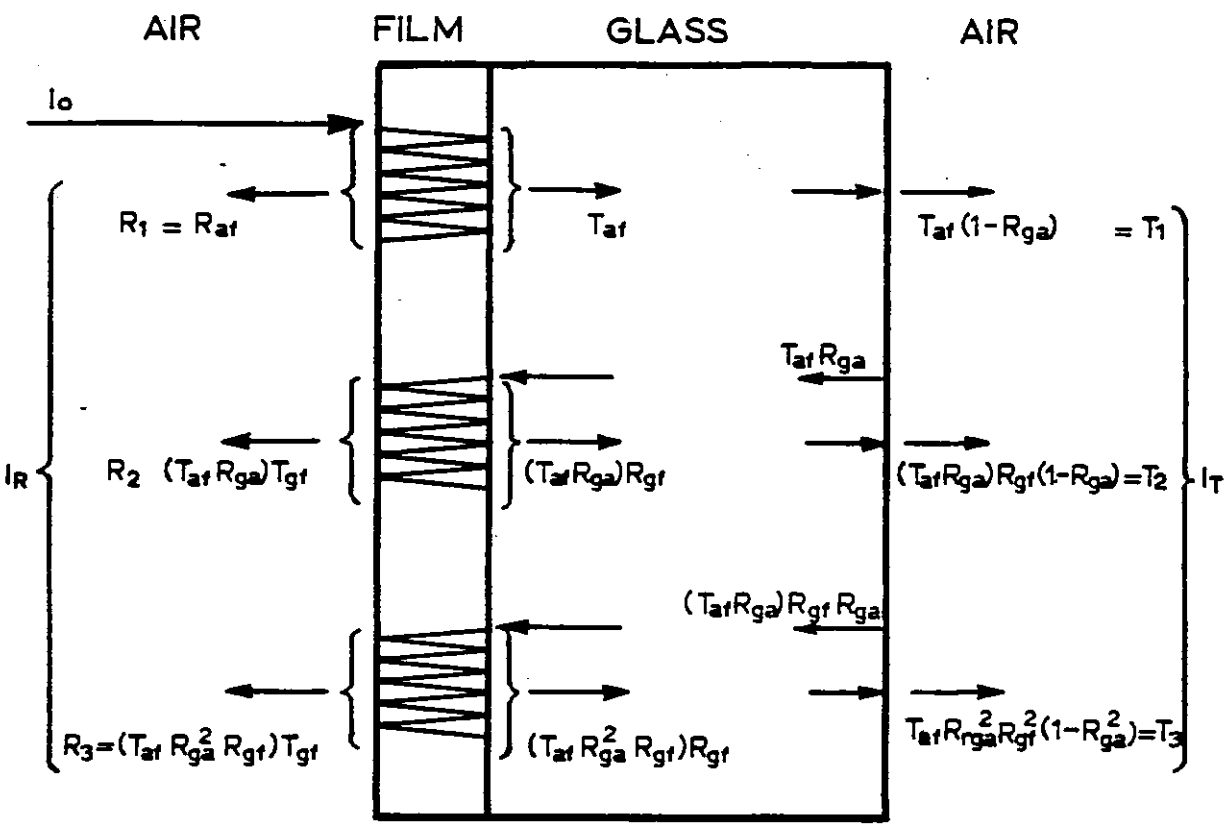

Fig. 4.1: Normal Incidence Transmission and Reflection of a Thin Film on a Thick Glass Substrate

In these equations:

(Taf) = (Transmittance) of the film, for incident light travelling
(Raf) (Reflectance) from air into film

(Tgf) = (Transmittance) of the film for incident light travelling
(Rgf) (Reflectance) from glass into film

Rga is the reflectance of glass for incident light travelling from glass into air.

In the derivation of equations (4.15) and (4.16) the glass is treated as a semi-infinite medium and only multiple reflections within the film are considered and the formulae for Taf, Rga and Rgf can be obtained by addition of amplitudes[4,5].

In order to determine the optical constants of the film alone, the quantities Taf and Raf must be obtained explicitly from the experimental measurements. To do this equations (4.15) and (4.16) must first be simplified. For the glass substrate Rga is given by[5]:

$$Rga = \frac{(n_g-1)^2}{(n_g+1)^2}$$

If the refractive index of glass n_g is taken as 1.5[4], then Rga = 0.04 and 1-Rga Rgf in equations (4.15) and (4.16) will have a minimum value of 0.96 occurring for the extreme case of Rgf = 1. However for a semiconductor film with typical value of refractive index n_g = 2.3-3, it can be shown that Rgf will be around ~0.3[4,5]. Therefore for most practical purposes 1-Rga Rgf will not be expected to deviate very much from unity so that equations (4.15) and (4.16) may be simplified to:

$$T = Taf\ (1-Rga) \qquad (4.18)$$

$$R = Raf + Taf^2\ Rga \qquad (4.19)$$

Thus the transmittance and reflectance of the thin film alone can be obtained without too much loss of accuracy by suitably correcting for the glass substrate. These can then be used to calculate the absorption coefficient and the refractive index of the films.

4.2.2 Experimental Details of Optical Measurements

The transmittance and reflectance of the samples were measured with a Beckman DK-2A double beam ratio recording spectrophotometer. A tungsten lamp source with a lead sulphide detector enabled the measurements to be carried over the wavelength range 0.6 μm - 2.5 μm.

The sample compartment which is shown in Fig. 4.2 had an integrating sphere consisting of two hollow metallic hemispheres fastened together. The inside surface of the sphere was coated with Magnesium Oxide to provide a pure white reflecting surface.

The reference and sample beams entered the sphere alternatively from the front entrance ports and were directed towards their respective exit ports. These ports at the back were usually covered with a reflecting surface so that the rays were deviated back inside the sphere. This radiation was then reflected back and forth by the walls of the sphere until it reached the detector placed on the opening at the top.

The instrument was adjusted to the 100% level by placing two identical highly reflecting Magnesium Oxide tiles at the sample and reference exit ports. The zero level was adjusted by closing the sample shutter.

For normal incidence transmission measurements the sample was placed at the sample entrance port. For reflectance measurements, the sample replaced the tile at the sample exit port. Near normal incidence conditions were achieved by placing the sample and reference tile at the 5° angle to the incident beam. This yielded the sample reflectance relative to that of the tile and to obtain the true value, readings were

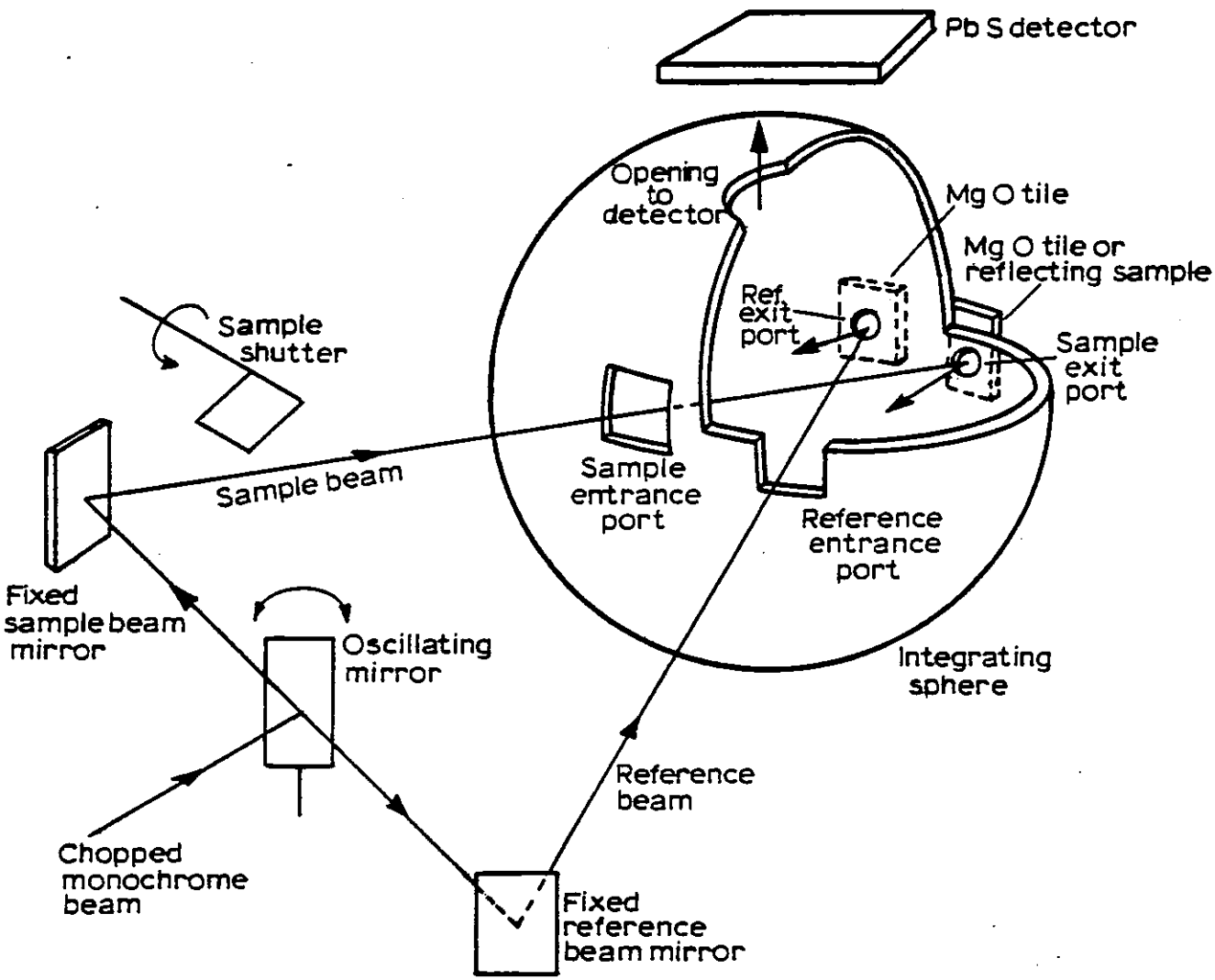

Fig. 4.2: Schematic View of the Spectrometer Sample Compartment Illustrating the Optical Ray Paths

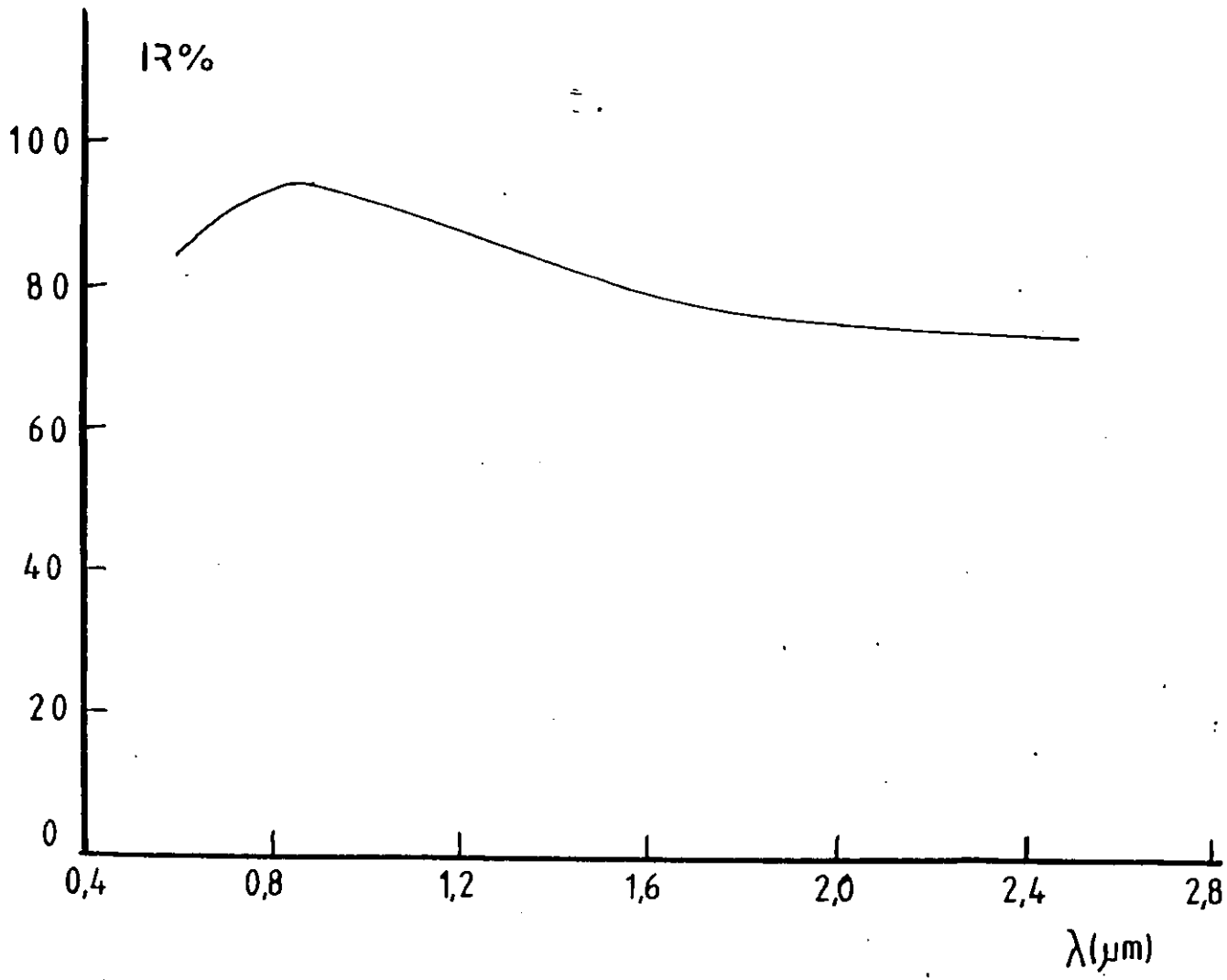

Fig. 4.3: Reflectance of MgO Tile used in the Measurements as a Function of Wavelength

multiplied by the reflectance of the tile. The calibration reflection chart of the tiles used in the experiments is reproduced in Fig. 4.3 and shows that considerable correction was necessary for the wavelength range $1.0 < \lambda < 0.7$.

The correction for the transmission of the glass was achieved by placing, at the reference entrance port, a blank glass slide of the same thickness as the film substrate. Correction for the reflectance of the glass was done by the procedure described in section 4.2.1.

4.2.3 Results

The transmittance spectra of a typical film annealed at 350°C is shown in Fig. 4.4 and it indicates that the films are transparent above about 1.4 μm and exhibit interference fringes. The films start to absorb very strongly below about 1.2 μm and this wavelength corresponds roughly to the expected absorption edge of $CuInSe_2$. The reflectance spectra for such a typical film is given in Fig. 4.5 where interference fringes are also evident. The reflectance rises slightly over the wavelength region 0.6-1.4 μm and then decreases slowly in the infra red region.

By contrast, the optical spectra of films deposited onto substrates held at temperatures less than ~250°C, were characterised by very high reflectance and a transmission less than 10% over the entire wavelength range. This is shown in Fig. 4.6 and indicates the presence of a highly reflecting metallic phase and confirms the structural investigations that the unannealed films are very inhomogeneous.

4.2.3.1 Absorption Coefficient

The absorption coefficients of three 350°C annealed $CuInSe_2$ films as a function of wavelength are shown in Fig. 4.7 for a high resistivity p-type sample (mc53); for a low resistivity p-type sample (mc56) and for an n-type sample (mc67) respectively.

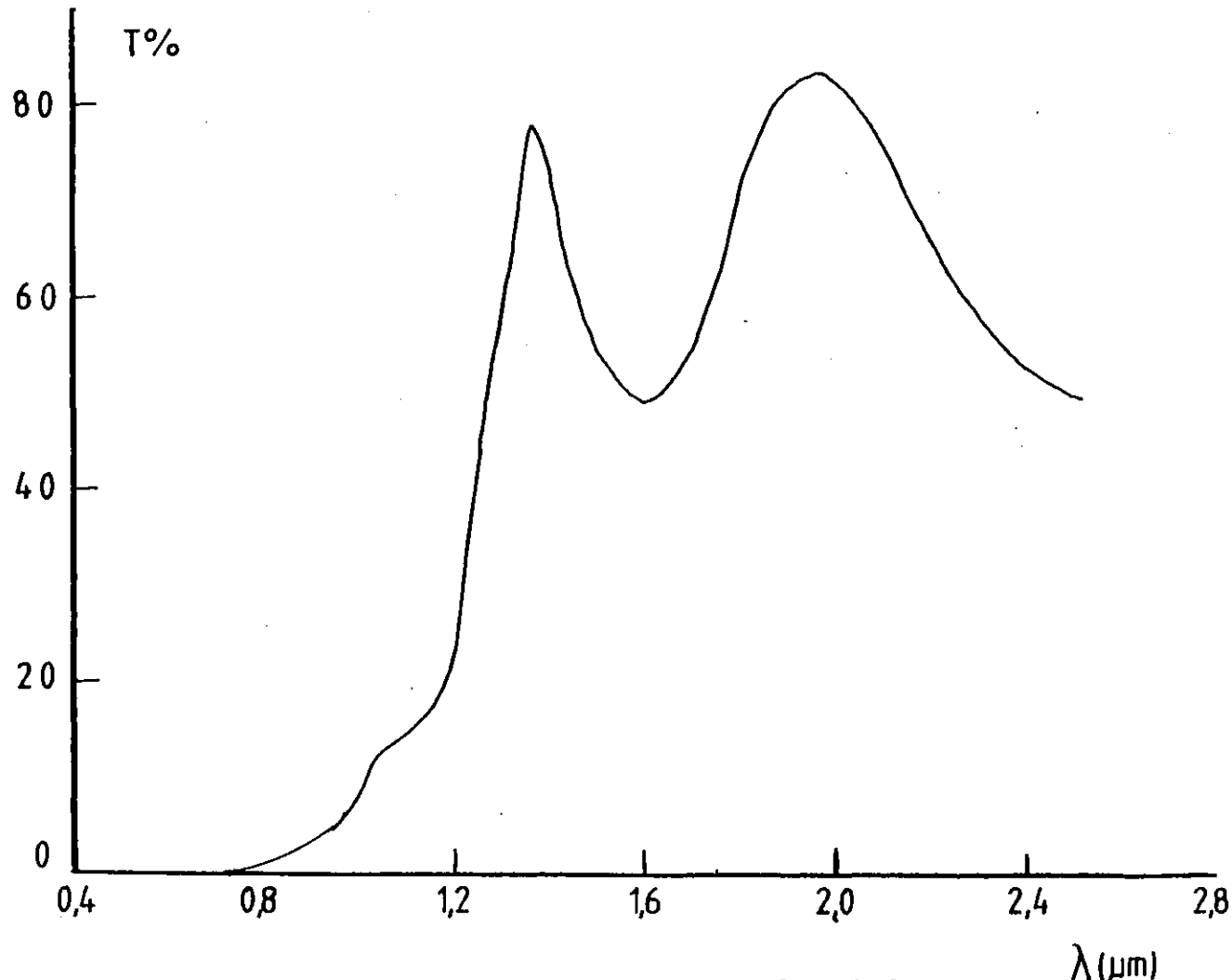

Fig. 4.4: Transmittance as a Function of Wavelength for a 350°C Annealed $CuInSe_2$ Film

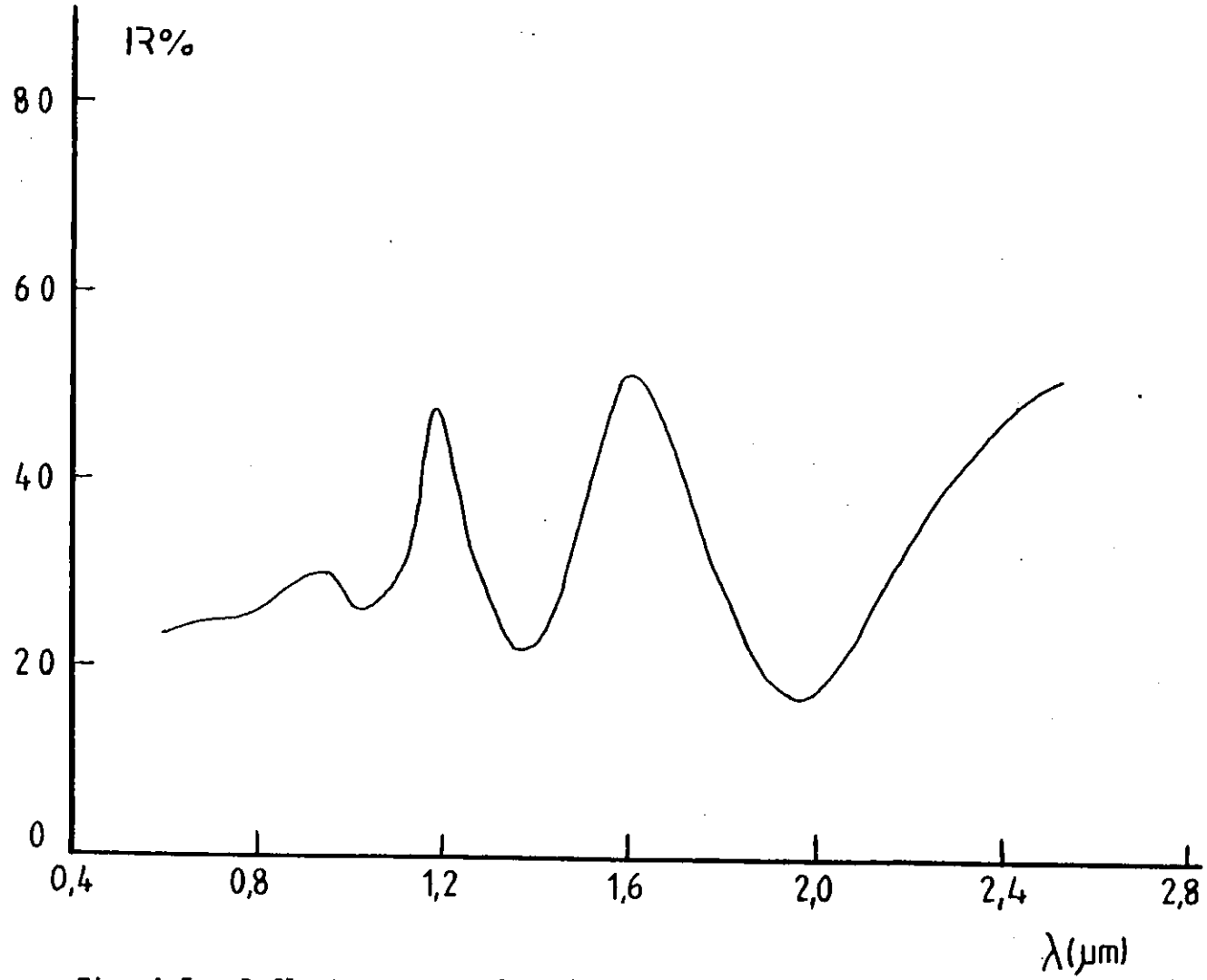

Fig. 4.5: Reflectance as a Function of Wavelength for a 350°C Annealed $CuInSe_2$ Film

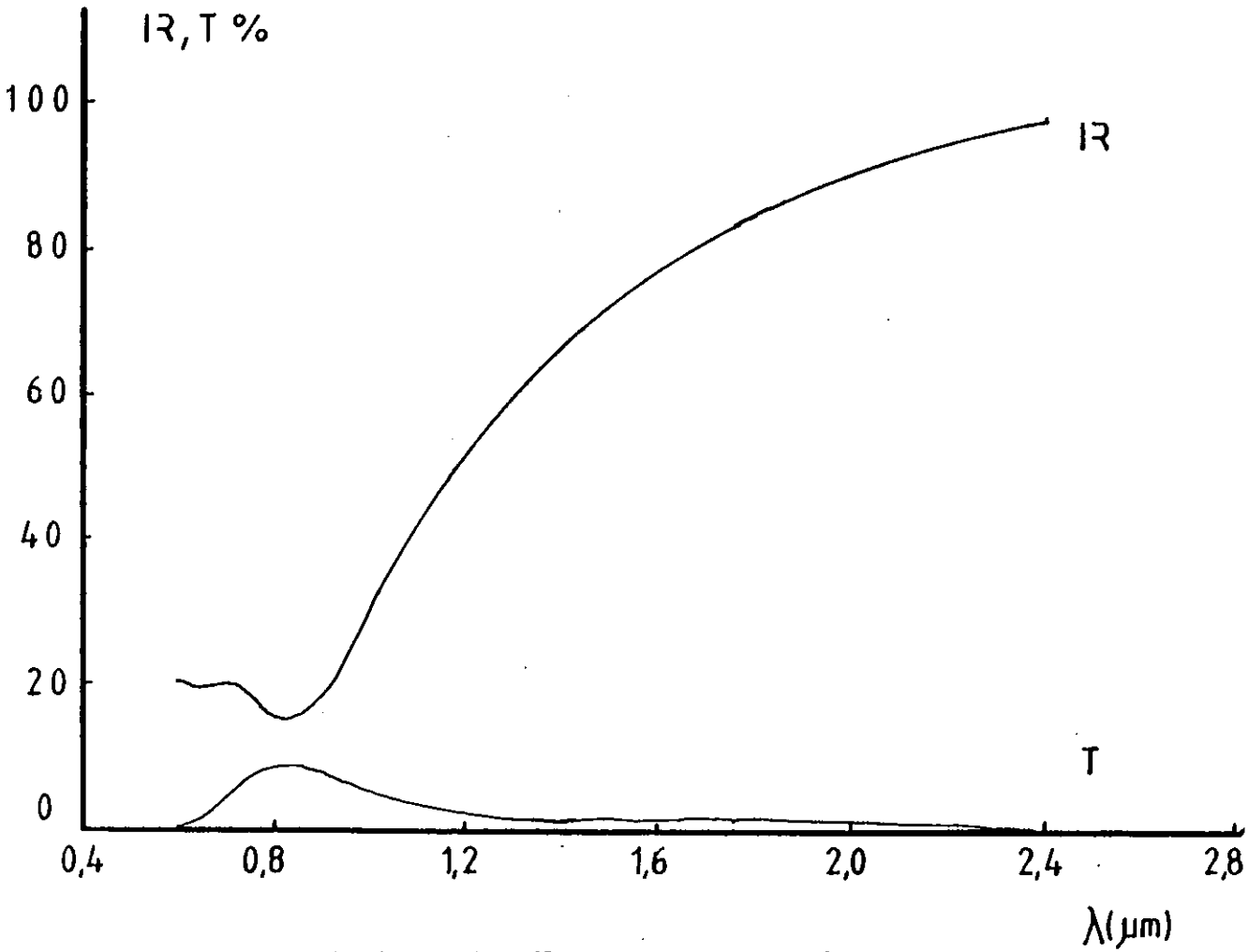

Fig. 4.6: Transmission and Reflectance Spectra of an Unannealed Film

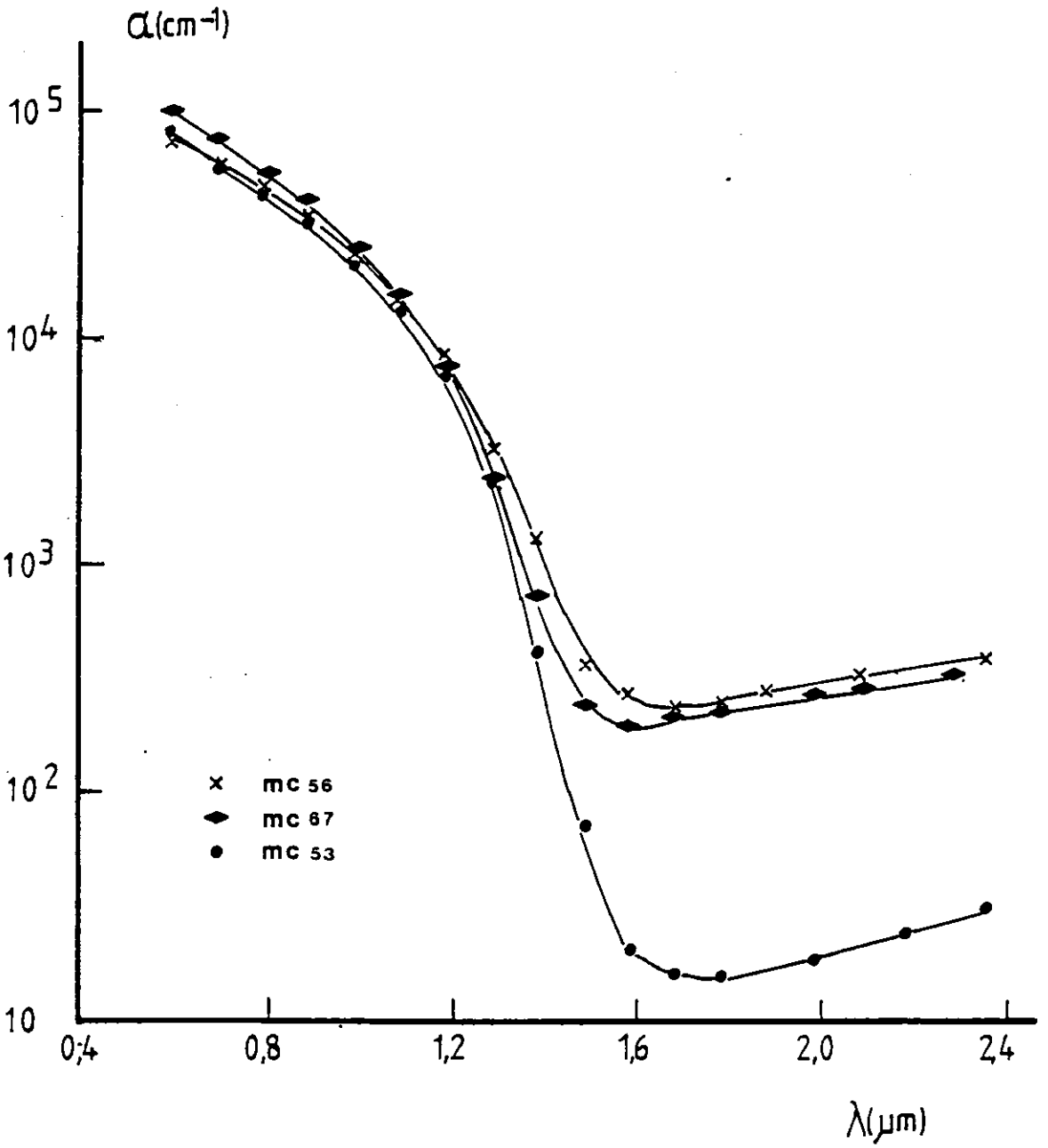

Fig. 4.7: Absorption Coefficient of 350°C Annealed $CuInSe_2$ Films as a Function of Wavelength

At wavelengths below about 1.4 μm, the absorption coefficient has values greater than 10^4 cm^{-1} for all the samples which show similar wavelength dependences in this region. This high absorption is associated with optical transitions involving the valence band and conduction band of the semiconductor and an analysis of this region will enable the energy gap to be determined.

For wavelengths greater than about 1.2 μm the absorption coefficient decreases dramatically by almost two orders of magnitude, indicating that the semiconductor is becoming transparent in this range. However rather than rapidly falling towards zero, the absorption coefficient levels off at around 1.6 μm and starts to increase again. It is interesting to note that the absorption coefficient of the more resistive sample (mc53) is much lower than the other samples. These observations are consistent with extra absorption due to free carriers.

This type of absorption, which is usually observed at wavelengths just below the fundamental edge, occurs when incoming photons interact with charge carriers in the main band. In this case, the absorption of a photon results in an electron making a transition to a higher empty state within the same band while conserving its momentum by scattering processes.

The value of the absorption coefficient due to free carriers may be related to the carrier concentration through the classical formula[6,7]:

$$\alpha_F = \frac{Ng\lambda^2}{m_c^2 \mu \eta} \left(\frac{e^3}{4\pi\varepsilon_o^2 c^3}\right) \quad (m^{-1})$$

where N is the carrier concentration, μ the mobility, m_c the conductivity effective mass, η is the refractive index, and g is a scattering factor which varies from 1.13 for acoustic lattice scattering to 3.4 for ionised impurity scattering.

By using typical values for $CuInSe_2$ an order of magnitude estimate of the carrier concentration of the samples may be deduced. The typical results were 2.6×10^{18} cm^{-3} for sample mc67; 6.4×10^{17} cm^{-3} for sample mc53 and 1.2×10^{19} cm^{-3} for sample mc56. These compared quite reasonably with the carrier concentrations obtained from electrical measurements which were 6.3×10^{18} cm^{-3}, 1.2×10^{17} cm^{-3} and 1.2×10^{20} cm^{-3} for the above specimens respectively.

In order to determine the optical band gap, the spectral dependence of the absorption coefficient due to fundamental absorption must first be isolated from the experimental data. This is usually done by subtracting the effects of free carrier absorption and is achieved by extrapolating the free carrier absorption curve back into the short wavelength region. However in the present case the correction for free carrier absorption was not very significant as the value of α_F extrapolated below the fundamental edge of 1.2 μm was less than 1% of the total α determined experimentally.

For a direct band gap semiconductor like $CuInSe_2$, the absorption coefficient due to fundamental absorption, arising from optical transitions between the valence and conduction bands, obeys the relationship[6,8]:

$$\alpha_d = A(h\nu - E_g)^{\frac{1}{2}} \quad (m^{-1})$$

where $h\nu$ is the energy of the incident photons and E_g is the band gap and A is a factor which takes into account the density of states and effective masses of electrons and holes.

By plotting graphs of $(\alpha_d)^2$ against $h\nu$, it is then possible to determine the direct energy gap of the semiconductor. Such a plot, typical of single-phased $CuInSe_2$ films, is given in Fig. 4.8. The graph has a linear region which can be extrapolated to zero absorption, to yield the forbidden bandwidth E_g. The value of this band gap was found to vary between 1.00 and 1.02 eV for various samples. These results are in excellent agreement with the accepted value of 1.02 eV in the literature

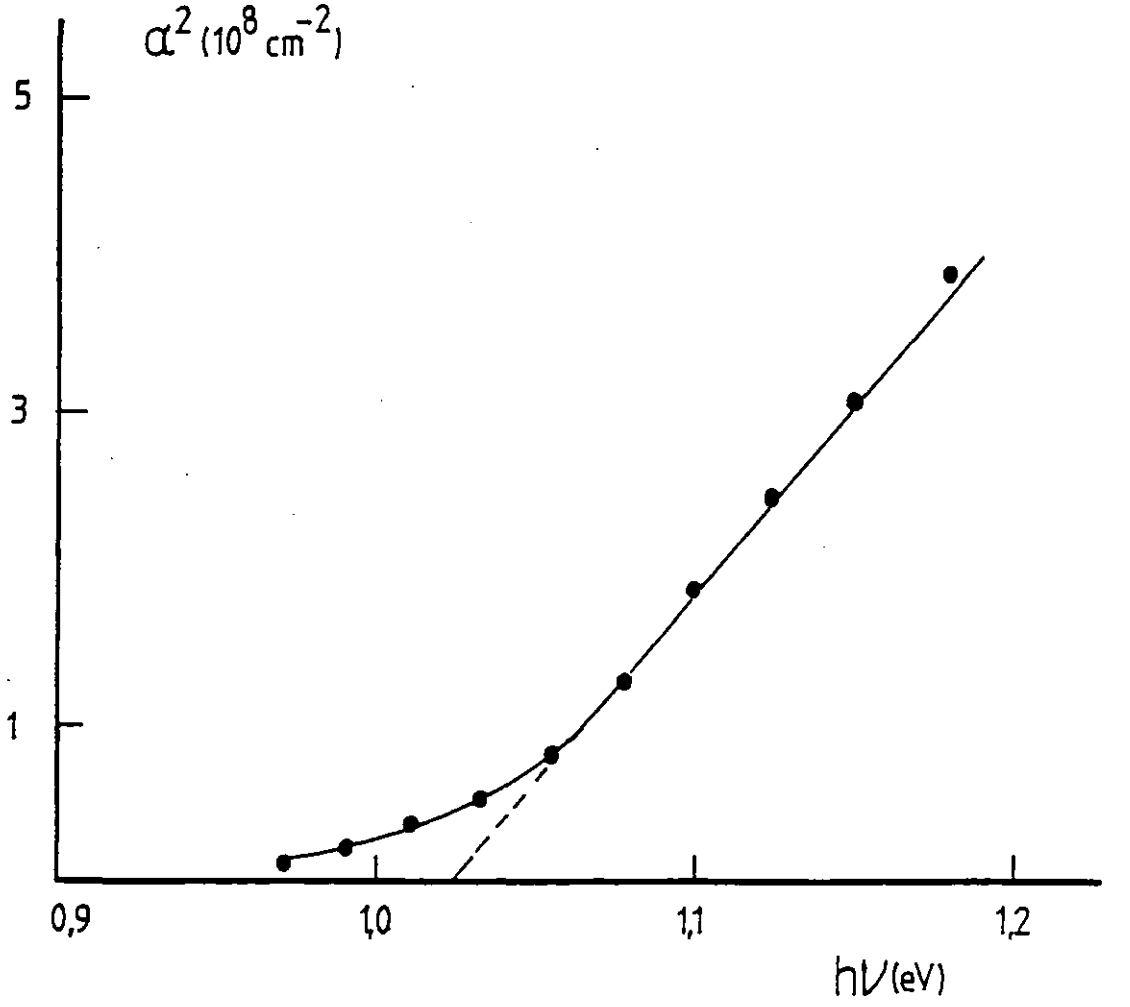

Fig. 4.8: Fundamental Absorption as a Function of Photon Energy for a 350°C Annealed $CuInSe_2$ Film

for single crystal $CuInSe_2$ and indicate that the films have optical properties similar to the bulk material.

4.2.3.2 Refractive Index

The wavelength dependence of the refractive index for the three representative samples considered previously, has also been determined and is given in Fig. 4.9.

For wavelengths shorter than 1.4 μm all the films exhibit a rapid increase in their refractive index. This reaches a peak around 1.1 μm and decreases as the wavelength of the incident radiation is reduced further. This is the typical behaviour associated with fundamental absorption in semiconductors[2,7]. The dispersion of the refractive index beyond the fundamental edge is small as would be expected for the transparent region. The refractive index varied amongst the different specimens and the value at λ = 2 μm had an average of 2.65.

The above experimental results may be compared with other published data on $CuInSe_2$. Only three papers have appeared in the literature so far and these were published during the course of this project and are plotted as the dashed lines in Fig. 4.9. At wavelengths near and below 0.8 μm the results of Löschke et al[9] agree very well with the data reported here. For the wavelength region beyond about 1.6 μm, the data of Hörig et al[10] and Sobota et al[11] also are in fair agreement with our results, though the latter authors report a somewhat higher value of the refractive index. Refractive index data for the absorption region (0.6 - 1.6 μm) has not been reported in the literature, so a comparison of our results in this region is not possible.

4.2.4 Conclusions

The optical measurements have shown that films deposited at substrate temperatures less than 250°C contain metallic second phases. Films annealed

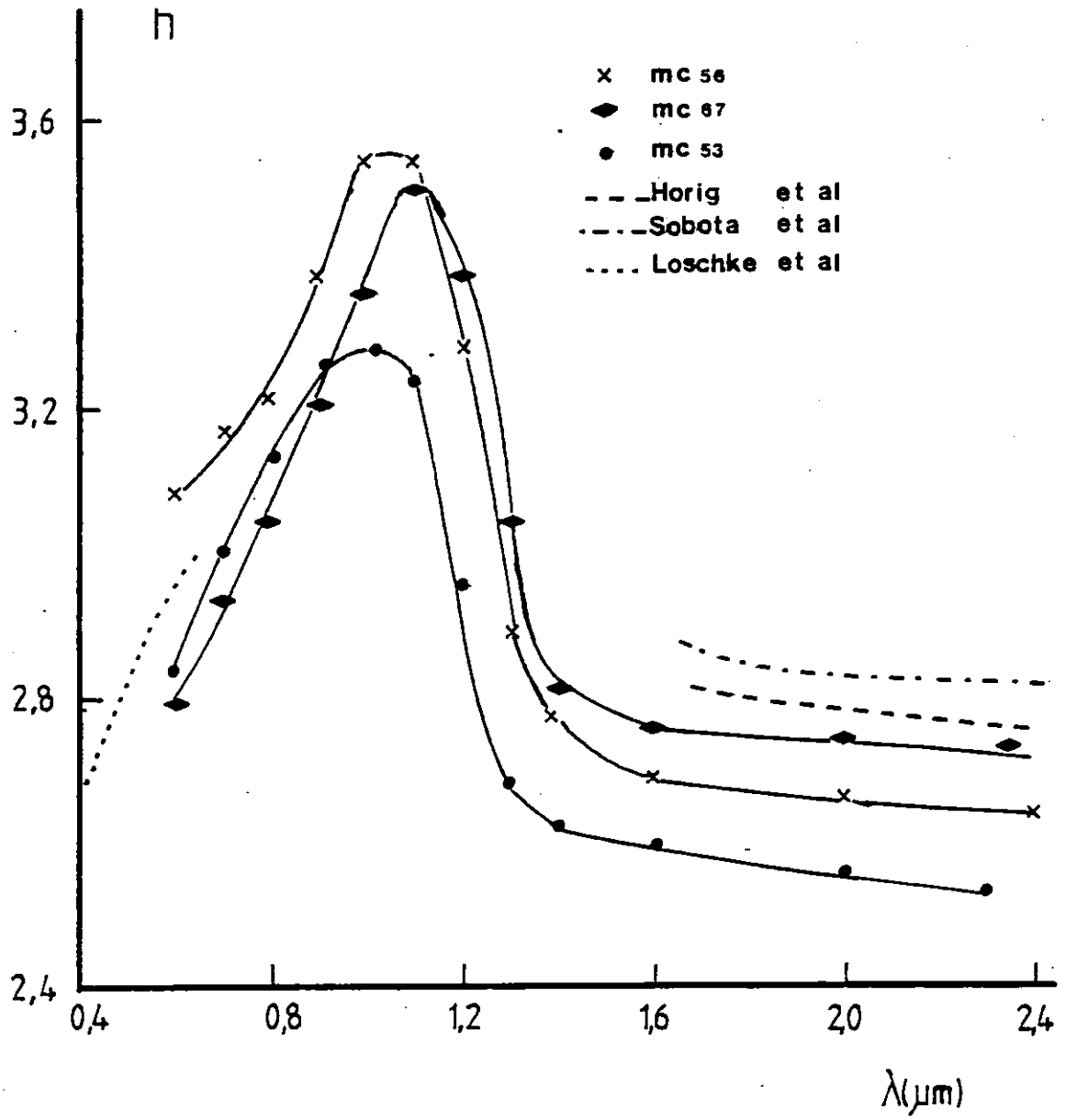

Fig. 4.9: Refractive Index of 350°C Annealed $CuInSe_2$ Films as a Function of Wavelength

at 350°C have band gaps and refractive indices which agree very well with published single crystal $CuInSe_2$ data[11,12], confirming the good quality of films prepared in this investigation.

4.3 ELECTRICAL TRANSPORT THEORY

4.3.1 The Hall Effect and Thermoelectric Effect in Semiconductors

4.3.1.1 Single Band Conduction

The Hall Effect

When a current-carrying conductor is placed in a transverse magnetic field, an electric field called the Hall field, E_H, appears in a direction perpendicular to both the magnetic field and current flow. This Hall field is related to the applied current density, J, and magnetic flux density, B, by the Hall coefficient R_H through the relationship:

$$E_H = R_H JB \quad (Vm^{-1})$$

In a semiconductor, in which condution occurs in a single band, the Hall coefficient is a direct measure of the type and volume concentration of the majority carriers. For n-type semiconductor

$$R_H = -\frac{r}{n_e}$$

and for a p-type semiconductor

$$R_H = +\frac{r}{p_e}$$

where n_e is the electron concentration and p_e is the hole concentration, r is the Hall factor which depends on the scattering mechanism and on whether the semiconductor is degenerate or not. It can take a value between 1 and 1.93, but since the scattering mechanism dominating in the semiconductor is not known prior to Hall measurements, it is usually taken to equal unity.

Thermoelectric Effect

When a temperature gradient is applied along a conductor an internal electric field, ε_T, is set up along the same direction as the temperature gradient. This is known as the Seebeck effect and the ratio of the thermoelectric field, ε_T, to the temperature gradient, $\frac{dT}{dx}$ is defined as the thermoelectric power or Seebeck coefficient of the material. The thermoelectric power is an alternative means of determining the type and density of carriers in a semiconductor.

The general expression for the Seebeck coefficient in a semiconductor, in which conduction takes place in a single band, can be obtained by the solution of Boltzmann transport equation. If the scattering of carriers is described by a relaxation time, τ, which varies with energy E as $\tau = AE^{-s}$, the formula is[6,13]:

$$S = \frac{k}{e}\left[\frac{(\frac{5}{2}-s)\ F_{3/2-s}(\eta)}{(\frac{3}{2}-s)\ F_{1/2-s}(\eta)} - \eta\right] \quad (\mu V\ K^{-1}) \tag{4.20}$$

where k is Boltzmann constant, e electronic charge, η is the reduced Fermi energy = E_F/kT, s has values of $\frac{1}{2}$ for acoustic lattice scattering and -3/2 for ionised impurity scattering. $F_r(\eta)$ is the Fermi Dirac integral defined[9,13] as:

$$F_r(\eta) = \int_0^\infty \frac{x^r\, dx}{1 + \exp[x-\eta]} \tag{4.21}$$

where x is the reduced energy $\frac{E}{kT}$.

The reduced Fermi energy, η, can be directly related to the carrier concentration in a band by the Fermi integral with one-half index:

$$n = \frac{2}{\sqrt{\pi}}\ N_c\ F_{1/2}(\eta) \tag{4.22a}$$

$$\dot{p} = \frac{2}{\sqrt{\pi}}\ N_v\ F_{1/2}(\eta) \tag{4.22b}$$

where N_c is the conduction band density of states and N_v is the valence band density of states which are given by:

$$N_c = 2\left(\frac{2\pi m_n kT}{h^2}\right)^{3/2} \tag{4.23a}$$

$$N_v = 2\left(\frac{2\pi m_p kT}{h^2}\right)^{3/2} \tag{4.23b}$$

in which m_n and m_p are the density of states effective masses of the carriers.

If the semiconductor is non-degenerate, that is the Fermi level is well away from either band edges so that $\eta < 0$, Boltzmann statistics can be used and the formula for the Seebeck coefficient simplifies to:

$$S_n = -\frac{k}{e}\left[A + \ell n\left(\frac{N_c}{n}\right)\right] \tag{4.24a}$$

$$S_p = +\frac{k}{e}\left[A + \ell n\left(\frac{N_v}{p}\right)\right] \tag{4.24b}$$

where A is the scattering factor which is 2 for acoustic lattice scattering and 4 for ionised impurity scattering.

4.3.1.2 Mixed Band Conduction

In general when conduction by minority carriers is likely to be significant, the contribution to transport from both holes and electrons must be taken into account. Such a situation arises very frequently in p-type semiconductors when the electron mobility is very much higher than the hole mobility. In this case the conductivity, Hall coefficient and Seebeck coefficient will be given by[6,14]:

$$\sigma = \sigma_n + \sigma_p \qquad (\Omega\text{-m})^{-1}$$

$$R_H = \frac{R_{Hn}\,\sigma_n^2 + R_{Hp}\,\sigma_p^2}{(\sigma_n + \sigma_p)^2}$$

$$S = \frac{S_n\sigma_n + S_p\sigma_p}{\sigma_n + \sigma_p}$$

where $\sigma_n = ne\,\mu_n$, $\sigma_p = pe\,\mu_p$ are the conductivities arising from electrons and holes respectively. In terms of electron to hole mobility ratio $b = \frac{\mu_n}{\mu_p}$, the expressions for mixed conduction are:

$$\sigma = e(p + nb)\,\mu_p \tag{4.25}$$

$$R_H = \frac{p-nb^2}{e(p+nb^2)} \tag{4.26}$$

$$S = \frac{k}{e}\left[\frac{A(p-nb) + p\,\ell n(\frac{N_v}{p}) - nb\,\ell n(\frac{N_c}{n})}{p + nb}\right] \tag{4.27}$$

The expressions for mixed conduction are of particular interest when a p-type semiconductor is converted to n-type. Then the measured Hall coefficient and thermopower will be expected to become zero at some stage during the p to n conversion. These effects will be considered later.

4.3.2 Electrical Transport in a Two-layer Model

There are certain situations, such as in a semiconductor doped non-uniformly in the thickness region, when the interpretation of the measured transport parameters is not straightforward. The electrical transport of a surface space charge layer or a thin conducting oxide layer on a slab is another example where the theory presented previously cannot be applied directly. In such cases it is expected that each layer will contribute to the transport properties and for this purpose, a simple two-layer conduction model will be considered.

Such a model was first used by Petritz[15] to explain conductivity and Hall effect measurements. His approach has been used here to develop also a model for thermoelectric effect. For completeness each transport parameter will be presented.

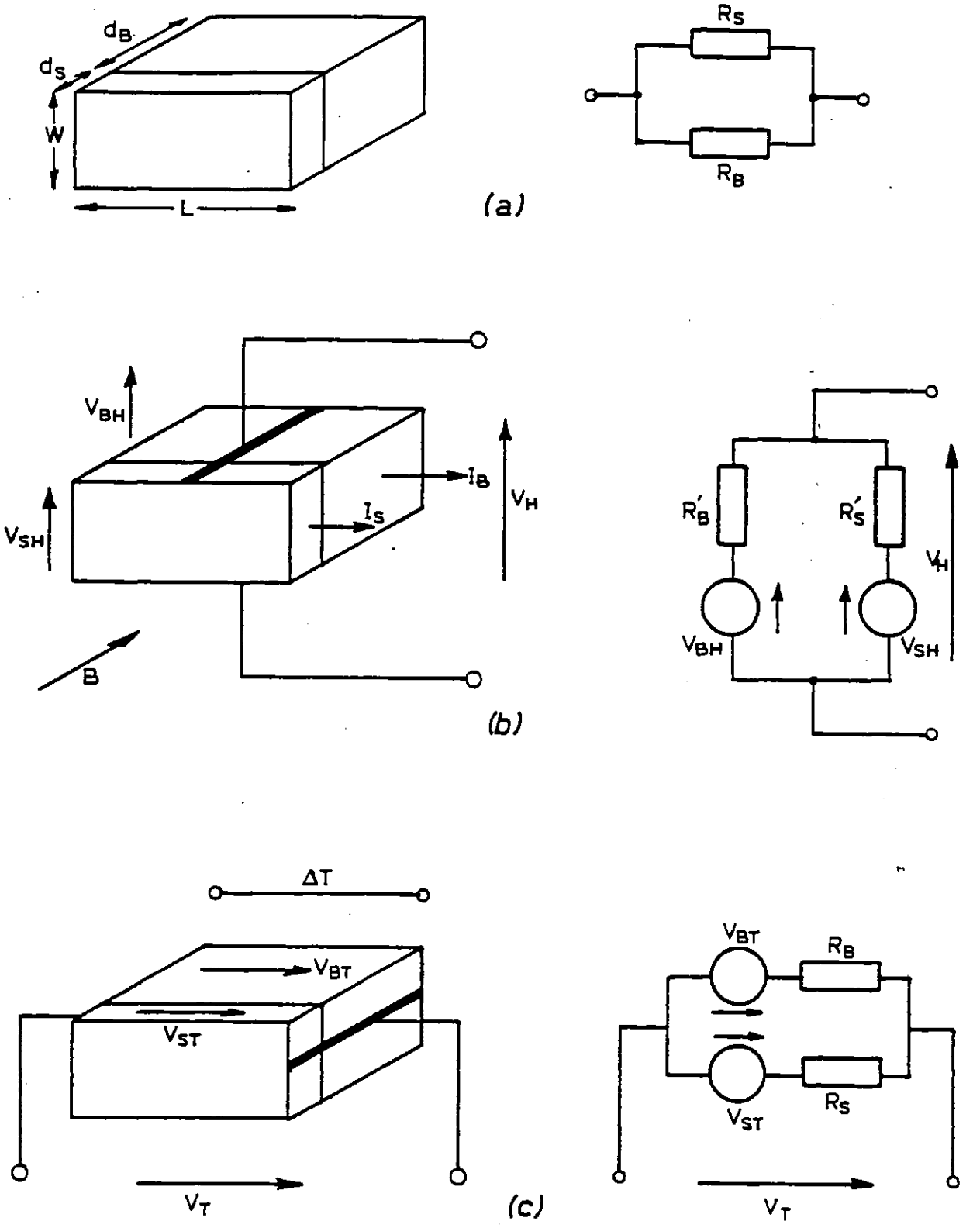

Fig. 4.10: Schematic Representation of Two-Layer Model with the Equivalent Electrical Circuits for

(a) Conductivity

(b) Hall Effect

(c) Thermoelectric Effect

In the two-layer model, a thick semiconductor slab with length, L, width, w, and thickness d_B, is assumed to be covered with a thinner conducting layer of thickness d_S. As shown in Fig. 4.10, the total measured conductivity, Hall coefficient and thermoelectric power of the system, may be determined by considering the resistance and voltages in each layer and by constructing an equivalent circuit.

4.3.2.1 Effective Conductivity

The total conductivity of the two layers may be calculated by the parallel combination of the respective resistances

$$G = \frac{1}{R} = \frac{1}{R_S} + \frac{1}{R_B}$$

where $R_S = \frac{L}{\sigma_S wd}$, $R_B = \frac{L}{\sigma_B wd_B}$

where σ_S and σ_B are the conductivities of each layer. In terms of measured conductance, G, this leads to

$$G = \frac{\sigma_T wd}{L} = \frac{w}{L} (\sigma_S d_S + \sigma_B d_B)$$

since $d = d_B + d_S$

$$\sigma_T = \frac{\sigma_S d_S + \sigma_B d_B}{d_S + d_B} \qquad (4.28)$$

4.3.2.2 Effective Hall Coefficient

For the Hall effect, each layer is assumed to give rise to a Hall voltage such that for the bulk

$$V_{BH} = \frac{I_B R_{BH} B}{d_B}$$

and for the surface layer

$$V_{SH} = \frac{I_S R_{SH} B}{d_S}$$

where B is the applied magnetic flux density R_{BH} and R_{SH} are respective Hall coefficient in the two layers.

The currents I_B and I_S are related to the total applied current, I, through the resistance of the layers

$$I_B = \frac{IR_S}{R_S+R_B} = I\left[\frac{\sigma_B d_B}{(\sigma_B d_B+\sigma_S d_S)}\right]$$

$$I_S = \frac{IR_B}{R_S+R_B} = I\left[\frac{\sigma_S d_S}{(\sigma_B d_B+\sigma_S d_S)}\right]$$

The total Hall voltage is obtained by treating the two layers as two voltage generators in parallel

$$V_H = \frac{V_{BH}R_S' + V_{SH}R_B'}{R_B' + R_S'}$$

where

$$R_S' = \frac{w}{\sigma_S L d_S}$$

and

$$R_B' = \frac{w}{\sigma_B L d_B}$$

are the effective resistances of the Hall generators.

In terms of the experimentally measured parameters

$$V_H = \frac{I_B}{d} R_{HT} ,$$

so that the total effective Hall coefficient of the two layers will be

$$R_{HT} = \frac{(d_S+d_B)\ (R_{HB}\sigma_B^2\ d_B + R_{HS}\sigma_S^2 d_S)}{(\sigma_B d_B + \sigma_S d_S)^2} \qquad (4.29)$$

4.3.2.3 Effective Seebeck Coefficient

For the thermoelectric effect again each layer is assumed to give rise to a thermoelectric voltage directly proportional to their Seebeck coefficients S_B and S_T respectively.

For the bulk, when the temperature difference, ΔT, is small,

$$V_{BT} = S_B \Delta T$$

and for the surface layer

$$V_{ST} = S_S \Delta T$$

The resulting thermoelectric voltage will be the parallel sum of each voltage generator so that

$$V_T = \frac{V_{BT} R_S + V_{ST} R_B}{R_B + R_S}$$

In terms of experimentally determined parameters

$$V_T = S_T \Delta T ,$$

so that the effective Seebeck coefficient of the two layers will be

$$S_T = \frac{S_S \sigma_S d_S + S_B \sigma_B d_B}{\sigma_S d_S + \sigma_B d_B} \tag{4.30}$$

Equations (4.28) to (4.30) may be rewritten in the terms of the bulk transport parameter so that

$$\frac{\sigma_T}{\sigma_B} = \frac{1 + (\frac{\sigma_S}{\sigma_B})(\frac{d_S}{d_B})}{1 + (\frac{d_S}{d_B})} \tag{4.31}$$

$$\frac{R_{HT}}{R_{HB}} = \frac{1 + (\frac{d_S}{d_B})[1 + (\frac{R_{HS}}{R_{HB}})(\frac{\sigma_S}{\sigma_B})^2 (\frac{d_S}{d_B})}{[1 + (\frac{\sigma_S}{\sigma_B})(\frac{d_S}{d_B})]^2} \tag{4.32}$$

$$\frac{S_T}{S_B} = \frac{1 + (\frac{S_S}{S_B})(\frac{\sigma_S}{\sigma_B})(\frac{d_S}{d_B})}{1 + (\frac{\sigma_S}{\sigma_B})(\frac{d_S}{d_B})} \tag{4.33}$$

As the conductivity and thermoelectric effect in a two-layer system will be considered later on, it is appropriate at this stage to look at these more extensively.

In Fig. 4.11 the total conductivity σ_T/σ_B has been plotted as a surface to bulk thickness ratio d_S/d_B. Various values of surface to bulk conductivity ratios σ_S/σ_B, ranging from 0.1 to 100, have been taken as the constant parameter to show how the total conductivity is affected. The main feature of these curves is that the total conductivity becomes dominated by the surface layer if this has a very high conductivity. For example, if σ_S/σ_B is equal to 100, then the total conductivity becomes twice the bulk value, even though the surface layer may only form less than 1% of the thickness. If the conductivity of the surface layer is comparable or lower than the bulk, then the total conductivity remains very much constant, until the surface layer is thicker than the original bulk.

In Fig. 4.12, the total thermopower S_T/S_B of equation (4.33) is plotted for a p-type surface on a p-type bulk, as a function of surface to bulk thickness ratio. Since the total thermopower will depend upon the values of the surface to bulk conductivity ratio σ_S/σ_B and the values of surface to bulk thermoelectric power ratio S_S/S_B, the thermopower is treated as two cases.

In the first instance, the value of S_S/S_B is held constant and the total Seebeck coefficient is plotted versus σ_S/σ_B. Such a plot is shown in Fig. 4.12(a) for values of σ_S/σ_B ranging from 100 to 0.1 and for an arbitrary value of $S_S/S_B = +3$. The exact value of this ratio is not crucial and the effect of choosing another Seebeck ratio is to merely change the final value of S_T/S_B. In these plots it is apparent that the measured Seebeck coefficient will be mainly due to the surface layer when this has a higher conductivity than the bulk. For example, for $\sigma_S/\sigma_B = 100$ the total thermoelectric power is nearly that of the surface, despite the fact that

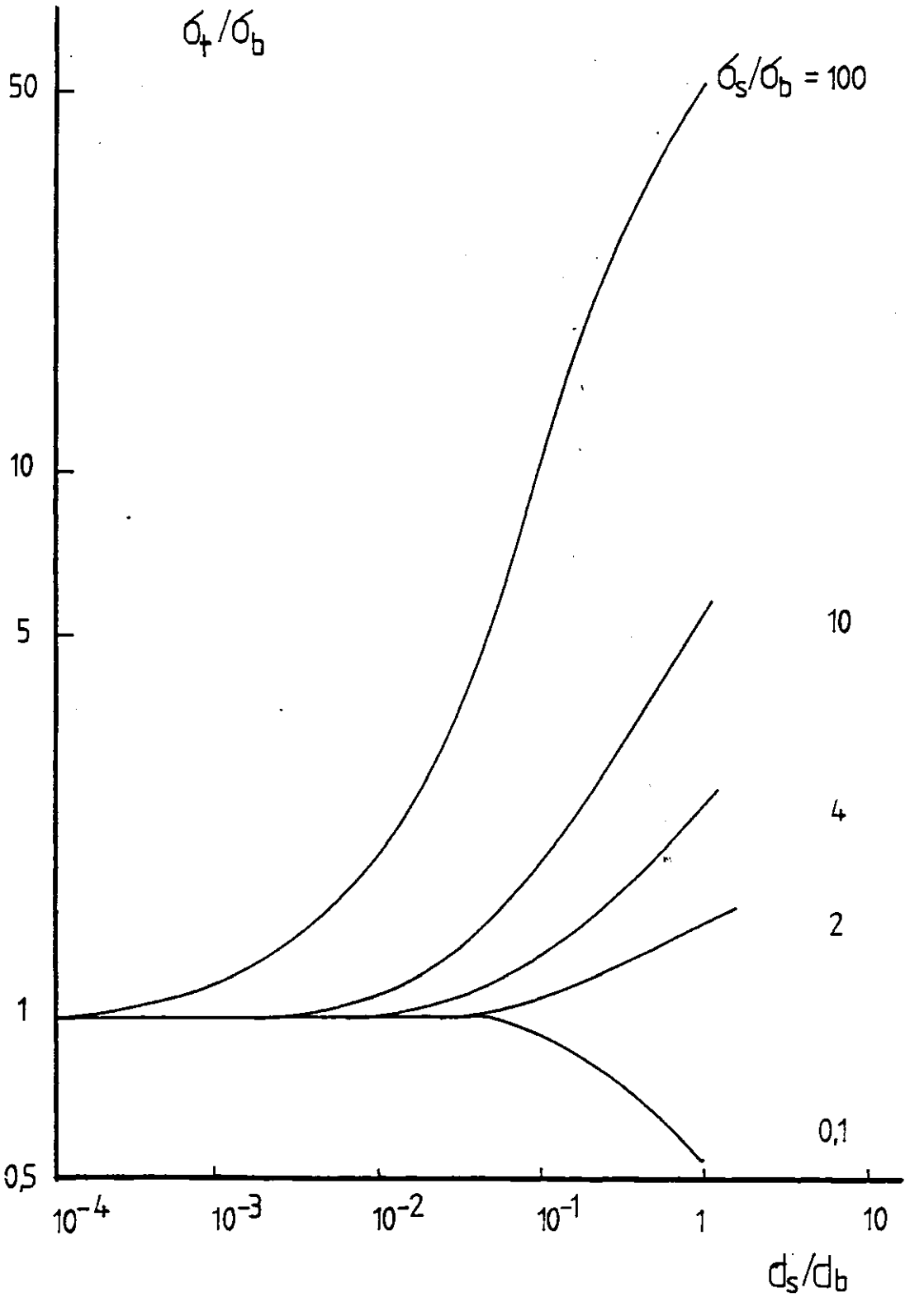

Fig. 4.11: Theoretical Variation of Total Conductivity as a Function of Thickness Ratio for Various Values of Surface to Bulk Conductivity Ratio in the Two-Layer Model

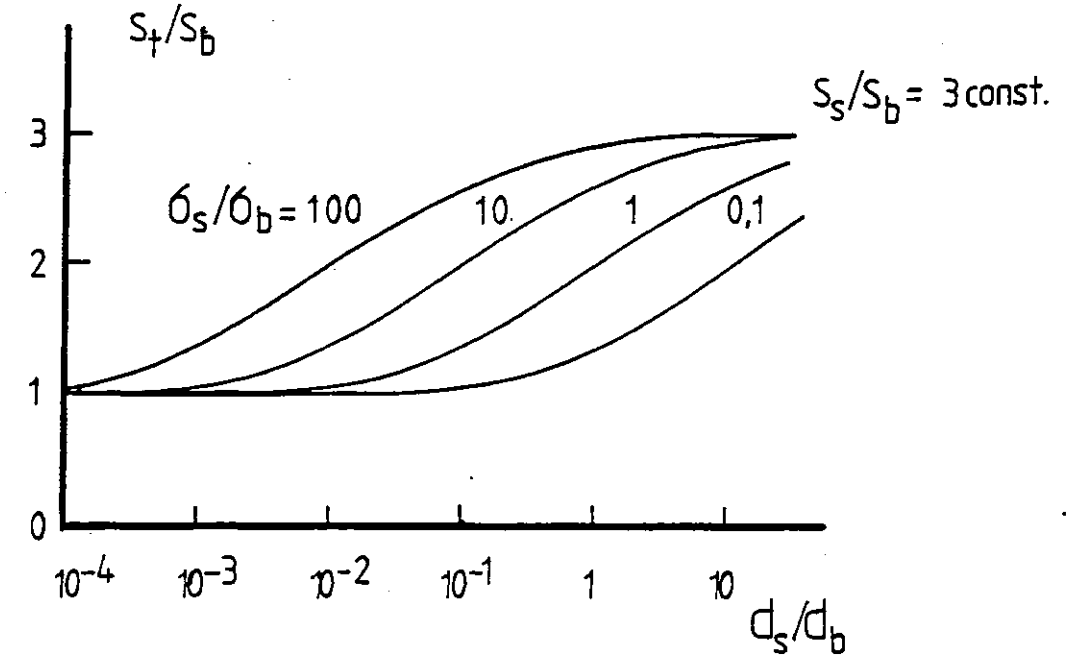

Fig. 4.12(a): Variation of Total Thermopower with Thickness Ratio for various Values of Surface to Bulk Conductivity Ratio for a p-type Surface on p-bulk.

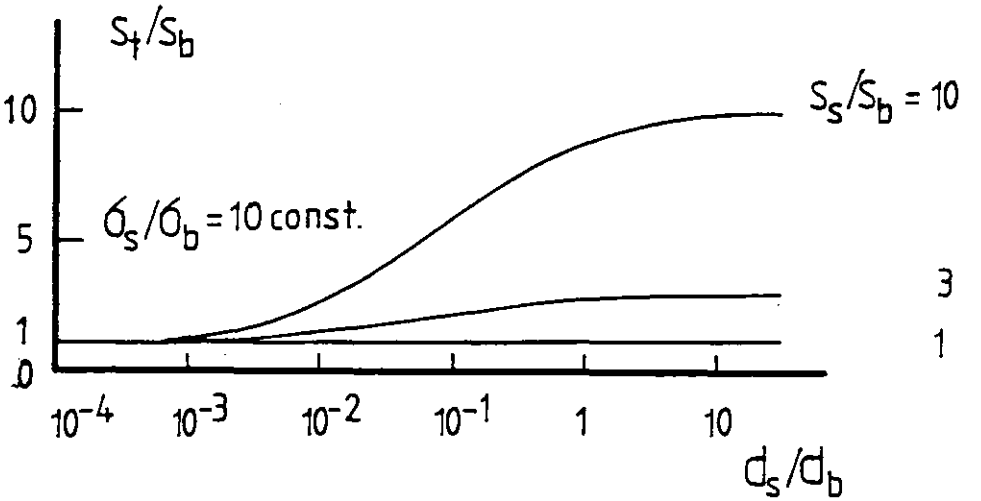

Fig. 4.12(b): Variation of Total Thermopower with Thickness Ratio for Various Values of Surface to Bulk Thermopower Ratio for a p-surface on p-bulk

this only forms less than 10% of the thickness. In other words, even if the surface layer is very thin compared to the bulk, it will dominate the measured Seebeck coefficients.

In Fig. 4.12(b) the other case for thermoelectric power is treated, where now the value of σ_S/σ_B is held constant at an arbitrary value of 10 and the total thermopower is plotted versus thickness ratio for various combinations of surface to bulk theremoelectric power ratio S_S/S_B. The main feature of these curves is that at any particular surface layer thickness, the higher the Seebeck coefficient of the surface layer the further the total thermopower deviates away from the bulk value. For example, at $d_S/d_B = 10^{-1}$, the measured thermopower is $2S_B$ for a surface having Seebeck coefficient $3S_B$, whereas it becomes $6S_B$ for a surface having Seebeck coefficient $10S_B$.

So far the majority carrier type of the two layers were assumed to be the same and the case of a p-type surface on p-type bulk was treated. The situation for n-type surface on n-type bulk will be the same except that the thermopowers will be negative.

If the surface layer has a majority carrier type which is opposite to that of the bulk then a new situation arises. While the total conductivity in such a case will still be represented by Fig. 4.11, the total thermoelectric power will behave differently. The case of an n-type surface on a p-type bulk is shown for the thermoelectric effect in Figs. 4.13(a) and 4.13(b). It will be evident that the comments made previously for a p-type layer on a p-type bulk are still valid here. There is now, however, an additional feature: the total thermopower crosses the zero level and changes sign at particular surface thicknesses.

In Fig. 4.13(a) it is apparent that the total thermopower will become zero, for a very small surface thickness, provided that it has a very much higher conductivity than the bulk. Similarly in Fig. 4.13(b)

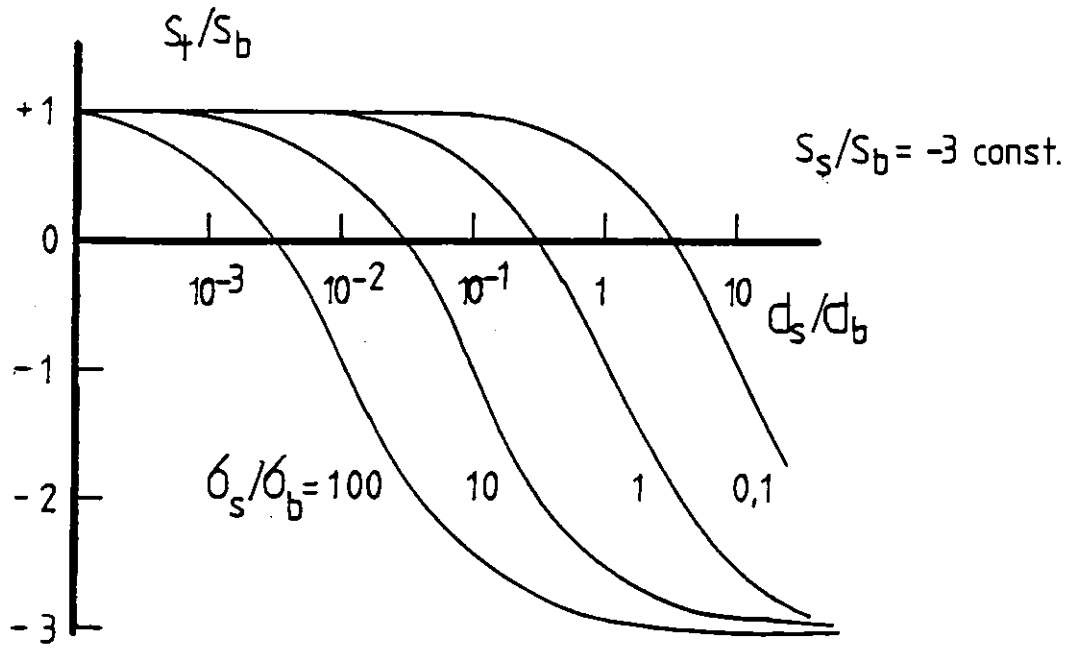

Fig. 4.13(a): Variation of Total Thermopower with Thickness Ratio for Various Values of Surface to Bulk Conductivity Ratio for an n-surface on p-bulk

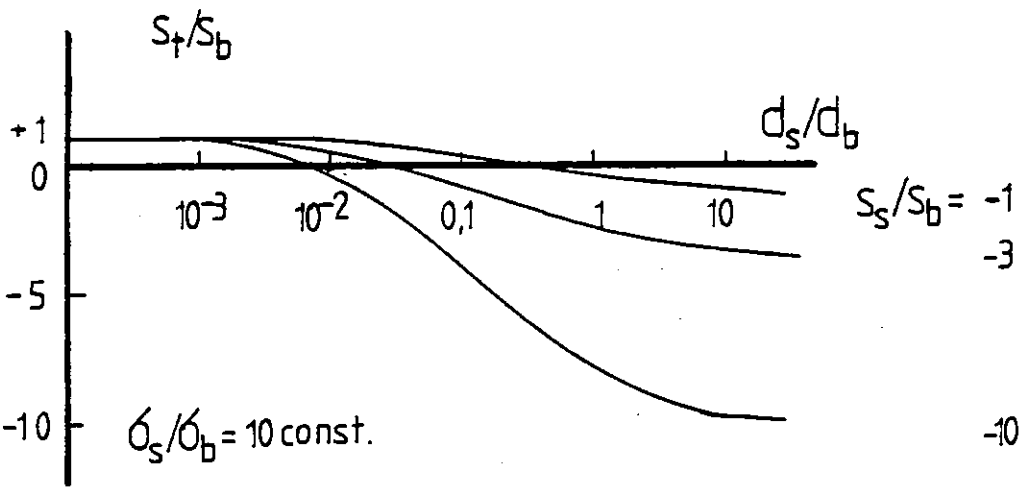

Fig. 4.13(b): Variation of Total Thermopower with Thickness Ratio for Various Values of Surface to Bulk Conductivity Ratio for an n-surface on p-bulk

it will be seen that the total thermopower begins to change sign at a smaller value of surface to bulk thickness ratio, if the surface layer has a higher Seebeck coefficient than the bulk.

The case of an n-type surface on a p-type bulk will be invoked later and its important prediction is that a zero crossover for thermoelectric power will occur, an effect which is quite similar to the case of mixed band conduction in semiconductors.

4.3.3 Electrical Transport in Polycrystalline Semiconductor Films

4.3.3.1 Effective Conductivity, Hall Coefficient and Seebeck Coefficient

The interpretation of electrical transport measurements on polycrystalline materials is complicated by the fact that these are composed of crystalline grains separated from one another by grain boundary regions. Treatment of this problem was first reported by Volger[16] for the Hall effect. This basic model is shown in Fig. 4.14 and consists of cubic grains length ℓ_1, resistivity ρ_1 and carrier concentration n_1, surrounded by intergrain domains of width ℓ_2, resistivity ρ_2 and carrier concentration n_2.

To determine the resistivity, Hall coefficient and theremoelectric power of such a structure, the electric fields and currents in a unit cell comprising the regions labelled A, B and C in Fig. 4.14 are considered. This approach is basically the same as in the two-layer model and leads to the representation of the basic unit cell by an equivalent electrical network. The effective transport parameter for the overall system is determined by summing over all the unit cells in the sample. These expressions are complex functions of the ratios $\frac{\ell_2}{\ell_1}$ and $\frac{\rho_1}{\rho_2}$ and it is impossible to get specific information on the local regions. However if the intergrain regions are more resistive and thinner than the grain regions, that is ℓ_2/ℓ_1 and ρ_1/ρ_2 are both very much less than unity, the expressions do simplify a little. and are given by[16-20]:

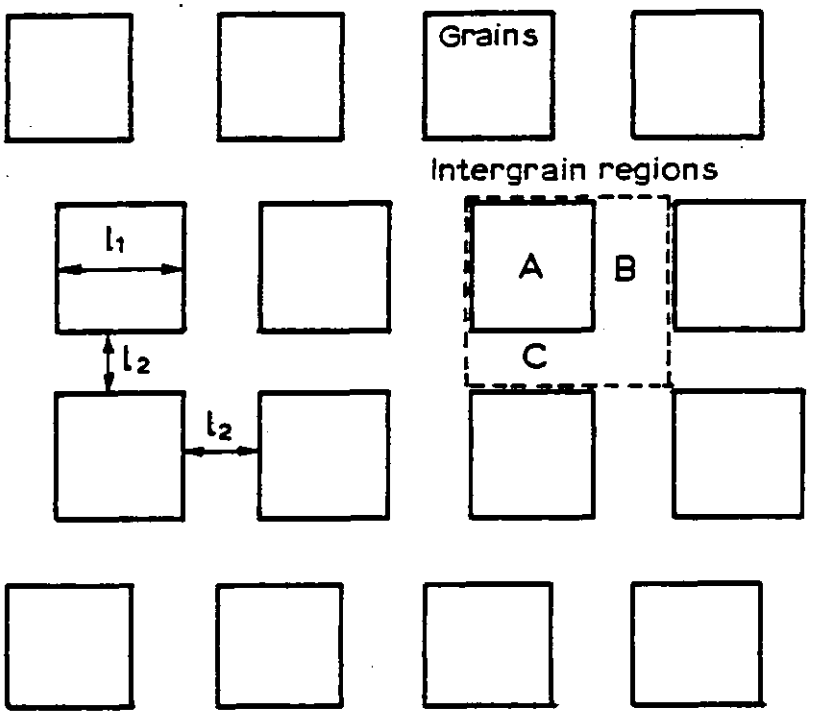

Fig. 4.14: The Volger Model of a Polycrystalline Material

$$\rho_T = \rho_1 + \rho_2 \left(\frac{\ell_2}{\ell_1}\right) \tag{4.34}$$

$$R_{HT} = R_{H1} + R_{H2} \left(\frac{\ell_2}{\ell_1} \frac{\rho_1}{\rho_2}\right) \tag{4.35}$$

$$S_T = S_1 + S_2 \left(\frac{\ell_2}{\ell_1}\right) \tag{4.36}$$

where the subscript T refers to the experimentally measured total transport parameter and subscripts 1 and 2 give the parameters at the grain and intergrain regions respectively.

Thus, if the above conditions are satisfied it is evident that the Hall effect in a polycrystalline sample will give the carrier concentration in the grain regions. Similarly, the thermoelectric power measurements will give the Seebeck coefficient of the grain regions only. The last statement effectively means that in the interpretation of thermoelectric measurements on polycrystals, only the prevailing carrier scattering in the bulk of the grains need be considered and that any additional scattering in the grain boundary region due, for example, to potential barriers, may be neglected.

In a polycrystalline semiconductor thin film, the intergrain domains may be taken to represent high resistance space charge regions. At the grain boundary, just as at the free surface of a crystal, there will be a high density of trapping states. Many of the charge carriers near the surface of the crystallite will become trapped at these sites and a depletion space-charge region will be set up. At each grain boundary there will be two such depletion regions, each extending into the bulk of the crystallite on each side of the intergrain boundary. This situation is represented, in an energy band diagram of an n-type semiconductor, by an upward bending of the conduction and valence band edges by an amount of $e\phi_0$, known as the barrier height (Fig. 4.15).

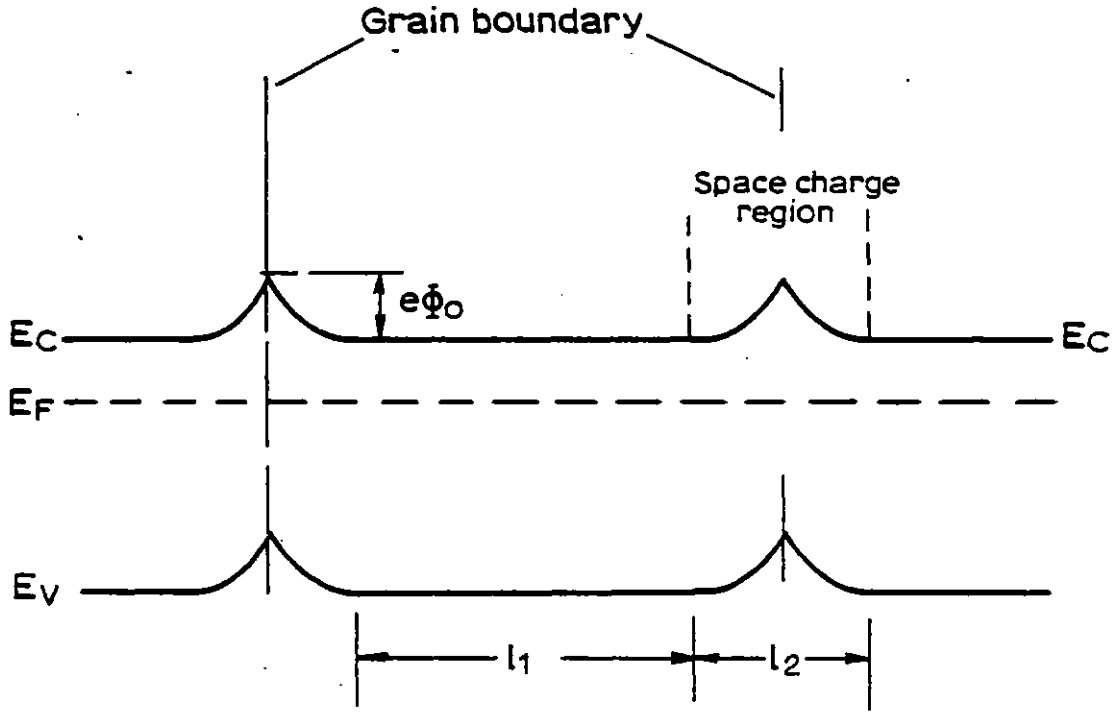

Fig. 4.15: Space Charge Regions due to Trapping at Grain Boundaries

As far as the polycrystalline model is concerned the width of the depletion regions will be equivalent to the intergrain width ℓ_2, and the undisturbed regions of the crystallite will be represented by the bulk grain of length ℓ_1.

In order to see whether the condition $\ell_2/\ell_1 \ll 1$ applies to $CuInSe_2$ films, the width of any space charge layer, ℓ_2, must be determined. This may not be known exactly but an estimate may be made by taking $\ell_2 \approx 2L_D$ where L_D is the effective Debye length for the semiconductor given by[21]:

$$L_D = \left[\frac{\varepsilon_0 \varepsilon_s \, kT}{e^2(n + p)}\right]^{\frac{1}{2}} \quad (m)$$

where ε_s is the static dielectric constant, n and p are the carrier concentrations in the conduction and valence bands.

For $CuInSe_2$ films, taking $\varepsilon_s = 13.6$[22] and T = 300K, ℓ_2 may be estimated to lie between 10-300Å for carrier densities in the range $10^{20} - 10^{17}$ cm^{-3}, which are typical of films in this work. As the grain size is approximately equal to the film's thickness, then the length ℓ_1 of the grains will be typically ~6000Å. It is thus clear that the width of any space charge region will be small compared to the grain dimensions so that the effect of the intergranular regions on the Hall and Seebeck effects of the $CuInSe_2$ films in this study may be neglected. In other words the Hall and Seebeck coefficient will be related to the carrier concentration inside the bulk grains.

4.3.3.2 Effective Mobility

So far nothing has been said about the mobility in polycrystalline semiconductors. This is usually obtained experimentally by a combination of the Hall effect and resistivity measurements on the polycrystalline sample.

In terms of equations (4.34) and (4.35)

$$\mu_T = \frac{R_{HT}}{\rho_T} = \frac{R_{H1} + R_{H2}\left(\frac{\ell_2}{\ell_1}\frac{\rho_1}{\rho_2}\right)}{\rho_1 + \rho_2\left(\frac{\ell_2}{\rho_1}\right)} \qquad (4.37)$$

for $(\frac{\rho_2}{\rho_1}\ \frac{\ell_2}{\rho_1}) \ll 1$ this can be approximated to

$$\mu_T = \frac{R_{H1}}{\rho_1+\rho_2(\frac{\ell_2}{\ell_1})}$$

and

$$\frac{1}{\mu_T} = \frac{1}{\mu_1} + \frac{1}{(\frac{n_2}{n_1}\ \frac{\ell_1}{\ell_2})\ \mu_2} \quad . \tag{4.38}$$

Equation (4.38) shows that the overall mobility in the polycrystalline semiconductor with thin and high resistivity intergrain regions will be determined by scattering in the bulk and in the integrain regions. Very often the bulk crystalline mobility is very high so that the mobility of the polycrystalline sample may be expected to be limited by the grain boundary regions.

The scattering mechanisms that are observed quite frequently in polycrystalline thin semiconductor films have been described by Anderson[23,24] and in general the film mobility, μ_T, will be given by Matthiesen's rule for different scattering mechanisms:

$$\frac{1}{\mu_T} = \frac{1}{\mu_c} + \frac{1}{\mu_s} + \frac{1}{\mu_D} + \frac{1}{\mu_{gb}} + \frac{1}{\mu_B} \tag{4.39}$$

where μ_c is the crystallite bulk mobility, μ_s is mobility due to surface scattering, μ_D is the dislocation scattering mobility, μ_{gb} is the grain boundary mobility and μ_B is the potential barrier limited mobility. Each of these will now be briefly introduced.

4.3.3.2(a) Surface Scattering

In a thin film the effect of the external surfaces will be important and a carrier approaching this region will be scattered such that the velocity component parallel to the surface may be altered.

Anderson[23] has shown that for the case of a semiconductor with flat bands at the surface, the surface scattered mobility, μ_s, can be written as

$$\mu_s = \frac{\mu_c}{1 + (\frac{2\lambda}{d})} \tag{4.40}$$

where μ_c is the bulk crystal mobility and d is the thickness of the film, λ is the mean free path of the carriers given,for non-degenerate semiconductors, with lattice scattering by[18]

$$\lambda = (\frac{m_c\ kT}{2\pi e^2})^{\frac{1}{2}}\ \mu_c \tag{4.41}$$

For degenerate statistics this becomes[23]:

$$\lambda = (\frac{3n}{8\pi})^{1/3}\ (\frac{m_c}{m_d})\ \frac{\mu_c}{d} \tag{4.42}$$

where m_c is the conductivity effective mass and m_d is the density of states effective mass, n is the carrier concentration.

The mobility of carriers in a thin film will be thus reduced by surface scattering when the mean free path of the carriers becomes comparable to the film thickness.

4.3.3.2(b) Dislocation Scattering

In general thin films tend to have a much larger concentration of crystal defects than bulk crystals and in this respect a high density of dislocations may be expected.

The effect of dislocation scattering has been discussed by Dexter et al[25], which assume that dislocations distort the crystalline lattice thus giving rise to a scattering (deformation) potential.

The dislocation limited mobility is given by:

$$\frac{1}{\mu_D} = \frac{3\pi^2}{16} \frac{E^2 b^2 m_c N}{h_e kT} \left(\frac{1-2v}{1-v}\right)^2 \quad (4.43)$$

where E is the deformation potential, b is Burger's vector, N is the density of dislocations per unit area and v is the Poisson ratio of the material. The dislocation mobility has a T' dependence on temperature whilst being inversely proportional to the density of dislocations. This means that at low enough temperatures and with a sufficiently high number of dislocations the mobility may become comparable to other scattering mechanisms.

4.3.3.2(c) Grain Boundary Scattering

In polycrystalline films the grain boundaries are regions of lattice mismatch and may act as scattering centres for carriers being transported from grain to grain. The physical interruption of carrier transport may be taken into account by allocating to the charge carriers a mean free path, λ_g, which is approximately half the distance between boundaries.

The grain boundary limited mobility is given for a non-degenerate semiconductor by[23]:

$$\mu_{gb} = e\lambda g \left(\frac{9\pi}{8} m_c kT\right)^{-\frac{1}{2}} \quad (4.44)$$

For a degenerate semiconductor this becomes

$$\mu_{gb} = \frac{e\lambda g}{h} (3\pi^2 n)^{-1/3} \left(\frac{m_d}{m_c}\right)^{\frac{1}{2}} \quad (4.45)$$

where n is the carrier density, m_c and m_d are the conductivity and density of states mass.

Grain boundary scattering has a $T^{-\frac{1}{2}}$ temperature dependence for classical semcionductors and is temperature independent in degenerate semiconductors.

4.3.3.2.(d) Potential Barrier Scattering

In this model depletion regions around the grain boundaries are assumed to give rise to Schottky type potential barriers. When an electric field is applied across such a barrier it increases the band bending on one side while reducing it on the other side of the boundary as shown in Fig. 4.16. Carriers cross the grain boundaries by a thermionic emission process and a current density across the barrier may be written as[24]:

$$J = J_2 - J_1 = J_o \left[\exp\left(\frac{eV_2}{kT}\right) - \exp\left(-\frac{eV_1}{kT}\right)\right] \tag{4.46}$$

where J_o is the equilibrium current density given by[24,26]:

$$J_o = en_c \left(\frac{kT}{2\pi m}\right)^{\frac{1}{2}} \exp\left[-\frac{e\phi_o}{kT}\right] \tag{4.47}$$

in which n_c is the carrier concentration of the crystallites.

If the voltage applied across the barrier $V_B = V_1 + V_2$ is small then the current density across the barrier may be written as

$$J = J_o \frac{eV_B}{kT} \tag{4.48}$$

This leads to the definition of potential barrier limited mobility so that:

$$\mu_B = \mu_o \exp\left[-\frac{e\phi_o}{kT}\right] \tag{4.49}$$

where

$$\mu_o = \frac{eL}{(2\pi m_c kT)^{\frac{1}{2}}} \tag{4.50}$$

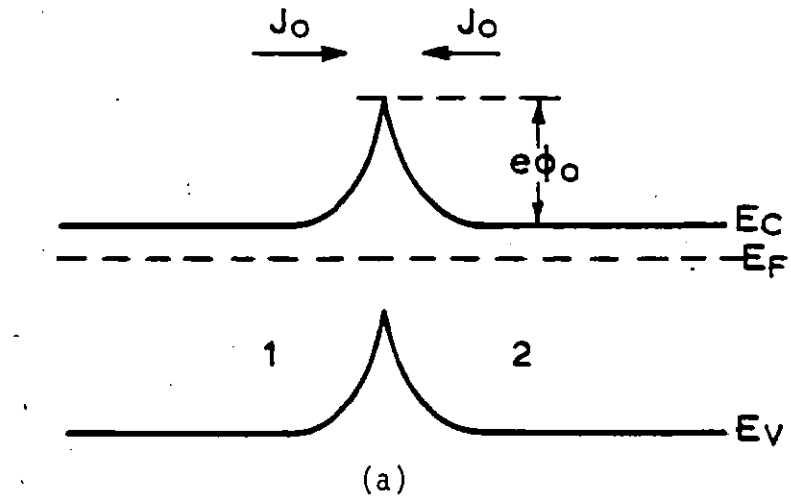

(a)

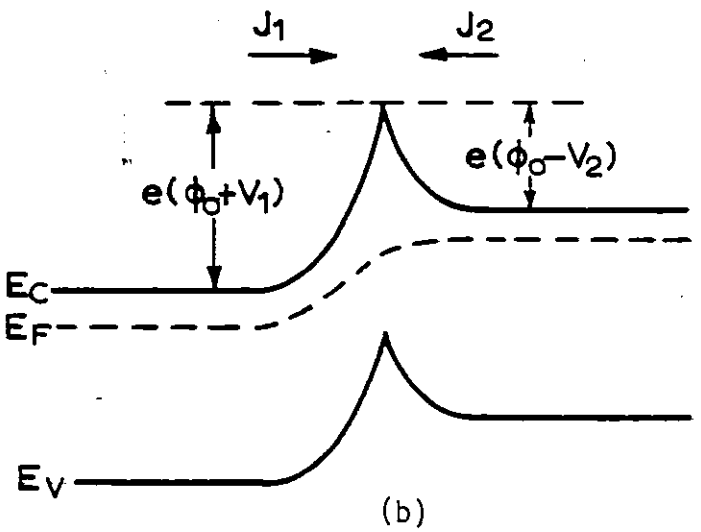

(b)

Fig. 4.16: Potential Barriers at a Grain Boundary for a Non-degenerate Semiconductor

(a) With no Applied Voltage

(b) With Applied Voltage

μ_o has units of mobility and L is the grain size of the polycrystalline film. The barrier limited mobility is thus typified by an exponential increase of mobility with increase in temperature, with the activation energy related to the band bending of the grain boundaries.

At this stage it should be pointed out that the usual potential barrier mobility, as described above, applies strictly to semiconductors obeying classical statistics and in which the barriers are higher than a few kT

If the semiconductor has a degenerate carrier population, then equations (4.49) and (4.50) will not be valid and a modified expression must be used. To do this, the Richardson-Dushmann expression for thermionic emission current must be considered and this is given by[26,27]:

$$J_o = \frac{e4\pi mk^2T^2}{h^3} \exp[-(\frac{e\phi_o - E_F}{kT})] \qquad (4.51)$$

Here $e\phi_o$ is the energy at the top of the barrier and E_F is the Fermi energy, both measured with respect to the bottom of the band. The thermionic current is derived under the assumption that $e\phi_o - E_F \gg$ 2-3 kT and $e\phi_o - E_F$ represents the work function, if emission from metals is considered, whilst $e\phi_o - E_F$ is the effective barrier height if thermionic emission from semiconductors is considered.

In a semiconductor, the thermionic emission current is independent of carrier density. For convenience in calculating mobility, this may be introduced using equation (4.22a) namely:

$$n = \frac{2}{\sqrt{\pi}} N_c F_{\frac{1}{2}}(\eta)$$

Combining this with equation (4.51) one obtains for the arbitrary degeneracy case:

$$J_o = \frac{n_e}{2} (\frac{kT}{2m})^{\frac{1}{2}} \frac{\exp[E_F/kT]}{F_{\frac{1}{2}}(E_F/kT)} \exp[-e\phi_o/kT] \qquad (4.52)$$

and this leads to a potential barrier limited mobility of the form:

$$\mu_B = \mu_o \exp[-e\phi_o/kT]$$

where

$$\mu_o = \frac{eL}{(8mkT)^{\frac{1}{2}}} \frac{\exp[E_F/kT]}{F_{\frac{1}{2}}(E_F/kT)} \qquad (4.53)$$

It should be noticed that equation (4.53) is a general expression and that if the semiconductor obeys Boltzmann statistics then as $[E_F/kT] \ll 0$, $F_{\frac{1}{2}}(E_F/kT) \rightarrow \frac{\pi^{\frac{1}{2}}}{2} \exp[E_F/kT]$ and the mobility reduces to the usual forms of equations (4.49) and (4.50).

It is apparent from the above expression that, if the Fermi level is located inside the conduction band of a degenerate semiconductor, then the effective barrier for crossing over the grains is now $e\phi_1$ as shown in Fig. 4.17.

The distinction between degenerate and non-degenerate conditions for thermionic emission over potential barriers is very important and has been overlooked in the literature. For example, for polycrystalline silicon films having a carrier density of 5×10^{19} cm^{-3}, Seto[28] has reported a potential barrier height of 0.005 eV. Similarly, Saitoh et al[29] have determined a barrier height of 0.007 eV for polycrystalline InP thin films having an electron density of 3×10^{19} cm^{-3}. Using the respective density of states masses, it can easily be shown that these two examples correspond to cases where the carrier population is degenerate, with the Fermi level positioned inside the band. No attempt was made to take this into consideration and the barrier limited mobility expression applicable to non-degenerate cases was used. Furthermore, the small barrier heights correspond to ~0.2 kT at room temperature and so are in direct violation of the requirement that the barrier height must be at least ~2 kT if thermionic emission over barrier is to hold.

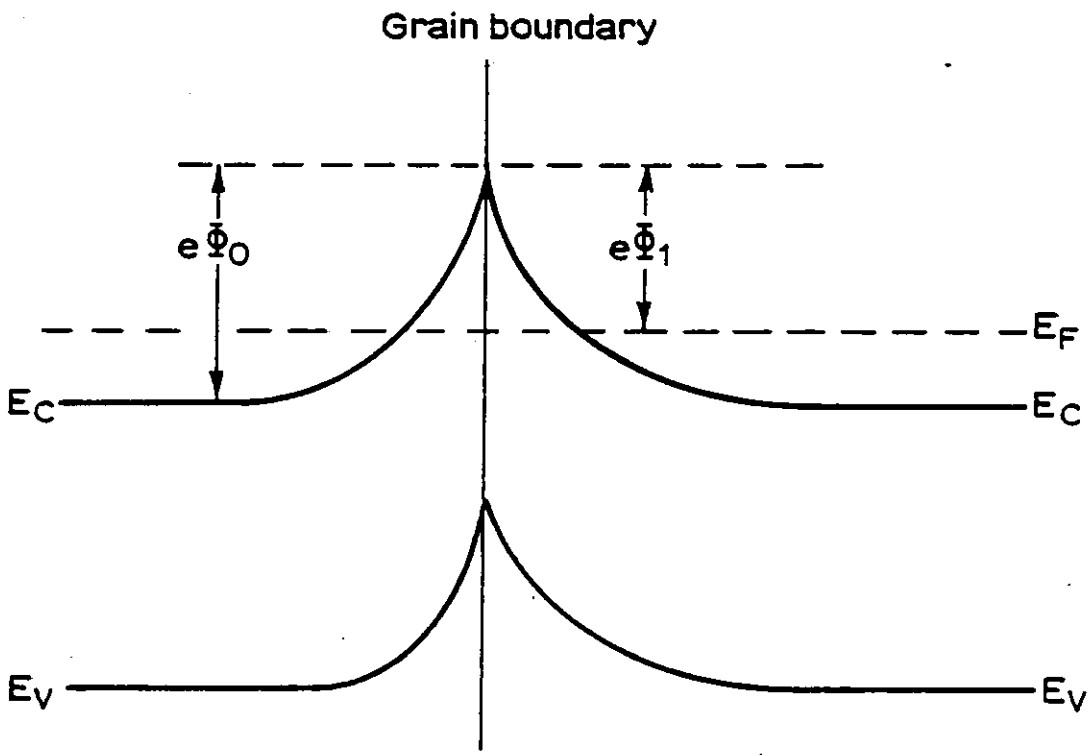

Fig. 4.17: Potential Barriers at a Grain Boundary for a Degenerate Semiconductor

The above discussion indicates that if a thin film sample is characterised as degenerate, then strictly speaking equation (4.53) must be used instead of the usual equation (4.50) for fitting the experimental mobility to a potential barrier model. Perhaps if such a procedure had been used by Seto and Saitoh et al, then a more sensible barrier height would have been obtained.

4.4 ELECTRICAL PROPERTIES OF FILMS

4.4.1 Experimental Details of Electrical Measurements

The physical shape and dimensions of the samples used for the electrical measurements was that of a double cross structure shown in Fig. 4.18. The length to width ratio was designed to be greater than 2.5, so that any reduction of the Hall voltage due to electrostatic shorting of the Hall field by the current electrodes was avoided[14].

Initial attempts to use permanent evaporated metal contacts were unsuccessful because electrical measurements on films subjected to heat treatments were very variable and unrealiable. However by using fresh contacts on already annealed films the measurements could be performed quite well. Obviously the electrical contacts deteriorated during the anneal stage, presumably due to interdiffusion effects. Since the advantage in laying metal contacts in the same pump down as in the deposition of fresh $CuInSe_2$ films was lost it was decided to use 'Silver Dag' as the contact material. This highly conducting paste has been reported to give good ohmic contacts to $CuInSe_2$[30,31] and was found, in this investigation also, to be highly satisfactory. Besides the ease of application, this metal paint had also the advantage of being easily removed prior to any heat treatment of the films.

All electrical measurements were carried out in the dark and, for the room temperature resistivity and Hall effect measurements, the experimental slide was placed on a sample holder fixed inside a cast aluminium

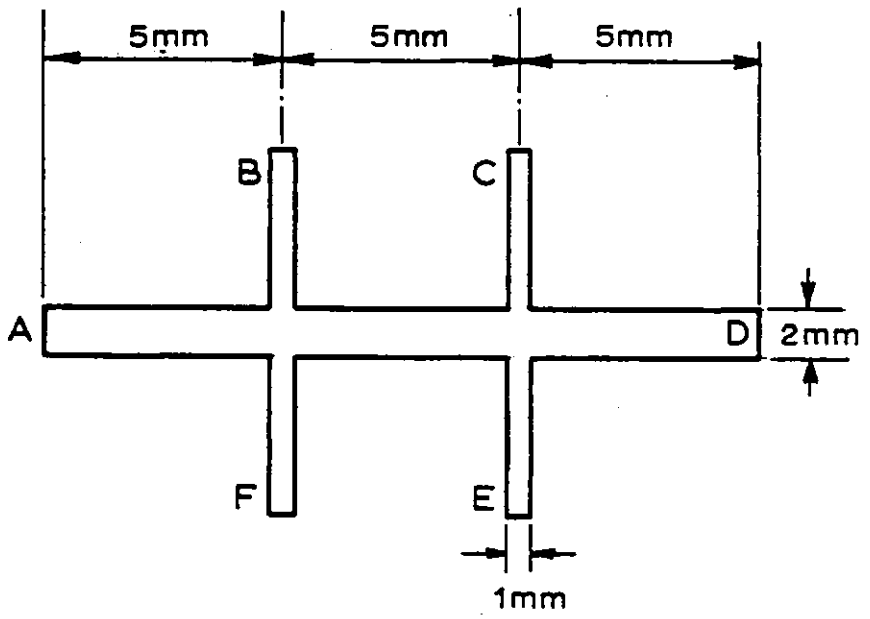

Fig. 4.18: Sample Geometry for Electrical Transport Measurements

box. For the measurement of the Hall coefficient the box was placed between the poles of a powerful electromagnet capable of supplying a field up to 1 tesla.

A constant D.C. current, typically 1-10 μA, as supplied by a Keithley 616 Electrometer, operating in the resistance mode, was passed between contacts A and B of the specimen. The conductivity voltages V_{BC} and V_{FE} were measured with a Daltron Digital Voltmeter, having an input impedance greater than 10^{10} Ω. Such a high input impedance was good enough to avoid significantly affecting readings. The Hall voltages between probes BF and CE were measured a few times for various current and magnetic field direction across the sample. This procedure was adopted in order to eliminate the effect of the offset voltage due to misaligned electrodes and any other thermomagnetic voltages that were invariably present.

The measurement of the Seebeck coefficient relied on the principle that if two conductors A and B are joined to form the junctions P and Q at temperatures T_1 and T_2 respectively (Fig. 4.19a), then the open circuit voltage V_o, measured between terminals C and H is given by:

$$V_o = \int_{T_1}^{T_2} (S_A - S_B) dT$$

Here S_A and S_B are the Seebeck coefficients of the two materials and usually A represents the semiconductor whose thermoelectric power is to be measured.

If the temperature across the two junctions, $\Delta T = T_2 - T_1$, is kept very small then the thermoelectric power of the materials A and B is given by:

$$S_A - S_B = \frac{V_o}{\Delta T} \qquad (4.54)$$

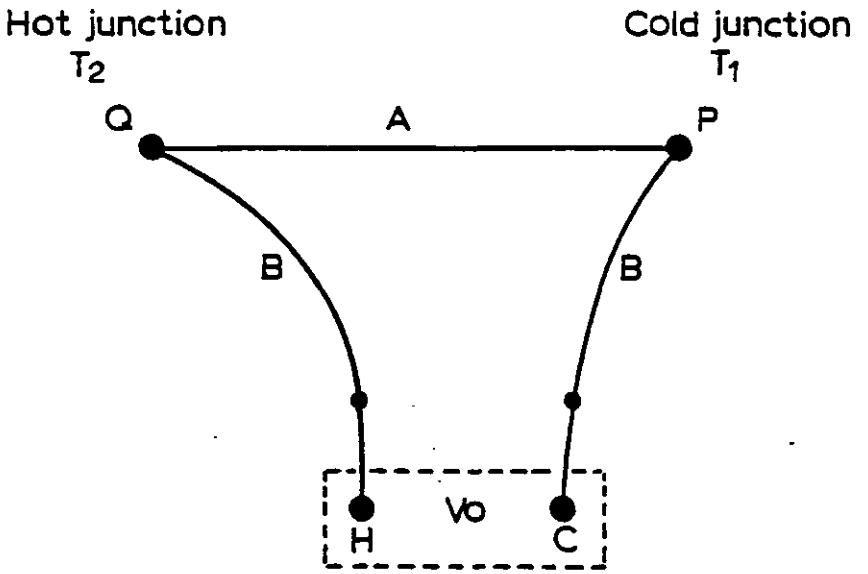

Fig. 4.19(a): Circuit Containing Two Junctions P and Q of Two Materials A and B for Measuring Thermoelectric Power

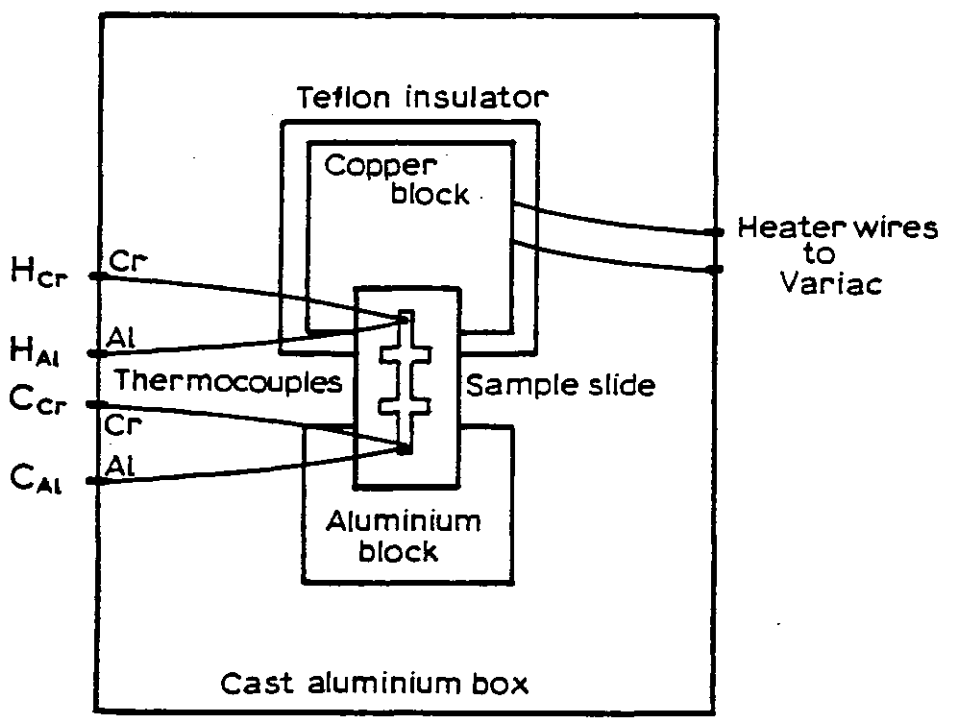

Fig. 4.19(b): Apparatus for Room Temperature Thermoelectric Power Measurements

Thermoelectric power measurements at room temperature were performed using the apparatus shown in Fig.(4.19b).

A solid, aluminium block was fixed directly to the base of a cast aluminium box, which acted as an infinite heat sink and also permitted measurements to be performed in the dark. This aluminium slab maintained one end of the semiconductor sample at room temperature. A solid copper block, having a small heater embedded in it, was used to warm the other end of the sample. This slab was placed approximately a centimetre away from the aluminium block and was thermally insulated from the enclosing box by a thick piece of Teflon.

The experimental slide was placed across the two blocks and fixed securely at the two ends to ensure good thermal contact. Two thin Chromel-Alumel thermocouples welded electrically so that their junctions were in the form of a small ball were used as the thermal probes. These were fixed on the semiconductor surface via a very small blob of silver paint which provided good thermal and electrical contact.

The measurements were performed after a steady state was reached and typically the temperature difference between the two ends of the sample was less than 3K. The thermal probes gave rise to four thermoelectric potentials. The terminal pairs H_{Cr}, H_{Al} gave the hot end temperature T_H, the pair C_{Cr},C_{Al} gave the cold end temperature, T_c. The pair C_{Cr} H_{Cr} gave the thermoelectric potential V_{Cr} developed across the semiconductor and the chromel wire and finally the pair C_{Al} H_{Al} gave the thermoelectric potential V_{Al} of the semiconductor and the alumel wire. The thermoelectric power of the semiconductor S_{Sc}, at a mean temperature $T = \frac{T_H+T_C}{2}$ is[32]:

$$S_{Sc} = S_{Cr} + \frac{V_{Cr}}{T_H-T_C} \qquad (4.55)$$

$$S_{Sc} = S_{Al} + \frac{V_{Al}}{T_H-T_C} \qquad (4.56)$$

In the above equations the sign of the voltages V_{Cr} V_{Al} is taken, by convention, to be the sign of the potential of the cold junction. In other words the cold end of the sample is connected to the positive terminal of the voltmeter.

S_{Cr} is the absolute thermoelectric power of chromel which is +21.5 μV K^{-1} at room temperature. Similarly S_{Al} is the absolute thermoelectric power of alumel which is -18.5 μV K^{-1} at room temperature. If equation (4.55) is subtracted from equation (4.56) then

$$\frac{1}{T_H - T_C} = \frac{S_{Cr} - S_{Al}}{V_{Al} - V_{Cr}} = \frac{40}{V_{Al} - V_{Cr}} \qquad (4.57)$$

Substituting equation (4.57) into equations (4.55) and (4.57) the thermopower at room temperature can be conveniently obtained from

$$S_{Sc} = \frac{40\ V_{Cr}}{V_{Al} - V_{Cr}} + 21.5 \qquad (4.58)$$

$$S_{Sc} = \frac{40\ V_{Al}}{V_{Al} - V_{Cr}} - 18.5 \qquad (4.59)$$

The temperature dependences of the transport parameters were measured in a stainless steel cryostat. This was evacuated to a vacuum better than 10^{-3} torr, using a small air cooled Edwards diffusion pump system, in order to minimise the problem of water condensation on the samples at very low temperatures. The schematic view of the cryostat is shown in Fig. 4.20. Here a large and thick copper block acted as the sample holder. This slab was connected to a protruding copper 'cold finger' which could be immersed in a dewar containing liquid nitrogen thus enabling the cooling of the sample. The copper slab also contained a heater controlled by a Stanton-Redcroft Model 681 temperature controller. A platinum resistance thermometer inserted inside the copper block acted as the feedback control and allowed any particular temperature setting to be held constant with a

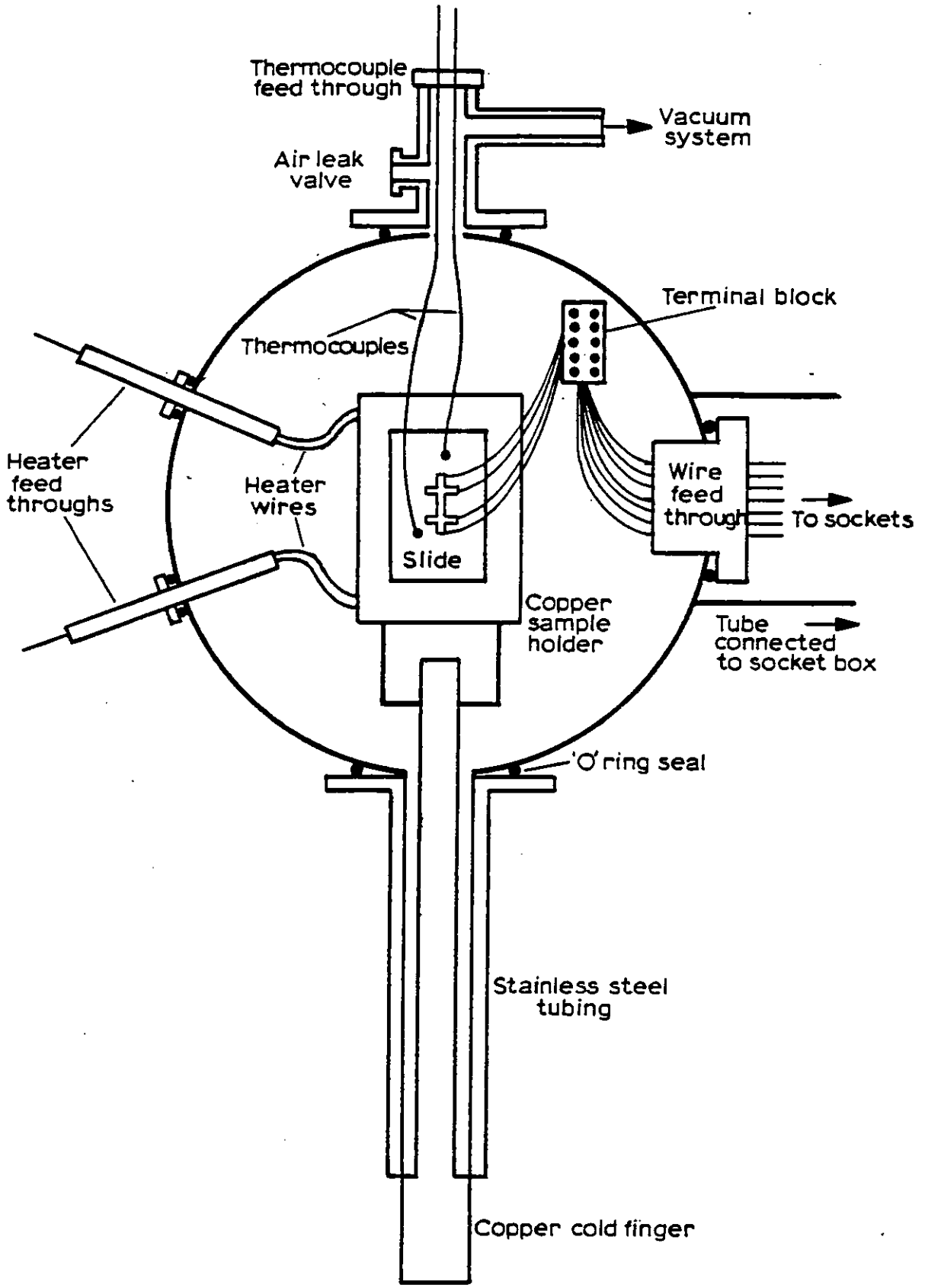

Fig. 4.20: Schematic Drawing of the Cryostat

maximum fluctuation of ± 0.5K. The samples could also be cooled and heated at controlled rates of 1K/min to 15K/min.

The sample slides were placed in good thermal contact with the sample holder using 'Silver Dag'. The temperature of the sample was monitored by means of a chromel-alumel thermocouples stuck in the vicinity of the double-cross structure and any temperature gradient across the sample was found to be less than 2K. The thermocouples were not broken at the air-vacuum feed-through. This was in order to minimise errors in the readings due to any thermal emf's generated at the interface. Araldite was used to form the necessary vacuum seal at the feed-through. The semiconductor sample was connected to external instrumentation via a terminal block connected to copper wires going through another vacuum feed-through.

4.4.2 Room Temperature Electrical Properties

4.4.2.1 As-deposited Films

The room temperature electrical properties of some films deposited on cold substrates and prior to annealing are given in Table 4.1.

Sample	Thickness Å	Resistivity (Ω-cm)	Thermopower ($\mu V\ K^{-1}$)	Carrier Concentration (cm^{-3})	Hall Mobility ($cm^2V^{-1}s^{-1}$)
MC53	7467	8.22×10^{-4}	+6	3.05×10^{21}	2.47
MC55	6696	7.56×10^{-4}	+7.2	6.88×10^{21}	1.18
MC56	7500	8.40×10^{-4}	+9.3	2.9×10^{21}	2.65
MC62	2788	5.11×10^{-4}	+2.4	5.14×10^{21}	2.32
MC67	7025	1.31×10^{-3}	+4	3.19×10^{21}	1.49

Table 4.1: Room temperature properties of as-deposited $CuInSe_2$ films

All these films were p-type as verified by thermopower and Hall measurements. They were all characterised by very high carrier concentrations in the 10^{21}-10^{22} cm^{-3} region. These high values of p and the very low values of Seebeck coefficient are typical of metals. Indeed, the carrier concentration and resistivity as a function of temperature, demonstrates the metallic type conduction quite well. In Fig. 4.21a it is evident that the carrier concentration does not vary over the temperature range investigated. The resistivity,(Fig. 4.21b), shows on the other hand a monotonic increase with temperature rise over the same temperature range. The temperature dependence of resistivity was $\rho \propto T^m$ where m = 0.7-0.9. This variation of resistivities is very similar to metals in which thermal scattering gives rise to a $\rho \propto T^1$ dependence[33].

The electrical properties of these as-deposited films must be discussed in the light of their structural characteristics. It must be recalled that these films are stratified prior to any heat treatment. The X-ray and electron diffraction analyses and the evaporating characteristics of $CuInSe_2$, had suggested the presence of In_2Se, $CuInSe_2$ and Cu_3Se_2. It is therefore expected that the overall electrical properties of the as-desposited films will be given by the parallel combination of the electrical conductivities, Hall coefficient and thermopower of each layer present. In other words a multilayer model, similar to the simple two-layer model described in section 4.3.2, but containing more complicated expressions due to extra terms,will be needed to express the measured overall transport parameters. However the comments on the two-layer model will still be applicable here. If one of the layers has a conductivity very much higher than the rest, then it will dominate the overall electrical characteristics.

If the room temperature electrical data of the various elements and compounds in the Cu-In-Se system are compared, then one can identify the layer or layers that give rise to the observed electridal properties.

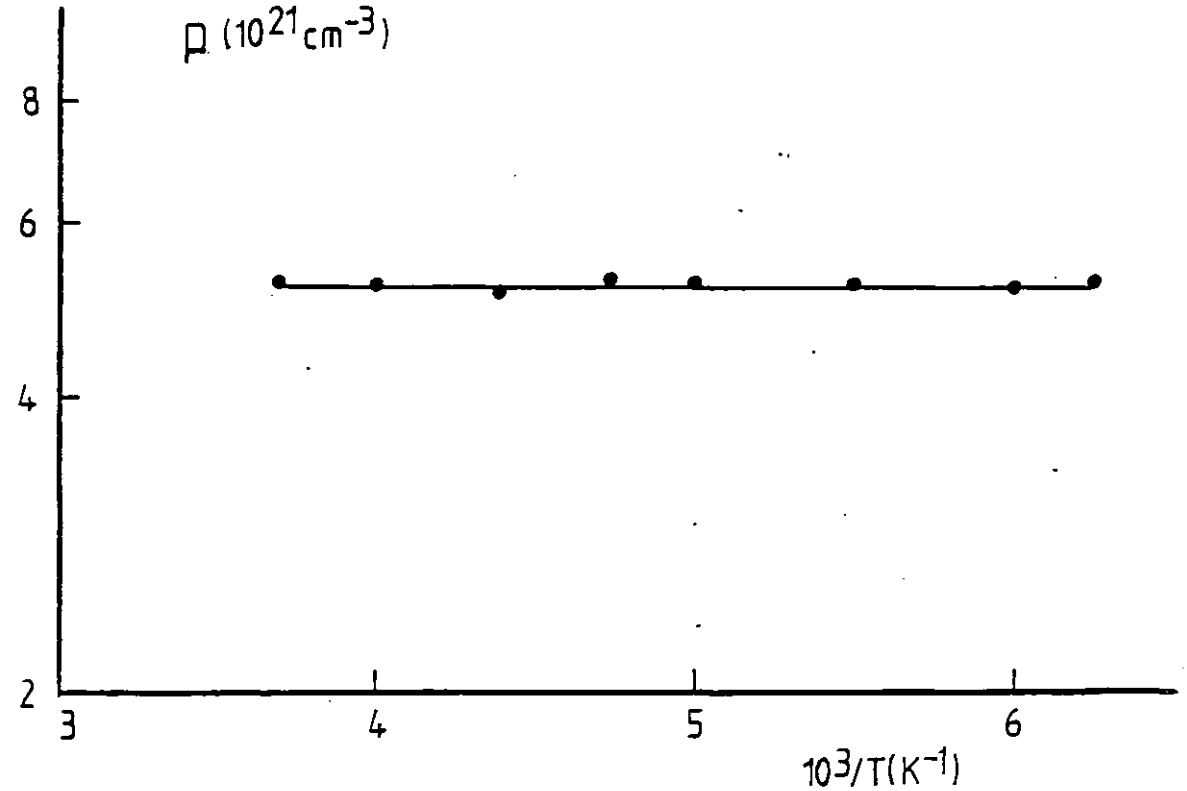

Fig. 4.21(a): Carrier Concentration as a Function of Temperature for an Unannealed $CuInSe_2$ Film

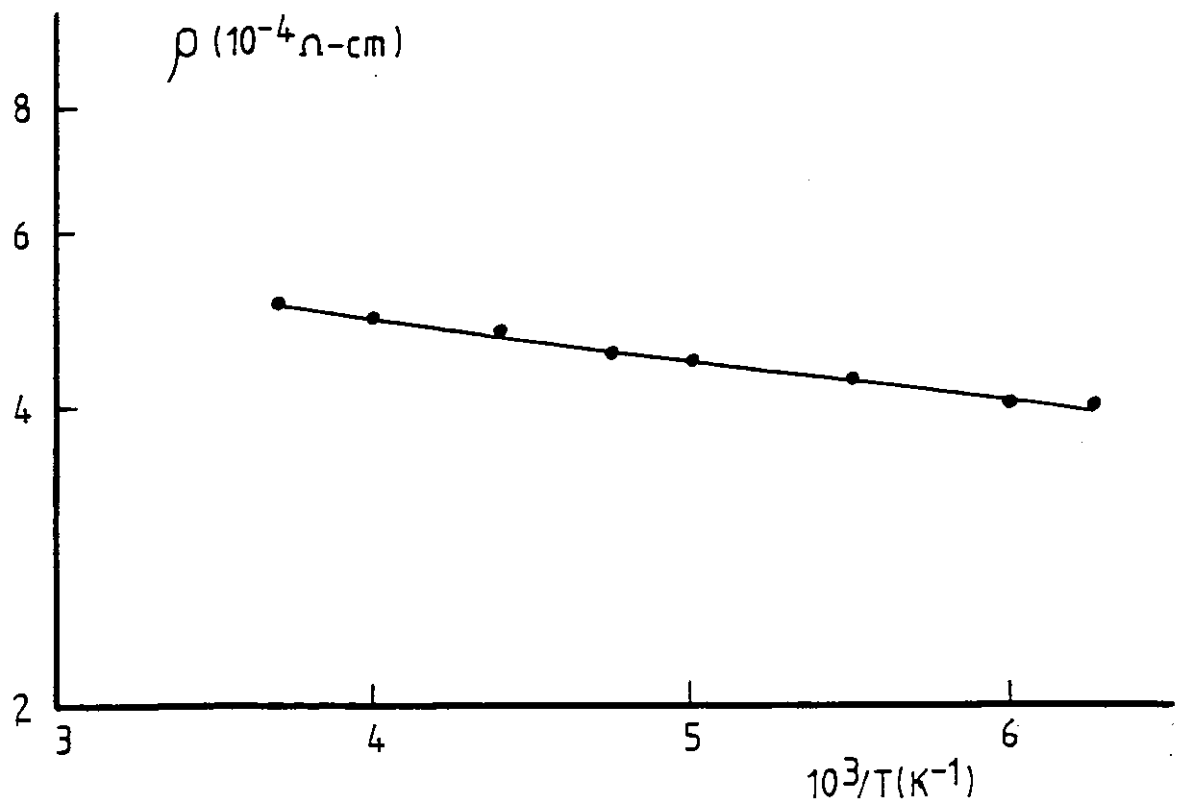

Fig. 4.21(b): Resistivity as a Function of Temperature for an Unannealed $CuInSe_2$ Film

Since the films are overall p-type conducting, then it is expected that the dominant layer must also be a p-type conductor.

All the In-Se compounds are n-type semiconductors and in this respect will not contribute to the overall properties[36]. Selenium which is a p-type semiconductor might be a suitable candidate but it can be dismissed on the grounds that it has resistivity orders of magnitude higher than the measured values[35]. Copper also has a positive thermoelectric power of +1.8 $\mu V\ K^{-1}$ at room temperature[36] with a typical resistivity of $\sim 10^{-6}\ \Omega$ cm[37] but these values are too low to account for the observations. The resistivity of $CuInSe_2$ will be shown later to be at least an order of magnitude higher than the as-deposited films and so will not dominate the properties of the unannealed layers.

This thus leaves the compound Cu_3Se_2, whose presence was confirmed by X-ray diffraction and electron diffraction as the layer that must give rise to the observed electrical properties of the unannealed films. Unfortunately no electrical data was found for Cu_3Se_2 in the literature. However CuSe, another compound in the Cu-Se system, is reported to be a p-type conductor with resistivity of $\sim 10^{-5}\ \Omega$ cm and thermopower of +69 $\mu V\ K^{-1}$ [38]. Also $Cu_{2-x}Se$ is a p-type semiconductor[39,40] with resistivities in the range 10^{-4} - $10^{-3}\ \Omega$ cm and hole concentration of 10^{21} - $10^{22}\ cm^{-3}$. These values would suggest that Cu_3Se_2 having a composition between $Cu_{2-x}Se$ and CuSe, is very likely to be also a p-type conductor with electrical properties similar to those observed in the unannealed $CuInSe_2$ layers.

4.4.2.2 Films Annealed at 350°C for 3 hours

A few as-deposited films which were subjected to a low temperature (150°C) nitrogen anneal for 3 hours showed little change in their electrical properties. It was observed that, on average, the resistivity of the films increased by about 1.5 times. The thermoelectric power showed a smaller increase and remained positive. X-ray and electron diffraction analyses had

indicated that $CuInSe_2$ started to become the major phase in these films and so the slight changes in the electrical properties towards semiconducting behaviour can be attributed to this effect.

Substantial changes in the electrical properties were observed, after films were heat treated at 350°C for 3 hours and these changes coincided with the conversion of stratified layers into a homogeneous $CuInSe_2$ phase. All but three of the films which underwent the above anneal retained the as-deposited majority carrier type and remained p-type as verified by thermopower measurements.

The Hall effect in most of these p-type films was not observed for the normal supply currents used, indicating that the Hall coefficients were very small. Attempts to use higher supply currents resulted in the drift of readings, very probably due to Joule heating effects in the specimens and only an estimate of the upper limit of the Hall coefficient could be made with these samples. However, since the thermoelectric power could be measured, this was used to obtain their carrier concentrations.

From equation (4.24b) it is evident that, in order to convert thermopower to carrier concentration, the dominant scattering mechanism and the density of states mass of the carriers must be known at the temperature of the measurement. The general procedure is to use the Seebeck formula for arbitrary degeneracy, equation (4.20), and determine the reduced Fermi energy, η, from the experimental thermoelectric power. This value of η can then be used in equation (4.22b) to obtain carrier concentration providing the density of states N_v is known. Of course if the Fermi level is determined to be well away from the bottom of the band, then the non-degenerate formula of equation (4.24b) will be used directly.

The density of states effective mass for holes has been reported to be $0.73\ m_o$ [41,42] for $CuInSe_2$, but as the dominant scattering mechanism at room temperature is not known in our thin film samples, the carrier

concentrations were initially calculated assuming acoustic lattice scattering. The validity of this procedure was then tested on a few samples where thermoelectric power and Hall effect measurements were possible. In all cases, the carrier concentration as obtained from thermoelectric effect was an order of magnitude higher than the carrier density determined from the Hall effect. The two measurements can be made to agree by changing either the type of scattering mechanism assumed or the value of effective mass in the formulae. In the first instance, if the value of 0.73 is kept in the calculations then the scattering mechanism must have a relaxation time with energy dependent E^{-S} such that $S > \frac{5}{2}$. In this case the Fermi integrals diverge and formula of equation (4.20) is not valid[6] and it is not possible to proceed further. Alternatively if the acoustic lattice mechanism was assumed to be dominant in the films, then an effective mass of 0.38 mo is required to bring Hall and thermopower effects into agreement.

The carrier concentration of the p-type films, whose Hall coefficient could not be measured, was thus determined by the latter procedure. In order to check the validity of this, the thermopower carrier concentrations were compared with the values estimated from the Hall effect. This is given in Table 4.2 where it is evident that the agreement between the two methods is very good.

The room temperature electrical properties of $CuInSe_2$ films after a standard 350°C anneal in nitrogen for 3 hours are shown in Table 4.3. As stated previously most samples were low resistivity p-type. However, due to variations, there were some samples which had higher resistivities and some which were n-type after the anneal. The EPMA analyses of all the films, irrespective of their electrical properties, were essentially similar although very slight compositional changes do appear to occur from time to time. Nevertheless the preparation method adopted can be considered to be reproducible because p-type $CuInSe_2$ films having carrier concentrations around 10^{20} cm^{-3} with resistivities in the range 10^{-2}-10^{-1} Ω cm could be

Sample	Carrier Concentration Calculated from Thermopower (cm^{-3})	Carrier Concentration from Hall effect (cm^{-3})
MC53	8.8×10^{16}	1.2×10^{17} measured
MC54	4.51×10^{16}	2.7×10^{16} measured
MC62	1.06×10^{21}	1.3×10^{21} measured
MC56	1.22×10^{20}	$> 2 \times 10^{20}$ estimated
MC65	6.73×10^{19}	$> 5 \times 10^{19}$ estimated
MC68	1.02×10^{20}	$> 6 \times 10^{20}$ estimated
MC66	3.39×10^{20}	$> 4 \times 10^{20}$ estimated
MC59	6.11×10^{20}	$> 7 \times 10^{20}$ estimated
MC61	4.95×10^{20}	$> 1 \times 10^{21}$ estimated
MC60	8.36×10^{20}	$> 8 \times 10^{20}$ estimated

Table 4.2: Comparison of carrier concentration obtained from thermopower and Hall effect measurements of films annealed at 350°C.

Sample	Thickness (Å)	Resistance (Ω cm)	Thermopower ($\mu V\ k^{-1}$)	Carrier Concentration cm^{-3}	Mobility $cm^2\ V\ s^{-1}$
MC69	7050	7×10^{-2}	-3	5.94×10^{19}	1.5
MC67	7025	1.35×10^{-1}	-10	6.33×10^{18}	7.30
MC63	6425	1.93×10^{-1}	-18.5	5.75×10^{18}	5.62
MC54	5966	4.69×10^{-1}	+592	2.70×10^{16}	4.5
MC53	7467	3.42×10^{-1}	+508	1.20×10^{17}	1.2
MC56	7500	2.5×10^{-1}	+31.5	1.22×10^{20}	0.21
MC65	6175	2.96×10^{-1}	+47	6.73×10^{19}	0.31
MC68	2338	1.86×10^{-1}	+33	1.02×10^{20}	0.33
MC66	7625	1.75×10^{-1}	+18	3.39×10^{20}	0.12
MC61	2775	4.9×10^{-2}	+12.2	4.95×10^{20}	0.26
MC59	5100	4.4×10^{-2}	+10.6	6.11×10^{20}	0.23
MC60	3933	3.92×10^{-2}	+8.6	8.36×10^{20}	0.19
MC62	2788	1.89×10^{-2}	+7.3	1.06×10^{21}	0.31
MC74	4810	5.09×10^{-2}	+7.7	9.87×10^{20}	0.12
MC76	4920	6.92×10^{-2}	+8.4	8.66×10^{20}	0.10

Table 4.3: Room temperature properties of homogeneous $CuInSe_2$ films

obtained consistently. Films with similar properties were also obtained when deposited directly onto hot substrates at 250°C and for completeness typical hot substrate samples MC74 and MC76 are also given in Table 4.3.

The reason why most of the $CuInSe_2$ films prepared in this study are p-type must be associated with the intrinsic defect population in the films. In this respect an excess of selenium, a deficiency of copper or indium will be expected to act as acceptors. The films were compositionally selenium rich and copper deficient and so this may be the cause of the p-typeness of these films.

The fact that some n-type $CuInSe_2$ films were also prepared indicates either a slight loss of selenium and/or the introduction of a slight excess copper or indium into the films. At this stage it will be appropriate to look into how these unintentionally doped n-type films could have arisen.

The loss of selenium during deposition is one likely possibility. It must be recalled that, during evaporation of $CuInSe_2$ powders, the vapour at some stage contains a fair amount of selenium molecules. If some of this volatile element re-evaporated from the substrate during a particular run, then this would explain the n-typeness. However the re-evaporation of selenium would be expected to be more likely from hot substrates than cold substrates. The fact that single phased $CuInSe_2$ films, deposited onto substrates at 250°C were still p-type,indicates that re-evaporating of selenium cannot explain the n-type characteristics of some films.

It is thought that the incorporation of a slight excess of copper into the films offers a more reasonable explanation. The small amount of Cu needed to dope the films n-type can come from the second phase Cu_3Se_2 precipitates present in the evaporating powder charge. During the pre-soak temperatures the selenium associated with the copper selenide will be evaporated onto the shutter, leaving behind excess copper. The evaporation of this Cu at the higher temperatures would thus result in slight increase

in copper concentration and lead to n-type films. This will only operate when the charge contains sufficient Cu_3Se_2 for the effect to occur.

4.4.2.3 Films Annealed at 350°C for Prolonged Times

The room temperature electrical properties of the films as a function of further anneal time at 350°C have been investigated, to check whether they could be altered by such a process. The resistivity, thermopower and carrier concentrations of some p-type samples are shown in Figs. 4.22, 4.23 and 4.24 respectively. The electrical properties at t = 0 correspond to the as-deposited films and the increase of resistivity and thermopower and the decreases of carrier density in the first 3 hours of anneal is due to the conversion of stratified layers into homogeneous $CuInSe_2$ films.

For anneal times longer than the standard 3 hour anneal, the resistivity and thermopower of the films both decrease continuously as the films are annealed progressively. Eventually after anneal times of ~35 hours, these properties converge to similar values irrespective of the starting level and in all cases the films remain p-type. As is evident from Fig. 4.24 the hole concentration increases continuously during the prolonged anneals reaching the $\sim 10^{21}$ cm^{-3} range. It should be mentioned that Figs. 4.22, 4.23 and 4.24 contain the behaviour of two samples annealed in a reducing N_2/H_2 (forming gas) environment. These samples did not behave differently from the samples annealed normally in N_2 gas and the implication of this will be considered later.

The effect of prolonged annealing on the n-type samples was also investigated and the results of room temperature resistivity, thermopower and carrier concentration are shown in Figs. 4.25, 4.26 and 4.27 respectively. It is obvious that the changes observed in the first 3 hours of anneal are essentially similar to p-type samples, namely an increase in resistivity and thermopower and a decrease in carrier concentration occurred.

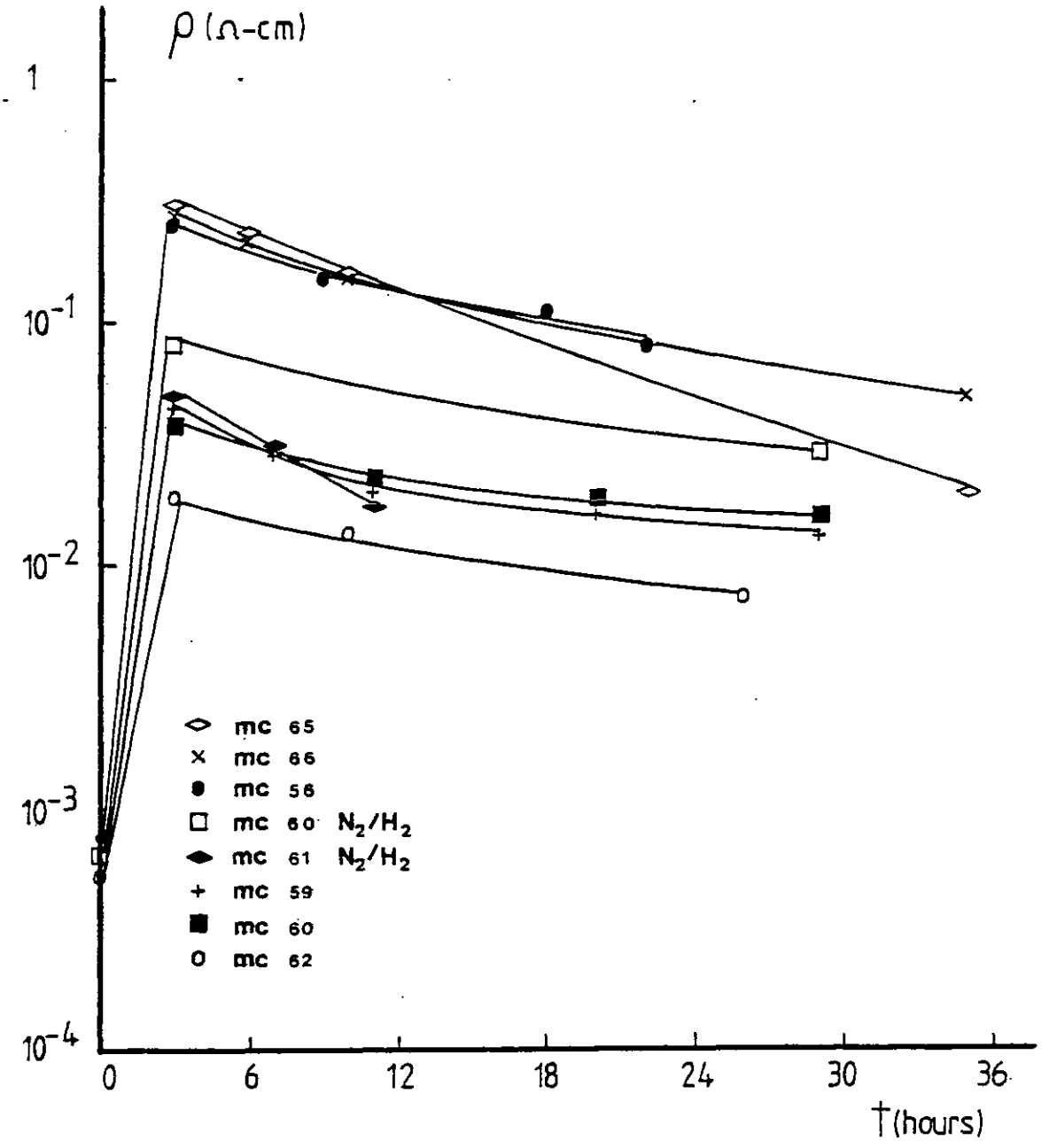

Fig. 4.22: Room Temperature Resistivity of p-type $CuInSe_2$ Films as a Function of Anneal Time at 350°C

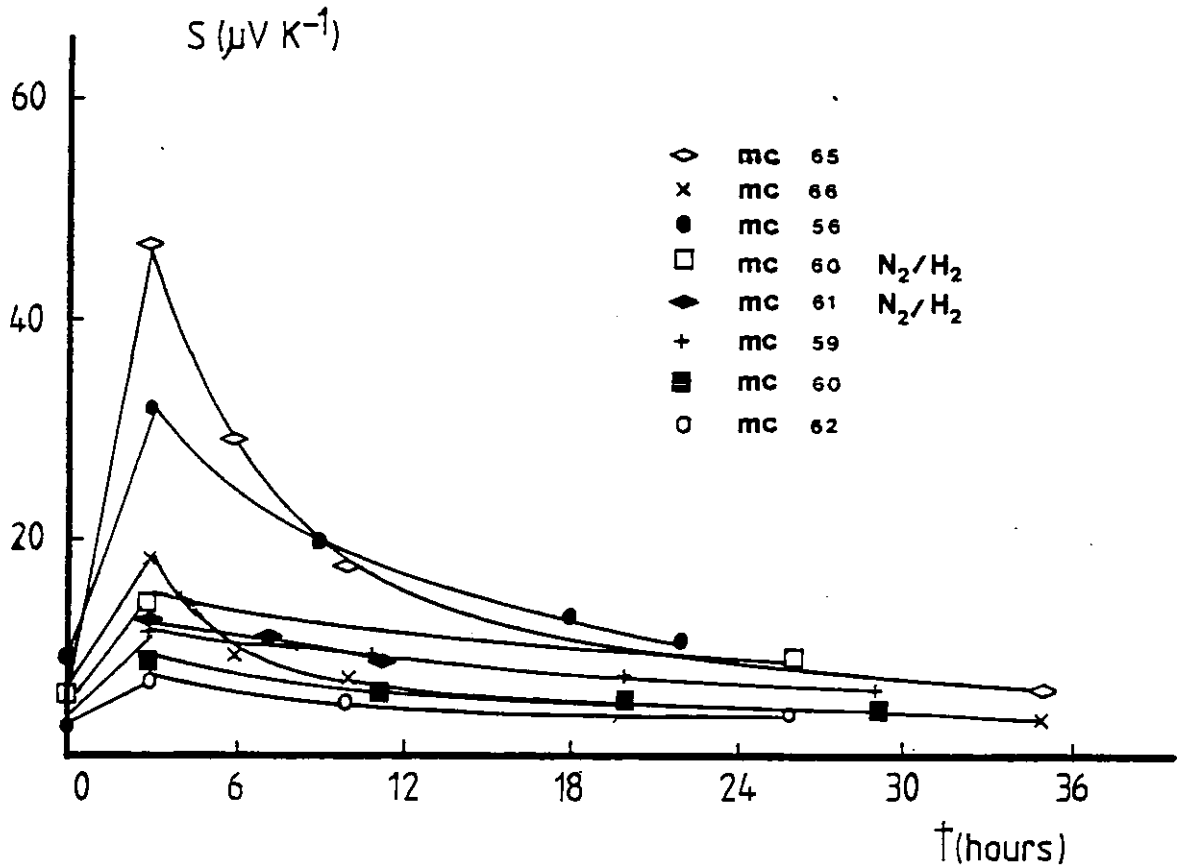

Fig. 4.23: Room Temperature Thermoelectric Power of p-type $CuInSe_2$ Films as a Function of Anneal Time at 350°C

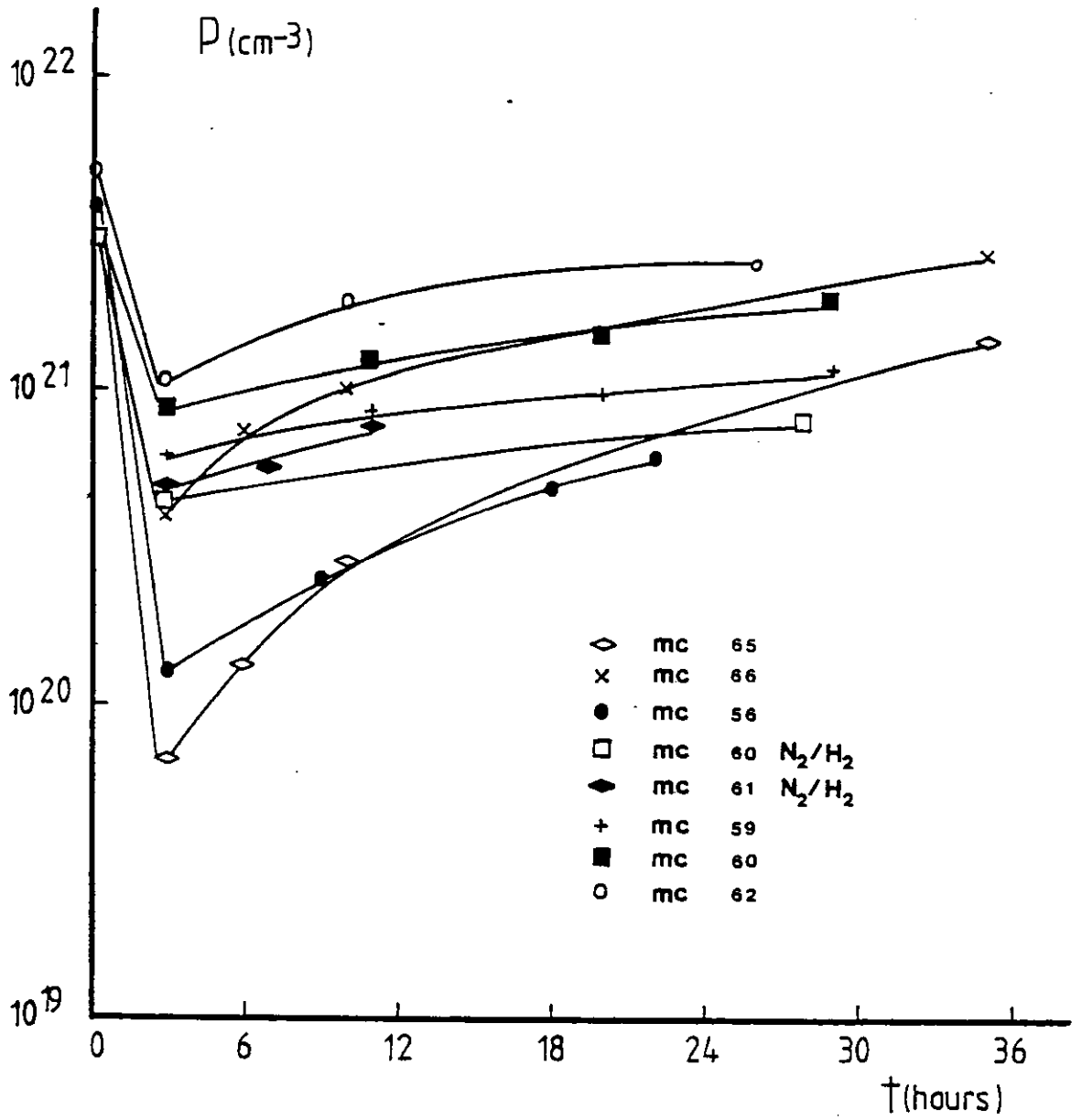

Fig. 4.24: Room Temperature Carrier Concentration of p-type $CuInSe_2$ Films as a Function of Anneal Time at 350°C

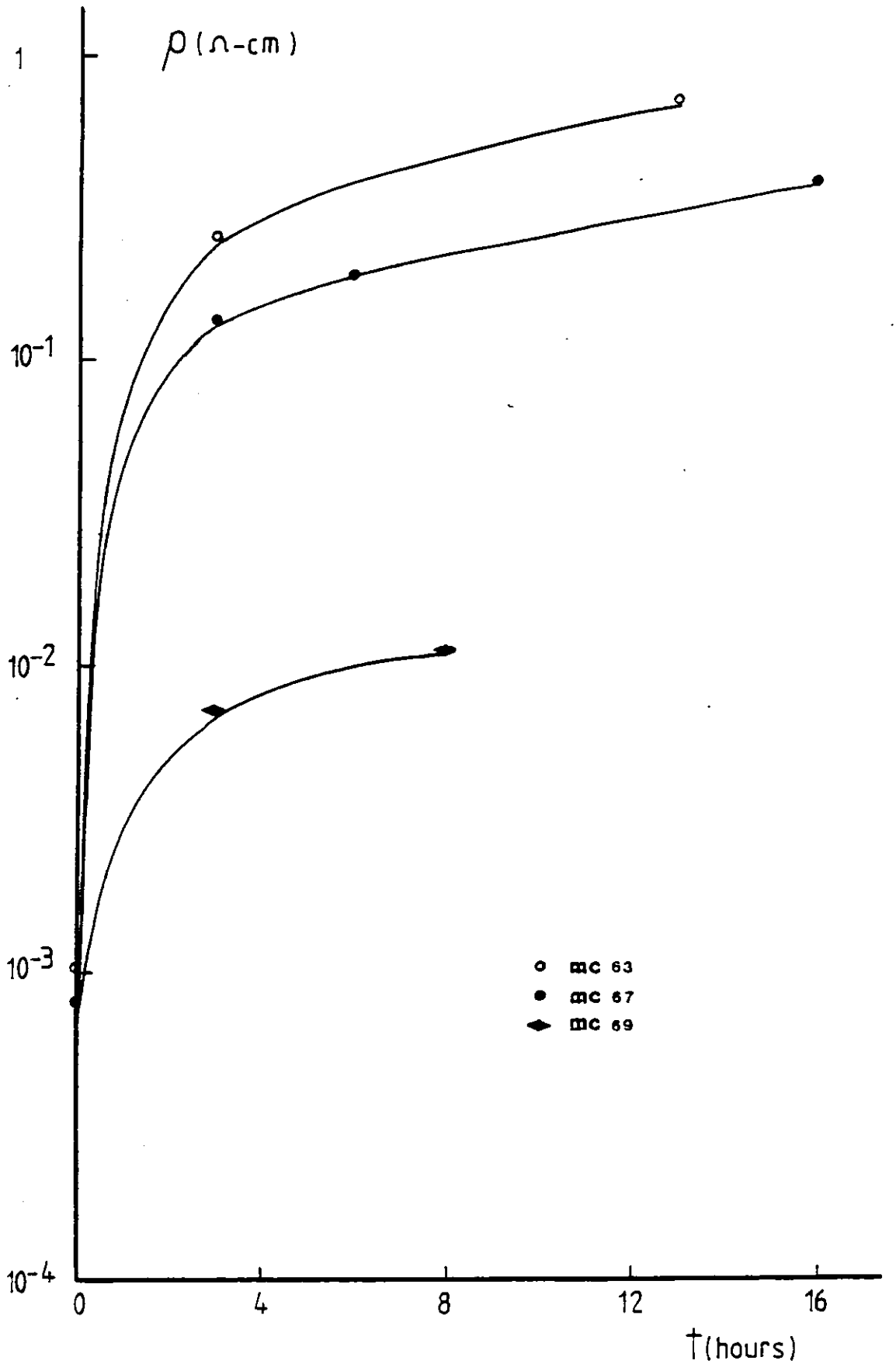

Fig. 4.25: Room Temperature Resistivity of n-type $CuInSe_2$ Films as a Function of Anneal Time at 350°C

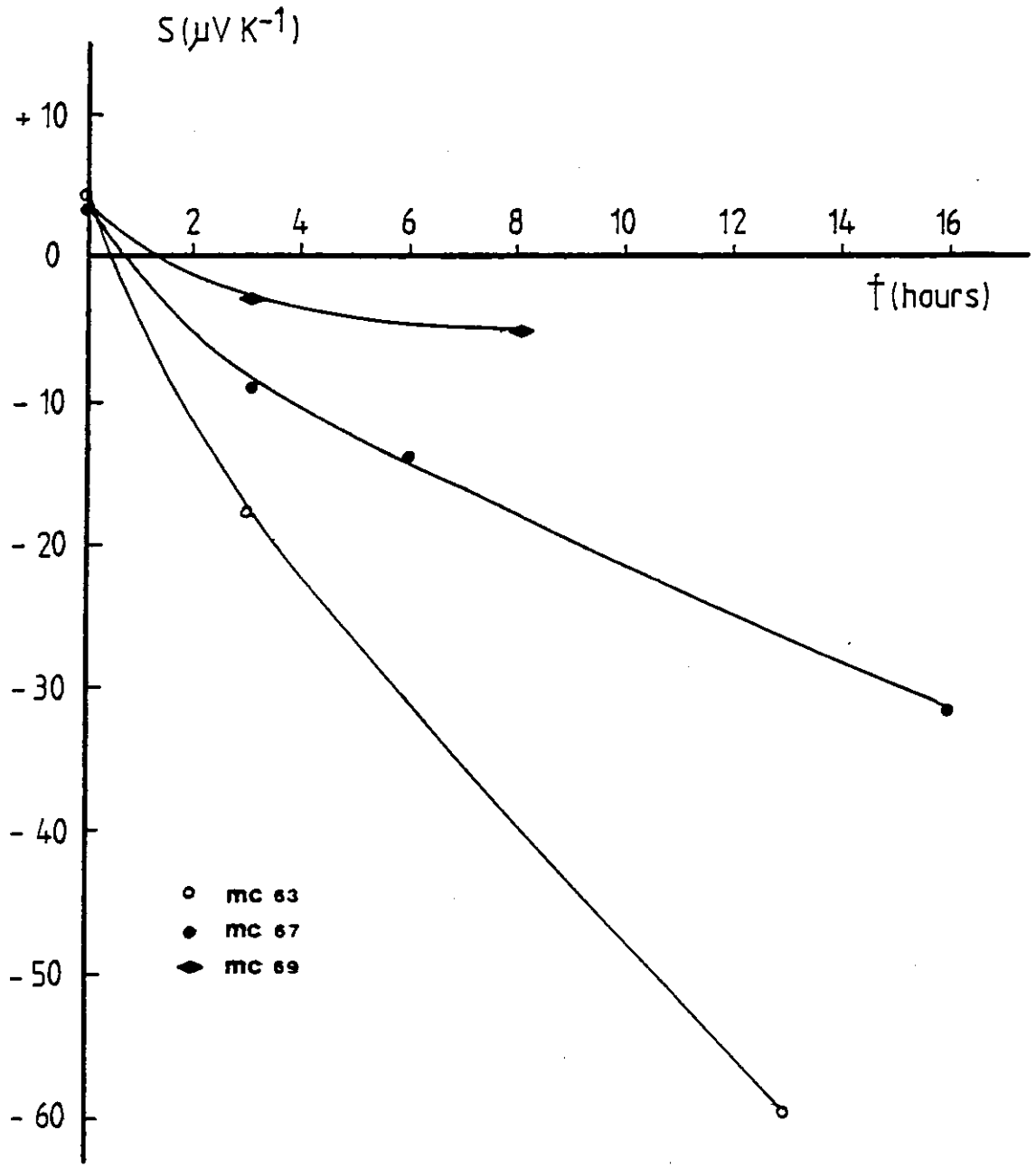

Fig. 4.26: Room Temperature Thermoelectric Power of n-type $CuInSe_2$ Films as a Function of Anneal Time at 350°C

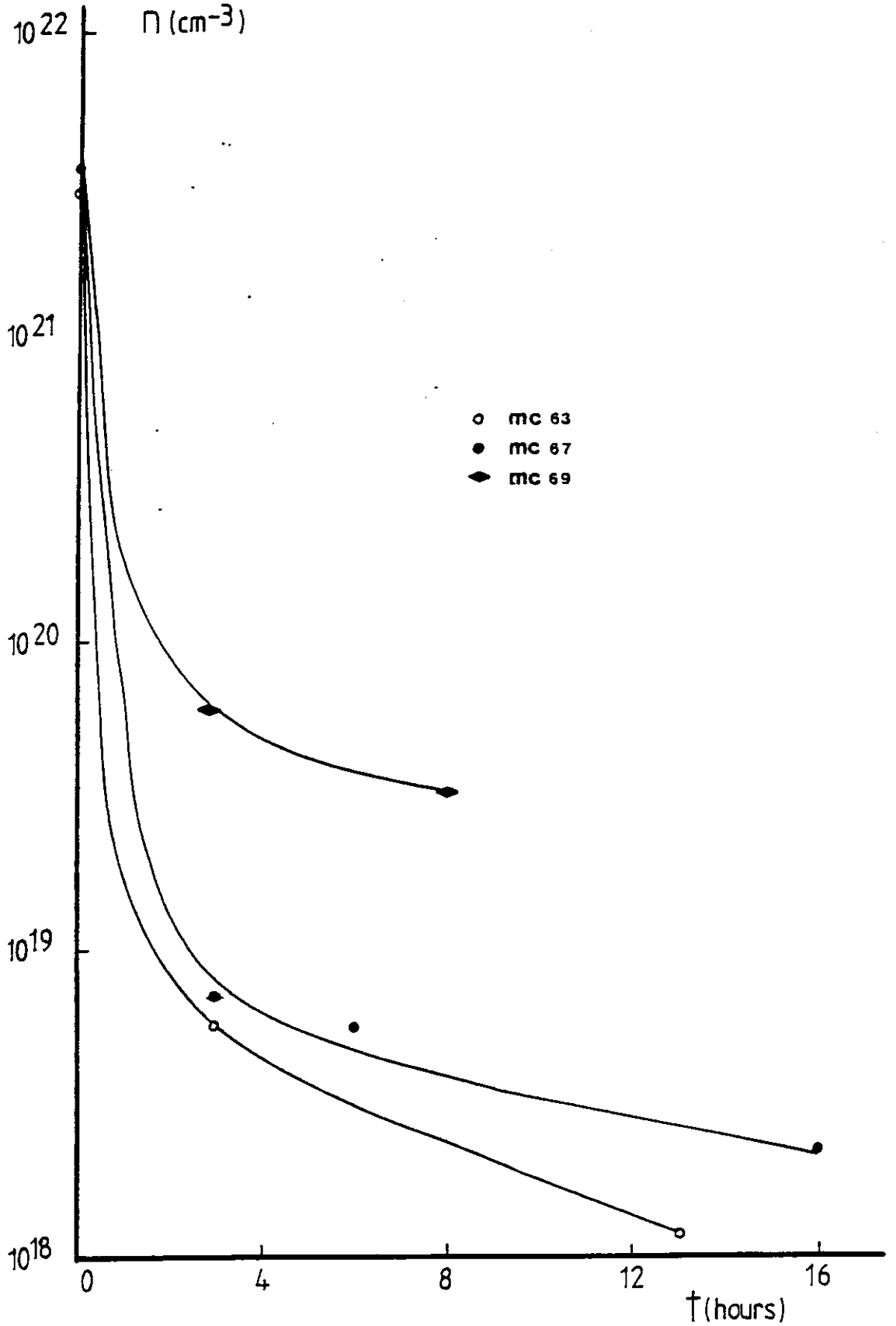

Fig. 4.27: Room Temperature Carrier Concentration of n-type $CuInSe_2$ Films as a Function of Anneal Time at 350°C

There is a distinct difference however in that the films changed from p-type during the first 3 hours.

However the variation observed for anneals longer than 3 hours are completely opposite to that of p-type films. In other words the thermopower and resistivity increase and the carrier concentrations decrease.

The main result of prolonged anneals can be seen to be an increase in the hole concentration of the p-type films and a reduction in the carrier concentration of the n-type films. These changes imply the introduction of acceptors into the films during the anneals, making the p-type samples more conducting whilst compensating the carrier population of the n-type specimens.

In terms of intrinsic defects, the production of extra acceptors in $CuInSe_2$ requires either the introduction of selenium or the removal of copper or indium from the films. The introduction of excess anions can be dismissed because the samples were not annealed in the presence of selenium.

On the other hand, the removal of cations from the samples is plausible during the anneals if it is recalled that the vapour above $CuInSe_2$ consists of In_2Se and Se_2 at temperatures up to about ~1000°C. At 350°C the partial pressures of In_2Se and Se_2 are 1×10^{-9} torr and 5×10^{-15} torr respectively[43] so that at the anneal temperatures In_2Se molecules will dominate the gas phase above $CuInSe_2$. During the long anneals some of these molecules will be expected to be swept away by the flowing nitrogen gas to condense onto cooler parts of the furnace tube. This effectively means that more indium atoms will be lost from the films than selenium atoms. In other words as anneal time increases there will be a net loss of indium from the samples, resulting in the creation of extra indium vacancies and hence an increase in carrier concentration of p-type films and a decrease in carrier concentration of n-type films.

The possibility of external contamination, in particular oxygen, giving rise to the change in carrier density of the films, must not be ruled out. The interaction of oxygen with surface atoms of $CuInSe_2$ may lead to chemisorption. This usually involves the capture of electrons from the semiconductor resulting in the formation of a depletion layer on a n-type semiconductor and an accumulation layer on a p-type semiconductor. If this surface region starts to dominate the underlying bulk then an effective reduction in the carrier concentration for n-type films and an effective increase of carrier concentration in p-type films would be observed. In other words chemisorption effects could possibly explain the experimental variation of carrier density with anneal.

In order to investigate whether oxygen does indeed affect the electrical properties of our films, some samples were heat treated in a hydrogen gas ambient. Such an anneal would be expected to reduce the extent of interaction of oxygen and thus would show a marked effect upon the electrical properties of the films should oxygen be the reason for the observed behaviour of films annealed at prolonged times.

However, as mentioned previously, the electrical measurements on samples that underwent heat treatment in forming gas (N_2/H_2), indicated that these had similar properties as the samples annealed in N_2.

It is thus concluded that oxygen does not affect the electrical properties of films annealed at 350°C and that the observed increase in carrier density of p-type films, and the decrease of carrier density of n-type films after prolonged anneals must be attributed to the net loss of indium from the samples.

4.4.2.4 Films Annealed at 450°C

Following anneals at 350°C, samples which were further heat treated in N_2 at a temperature of 450°C had their majority carrier type change from p- to n-type. This majority carrier conversion coincided with a net loss

of selenium from the films as determined by Electron Probe Microanalysis (see Section 3.5.1.4) and the appearance of In_2O_3 in the layers as detected by X-ray diffraction analysis (see Section 3.3.2.1).

The p- to n-type conversion was looked at further, by annealing some samples for successive times and measuring their resistivity and thermopower at room temperature. The thermopower results are shown in Fig. 4.28, where the Seebeck coefficient is seen to decrease from positive values to zero and eventually becomes negative after about 2-3 hours of anneal. Over the same period of time the resistivity,as shown in Fig. 4.29, remains more or less constant but then starts to decrease as films are annealed for progressively longer times.

As mentioned earlier, any loss of selenium from $CuInSe_2$ will have the effect of introducing extra donors and make the samples change to n-type. It is tempting therefore to connect the loss of selenium detected by EPMA with the electrical changes observed after the 450°C anneals. However, if the change is purely due to a new balance of intrinsic defects, then one would expect the samples to be in the mixed conduction regime before changing from p- to n-type. In this case equations (4.25), (4.26) and (4.27) would be expected to describe the transport parameters.

Of particular interest here is the zero crossover point for the Hall coefficient and for the Seebeck coefficient. The Hall coefficient will pass through zero when

$$p = nb^2$$

where p is the hole concentration, n is the electron concentration and b is the electron to hole mobility ratio. This relationship can be substituted in the conductivity and thermopower expressions to determine the value of these parameters at the Hall crossover. If use of the fact that at the Hall crossover $n_i^2 = (nb)^2$ is made, where n_i is the intrinsic carrier density of the

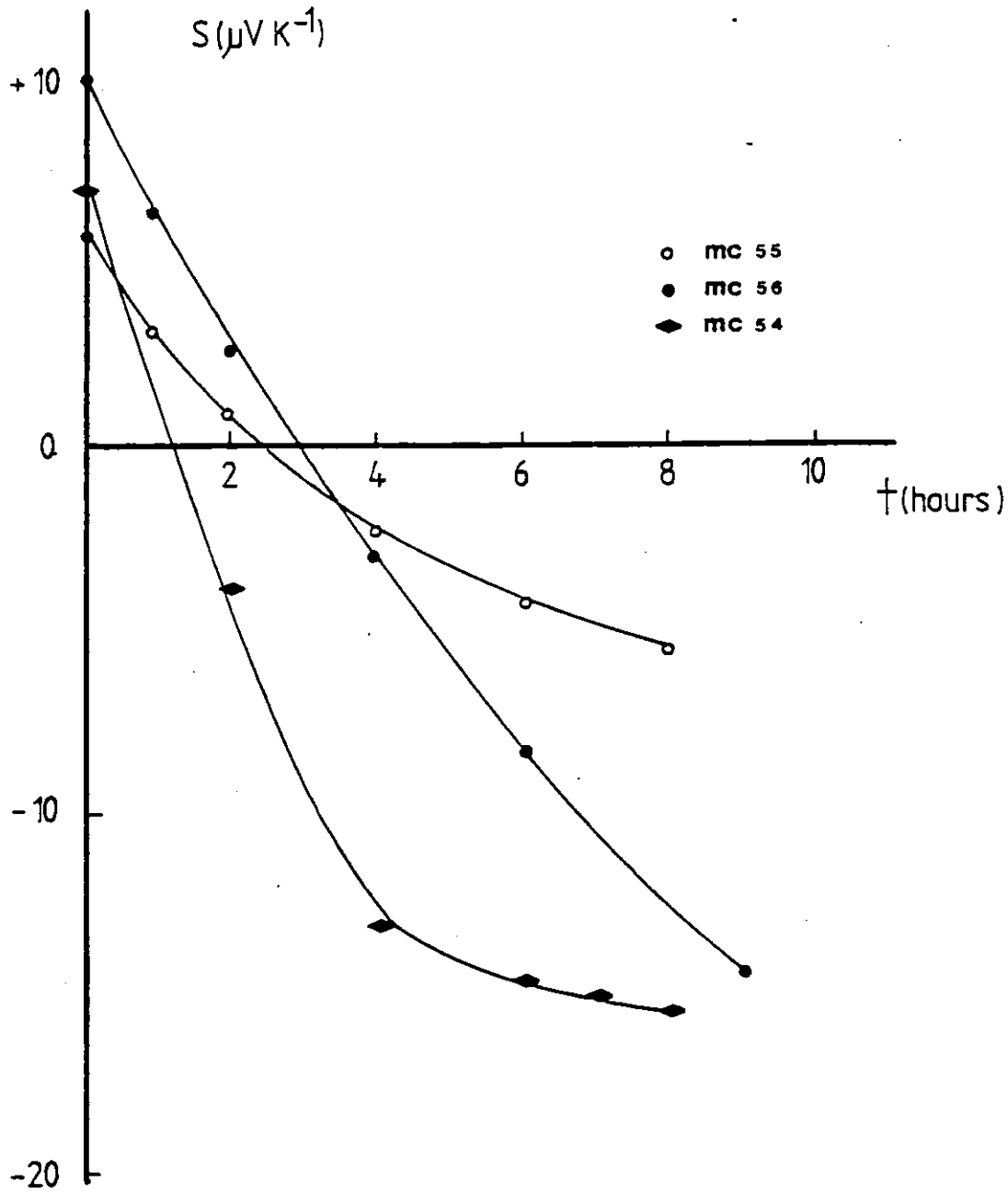

Fig. 4.28: Room Temperature Thermoelectric Power of previously Heat Treated $CuInSe_2$ Films as a Function of Anneal Time at 450°C

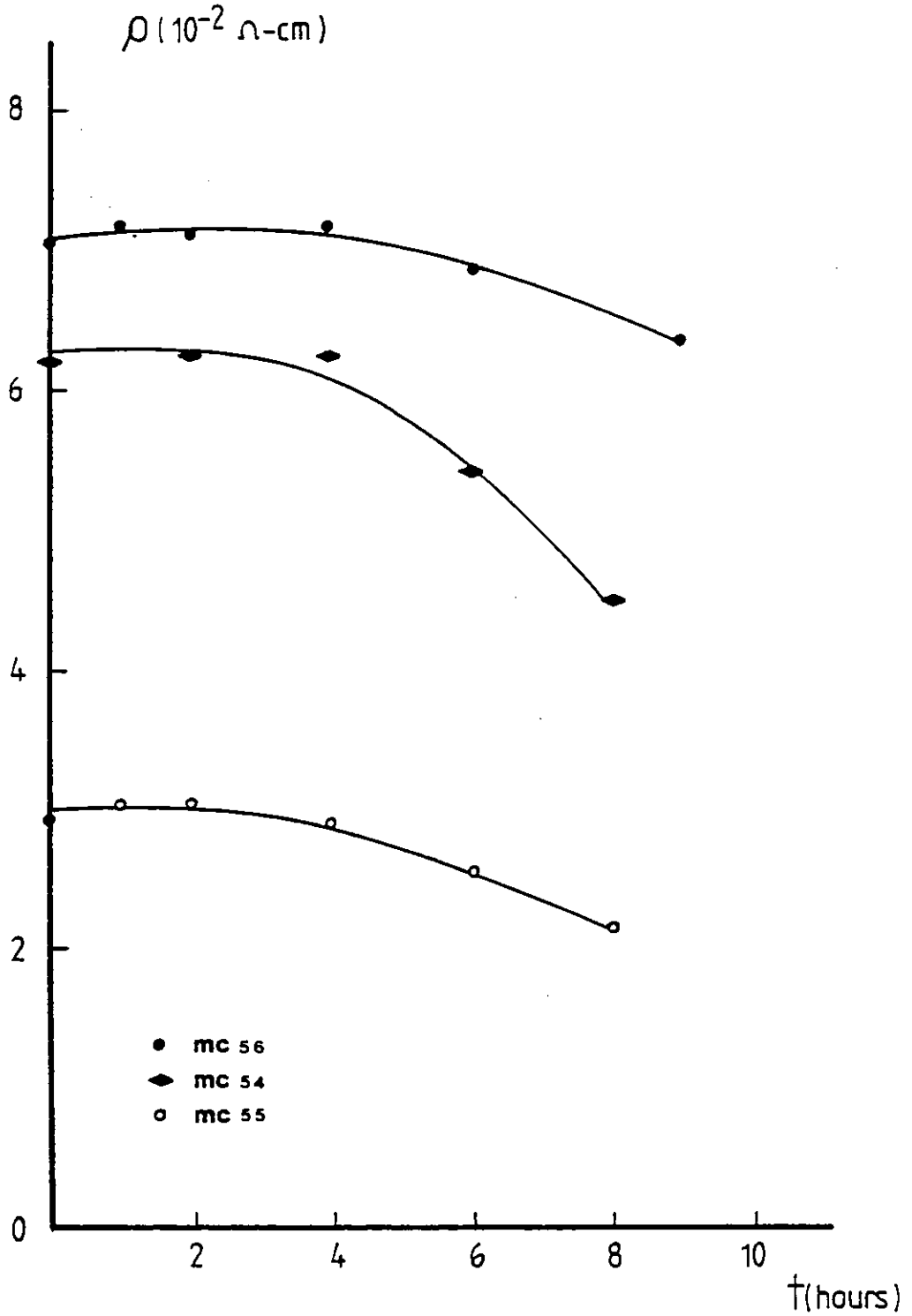

Fig. 4.29: Room Temperature Resistivity of Previously Heat Treated $CuInSe_2$ Films as a Function of Anneal Time at 450°C

semiconductor then it can be shown that:

(i) The resistivity of the sample at the crossover is equal to the resistivity of the pure intrinsic semiconductor at the temperature of the Hall crossover.

(ii) The thermoelectric power is not zero but is still positive for $b > 1$

The thermopower crossover occurs approximately when $p = nb$[14] when the Seebeck coefficient has the value:

$$S = \frac{k}{2e} \left[\ell n \left[\frac{1}{b} \left(\frac{m_p}{m_n}\right)^{3/2} \right] \right]$$

where m_p and m_n are the density of states effective massives for holes and electrons. Since $m_p > m_n$ and $b > 1$, then the thermopower at $p = nb$ is indeed nearly zero and indicates that the thermopower zero crossover occurs after the Hall crossover is observed.

From the above discussion it is expected that the sample resistivity will reach its intrinsic value before the thermopower becomes zero. At 300K the intrinsic carrier concentration of $CuInSe_2$ may be calculated to be ~9×10^9 cm^{-3} and for typical mobilities this corresponds roughly to an intrinsic resistivity around 10^6 Ω cm.

Such a high value of resistivity was not observed in our $CuInSe_2$ films during their p- to n-type transition. Therefore self compensation effects due to selenium losses cannot explain the experimental results of films annealed at 450°C.

So far the effect of In_2O_3 on the electrical properties has not been considered. It is of interest to note that In_2O_3 is an n-type semiconductor having a bandgap of 2.62 eV[44]. Unlike most oxides its electrical properties are more reminiscent of metals and thin films with resistivities in the range 10^{-3} - 10^{-1} Ω cm have been prepared[44,45].

These resistivities are very much lower than those of annealed $CuInSe_2$ films so that if In_2O_3 forms a progressively thicker layer after the anneals at 450°C, then its high conductivity would be expected to have a marked effect upon the transport properties of the $CuInSe_2$ films.

In this case conduction through a two-layer,as described in Section 4.3.2, will be appropriate for consideration. For this purpose the experimental data of Figs. 4.28 and 4.29 were replotted in a manner which can be compared with the theoretical conductivity and thermoelectric power of an n-type surface on p-type bulk.

In Fig. 4.30a the experimental conductivities are plotted as σ_T/σ_B versus time. Here σ_B represents the conductivity of the bulk and is theconductivity of the samples annealed at 350°C but prior to the anneal at 450°C, when the effect of any surface oxide is still negligible. σ_T represents the combined conductivity of the bulk and surface and is the conductivity of the samples measured after the anneals at 450°C. Similarly, in Fig. 4.30b,the experimental thermopower results have been plotted as S_T/S_B, where S_B represents the bulk thermopower and is the thermopower of the films before the anneals at 450°C and S_T is the total thermopower measured after the heat treatments.

It must be pointed out that the experimental conductivity and thermopower data of Figs. 4.30a and 4.30b have been plotted versus time of anneal, whereas the theoretical plots (Figs. 4.11 and 4.13) had been obtained as a function of surface to bulk thickness ratio. Nevertheless qualitative comparison between the two-layer model and experiment is still possible, because the surface oxide will be expected to grow with anneal time. The relationship between time of anneal and oxide thickness may not necessarily be a linear one, but the choice of a different functional time scale will only expand or compress the experimental curves without changing their basic features.

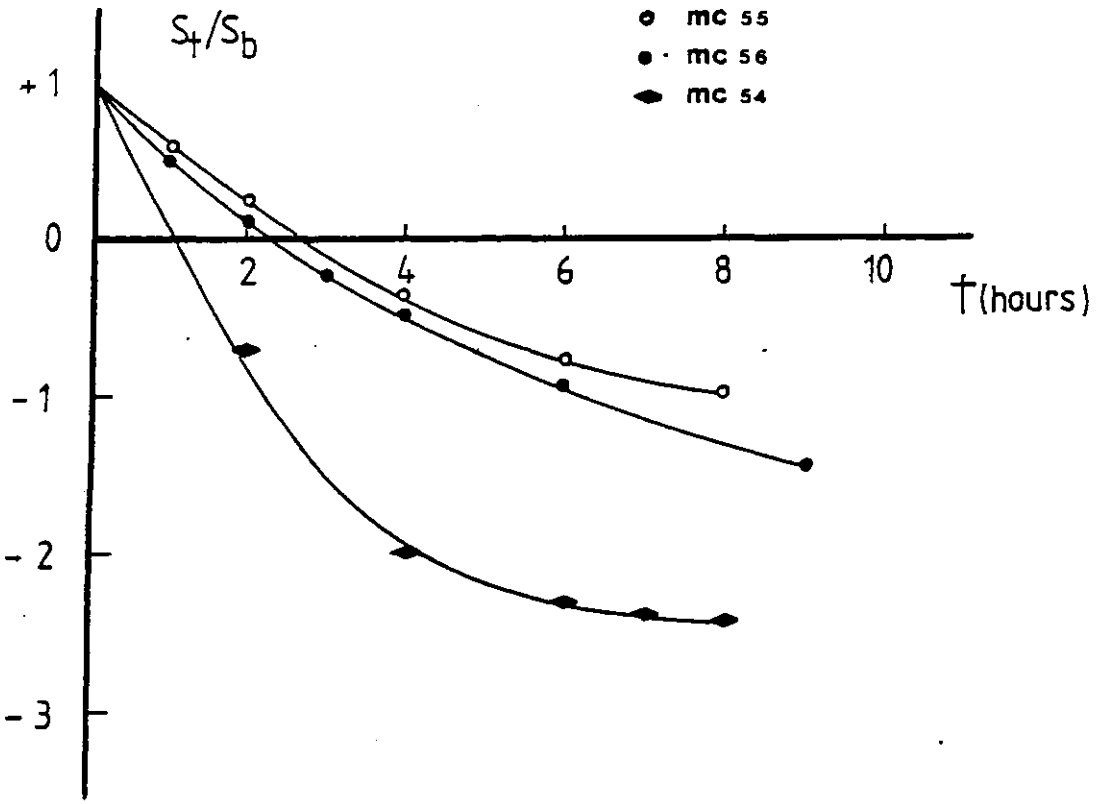

Fig. 4.30(b): The Variation of Total Thermopower of 450°C Annealed Films Normalised with Respect to Thermopower at the Start of Anneal

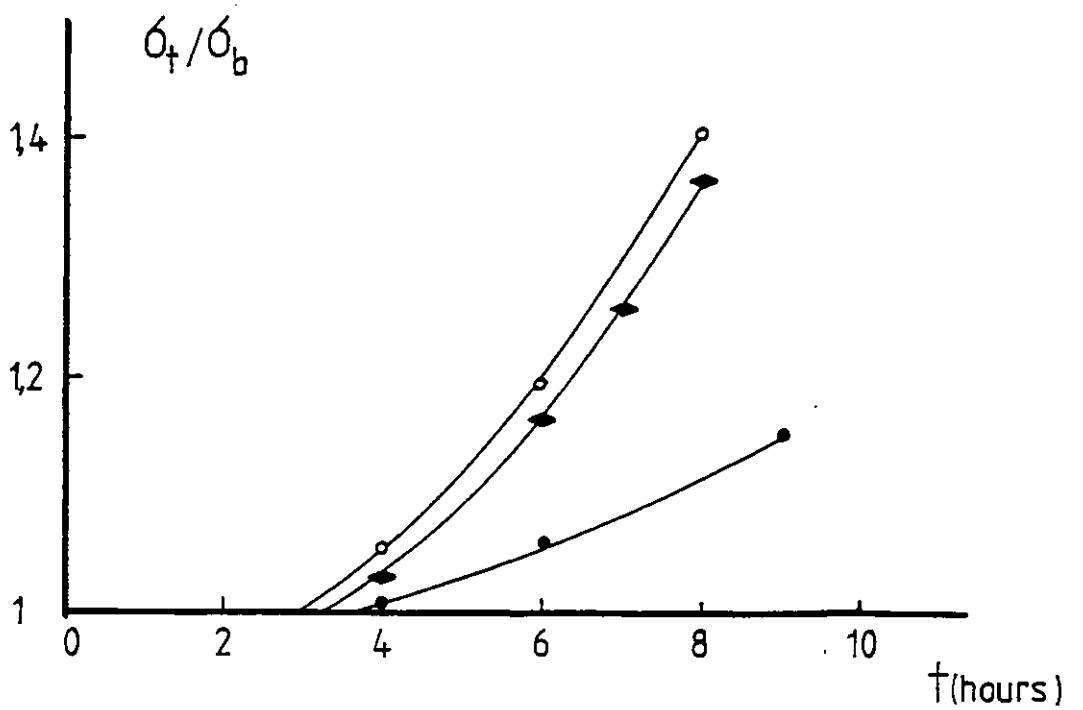

Fig. 4.30(a): The Variation of Total Conductivity of 450°C Annealed Films Normalised with respect to Conductivity at the Start of Anneal

Thus it will be seen that the experimental data of films annealed at 450°C follow the predictions of a two-layer model of a conducting n-type layer on p-type bulk quite well. Namely, the thermoelectric power ratio crosses the zero level changing from p- to n-type at some particular time which corresponds to a particular surface to bulk thickness ratio. Also the conductivity ratio during this time increases in a manner consistent with theory.

In conclusion the p- to n-type conversion observed for films annealed at 450°C, is due to the shunting effect of a highly conducting In_2O_3 oxide layer that grows with time of anneal.

4.4.3 Temperature Dependence of Electrical Properties

4.4.3.1 Carrier Concentration of Films

The carrier concentration of n-type samples annealed at 350°C is shown in Fig. 4.31 as a function of temperature. This figure also includes as shown by the dashed line, the carrier concentration at the degeneracy temperatures for direct comparison. This line represents the carrier concentration at which the Fermi level is just at the edge of the conduction band at various temperatures. These have been calculated from equation (4.22) and the semiconductor is considered to have a degenerate carrier population at a particular temperature when the reduced Fermi energy $\eta = E_F/kT = 0$. In this case the Fermi integral of equation (4.22) has a value[13] $F_{\frac{1}{2}}(0) = 0.678$, so that

$$n = 3.695 \times 10^{15} m_d^{3/2} T_{degen}^{3/2} \quad cm^{-3}$$

where n is the carrier density and m_d is the density of states mass.

From Fig. 4.31 it is evident that for all the n-type samples the measured carrier concentrations are above the degeneracy limit at all temperatures, indicating that the Fermi level is situated within the conduction band. The electron concentration is also independent of temperature as would be expected for a degenerate carrier population.

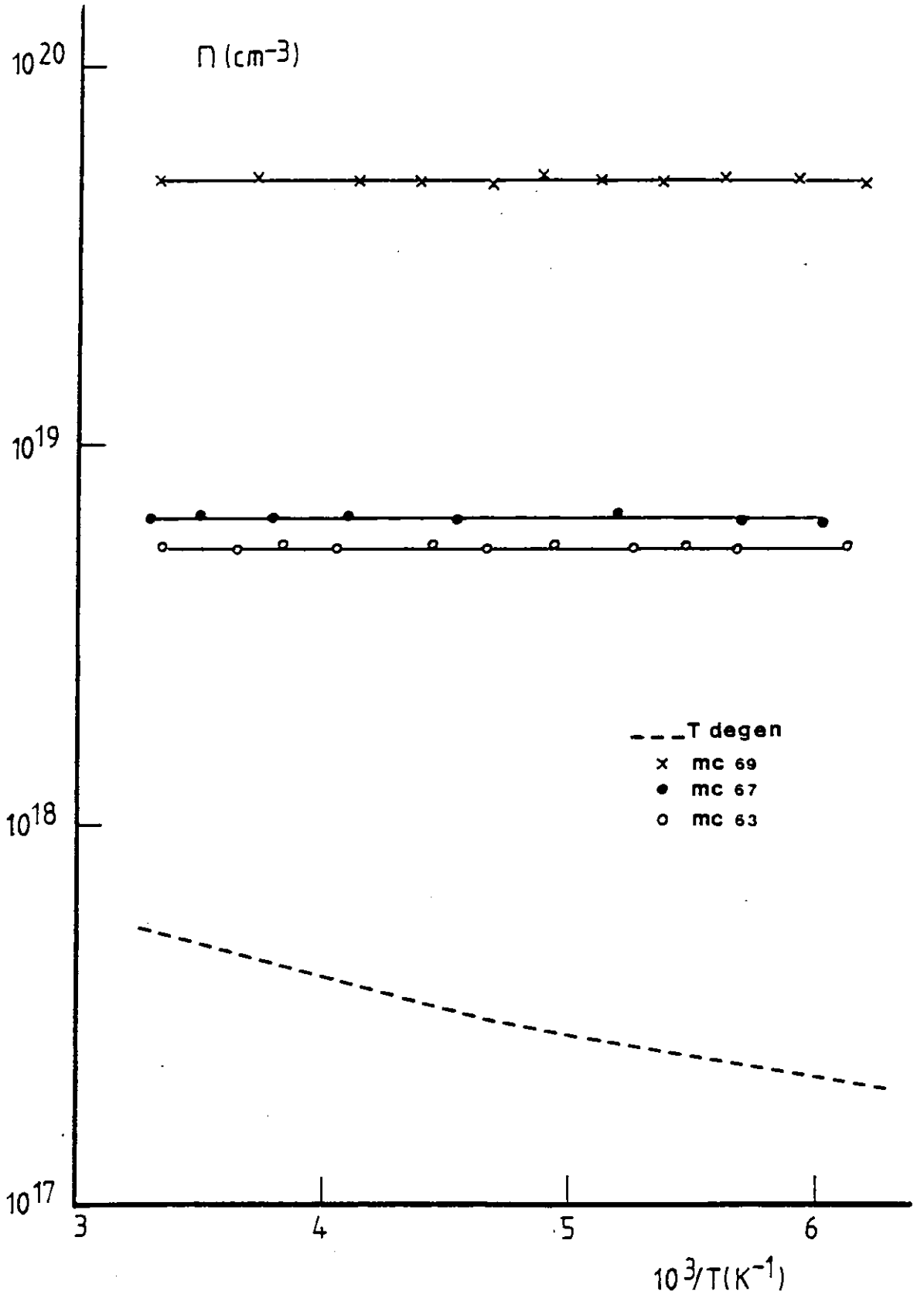

Fig. 4.31: Carrier Concentration as a Function of Temperature for n-type $CuInSe_2$ Films

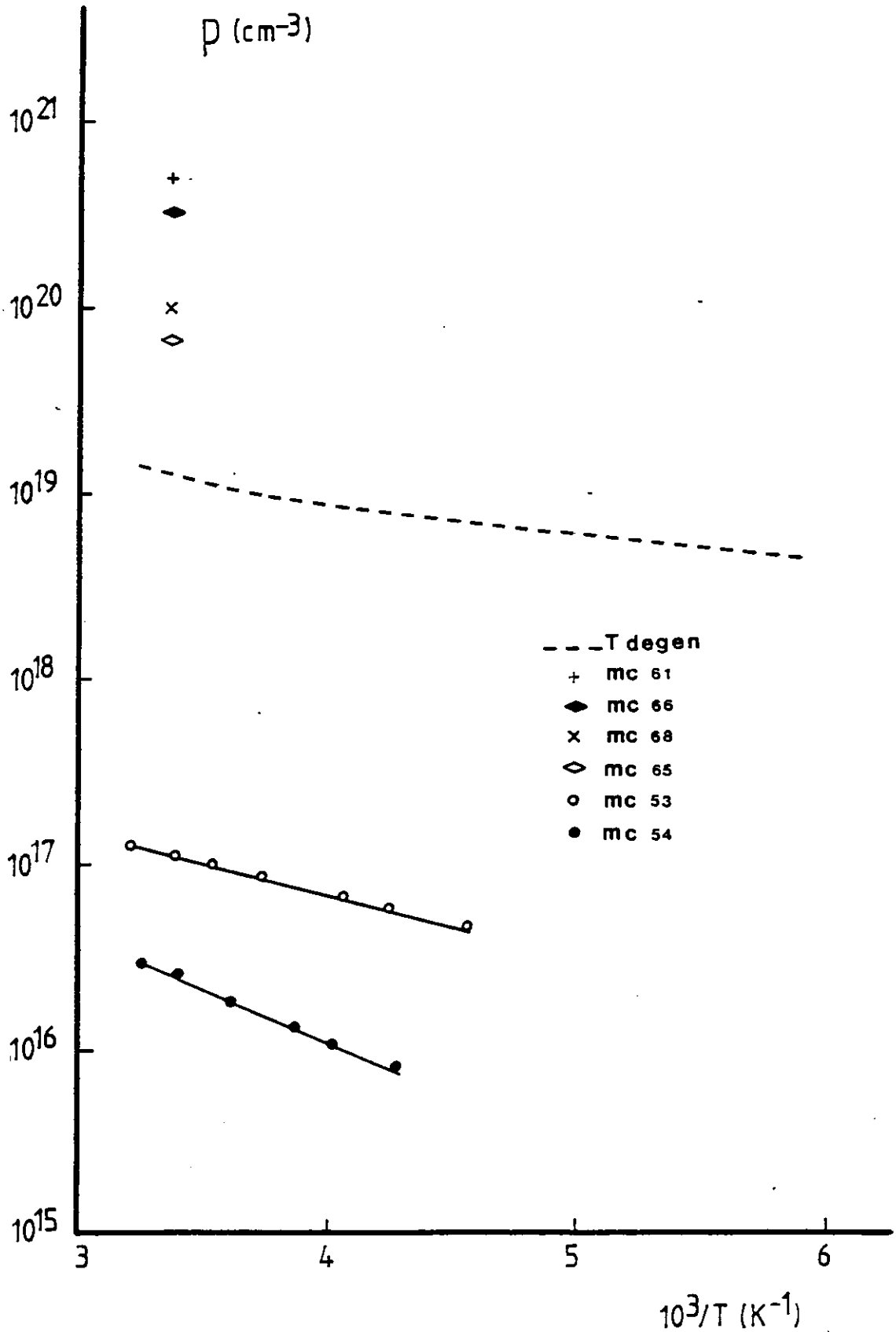

Fig. 4.32: Carrier Concentration as a Function of Temperature for p-type $CuInSe_2$ Films.

The hole concentrations of low resistivity and high resistivity p-type films are given in Fig. 4.32, where concentration at the degeneracy temperature, as shown by the dashed lines, has also been plotted. The low resistivity samples have carrier densities which lie above the degeneracy limit, indicating that these have a degenerate population. Due to the fact that the Hall voltage was too small to be measured, only the room temperature carrier density as obtained from thermopower measurements is shown for these particular samples. The hole concentration is expected to remain constant at lower temperatures, just as in the case of the degenerate n-type samples.

The carrier concentration of the high resistivity samples lay well below the degeneracy limit indicating that they are not degenerate. The hole concentrations of these samples have been measured only over a resistricted temperature range due to high sample resistances at low temperatures when the noise in the Hall voltage made the measurements unreliable. Over the limited temperature range, the carrier density of these non-degenerate samples showed a steady increase with temperature. The carrier density is activated with activation energies of 0.07 eV and 0.10 eV for samples MC53 and MC54 respectively.

These carrier activation energies can be compared with literature data on $CuInSe_2$. In this respect Schumann et al[46] observed acceptor energies of 0.085 eV to 0.095 eV in their epitaxial $CuInSe_2$ thin films. These values are very similar to the activation energies observed in this study and imply that the variation of hole concentration of the non-degenerate p-type films is due to carrier excitation from one of the acceptor levels of $CuInSe_2$.

4.4.3.2 Carrier Mobilities

The carrier mobilities as a function of temperature for p- and n-type samples are shown in Figs. 4.33 and 4.34 respectively. The two non-degenerate p-type samples in Fig. 4.33 are characterised by a mobility which increases continuously with temperature. The mobilities could be described as being activated with activation energies of around 0.04 eV.

The degenerate p-type samples also exhibit an increase in mobility with temperature, but this increase is not as steep as in the non-degenerate samples. The n-type $CuInSe_2$ films have a mobility variation very similar to these degenerate p-type samples. In both types of sample a slight increase in mobility was observed in the temperature range 150-260K, after which the mobility exhibited a decrease with temperature. In order to determine the type of scattering mechanism that gives rise to the experimental film mobilities each of the mobility limiting mechanisms in equation (4.39) was examined in turn.

For surface scattering the greatest reduction in mobility is expected for carriers having a mean free path comparable to film thickness. In the $CuInSe_2$ films here the mean free path is approximately ~40Å for a p-type degenerate film with hole concentration of $\sim 10^{21}$ cm^{-3} and ~80Å for a n-type film with electron densities of $\sim 10^{19}$ cm^{-3}. Since the films investigated had typical thicknesses of 6000Å, these mean free paths are negligibly small and hence any reduction of mobility due to surface scattering will be insignificant.

To estimate the effect of dislocation scattering a deformation potential of ~6.5 eV, Burger's vector of ~2.5Å and a Poisson ratio of 0.37, quoted by Dexter et al[25] for typical semiconductors, was used in the calculations. The dislocation density in the films is not known but a high value such as $\sim 10^{12}$ cm^{-2}, which may be observed in severely cold worked metals, was taken as an estimate. The calculated room temperature mobilities

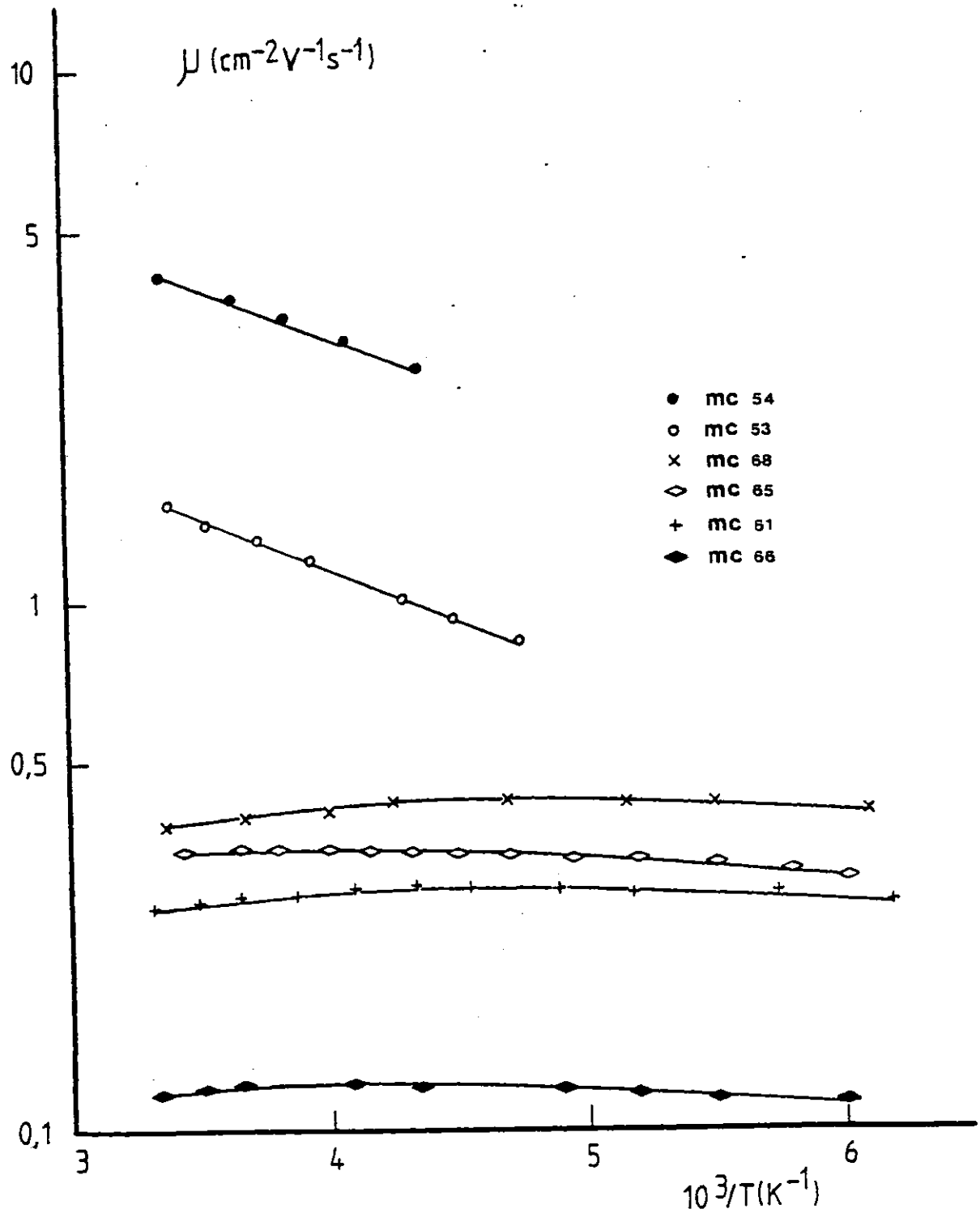

Fig. 4.33: Carrier Mobility as a Function of Temperature for p-type $CuInSe_2$ Films

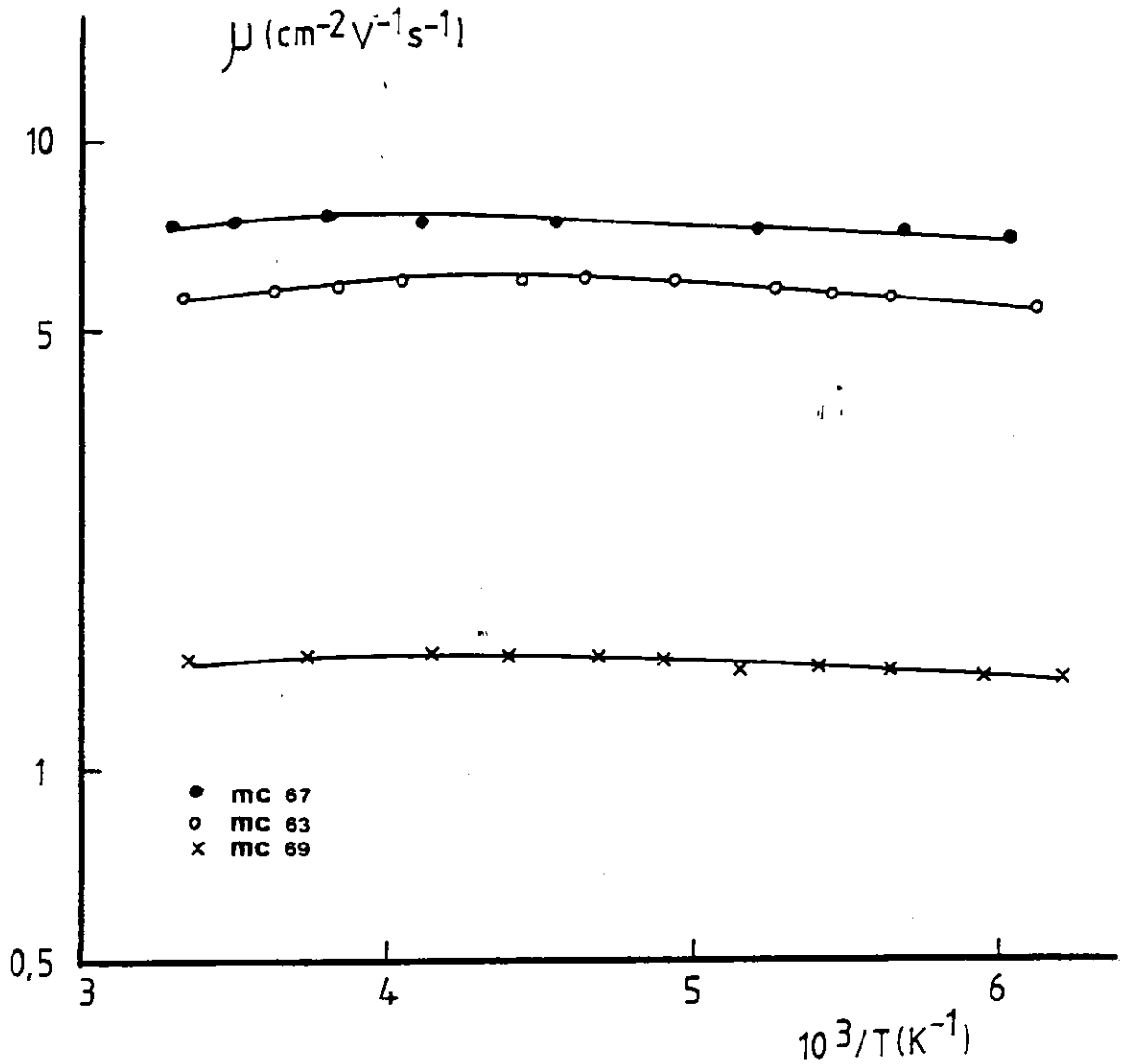

Fig. 4.34: Carrier Mobility as a Function of Temperature for n-type $CuInSe_2$ Films

were 50 $cm^2\ V^{-1}\ s^{-1}$ for the p-type films and 300 $cm^2\ V^{-1}\ s^{-1}$ for the n-type films. These values are obviously very much higher than the experimental mobilities and thus dislocation scattering may also be neglected here.

For mobilities limited by grain boundary scattering the mean free path of the carriers was taken as ~3000Å, being approximately half the film thickness and hence half the mean grain size. As is evident from equation (4.45) the grain boundary limited mobility is smallest for samples having the greater carrier concentration. This mobility was calculated to be about $2 \times 10^3\ cm^2\ V^{-1}\ s^{-1}$ for a p-type sample with $p = 10^{21}\ cm^{-3}$ and $8 \times 10^3\ cm^2\ V^{-1}\ s^{-1}$ for an n-type sample with $n = 10^{19}\ cm^{-3}$. Clearly these mobilities are orders of magnitude higher than the measured values so that grain boundary limited mobility may also be discarded from the mobility analysis.

To check the applicability of scattering by potential barriers at grain boundaries, the mobility data were plotted following Section 4.3.3.2(d) as $\ell n[\mu T^{\frac{1}{2}}]$ versus 1/T for the non-degenerate samples and as $\ell n[\mu T^{\frac{1}{2}} F_{\frac{1}{2}}(\eta) \exp[-\eta]]$ versus 1/T for the degenerate samples. The results of such plots for a non-degenerate p-type, degenerate p-type and degenerate n-type $CuInSe_2$ film are shown in Fig. 4.35.

The plots yielded quite good straight lines indicating that the potential barrier model may explain the experimental mobilities. The band bending, $e\phi_0$, was obtained from the slopes of these linear graphs. At room temperature the barrier height $e\phi_0 - E_F$ was ~2kT for the non-degenerate p-type samples but was very much smaller than kT for the degenerate p- and n-type $CuInSe_2$ samples.

It must be borne in mind that the derivation of thermionic emission over barriers is based on the assumption that the barrier height must be at least ~2kT or higher. While this condition is fulfilled for the non-degenerate samples it clearly was not for the degenerate films.

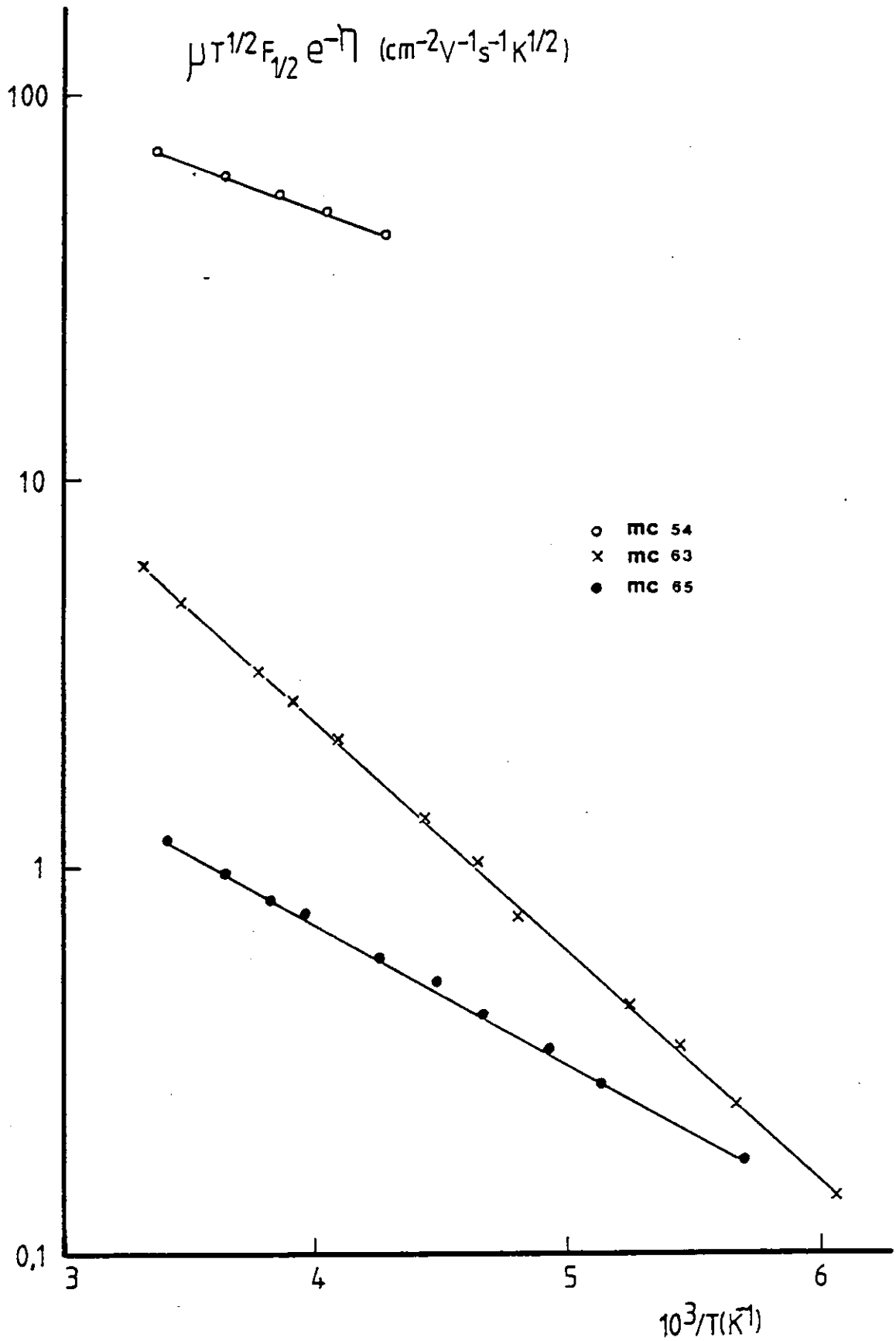

Fig. 4.35: Curve Fits (solid lines) of Experimental Mobility using the Potential Barrier Scattering Model

Therefore a description of the mobility of these latter samples by a potential barrier scattering mechanism is meaningless, even though the experimental data fits the theoretical temperature dependence.

As far as the non-degenerate p-type samples were concerned, the fit to the barrier model was used to calculate the mean grain size of the films and to compare them with experimentally (by T.E.M.) measured values. The grain size can be obtained from the intercept of the $\ell n[\mu T^{\frac{1}{2}}]$ versus 1/T plots which should yield from equation (4.50)

$$\mu_o' = \frac{eL}{(2\pi mk)^{\frac{1}{2}}}$$

where L is the mean grain dimension. Such a calculation yielded values of L lying in the range 8-20Å. These sizes are orders of magnitude lower than the grain size measured on transmission electron micrographs which were approximately the film thickness of ~6000Å. Thus while scattering by potential barriers is able to explain the temperature dependence of the mobility of non-degenerate p-type $CuInSe_2$ samples, it does not tie in well with the grain dimensions. In fact using the experimentally determined crystallite size, it is calculated that the potential barrier limited mobility is much higher than the experimental values.

It is thus apparent that the principal scattering mechanism peculiar to thin polycrystalline semiconductor films do not explain the mobility of the $CuInSe_2$ films prepared in this study and that alternative models are required, which are characterised by a mobility which increases with temperature. Ionised impurity scattering is such a mechanism, resulting in a mobility with a nearly temperature independent mobility in degenerate semiconductors[14]. It is therefore worthwhile to consider the applicability of this scattering model to our films.

The contribution of ionised impurity scattering to the mobility was analysed in accordance with a treatment valid for arbitrary degeneracy

in the semiconductor. In this model the ionised impurity mobility is given by[49]:

$$\mu_i = \frac{2^{3/2} (\varepsilon_o \varepsilon_s)^2 (kT)^{3/2} F_2(\eta)}{N_i \pi e^3 (m_d)^{\frac{1}{2}} g(z) F_{\frac{1}{2}}(\eta)}$$

where N_i is the density of ionised impurities, ε_s is the static dielectric constant, η is the reduced Fermi energy, $F_{\frac{j}{2}}(\eta)$ are the Fermi-Dirac integrals and $g(z)$ is a slowly varying function given by:

$$g(z) = \ell n(1 + z) - z/(1 + z)$$

where

$$z = \frac{4 \varepsilon_o \varepsilon_s m_d (kT)^2 \eta F_{\frac{1}{2}}(\eta)}{P \pi e^2 \hbar^2 F_{-\frac{1}{2}}(\eta)}$$

in which P is the carrier concentration.

In the above mobility expression, N_i represents the total ionised donor and acceptor concentrations. In a p-type semiconductor, if all the donors N_D are assumed to be fully ionised, then N_i is given by:

$$N_i = (N_A - n_A) + N_D$$

where N_A is the total concentration of acceptors and n_A is the concentration of unionised acceptors. Since charge neutrality in the semiconductor must be maintained then:

$$N_A - n_A = p + N_D$$

and

$$N_i = p + 2 N_D$$

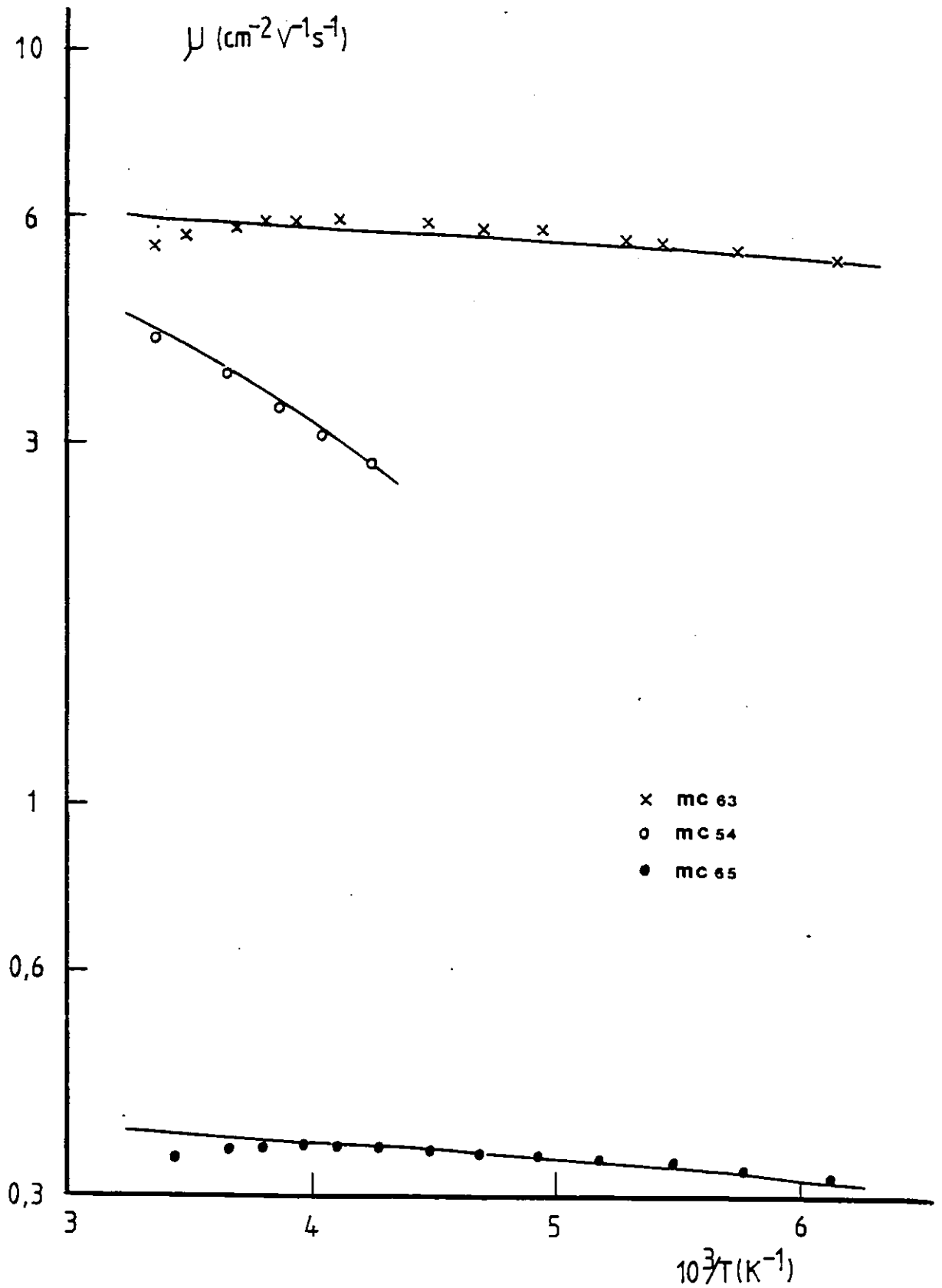

Fig. 4.36: Curve Fits (solid lines) to Experimental Mobility using the Ionised Impurity Scattering Model

This indicates that the ionised impurity concentration is related to the carrier concentration as well as to the concentration of compensating donors in the p-type semiconductor. Usually the latter is not known and so N_i must be taken as a fitting parameter to bring experiment and theory into close agreement.

Using the above approach, the fit of ionised impurity mobility to the experimental results has been tried for our $CuInSe_2$ samples and results for typical p-type and n-type films are given in Fig. 4.36, where the experimental points are shown as dots and crosses and the solid lines represent theory.

It is apparent that over most of the temperature range, the calculated ionised impurity scattered mobilities fit the experimental data quite well. This indicates that this scattering model may explain the mobilities and their temperature dependence in $CuInSe_2$ films. The theoretical fits to these three representative samples were obtained by taking N_i to be 4.1×10^{20} cm^{-3} for sample MC54, 3.4×10^{21} cm^{-3} for MC65 and 1.5×10^{20} cm^{-3} for sample MC63. In all fits the ionised impurity concentration that gave good agreement between theory and experiment was determined to be much higher than the measured carrier concentrations. This indicated that the $CuInSe_2$ films in this investigation are compensated with $P < N_D < N_A$ for the p-type films and $n < N_A < N_D$ for the n-type films.

In conclusion,the temperature dependence of the mobility of p- and n-type $CuInSe_2$ films, is described by dominant ionised impurity scattering, which leads to an increase in mobility with increasing temperature.

4.5 SUMMARY

The optical transmission and reflection of $CuInSe_2$ films, in the wavelength region 0.6-2.5 μm, confirmed that unannealed films were inhomogeneous. Annealed films displayed an absorption coefficient which

varied very sharply around ~1.2 μm and the analysis in this region yielded a direct band gap with E_g = 1.01 eV in very good agreement with published data for bulk $CuInSe_2$.

The optical measurements also enabled the refractive index of $CuInSe_2$ to be determined and new data for the wavelength region $0.7 < \lambda < 1.7$ μm were obtained. Outside this wavelength range our values compared quite well with recently published data.

Overall, the optical measurements confirmed that the $CuInSe_2$ films in this study were of good quality.

The electrical properties of the films were determined by D.C. resistivity, Hall effect and thermoelectric power measurements. The samples in the as-deposited state were p-type with very low resistivities in the range 10^{-4} - 10^{-3} Ω cm. The metallic behaviour of these films was attributed to Cu_3Se_2 in the inhomogeneous stratified layers.

A heat treatment at 350°C in inert gas and deposition onto hot substrates at ~250°C were found to result in p-type films with resistivities in the range 10^{-2} - 10^{-1} Ω cm. These resistivities could be obtained consistently with the preparative method adopted, but a few films turned out to be either high resistivity p-type or even n-type. This was attributed to the inhomogeneity of the starting bulk material, which contained, as determined by XRD and EPMA, various amounts of copper selenide as second phase.

Prolonged anneals at 350°C resulted in the decrease in carrier concentration of the p-type films whilst it had the opposite effect on n-type films. These effects were discussed in the light of intrinsic and extrinsic impurities in $CuInSe_2$ and it was concluded that a net loss of indium from the films could explain the observations.

Annealing of films at a higher temperature of 450°C resulted in p-type films being converted to n-type. The X-ray analysis had shown that

In_2O_3, a very low resistivity n-type semiconductor, had formed during such anneals. A two-layer model consisting of an n-type oxide on p-type $CuInSe_2$ was considered and this could explain the p- to n-type conversion qualitatively.

From the measurement of electrical properties as a function of temperature, it was determined that the n-type and low resistivity p-type $CuInSe_2$ samples had a degenerate carrier population independent of temperature. On the other hand, high resistivity p-type samples had a carrier density which increased with temperature with an activation energy in the range 0.07 - 0.10 eV being due to carrier excitation from one of the acceptor levels in $CuInSe_2$.

The mobilities of the degenerate p- and n-type samples were very similar and increased slightly with increase in temperature, whilst the non-degenerate p-type samples exhibited a much steeper rise of mobility with temperature. Scattering mechanisms pertinent to thin polycrystalline films such as surface scattering, dislocation scattering, grain boundary scattering and potential barrier scattering, were all considered in the mobility analysis. None of these were the mobility limiting mechanism; instead a good fit with experimental data was obtained using ionised impurity scattering as the model, which also indicated that the films were compensated.

REFERENCES - CHAPTER 4

(1) V.S. VAVILOV, "Effects of radiation on semiconductors". Consultant Bureau, New York (1965)

(2) T.S. MOSS, "Optical properties of semiconductors", Butterworths (1959)

(3) W. NAZAREWICZ, P. ROLLAND, E. da SILVA and M. BALKANSKI, "Abac chart for fast calculation of the absorption and reflection coefficients". Appl. Opt. 1 369 (1962)

(4) O.S. HEAVENS, "Optical properties of thin films". Butterworths (1955)

(5) L. HARRIS, J.K. BEASLEY and A.L. LOEB, "Reflection and transmission of radiation by metal films and the influence of non-absorbing backings". J. Opt. Soc. Amer. 41, 604 (1951)

(6) R.A. SMITH, "Semiconductors". Cambridge University Press (1978)

(7) T.S. MOSS, "Semiconductor Opto-electronics". Butterworths (1973)

(8) J.I. PANKOVE, "Optical processes in semiconductors". Dover Publications (1971)

(9) K. LÖSCHKE, H. NEUMANN, R.D. TOMLINSON, W. HÖRIG, E. ELLIOTT, N. AVGERINOS and L. HOWARTH, "Optical constants of $CuInSe_2$ and $CuInTe_2$". Phys. Stat. Sol. (a) 61 K39 (1980)

(10) W. HÖRIG, H. NEUMANN, V. SAVELEV and J. LAGZONIDAS, "Refractive indices of $CuInSe_2$, $CuInTe_2$ and $CuGaTe_2$". Phys. Lett. 78A, 189 (1980)

(11) H. SOBOTA, H. NEUMANN, V. RIEDE, G. KÜHN, J. SELTMANN and D. OPPERMANN, "Influence of impurities and free carriers on the optical properties of $CuInSe_2$". Phys. Stat. Sol. (a) 60, 531 (1980)

(12) J.N. GAN, J. TAUC, U.G. LAMBRECHT, Jr. and M. ROBBINS, "Optical properties of the $(CuInSe_2)_{1-x}(2ZnSe)_x$ system". Phys. Rev. B12, 5797 (1973)

(13) V.I. FISTUL, "Heavily doped semiconductors", Plenum Press (1969)

(14) E.H. PUTLEY, "Hall effect and related phenomena". Butterworths (1960)

(15) R.L. PETRITZ, "Theory of an experiment for measuring the mobility and density of carriers in the space charge region of a semiconductor surface." Phys. Rev. 110, 1254 (1958)

(16) J. VOLGER, "Note on the Hall potential across an inhomogeneous conductor". Phys. Rev. 79, 1023 (1950)

(17) R.H. BUBE, "Interpretation of Hall and Photo-Hall effects in inhomogeneous materials". Appl. Phys. Letts. 13, 136 (1968)

(18) J.W. ORTON and M.J. POWELL, "The Hall effect in polycrystalline and powdered semiconductors". Rep. Prog. Phys. 43, 1263 (1980)

(19) G.H. BLOUNT, R.H. BUBE and A.L. ROBINSON, "Interpretation of equilibrium and steady-state Hall and thermoelectric effects in inhomogeneous materials". J. Appl. Phys. 41, 2190 (1970)

(20) J.J. ERHOT and J. VLCEK, "Seebeck effect in polycrystalline semiconductors". Thin Solid Films 92, 259 (1982)

(21) A. MANY, Y. GOLDSTEIN and N.B. GROOVER, "Semiconductor Surfaces". North-Holland (1964)

(22) P.W. LI, R.A. ANDERSON and R.H. PLOUNICK, "Dielectric constant of $CuInSe_2$ by capacitance measurements". J. Phys. Chem. Solids 40, 333 (1979)

(23) J.C. ANDERSON, "Conduction in thin semiconductor films". Adv. Phys. 19, 311 (1970)

(24) J.C. ANDERSON, "Polycrystalline semiconductor thin films". Vacuum 27, 263 (1977)

(25) D.L. DEXTER and F. SEITZ, "Effects of dislocations on mobilities in semiconductors". Phys. Rev. 86, 964 (1952)

(26) S.M. SZE, "Physics of Semiconductor Devices". Wiley-Interscience (1969)

(27) J.S. BLAKEMORE, "Solid State Physics", 2nd edition, W.B. Saunders Co. (1974)

(28) J.Y.W. SETO, "The electrical properties of polycrystalline silicon films". J. Appl. Phys. 46, 5247 (1975)

(29) T. SAITOH and S. MATSUBARA, "Electrical properties of n-type polycrystalline indium phosphide films". J. Electrochem. Soc. 124, 1065 (1977)

(30) J. PARKES, R.D. TOMLINSON and M.J. HAMPSHIRE, "Electrical properties of $CuInSe_2$ single crystals". Sol. State Electron. 16, 773 (1973)

(31) H. HAUPT and K. HESS, "Growth of large $CuInSe_2$ single crystals". Third Intern. Conf. on Ternary Comp9unds, Edinburgh (April 1977), p.5 Institute of Physics Conf. Series No. 35

(32) W. GEE and M. GREEN, "An improved hot-probe apparatus for the measurement of Seebeck coefficient". J. Phys. E., Sci. Instr. 3, 135 (1970)

(33) G.T. MEADEN, "Electrical resistance of metals". Butterworths (1966)

(34) M. MAVLONAVA, "Temperature dependences of the electrical conductivity and thermo-emf of thallium and indium selenides". Inorg. Matls. 17, 867 (1981)

(35) R.A. ZINGARO and W.C. COOPER, "Selenium". Van-Nostrand Reinhold (1974).

(36) R.D. BARNARD, "Thermoelectricity in metals and alloys". Taylor and Francis Ltd. (1972)

(37) R.C. WEAST, "CRC Handbook of Chemistry and Physics". F.171 (1980). Chemical Rubber Co. Inc.

(38) Z. OGORELEC and D. SELINGER, "Some electrical properties of synthetic klockmannite, CuSe". J. Mats. Sci. 6, 136 (1971)

(39) O.O. ASTRAKOU and A.B. IVANOVA, "Electrical transfer phenomena in copper selenide at low temperatures". Inorg. Matls. 10, 466 (1974)

(40) H.O. KIMURA, T. MATSUMAE and R. MAKABE", "Electrical properties of $Cu_{2-x}Se$ thin films and their application for solar cells". Thin Solid Films 71, 53 (1980)

(41) T. IRIE, S. ENDO and S. KIMURA, "Electrical properties of p- and n-type $CuInSe_2$ single crystals". Jap. J. Appl. Phys. 18, 1303 (1979)

(42) H. NEUMANN, H. SOBOTA, W. KISSINGER, U. RIEDE and G. KÜHN, "Hole effective masses in $CuInSe_2$", Phys. Stat. Sol. (b) 108, 483 (1981)

(43) S.S. STRLENCHENKO, S.A. BONDAR, A.O. MOLODYR, L.I. BERGER and A.E. BALANEVSKAYA, "Mass spectrometric investigation of the sublimation of certain ternary semiconductors of the $A^{I}B^{III}C_2$ type". Inorg. Matls. 5, 502 (1969)

(44) C.A. PAN and T.P. MA, "Evaporation of high quality In_2O_3 films from In_2O_3/In source". J. Electrochem. Soc. 128, 1953 (1981)

(45) D. LASER, "Properties of indium oxide films prepared by the reactive evaporation of indium". Thin Solid Films 90, 317 (1982)

(46) B. SCHUMANN, C. GEORGE, A. TEMPEL, G. KÜHN, V. VAN-NAM, H. NEUMANN and W. HÖRIG, "Epitaxial layers of $CuInSe_2$ on GaAs". Thin Solid Films 52, 45 (1978)

(47) A.C. BEER, "Galvanomagnetic effects in semiconductors". Solid State Phys. Suppl. 4, Academic Press (1963)

CHAPTER 5

CONCLUSIONS

The work presented in this thesis has been concerned with the preparation and characterisation of single phased $CuInSe_2$ films.

When films containing multi-elements are grown, it is very important that these have the correct ratio of the constituent elements, otherwise the resulting films will not be homogeneous. To overcome this problem, different techniques have been used to prepare $CuInSe_2$ films, with varying success and reported in the literature. In this study a simple evaporation method was adopted, whereby a small charge of bulk $CuInSe_2$ powder was evaporated to completion at a very fast rate.

As the composition of the films using such a technique will be expected to be related to that of the starting material, the composition of the bulk $CuInSe_2$ was determined by Electron Probe Microanalysis. X-ray diffraction techniques were also used to verify the chalcopyrite structure of $CuInSe_2$ and to check the homogeneity of the bulk ingot.

The above techniques showed that the bulk contained varying amounts of Cu_3Se_2 precipitates having dimensions of the order of ten microns. The composition of the matrix $CuInSe_2$ varied within the bulk material and excess solubility for Se and In_2Se_3, but absence of solubility for Cu_xSe was determined in the different parts of the ingot. This inhomogeneity thus necessitated the careful comparison of the properties of films prepared from material obtained from the different sections of the bulk $CuInSe_2$.

X-ray diffraction of the powders indicated the presence of Bragg reflections which were additional to those tabulated in the literature for $CuInSe_2$ and Cu_3Se_2. Structure factor calculations on the allowed

hk& reflections of the chalcopyrite structure confirmed that these spurious lines were due to weak and unreported $CuInSe_2$ reflections.

In order to establish the experimental conditions necessary to yield films with the correct composition, the evaporation rates of the powders have been measured using an oscillating quartz crystal microbalance. The nature of the evaporating species as evaporation progressed was determined by composition analysis of condensates obtained at different stages of evaporation.

Three distinct evaporation regimes were identified. The first occurred at low temperatures and was associated with excess second phase material in the ingot. The second regime was due to the dissociation of $CuInSe_2$ into In-Se, whilst the third regime was due to the remaining Se-Cu in the boat, once all the indium from the finite copper indium selenide charge was depleted. These experiments indicated that boat temperatures greater than 1500°C are needed, to evaporate $CuInSe_2$ to completion, so as to preserve the stoichiometry of the films.

The structure of the films, as investigated by X-ray diffraction and transmission electron microscopy techniques, revealed that films deposited onto cold substrates were stratified consisting of amorphous In_2Se and crystalline Cu_3Se_2 and $CuInSe_2$ phases. When these films were heat treated at 350°C in inert gas, conversion to polycrystalline $CuInSe_2$ was achieved. Single phased films could also be prepared by depositing directly onto heated substrates held at 250°C. The homogeneous $CuInSe_2$ films were found to have a fibre texture with a predominant (112) preferred orientation. The grain size distribution of the films indicated that the mean crystallite size was approximately equal to the film thickness, and that no significant increase occurred for anneals longer than 3 hours.

The chemical composition of films deposited at substrate temperatures of 250°C and of those annealed at 350°C, were consistently indium and

selenium rich. This was the same irrespective of the starting powders taken from different sections of the bulk ingots and the composition of all the films lay on the $CuInSe_2$ - InSe join of the ternary phase diagram.

Films deposited at substrates held at temperatures higher than 300°C were selenium deficient and had Cu_7In_4 as a second phase. Homogeneous single phased films annealed at 450°C were also Selenium deficient but contained In_2O_3 as a result of the thermal oxidation of $CuInSe_2$.

The optical transmission and reflection measurements of single phased $CuInSe_2$ films gave a mean refractive index of 2.65 at wavelengths well beyond the fundamental absorption edge. The analysis of the absorption coefficient above the absorption edge resulted in a direct band gap of 1.01 eV, in very good agreement with published single crystal data.

The electrical properties of $CuInSe_2$ films as determined by D.C. resistivity, Hall effect and thermoelectric power measurements, indicated that films deposited at temperatures below about 250°C were p-type with resistivities in the range 10^{-4}-10^{-3} Ω cm. The metallic behaviour of the layers was due to Cu_3Se_2 phase in the films, which dominated the transport properties.

Films deposited at substrates of 250°C and films deposited onto cold substrates followed by an anneal at 350°C in inert gas were consistently p-type with resistivities in the 10^{-2}-10^{-1} Ω cm range. However due to the inhomogeneity of the starting material, a few films annealed at 350°C were somewhat of higher resistivity and some were even n-type. The chemical compositions of these films were not significantly different from the low resistivity p-type films, indicating that the small change in stoichiometry is sufficient to give them their somewhat different electrical properties.

Prolonged annealing at 350°C of p-type films resulted in the increase in carrier concentration, whereas it resulted in the decrease in carrier

density of n-type films. This was attributed to the net loss of indium from the films during the heat treatment.

Annealing at 450°C resulted in the eventual conversion from p- to n-type conductivity of the films. Such heat treatment was shown to coincide with the formation of In_2O_3 and a two layer model consisting of highly conducting n-type oxide film on p-type $CuInSe_2$ films was considered to explain the experimental results qualitatively.

The carrier populations of the highly conducting p-type and n-type films were determined to be constant and degenerate over the temperature range -125 to 30°C. On the other hand, the carrier concentrations of the high resistive p-type samples increased with increase in temperature and the activation energies of around 0.08 eV were interpreted as due to carrier excitation from one of the acceptor levels of $CuInSe_2$.

The mobility of all the p- and n-type samples increased with increasing temperature. Scattering mechanisms pertinent to thin polycrystalline films were not found to fit the experimental data, but ionised impurity scattering, taking into account the degeneracy of the carrier population, was considered to be the mobility limiting mechanism.

This study has shown that homogeneous $CuInSe_2$ films can be reproducibly prepared by evaporating the bulk material. Deposition of films onto cold substrates, followed by an anneal at 350°C or deposition onto substrates held at 250°C were established to be the conditions necessary to obtain single phased films with reproducible chemical compositions. In either method, the electrical properties were essentially similar and repeatable between deposition runs, but it may be more convenient to use cold rather than hot substrates.

While the $CuInSe_2$ films prepared in this work have carrier concentrations too high for thin film transistor applications, their low resistivity and good optical properties make them suitable for thin

film solar cells. The requirement for a p-$CuInSe_2$/n-CdS photovoltaic cell is a chalcopyrite layer having resistivity in the range 10^{-2}-1.0 Ω cm[1]. Piekoszewski et al[2] have prepared cells with efficiencies of 5%, by evaporating CdS onto RF sputtered p-$CuInSe_2$ films, whilst 6.6% efficient cells have been reported for p-$CuInSe_2$ films prepared by double source evaporation of $CuInSe_2$ and Se[3]. Recently, Mickelsen et al[4] have succeeded in producing heterojunction solar cells with efficiencies up to 9.4% by three source elemental evaporation of Cu, In and Se. All the above methods of preparation of $CuInSe_2$ film are more complex and difficult to reproduce whilst the simple evaporation method adopted in this study offers a low cost and more controllable process for the fabrication of the chalcopyrite film.

As far as preparing $CuInSe_2$ films suitable for TFT applications is concerned, several approaches may be worthy of investigation. In single crystals a net loss of selenium had been found to give rise to high resistivity p-type and also n-type samples[5]. Hence more experiments using hot substrates in small steps between 250°C and 300°C may define a short temperature interval where the required low carrier concentrations may be achieved. Alternatively the slight change in stoichiometry may be achieved through the evaporation charge, if it is recalled that excess indium or copper in $CuInSe_2$ gives rise to n-type crystals[5]. By adding suitable amounts of Cu or In into the evaporating powder charge, low carrier density films may be obtained.In this respect the addition of copper may be preferred because the films were already indium rich and any more indium incorporated into the films may result in secondary phases precipitating out.

REFERENCES - CHAPTER 5

(1) N. ROMEO, "Solar cells made by chalcopyrite materials". Japan J. Appl. Phys. 19 (Supplement 19-3) 5 (1980)

(2) J. PIEKOSZEWSKI, J.J. LOFERSKI, R. BEAULIEU, J. BEALL, B. ROESSLER and J. SHEWCHUN, "RF-sputtered $CuInSe_2$ thin films", Solar Energy Mater. 2, 363 (1980).

(3) L.L. KAZMERSKI, "The utilisation of I-III-VI_2 ternary compound semiconductors in thin film heterojunction and homojunction photovoltaic devices". Third Intern. Conf. on Ternary Compounds, Edinburgh (April 1977) p.217 (Inst. of Physics Conf. Series No. 35)

(4) R.A. MICKELSEN and W.S. CHEN, "Development of a 9.4% efficient thin film $CuInSe_2$/CdS solar cell". Proc. 15th IEEE Photovoltaic Specialists Conf., Florida, 1981 p.800, IEEE, New York (1981)

(5) P. MIGLIORATO, J.L. SHAY, H.M. KASPER and S. WAGNER, "Analysis of the electrical and luminescent properties of $CuInSe_2$". J. Appl. Phys. 46, 1777 (1975)